UAB
Universitat Autònoma de Barcelona

UNIVERSIDAD AUTÓNOMA DE BARCELONA (UAB)

Department of Physics
Institut de Física d'Altes Energies (IFAE)

Study of Gravitational Waves using the LIGO/Virgo data

PhD thesis by

Alba Romero-Rodríguez

Director:
Prof. Dr., Mario Martínez-Pérez

Tutor:
Prof. Dr., Eduard Massó

Year 2022

Acknowledgements

There are many people I must thank for the development of this thesis and the wonderful years that I have spent doing my PhD.

First I would like to thank my supervisor, Mario Martínez, for giving me the opportunity to do this PhD under his supervision and for his feedback on the writing of this thesis. I would like to thank Lluïsa M. Mir for her continuous support through these years, and for having gone through all the hardships of the process of submissions and reviews with me.

I have been very fortunate to learn from Hiro Yamamoto and no amount of words can describe how thankful I am for all that he has taught me over the years. His passion and patience are unmatched and I will always be grateful to him for helping me grow from an enthusiastic, optimistic but mostly confused student to who I am today. Our weekly call on Thursdays would be one of the highlights of my week as Hiro would have the answer to any question or problem that I would be stuck on. My gratitude is immeasurable and I will always keep Hiro in a very special part of my heart as my mentor and friend.

I would like to thank my close collaborators whom I had the pleasure of working with. This especially includes Andrew Matas and Tom Callister for their clear explanations, help, and constant support. Andrew's guidance was essential for me to be part of the gravitational wave background community. I will be forever grateful and honored for the wonderful year I had the chance to spend learning from him. Tom taught me the powerful tool of Bayesian searches, without which none of the major work I have produced during this PhD would have been possible. They are one of the most intelligent yet humble people I know and I look up to both of them as my role models. I would like to thank Mairi Sakellariadou, Ville Vaskonen, Oriol Pujolàs, Huai-Ke Guo, Feng-Wei Yang, and Yue Zhao for always feeding my curiosity and answering all my questions, no matter how simple or silly they were. I also feel very lucky to have had the chance to learn from the brilliant minds of Shivaraj Kandshasamy, Vuk Mandic, and Joe Romano in all the meetings, conferences, and summer schools that we attended.

I would like to thank everyone who contributed to my experience at IFAE, including Machiel Kolstein for helping me set my foot when I started at IFAE, and everyone in the workshop, especially Laia, Otger, Pepe, and Óscar for helping me solve all the problems I would encounter with the calibration measurements, the optical setup and the computer in the laboratory.

I would like to give a million thanks to Irene and Federico for taking Alexis and me as their mentees when we had just started at VIRGO. Having spent the first couple of months of our PhD with them was one of the best possible ways to get started in this field. Their always cheerful smiles, constant support, and explanations helped us feel comfortable and develop a sense of belonging. I would also like to thank Annalisa, Julia, Maria, and Antonino. Annalisa was the one who introduced me to SIS and made me embark on such a wonderful path. Julia took us as her wards as soon as we reached Virgo and what started as a "circumstantial friendship" because of her being the only Spanish in Virgo has become a real friendship. Maria's presence was enough to spread contagious happiness all around the room. I would like to thank her for having made these times so cheerful. I think I had never laughed more than when Antonino was around as even though he is a very serious person when it comes to work, his occasional jokes always lighten up the mood.

Para papá y mamá. Gracias por todo.

Contents

Introduction

General Relativity predicted the existence of gravitational waves in 1916. However, it was not until September 14th, 2015 that the LIGO interferometers made the first gravitational wave detection. After several analyses, it could be concluded that the source of these gravitational waves was the merger of a binary of black holes, named after its detection date, GW150914. To this date, roughly 100 detections have been claimed by the network of two LIGO interferometers and the Virgo interferometer. These detections have been possible thanks to the increased sensitivity of the detectors, the result of several upgrades the interferometers have undergone. One of the main culprits that compromises the sensitivity is environmental noise. Properly characterizing these noises allows to either subtract them from the analysis or find possible ways to reduce them. One of these noises is scattered light, which can be reduced by using mechanical devices called baffles that absorb this light. The absorbed scattered light is then lost in its majority. However, scattered light contains important information about the scatterer. A new type of baffles instrumented with photodiodes has been designed to retrieve the information from scattered light that was lost until now. As part of the upgrades for Advanced Virgo, these baffles will be installed around the main test masses of the interferometer.

Gravitational waves are not just important probes of massive asymmetric astrophysical bodies, but they can also probe models Beyond the Standard Model in the early Universe. These cosmological models, alongside the contribution from a large number of unresolved astrophysical objects such as binary neutron stars and black holes, are believed to source a background of gravitational waves. The detection of this background would provide essential information about the very early Universe. However, the amplitude of this background is much lower than that of gravitational waves coming from mergers of binary black holes. Hence, a cross-correlation between data from different interferometers is performed to try to estimate the amplitude of the background, though the current sensitivity of the gravitational wave ground-based detectors is still not enough to make a detection. Nevertheless, a rigorous formalism has been derived that allows to constrain the models describing the background. As mentioned above, the background is modeled as the superposition of an astrophysical contribution and a cosmological. Two of these cosmological sources are first-order phase transitions and primordial black holes, which can be constrained according to the above-mentioned formalism.

In this thesis, all of these topics are covered. The basic properties of gravitational waves (GWs) and the main sources are described in Chapter 1. The current ground-based gravitational wave detectors are introduced in Chapter 2. In Chapter 3 a simulation tool used to compute fields in optical systems is introduced, since it is used to understand the light distribution around test masses. Chapter 4 is devoted to an explanation of scattered light and the instrumented baffles. In Chapter 5 the frequentist and Bayesian approaches of statistics are introduced since they are essential to set constraints on the model describing the gravitational wave background (GWB). Chapter 6 is devoted to the GWB and its detection method. Finally, in chapter 7, the GWB is re-interpreted as being sourced by first-order cosmological phase transition or primordial black holes, and constraints on the model parameters are set.

This work has translated into the following publications:

- A. Romero-Rodríguez, M. Martínez, O. Pujolàs, M. Sakellariadou, and V. Vaskonen, "Search for a scalar induced stochastic gravitational wave background in the third ligo-virgo observing run," *Phys. Rev. Lett.*, vol. 128, p. 051301, Feb 2022. [Online].

  Available:https://link.aps.org/doi/10.1103/PhysRevLett.128.051301

- A. Romero, K. Martinovic, T. A. Callister, H.-K. Guo, M. Martínez, M. Sakellariadou, F.-W. Yang, and Y. Zhao, "Implications for first-order cosmological phase transitions from the third ligo-virgo observing run," Phys. Rev. Lett., vol. 126, p. 151301, Apr 2021. [Online]. Available:https://link.aps.org/doi/10.1103/PhysRevLett.126.151301

- A. Romero-Rodríguez, A. Allocca, A. Chiummo, M. Martínez, L. M. Mir, and H. Yamamoto, "Determination of the light exposure on the photodiodes of a new instrumented baffle for the virgo input mode cleaner end-mirror," Classical and Quantum Gravity, vol. 38, no. 4, p. 045002, dec 2020. [Online]. Available:https://doi.org/10.1088/1361-6382/abce6b

- O. Ballester, O. Blanch, L. Cardiel, M. Cavalli-Sforza, A. Chiummo, C. García, J. M. Illa, C. Karathanasis, M. Kolstein, M. Martínez, A. Menéndez-Vázquez, L. M. Mir, J. Mundet, A. Romero-Rodríguez, D. Serrano, and H. Yamamoto, "Measurement of the stray light in the advanced virgo input mode cleaner cavity using an instrumented baffle," Classical and Quantum Gravity, vol. 39, no. 11, p. 115011, may 2022. [Online]. Available:https://doi.org/10.1088/1361-6382/ac6a9d

- e. a. Abbott, R., "Upper limits on the isotropic gravitational-wave background from advanced ligo and advanced virgo's third observing run," Phys. Rev. D, vol. 104, p. 022004, Jul 2021. [Online]. Available:https://link.aps.org/doi/10.1103/PhysRevD.104.022004

- I. Fiori, F. Paoletti, M. C. Tringali, K. Janssens, C. Karathanasis, A. Menéndez-Vázquez, A. Romero-Rodríguez, R. Sugimoto, T. Washimi, V. Boschi, A. Chiummo, M. Cieślar, R. De Rosa, C. De Rossi, F. Di Renzo, I. Nardecchia, A. Pasqualetti, B. Patricelli, P. Ruggi, and N. Singh, "The hunt for environmental noise in virgo during the third observing run," Galaxies, vol. 8, no. 4, 2020. [Online]. Available:https://www.mdpi.com/2075-4434/8/4/82

- A. Cirone, I. Fiori, F. Paoletti, M. M. Perez, A. R. Rodríguez, B. L. Swinkels, A. M. Vazquez, G. Gemme, and A. Chincarini, "Investigation of magnetic noise in advanced virgo," Classical and Quantum Gravity, vol. 36, no. 22, p. 225004, oct 2019. [Online]. Available:https://doi.org/10.1088/1361-6382/ab4974

Chapter 1

Gravitational waves

1.1 General Relativity

General Relativity (GR) is the theory of space, time, and gravitation formulated by Albert Einstein in 1915 [1, 2, 3, 4]. Spacetime can be thought of as a continuum composed of events, which are points of space at a given time. All events can be uniquely characterized by three numbers indicating the spatial position and one indicating the time, $\xi^\mu = (t, x^1, x^2, x^3)$. Given an event denoted by p, the causal structure of spacetime looks like Figure 1.1. Events that lie on the boundary of the set of points to the future of p (represented by blue points in Figure 1.1) cannot be reached by a particle starting from event p but they can be reached by a light signal emitted from p. These events form the light cone future of p. Similarly, a light signal sent from the events in the boundary of the past light cone (represented by yellow) can reach p. Events that are neither in the past nor future light cone are spacelike related to p, i.e.: they are not causally related to p.
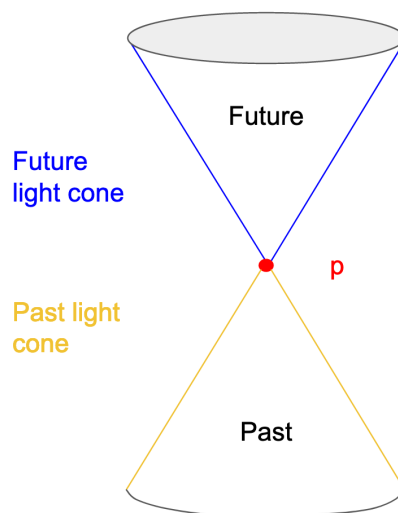
Figure 1.1: Causal structure of spacetime for event p. The future light cone of p is represented in blue. The past light cone of p is represented in yellow.

After special relativity (SR) was proposed, there was still another task left, modifying and reformulating physical laws so that they were consistent with the new notion of spacetime. Maxwell's theory of electromagnetism (EM) was already consistent with SR. Two key ideas motivated Einstein to develop GR. First of all, all bodies are influenced by gravity and they fall the same way in a gravitational field. This is known as the *equivalence principle*. The paths of freely falling bodies (bodies not influenced by any external force) define a preferred set of curves in spacetime known as *geodesics*, independent of the bodies' nature. This suggests the possibility of associating properties of the gravitational field to

the structure of spacetime. The second was Mach's principle, which states that all the matter in the Universe should contribute to the local definition of non-accelerating and non-rotating bodies [5]. GR states that the intrinsic, observer-independent, properties of spacetime are described by a spacetime metric $g_{\mu\nu}$ which is a function of the coordinates mentioned above, $\xi^\mu = (t, x^1, x^2, x^3)$. This metric is not necessarily flat and can have some curvature, which is defined as the deviation from flat spacetime and it accounts for the effects related to a gravitational field [5]. Furthermore, the stress energy-momentum tensor, $T_{\mu\nu}$, represents the mass-energy content that produces the curvature. The components of this tensor can be understood as the energy density, T_{00}, the energy flux in the i-th direction $T_{0i} = T_{i0}$ (also known as the density of i-momentum), and finally the flux of the i-momentum in the j-direction, T_{ij}. The stress energy-momentum tensor is related to the curvature of spacetime via Einstein's equations. The curvature of spacetime is represented by the Riemann curvature tensor

$$R^\sigma_{\mu\lambda\nu} \equiv \partial_\lambda \Gamma^\sigma_{\mu\nu} - \partial_\nu \Gamma^\sigma_{\mu\lambda} - \Gamma^\rho_{\mu\nu} \Gamma^\sigma_{\rho\lambda} - \Gamma^\rho_{\mu\lambda} \Gamma^\sigma_{\rho\nu}, \tag{1.1}$$

where ∂_λ represents the partial derivative with respect to a coordinate x^λ and $\Gamma^\alpha_{\beta\gamma}$ are the Christoffel symbols, defined as

$$\Gamma^\alpha_{\beta\gamma} \equiv \frac{1}{2} g^{\alpha\epsilon} (\partial_\gamma g_{\beta\delta} + \partial_\beta g_{\gamma\delta} - \partial_\delta g_{\beta\gamma}). \tag{1.2}$$

The *equivalence principle* mentioned above has major implications. Let us consider that we are measuring an EM field in special relativity. To start with the experiment, we have to set up an observer not affected by an EM field. Then, a charged test body is released and by observing the difference in path between the path it takes and the one it would have taken under no influence of an EM field, the force exerted by the field can be calculated. For gravitation this cannot be done, since the *equivalence principle* states that all bodies, even observers, are affected by the gravitational force. This is the basis of the theory of GR. GR states that spacetime must be curved in all situations where a gravitational field is present. The laws of Physics in GR are governed by two principles

- *General covariance*, which states that the metric of spacetime and quantities derived from it are the only spacetime quantities appearing in the equations of Physics [5]. In many treatments, it is assumed that a coordinate system has been chosen and the equations of Physics have been written in terms of the coordinate basis. If general covariance was violated by the existence of a preferred vector v_a, it would be possible to adapt a coordinate system so that $(\partial/\partial x^1)_a = v_a$. If the components of an equation of physics were written without incorporating v_a but instead substituting it by $(1, 0, ...0)$, the form of the equation would not be preserved when performing a coordinate transformation, violating $(\partial/\partial x^1)_a = v_a$. This would imply that the equations are not preserved under general coordinate transformations [5].

- Equations must reduce to the equations satisfied in special relativity when the metric is flat.

As mentioned above, GR asserts that the spacetime geometry is influenced by the matter distribution in the Universe. The spacetime is thus a dynamical variable that responds to the matter content of spacetime. The equations that describe the relationship between spacetime geometry and matter distribution are the Einstein's equations

$$R_{\mu\nu} - \frac{1}{2} g_{\mu\nu} R = -\frac{8\pi G}{c^4} T_{\mu\nu}, \tag{1.3}$$

where $R_{\mu\nu}$ is the Ricci tensor and R is the Ricci scalar, which are obtained computing derivatives of the metric $g_{\mu\nu}$. The Ricci tensor is the contraction of the Riemann tensor $R_{\mu\nu} \equiv R^\lambda_{\mu\lambda\nu}$ and the Ricci scalar the contraction of the Ricci tensor with the metric $R = g^{\mu\nu} R_{\mu\nu} = R^\mu_\mu$. Einstein's equations are ten equalities and not sixteen because $R_{\mu\nu}$, $g_{\mu\nu}$ and $T_{\mu\nu}$ are symmetric [6]. In what follows, these ten equations will also be referred to as ten degrees of freedom.

When gravity is "weak", an approximation known as *linearized gravity* is used. In nature, this approximation is good except for phenomena dealing with gravitational collapse and black holes or with the large-scale structure of the universe [5]. In *linearized gravity*, spacetime is nearly flat. The metric can thus be expressed as the flat metric $\eta_{\mu\nu} = diag(-1, 1, 1, 1)$, *Minkowski* metric, plus a small deviation $|h_{\mu\nu}| << 1$: $g_{\mu\nu} = \eta_{\mu\nu} + h_{\mu\nu}$ [7]. Another useful approximation is the Newtonian limit, used when gravity is weak, the relative motion of the sources is much slower than the speed of light, and the

material stresses are much smaller than the mass-energy density. In this limit, all GR predictions reduce to those of Newtonian gravity. In what follows, *linearized gravity* is assumed unless stated otherwise.

In field theories, different configurations of the unobservable fields can lead to the same observable quantities. For instance, in EM the electric and magnetic fields (denoted by E and B, respectively) are observable, while the potential V and vector potential A are not. A transformation that alters non-observable properties of fields (such as V and A) without changing the physically-meaningful measurable magnitudes (such as the intensity, which is proportional to $|E|^2$) is called a *gauge transformation* [8]. The fact that measurable quantities are not changed is known as *gauge invariance*. Since any invariance under a field transformation is a symmetry, *gauge invariance* is sometimes called *gauge symmetry*. If the transformation is chosen wisely, the form of the field equations can be simplified. This is the case with Einstein's equations. Small coordinate translations can be applied to the perturbed spacetime metric, still satisfying the condition $|h_{\mu\nu}| << 1$. For instance, the transformation $x^\mu \to x'^\mu = x^\mu + \xi^\mu(x)$ can be used, where ξ^μ are four arbitrary functions and the derivatives $|\partial_{\mu\nu}\xi^\mu|$ are of the same order as the metric perturbations $|h_{\mu\nu}|$. With this transformation of coordinates, the metric will transform as

$$g'_{\mu\nu}(x') = \frac{\partial x^\rho}{\partial x'^\mu}\frac{\partial x^\sigma}{\partial x'^\nu}g_{\rho\sigma}(x) = \eta_{\mu\nu} + h'_{\mu\nu}, \tag{1.4}$$

where $h'_{\mu\nu}(x')$ is the perturbation in the new coordinates and it transforms as

$$h_{\mu\nu}(x) \to h'_{\mu\nu}(x') = h_{\mu\nu}(x) - \partial_\mu\xi_\nu - \partial_\nu\xi_\mu. \tag{1.5}$$

In addition to small coordinate translations, Lorentz rotations of the coordinate system are also allowed $x'^\mu = \Lambda^\mu_\nu x^\nu$, where Λ^μ_ν satisfies $\Lambda^\rho_\mu\Lambda^\sigma_\nu\eta_{\rho\sigma} = \eta_{\mu\nu}$. Under this transformation the metric becomes

$$g'_{\mu\nu}(x') = \eta_{\mu\nu} + \Lambda^\rho_\mu\Lambda^\sigma_\nu h_{\rho\sigma}(x), \tag{1.6}$$

which still satisfies $|h_{\mu\nu}| << 1$. These gauge freedoms can be used to choose a coordinate system that will help to express the Einstein's equations in the weak field limit in a simplified form. One of the two definitions that simplify Einstein's equations is the trace reverse of $h_{\mu\nu}$, defined as

$$\bar{h}_{\mu\nu} \equiv h_{\mu\nu} - \frac{1}{2}\eta_{\mu\nu}h, \tag{1.7}$$

where h is the trace of $h_{\mu\nu}$, i.e.: $h \equiv h^\mu_\mu$. Under a transformation of coordinates of the kind $x^\mu \to x'^\mu = x^\mu + \xi^\mu(x)$, $\bar{h}_{\mu\nu}$ transforms as

$$\bar{h}_{\mu\nu} \to \bar{h}'_{\mu\nu} = \bar{h}_{\mu\nu} - (\partial_\mu\xi_\nu + \partial_\nu\xi_\mu - \eta_{\mu\nu}\partial_\rho\xi^\rho). \tag{1.8}$$

The definition in Eq. (1.7) reduces the left hand side of Eqs. (1.3) to

$$R_{\mu\nu} - \frac{1}{2}g_{\mu\nu}R = \frac{1}{2}(\partial^\sigma\partial_\mu\bar{h}_{\sigma\nu} - \partial^\sigma\partial_\sigma\bar{h}_{\mu\nu} + \partial_\nu\partial_\alpha\bar{h}_{\mu\alpha} - \eta_{\mu\nu}\partial^\alpha\partial_\beta\bar{h}_{\alpha\beta}). \tag{1.9}$$

The other condition relies on the gauge freedom, Eq. (1.5), which allows choosing the harmonic gauge condition or Lorentz gauge [9]

$$\partial^\nu\bar{h}_{\mu\nu} = 0. \tag{1.10}$$

This Lorentz gauge fixes four of the ten degrees of freedom that the tensor $h_{\mu\nu}$ could have. In this Lorentz gauge, Einstein's equations, Eqs. (1.3), are simplified to

$$\Box\bar{h}_{\mu\nu} \equiv \partial^\sigma\partial_\sigma\bar{h}_{\mu\nu} = -\frac{16\pi G}{c^4}T_{\mu\nu}, \tag{1.11}$$

where $\Box \equiv \eta_{\mu\nu}\partial^\mu\partial^\nu = \partial_\mu\partial^\nu$ is the flat space d'Alembertian. The weak field equations, Eq. (1.11), can be considered far away from any source of mass or energy such that $T_{\mu\nu} = 0$. In this case, it is a 4-dimensional wave equation whose simplest solutions are plane waves[1]. The plane wave equation is

$$\bar{h}^{\mu\nu} = A^{\mu\nu}e^{ik_\alpha x^\alpha}, \tag{1.12}$$

---

[1] More complicated GWs of arbitrary shape and spectral structure can be expressed as a superposition of monochromatic plane waves [10].

where $A^{\mu\nu}$ is a matrix with constant components and $k_\alpha = (\omega, k_i)$ is the wave vector, that satisfies $k^\alpha k_\alpha = 0$ and ω is the angular frequency of the wave. From $k^\alpha k_\alpha = 0$ it can be concluded that $\omega^2 = |k_i|^2$. Since $|k_i| = \omega/v$, for $\omega^2 = |k_i|^2$ to be satisfied, the speed at which GWs travel must be equal to the speed of light $v = c = 1$. Furthermore, applying the Lorentz gauge condition, Eq. (1.10), to the wave equation and assuming $T_{\mu\nu} = 0$, results in $k_\mu A^{\mu\nu} = 0$. This implies that GWs are transverse.

1.1.1 Schwarzschild solution

As mentioned in the previous section, in the slow-motion weak field limit, the predictions of GR reduce to those of Newtonian theory. However, this limit cannot be used for phenomena dealing with gravitational collapse and black holes and phenomena dealing with the large-scale structure of the universe [5]. In cases where there are very massive bodies that cannot support themselves and thus end up collapsing, the entire spacetime geometry is described by the Schwarzschild solution to the Einstein's equations. The Schwarzschild solution contains information about the strong field behavior of general relativity, since it predicts the departure from Newtonian theory for the motion of planets, it predicts the *bending of light*, the gravitational redshift of light and time delay effects [5].

The Schwarzschild solution which describes the exterior gravitational field of a static, spherically symmetric body of mass M is expressed in terms of spherical coordinates (t, r, θ, ϕ) as

$$ds^2 = -(1 - \frac{2M}{r})dt^2 + (1 - \frac{2M}{r})^{-1}dr^2 + r^2 d\Omega^2, \tag{1.13}$$

where $d\Omega^2 = d\theta^2 + \sin(\theta)d\phi^2$. This solution has major implications. One of them is due to the fact that the metric components are singular when $r = 2M$ and r=0. It can be shown that the singularity at $r = 2M$ is due to a breakdown of the coordinates, i.e.: the coordinates fail to properly cover a region of spacetime. However, we will see that $r = 0$ is a real Physical singularity. To prove this, the Kruskal–Szekeres coordinate transformation is used, which substitutes (t, r) by (T, X), which are related to the old coordinates by

$$\left(\frac{r}{2M} - 1\right)e^{2/(2M)} = X^2 - T^2 \tag{1.14}$$

$$\frac{t}{2M} = \ln\left(\frac{T + X}{X - T}\right) = 2\tanh^{-1}\left(\frac{T}{X}\right) \tag{1.15}$$

From this coordinate transformation the Schwarzschild solution from Eq. (1.13) can be rewritten as

$$ds^2 = \frac{32M^3 e^{-r/(2M)}}{r}(-dT^2 + dX^2) + r^2 d\Omega^2, \tag{1.16}$$

where the notion of r changes to the function derived from Eq. (1.14). From inspection of Eq. (1.16) one can see that $r = 2M$ is no longer a singularity, as mentioned above, while $r = 0$ still remains. The allowed X and T are given by r>0, which yields $X^2 - T^2 > -1$. A spacetime diagram for the Kruskal extension is that in Figure 1.2. Each point in this diagram represents a two-dimensional sphere of radius r. There are four well-identified regions [5]

- Region I corresponds to r > 2M, i.e.: the exterior gravitational field of a spherical body. A radially infalling observer going from region I and reaching region II will never be able to escape. An observer in region I cannot communicate with one in region IV.

- Region II does not allow any light signal to escape and the light will eventually fall into the singularity $r = 0$. Region II is known as a **Black Hole** (BH).

- Region III has the time-reversed properties of region II and is commonly referred to as a white hole.

- Region IV has the same properties as region I. It represents another asymptotically flat region of spacetime that lies "inside" the "radius" r= 2M.

Singularities at $r = 0$ have a spacelike character and exist in the future and past of regions II and III, respectively.
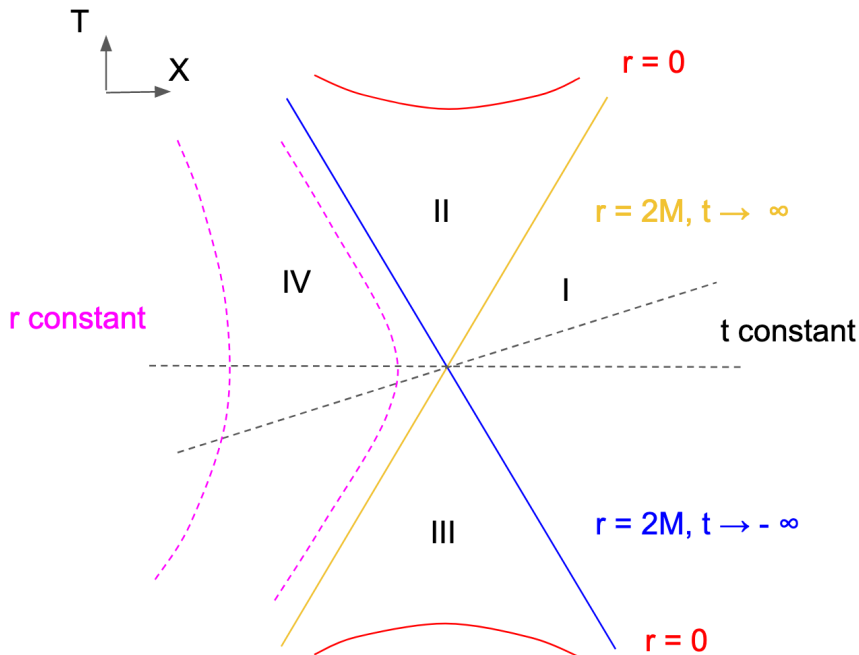
Figure 1.2: Spacetime diagram for the Kruskal–Szekeres extension. Four regions can be differentiated. They are separated by lines of constant r and t. The yellow line corresponds to r=2M and $t \to \infty$ and the blue one to r=2M and $t \to -\infty$. The singularities at $r = 0$ are represented by the red curves. Dashed black lines represent constant time and the pink dashed curves constant r.

1.2   Tranverse Traceless gauge

As already mentioned, an appropriate choice of reference frame or coordinates can simplify Einstein's equations. In this section, we describe a convenient frame known as Tranverse Traceless(TT). In the TT frame, particles that were initially at rest before the passage of the GW will remain at rest during and after the passage of the wave. Note that this is not the usual frame used in real detectors. The usual one is called the detector frame, in which free-falling particles do move due to the passage of a GW [9]. This is the principle of GW interferometry.

In the previous section the Lorentz gauge has been used to demonstrate that gravitational radiation propagates in vacuum as transverse plane waves at the speed of light. However, there are still more gauge freedoms that can be used to further simplify the form of $h_{\mu\nu}$. Under a transformation of coordinates $x^\mu \to x'^\mu = x^\mu + \xi^\mu(x)$, $\partial^\nu \bar{h}_{\mu\nu}$ transforms as

$$\partial^\nu \bar{h}_{\mu\nu} \to (\partial^\nu \bar{h}_{\mu\nu})' = \partial^\nu \bar{h}_{\mu\nu} - \Box \xi_\mu. \tag{1.17}$$

For this reason, the Lorentz gauge, Eq. (1.10), is not spoilt by a further transformation of the sort $x^\mu \to x'^\mu = x^\mu + \xi^\mu(x)$ such that $\Box \xi_\mu = 0$. If $\Box \xi_\mu = 0$, then $\Box \xi_{\mu\nu} = 0$, where $\xi_{\mu\nu} \equiv \partial_\mu \xi_\nu + \partial_\nu \xi_\mu - \eta_{\mu\nu} \partial_\rho \xi^\rho$. From Eq. (1.8) it can be concluded that the functions $\xi_{\mu\nu}$ can be subtracted from the six components $\bar{h}_{\mu\nu}$. This means that ξ^0 can be chosen such that $\bar{h} = 0$. If $\bar{h} = 0$ then $\bar{h}_{\mu\nu} = h_{\mu\nu}$. The three functions $\xi^i(x)$ are chosen so that $h^{0i} = 0$. From $\bar{h}_{\mu\nu} = h_{\mu\nu}$ the Lorentz condition turns into [9]

$$\partial^0 h_{00} + \partial^i h_{0i} = 0. \tag{1.18}$$

Since $h_{0i} = 0$ then Eq. (1.18) turns $\partial^0 h_{00} = 0$, which implies that h_{00} is constant in time. All four components are set to $h_{0\mu} = 0$ and only the spatial components h_{ij} are left, for which the Lorentz

gauge condition is $\partial^j h_{ij} = 0$ and the trace $h^i_i = 0$ [9]. To sum up

$$h^{0\mu} = 0 \quad , \quad h^i_i = 0 \quad , \quad \partial^j h_{ij} = 0, \tag{1.19}$$

which define the transverse-traceless (TT) gauge. The TT gauge implies that the metric is purely spatial $h_{\mu 0} = 0$, the wave is excited transversely to its direction of propagation $\partial_j h_{ij} = 0$, and it is traceless $h^i_i = 0$.

The combined harmonic ($\partial^j h_{ij} = 0$) and TT gauges leave only 2 degrees of freedom in $h_{\mu\nu}$. For GWs propagating in the +z direction, the expression for the metric perturbation of a plane wave is

$$h_{\mu\nu} = \begin{pmatrix} 0 & 0 & 0 & 0 \\ 0 & h_+ & h_x & 0 \\ 0 & h_x & -h_+ & 0 \\ 0 & 0 & 0 & 0 \end{pmatrix}, \tag{1.20}$$

where h_+ is the plus polarization of the GW and h_x is the cross-polarization, given by

$$h_+(t,z) \equiv A_+ \cos(\omega(t - z/c) + \phi_+) \tag{1.21}$$
$$h_x(t,z) \equiv A_x \cos(\omega(t - z/c) + \phi_x). \tag{1.22}$$

A_+ and A_x are the amplitudes of the plus and cross polarizations, respectively, and ϕ_+ and ϕ_x the phases of the plus and cross polarizations, respectively. Each of h_+, h_x by itself corresponds to a linearly polarized wave. Given a plane wave solution $h_{\mu\nu}(x)$ propagating in the direction $\hat{n}$ and far away from the source, the form of the wave in the TT gauge is given in terms of the spatial components h_{ij} of $h_{\mu\nu}$, where the indices {i,j = 1,2,3} represent spatial coordinates. In the TT gauge, the plane wave is thus expanded as

$$h_{ij}^{TT}(x) = \int \frac{d^3k}{(2\pi)^3} (\mathcal{A}_{ij}(\mathbf{k}) e^{ikx} + \mathcal{A}_{ij}^*(\mathbf{k}) e^{-ikx}), \tag{1.23}$$

where $\mathcal{A}_{ij}(\mathbf{k})$ is the amplitude of the wave as a function of $\mathbf{k}$. When GWs are produced by one single point-like source, the direction of propagation of the wave is $\hat{n}_o$, and $\mathcal{A}_{ij}$ can be expressed as

$$\mathcal{A}_{ij}(\mathbf{k}) = A_{ij}(f)\delta^{(2)}(\hat{n} - \hat{n}_o), \tag{1.24}$$

Eq. (1.23) can be re-written using $d^3\mathbf{k} = |\mathbf{k}|^2 d|\mathbf{k}| d\Omega = (2\pi/c)^3 f^2 df d\Omega$ and $d^2\hat{n} \equiv d\cos(\theta)d\phi$ as

$$h_{ij}^{TT}(x) = \frac{1}{c^3} \int_0^\infty df f^2 \int d^2\hat{n}(\mathcal{A}_{ij}(f,\hat{n}) e^{-2\pi i f(t-\hat{n}\mathbf{x}/c)} + \mathcal{A}^*{}_{ij}(f,\hat{n}) e^{2\pi i f(t-\hat{n}\mathbf{x}/c)}). \tag{1.25}$$

The content of the parenthesis represents a wave travelling in the direction $\hat{n}$. The only non-vanishing components are those in the plane transverse to the propagation direction $\hat{n}_o$. The indices in this plane are denoted by {a,b = 1,2}. Then, Eq. (1.25) can be rewritten as

$$h_{ab}(t,\mathbf{x}) = \int_0^\infty df(\tilde{h}_{ab}(f,\mathbf{x}) e^{-2\pi i f t} + \tilde{h}_{ab}^*(f,\mathbf{x}) e^{2\pi i f t}), \tag{1.26}$$

where

$$\tilde{h}_{ab}(f,\mathbf{x}) = \frac{f}{c^3} \int d^2\hat{n} \mathcal{A}_{ab}(f,\hat{n}) e^{2\pi i f \hat{n}\mathbf{x}/c} = \frac{f}{c^3} A_{ab}(f) e^{2\pi i f \hat{n}_o \mathbf{x}/c}. \tag{1.27}$$

The previous equations only accounted for Physical values of frequencies. However, if $f \in R$ and $\tilde{h}_{ab}(-f,\mathbf{x}) = \tilde{h}_{ab}^*(f,\mathbf{x})$ then Eq. (1.26) can be rewritten in a more compact form

$$h_{ab}(f,\mathbf{x}) = \int_{-\infty}^\infty df \tilde{h}_{ab}(f,\mathbf{x}) e^{-2\pi i f t}, \tag{1.28}$$

where $\tilde{h}_{ab}(f,\mathbf{x})$ is the Fourier transform of $h_{ab}(t,\mathbf{x})$. Another useful way of expressing the plane wave expansion is using the polarization tensors $e_{ij}^A(\mathbf{n})$, where A denotes the polarization {+,x} (see

Appendix A). Finally, defining the amplitudes $\tilde{h}_A(f, \hat{n})$ as $f^2/c^3 \mathcal{A}_{ij}(f, \hat{n}) = \sum_{A=+,\times} \tilde{h}_A(f, \hat{n}) e_{ij}^A(\hat{n})$, a further simplification can be made

$$h_{ab}(t, \mathbf{x}) = \sum_{A=+,\times} \int_{-\infty}^{\infty} df \int d^2\hat{n} \tilde{h}_A(f, \hat{n}) e_{ab}^A(\hat{n}) e^{-2\pi i f(t - \hat{n}\mathbf{x}/c)}, \tag{1.29}$$

where $\tilde{h}_A(-f, \hat{n}) = \tilde{h}_A^*(f, \hat{n})$ [9]. The expansion of the plane wave in TT gauge, Eq. (1.29), will be relevant in following chapters.

1.3 GW emission, quadrupole formalism

In this section we show how only bodies with non-null quadrupole moment generate GWs. Any GW that could be observed with the current detectors is weak and linearised gravity can well describe it. However, the source of GWs must have a strong field, and thus a different formalism is needed to describe the GW emission [10]. To leading order, GWs are a form of quadrupole radiation. Let us show how to derive this conclusion following Refs. [9, 6]. Given a source at the origin of the coordinate system and a distant observer displaced by $\mathbf{n}$ from the origin, a solution to Eq. (1.11) can thus be obtained [6]

$$\bar{h}_{\mu\nu}(t, \mathbf{n}) = 4 \int d^3x \frac{1}{|\mathbf{n} - \mathbf{x}|} T_{\mu\nu}(t - |\mathbf{n} - \mathbf{x}|, \mathbf{x}), \tag{1.30}$$

where $|\mathbf{n}|$ is the distance to the observer (see Figure 1.3) and it will be denoted by D. The vector $\mathbf{x}$ are the spatial coordinates of the mass elements generating the gravitational radiation. For a distant observer ($|\mathbf{n}| >> |\mathbf{x}|$, see Figure 1.3), $|\mathbf{n} - \mathbf{x}|$ can be expanded as

$$|\mathbf{n} - \mathbf{x}| = D - \mathbf{x} \cdot \mathbf{n} + \mathcal{O}(r^2/D), \tag{1.31}$$

where r is the typical size of the source. Using this expansion and keeping only dominant terms in $|\mathbf{n} - \mathbf{x}|$, Eq. (1.30) can be rewritten as

$$\bar{h}_{\mu\nu}(t, \mathbf{n}) = \frac{4}{D} \int d^3x T_{\mu\nu}(t - D, \mathbf{x}), \tag{1.32}$$
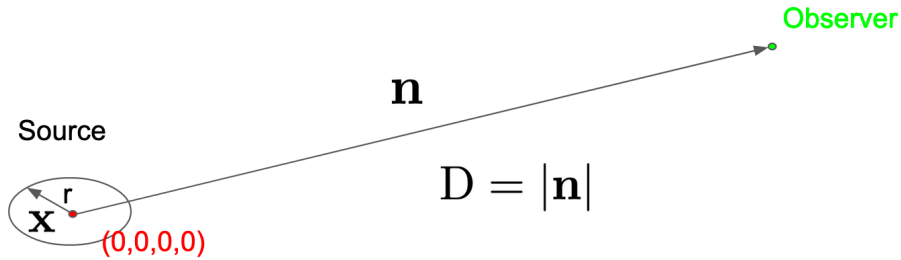
Figure 1.3: GW source located at the origin of the coordinate system and distant observer displaced by $\mathbf{n}$ from the origin. The distance to the observer is $D = |\mathbf{n}|$ and $\mathbf{x}$ are the spatial coordinates of the mass elements generating the gravitational radiation. The observer is assumed to be very distant, i.e.: $|\mathbf{n}| >> |\mathbf{x}|$.

implying the amplitude of a GW decreases linearly with the distance between the source and the observer. Using the TT gauge, a further approximation can be made

$$h_{ij}^{TT}(t, \mathbf{n}) = \frac{4}{D} S_{ij}(t - D), \tag{1.33}$$

where S_{ij} is the first momentum of the stress tensor T_{ij} and is given by

$$S^{ij}(t) = \int d^3x T_{ij}(t, \mathbf{x}). \tag{1.34}$$

To understand the physical meaning of S_{ij}, it is useful to express it in terms of T_{00} and T_{0i}. For that purpose, the first three mass momenta are defined

$$M(t) = \int d^3x T_{00}(t, \mathbf{x}), \tag{1.35}$$

$$M_i(t) = \int d^3x T_{00}(t, \mathbf{x})x_i, \tag{1.36}$$

$$M_{ij}(t) = \int d^3x T_{00}(t, \mathbf{x})x_i x_j. \tag{1.37}$$

The mass monopole momentum is $M(t)$ and, in linearised gravity, it is considered as the total mass of the source. The mass dipole momentum is $M_i(t)$ and $M_{ij}(t)$ is the mass quadrupole momentum. The quadrupole moment takes the form

$$M_{ij}(t) \equiv \rho(t, \mathbf{x})(x_i x_j - \frac{1}{3}r^2\delta_{ij})d^3x \tag{1.38}$$

in the Newtonian limit. The matrix $\rho(t, \mathbf{x})$ is the mass distribution of the source and r is the distance to the centre of the source. The first momenta can also be written in terms of

$$P_i = \int d^3x T_{0i}(t, \mathbf{x}), \tag{1.39}$$

$$P_{ij} = \int d^3x T_{0i}(t, \mathbf{x})x^j, \tag{1.40}$$

which are the momenta of the momentum density, T_{0i}. The quantity P_i is the total momentum of the system in linearised gravity. From the Lorentz gauge, $\partial^\mu \bar{h}_{\mu\nu} = 0$, and applying it to Eq. (1.11), the condition $\partial^\mu T_{\mu\nu} = 0$ is derived. This last condition is used to express S_{ij} in terms of the mass multipole momenta alongside with the divergence theorem [9], which leads to the following identities

$$\dot{M} = 0, \quad \dot{M}_i = P_i, \quad \dot{M}_{ij} = P_{i,j} + P_{j,i}, \quad \dot{P}_i = 0, \quad \dot{P}_{i,j} = S_{ij}. \tag{1.41}$$

From these identities and the fact that $S_{ij} = S_{ji}$, the following identity is obtained

$$\ddot{M}_{ij} = 2S_{ij}. \tag{1.42}$$

Eq. (1.42) shows that since S_{ij} is the leading term in the expansion of h_{ij}, then the gravitational wave radiation has no monopole or dipole component and the leading order term is the quadrupole moment. The solution for the linearised Einstein's equations in the TT gauge is thus

$$h_{ij}^{TT}(t) = \frac{2}{D}\ddot{M}_{ij}(t - D), \tag{1.43}$$

Hence, sources whose mass have a varying quadrupolar moment will generate time and amplitude dependent GWs. The h_+ and h_x components can also be expressed in terms of the mass momenta as

$$h_+ = \frac{1}{D}(\ddot{M}_{11} - \ddot{M}_{22}), \quad h_x = \frac{2}{D}\ddot{M}_{12}. \tag{1.44}$$

Let us estimate the order of magnitude of the strain produced by a binary system of objects with masses m_1 and m_2 in a circular orbit with radius R. As shown in Ref. [9], the non-null components of the quadrupole momentum of this system are given by

$$M_{11} = \mu R^2 \frac{1 - \cos(2\omega_s t)}{2},$$

$$M_{22} = \mu R^2 \frac{1 + \cos(2\omega_s t)}{2},$$

$$M_{12} = -\frac{1}{2}\mu R^2 \sin(2\omega_s t), \tag{1.45}$$

where μ is the reduced mass of the system, defined by $\mu = \frac{m_1 m_2}{(m_1 + m_2)}$, and ω_s is the orbital frequency. The second derivatives of Eqs. (1.45) are

$$
\begin{aligned}
\ddot{M}_{11} &= 2\mu R^2 \omega_s \cos(2\omega_s t), \\
\ddot{M}_{22} &= -\ddot{M}_{11}, \\
\ddot{M}_{12} &= 2\mu R^2 \omega_s \sin(2\omega_s t).
\end{aligned}
\tag{1.46}
$$

Substituting these derivatives in Eqs. (1.44) and assuming that $2\omega_s t = 2n\pi$, where n is an integer, Eqs. (1.44) can be rewritten as

$$
h_+ = \frac{1}{D} 2\ddot{M}_{11} = \frac{4}{D}\mu R^2 \omega_s, \quad h_x = 0.
\tag{1.47}
$$

For the ease of all derivations the gravitational constant and the speed of light have been set to one. To determine an estimate of h_+ we need to reinstate these variables. Furthermore, from Kepler's law the orbital frequency is related to R as $\omega_s^2 = G(m_1 + m_1)/R^3$. Hence, h_+ is rewritten as

$$
h_+ = \frac{4}{D}\frac{G}{c^4}\mu R^2 \omega_s^2 = \frac{4G^2}{Dc^4}\mu\frac{m_1 + m_2}{R}.
\tag{1.48}
$$

Let us now assume the masses are $m_1 = m_2 = 1$kg, the distance from the observer is $D = 10^3$km and the orbital radius $R = 1$m. The order of magnitude of the produced GW strain is 5.9×10^{-35}. In chapter 2 it will be shown that this value of strain cannot be detected by current interferometers but instead values of the order of 10^{-21} or larger. As we will show later in the chapter, for massive bodies like black holes or neutron stars the strain amplitude can be detected by the current GW detectors.

1.4   GW interactions with free-falling masses

It can be shown that a GW passing through a particle at rest in the TT gauge leaves it at rest [9]. However, the proper distance between particles does change due to the passage of GWs. In the TT gauge, the space-time interval ds^2 is given by

$$
ds^2 = -dt^2 + dz^2 + (1 + h_+(t,z))dx^2 + (1 - h_x(t,z))dy^2 + 2h_x(t,z)dxdy.
\tag{1.49}
$$

Analytically, the proper distance at time t between two particles located at $(x_1, y_1, 0)$ and $(x_2, y_2, 0)$, and assuming $y_2 - y_1 = 0$, is

$$
ds = (1 + \frac{1}{2}h_+(t,0))(x_1 - x_2).
\tag{1.50}
$$

The long-wavelength approximation has been used, i.e. the wavelength of the GW is much larger than the distance between particles ($L \equiv x_2 - x_1$). Eq. (1.50) shows that the distance between two free masses changes as GWs pass by. This effect is used to detect GWs in the interferometers. The second term in Eq. (1.50) represents the fractional change in the distance between free masses, commonly known as strain.

Graphically, the effect that the passage of GWs have on the proper distance between particles is represented in Figure 1.4. A ring of particles is shown and how the passage of a plus or cross-polarized GW with different values of ϕ_+ and ϕ_x can affect the proper distance between particles.
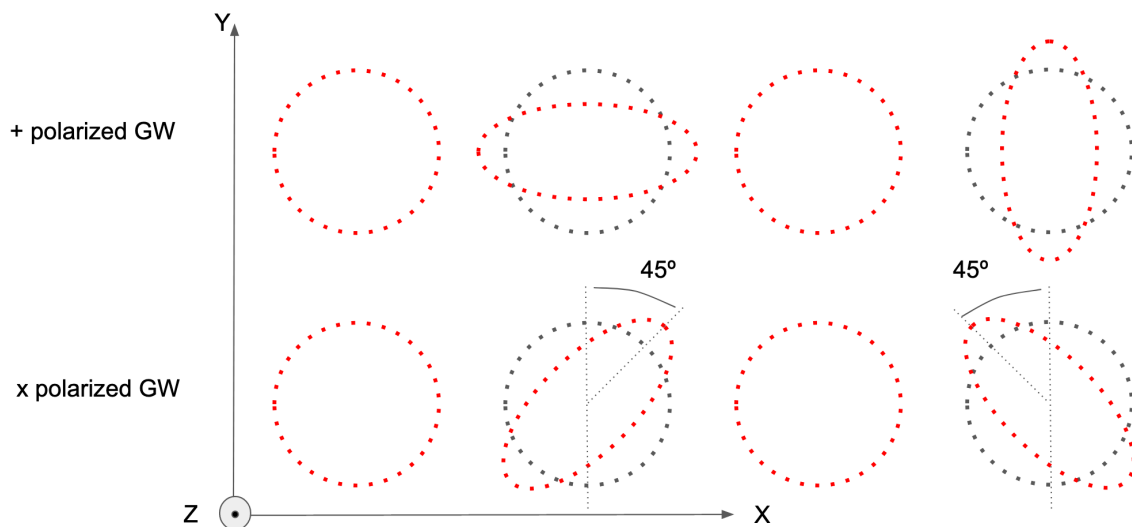
Figure 1.4: Effect in the proper distance of a ring of particles due to the passage of a GW propagating in the +z direction. The upper row shows the effect a + polarized GW has. The lower row shows the effect due to an x polarized GW. From left to right, the effect is shown for different values of ϕ_+ and ϕ_x. The left-most corresponds to a phase of 0, the second column to a phase of $\pi/2$, the third column π, and the last column $3\pi/2$. The x and + components are interchangeable under a 45º rotation.

1.5 Sources of GWs

As derived in section 1.3, any non-axisymmetric mass which accelerates, i.e.: any body with a non-null quadrupole moment, produces GWs. As mentioned above, the values of strain that can be detected are of the order of 10^{-21}. We will show in this section that these amplitudes are achieved by very heavy astrophysical bodies or very violent astrophysical events. Sources can be classified into two categories according to the type of GW signal they produce. There are signals that can be modeled, such as compact binary coalescences, while others are hard to model. For signals that can be modeled, i.e.: signals whose waveform is known, matched filtering can be used to extract the signal from the detector noise [11].

1.5.1 Transient sources

Transient source, or burst, is the name given to an event that releases a large amount of gravitational energy over a very short period (less than a few seconds). Astrophysical events that result in a burst of GWs include gamma-ray bursts and supernovae explosions [12], as well as the final stages of coalescing binaries [13, 14]. In the search for transient sources, no assumption is made about the form of gravitational radiation. The only assumption is that the signal is of short duration. The results from searches for transient sources can be found in Refs. [15, 16, 17, 18].

1.5.2 Compact Binary Coalescences

Two compact binary objects orbiting around each other constitute a time-varying mass quadrupole, and so the system will radiate away energy in the form of GWs. This emission is compensated by a reduction of the binding energy between the objects and thus a shrinking of the orbital separation and an increased orbital speed [19] until the objects coalesce. The signal from these orbiting objects is known as compact binary coalescence (CBC) signal. Examples of CBCs are Binary Black Holes (BBH), Binary Neutron Stars (BNS), and a binary composed of one black hole (BH) and one neutron star (NS). Using Eq. (1.48) we can compute the strain produced by a system of BBHs with masses $m_1 = 10 M_\odot$ and $m_2 = 20 M_\odot$, at a distance of $D = 100 Mpc$ and orbital radius of twice the Schwarzschild radius, resulting in $9.6 \cdot 10^{-21}$.

The inspiral phase leading up to the merger lasts for most of the binary's lifetime, but only the last few minutes before the merger can be detected with the current detectors. Right before the merger, the

power and the frequency of the emitted gravitational energy will increase, producing a chirp-like signal which is detectable. The long, low-frequency part of the inspiral phase (f < 10Hz) is undetectable due to the high seismic noise level below 10Hz in the detectors. After the merger, there is also a ringdown phase in which the newly formed BH can produce GWs. These stages are represented in Figure 1.5 on top of an example of a CBC waveform. Searches for CBCs use matched filtering techniques and signal consistency tests to detect these signals. Search techniques for CBCs are detailed in Ref. [6].
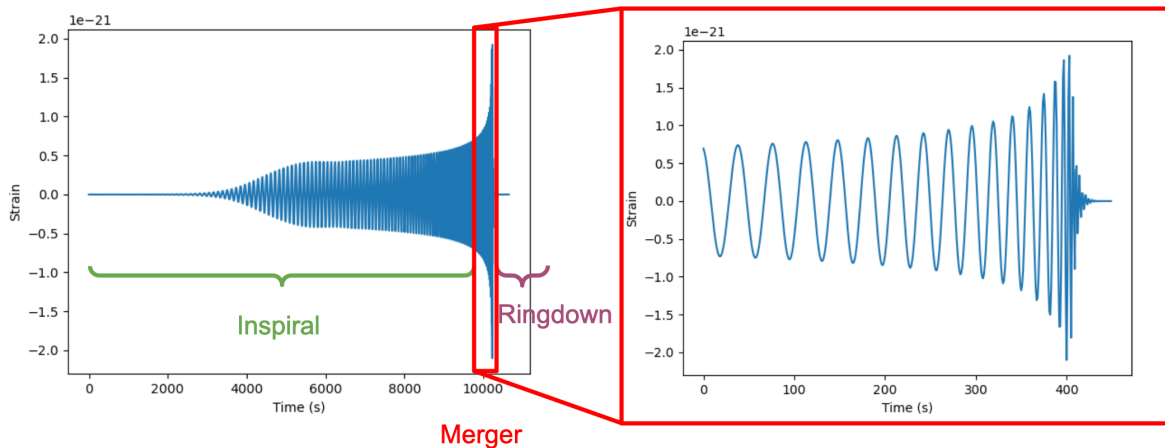
Figure 1.5: Example of a modeled source. The image to the left shows the waveform of a BBH with components of mass 10 and 8 $M_\odot$, and z component of the two binaries' dimensionless spin equal to 0.1. The distance to the observer is 100Mpc. This waveform was generated with pycbc [20] using the approximant 'IMRPhenomPv2'. The image to the right is a zoomed image of the merger.

For a signal detection to be claimed, the signal to noise ratio (SNR) produced in a single detector must be of at least 8. In a single detector, the SNR is defined as [9]

$$\text{SNR}^2 = 4 \int_0^\infty \text{df} \frac{|\tilde{\text{h}}(\text{f})|^2}{\text{S(f)}}, \tag{1.51}$$

where $S(f)$ is the noise power spectral density and $\tilde{h}(f)$ is the Fourier transform of the strain $h(t)$, given by Eq. (1.29).

1.5.3 Periodic sources

These sources produce quasi-monochromatic GWs. Rapidly spinning, slightly spherically asymmetric neutron stars generate continuous waves. The GW emission of a rapidly spinning NS has a much slower frequency evolution than a CBC event. NSs lose energy and spin over time, so they become less efficient emitters of GWs with time. The GWs emitted by NSs are thus referred to as continuous waves (CWs) since the signals last for a long time with small changes in frequency [10]. The minimum value of strain detectable for periodic signals is much smaller than for bursts [9]. The searching technique is thus very different from that of CBCs since one looks for long-lasting, narrowband signals, instead of short, broad-band transients. This is why long observation times are needed, as the integration over time increases the signal-to-noise ratio of the weak signal. Details on the analysis technique are provided in Ref. [10].

1.5.4 Sources of the gravitational wave background

The GWB is the superposition of a large number of independent and unresolved GW sources of either astrophysical or cosmological origin. Among the astrophysical sources are the compact binary coalescences (CBCs) that cannot be resolved individually, core-collapse supernovae, rotating neutron stars, stellar core collapses, and then among the cosmological are cosmic strings, primordial black holes, superradiance of axion clouds around black holes, phase transitions in the early universe, and GWs

produced during inflation [21]. The GWB is best characterized statistically (see Chapter 6 for further information). Then GWB is said to have a *primordial* and *contemporary* parts [22]. The *primordial* background is composed of gravitational radiation emitted in the early universe at very large redshifts. This primordial GWB was produced in a tiny fraction of the first second of the universe and it is composed of the GWs from inflation, cosmic strings, primordial black holes, and first-order phase transitions. The other part of the GWB that is still being produced is the *contemporary* background. It is composed of many different systems formed in the past and that can also be formed today. Examples of these are coalescing binaries, rapidly-rotating compact objects, or core-collapse supernovae. In the literature, primordial and contemporary backgrounds are often called cosmological and astrophysical, respectively.

The astrophysical contribution to the GWB is important because it has information about the star formation history, the mass range of neutron star or black hole progenitors, the statistical properties of populations of compact objects (ellipticity, magnetic field, ...) or the rate of CBC mergers [23]. Also, it can be a foreground to the cosmological GWB, so it must be well modeled to resolve it from the cosmological GWB once a detection is claimed. Some of these sources are coalescing binary systems, which are isolated pairs of massive objects that inspiral towards each other by emitting gravitational radiation until they coalesce [22, 24]. The other two processes that can produce a continuous stochastic background in the frequency band of our current interferometers are magnetars and double neutron star coalescence, which are modeled in Ref. [23].

Core-collapse supernova (SN) explosions are among the most powerful astrophysical phenomena. The total energy released is about $3 \cdot 10^{53}$ erg [25] and it comes in the form of neutrino bursts that last for a few seconds. However, they are weakly interacting, which retains information about their origins [26]. Only about 1% of the energy released goes into the explosion and only a fraction of 10^{-4} is emitted in the visible spectrum. SNe are expected to be strong GW sources contributing to the GWB. The GWB from SNe resulting in BHs has been calculated in Ref. [27], where the estimate of the peak of the energy density spectrum is calculated to be $\Omega_{gw}h^2 = 10^{-11}$ and it lies between a few hundred Hz to a few thousand Hz. Even though the fraction going into gravitational radiation is very small, the improved sensitivities of our detectors and the search techniques make the detection of the GWB from SNe plausible [26]. Similar to what happens with the background sourced by CBCs, the background from SNe would be very informative, but it would mask the cosmological background. It is thus essential to properly model it. The background sourced by SNe is described in Ref. [25, 28, 26].

Cosmic strings are line-like topological defects [29] which are formed from spontaneous symmetry-breaking phase transitions [30, 31]. These phase transitions may have occurred at grand unification [32], when the energy scale was of the order of 10^{16}GeV. Observational predictions from cosmic strings can thus probe particle Physics beyond the Standard Model (BSM) at energies unreachable by particle accelerators. One of the observables from cosmic strings are GWs [33, 34]. In Ref. [35] the energy density spectrum of the GWB Ω_{GW} is derived. Constraints on Ω_{GW} are set in Ref. [31] which are then translated into constraints on the parameters of the model. Detailed derivations on the GW generation mechanisms from cosmic strings is provided in Refs. [36, 33, 34, 37, 35].

The superradiance of axion clouds around black holes (BHs) does also contribute to the GWB. Ultralight bosons are relevant because they could be a significant component of dark matter [38, 39]. They interact weakly with baryonic matter, but their gravitational interaction does exist [40]. When these bosons are near spinning BHs and their frequency ω_R satisfies the superradiant condition $0 < \omega_R < m\Omega_H$ (Ω_H is the horizon angular velocity and m is an azimuthal quantum number), they can trigger a superradiant instability [40]. This instability leads to the formation of a rotating "bosonic cloud" around the BH, which can emit GWs [41]. As shown in Ref. [42], the way GWs are generated starts with the BH spinning down, transferring energy and angular momentum to the boson condensate until $\omega_R \sim m\Omega_H$. The condensate is then dissipated through the emission of GWs with frequency μ, which coincides with the boson mass [40]. The ultralight boson condensates that could be probed by LIGO have bosons with estimated masses of $m_s \sim 10^{-13} - 10^{-12}$eV [41]. Comprehensive works on the emission of GWs by axion clouds and the possibility to detect them with current detectors are given in Refs. [40, 43, 44, 41].

Gravitational waves are a probe of inflation and they would contribute to the GWB. If the GWB from inflation was detected, the understanding of the Universe could be as early as 10^{-32}s and light would be shed over Physics taking place at energies of order 10^{15}GeV [45]. Gravitational waves would also help in understanding the scalar potential driving inflation [45].

Finally, particular attention will be given in this thesis to Primordial Black Holes (PBHs) and First-order phase transitions (FOPTs). They are described in detail in Chapter 7.

Chapter 2

Ground based gravitational wave detectors

In this chapter, the principles of GW detectors are introduced. The instrument used for GW detection is an evolved version of a Michelson interferometer (IFO). It will be shown that the signal-to-noise ratio increases with the length of the arms and the laser power. However, infinitely large arms are financially and technologically unfeasible. For that reason, an alternative to increasing the arm's length is adding Fabry-Pérot (FP) cavities to the Michelson's arms. The power in the cavity is increased by the addition of a signal recycling mirror. Then, the effect of GWs passing through a detector will be explained as well as how to extract the signal from the IFO. Finally, the different sources of noise that diminish the sensitivity for the detection of GW signals will be explained.

2.1   Michelson interferometer

The simplest Michelson interferometer is composed of a source, a beam splitter, and two mirrors at the end of orthogonal arms or cavities. The source is usually a laser that emits light that propagates towards the beam splitter, where it splits with an equal probability towards each arm, directing towards the end mirrors M_1 and M_2, schematically represented in Figure 2.1. Once the light reaches the end mirrors it gets reflected and then propagates back towards the beam splitter, where it recombines and interference takes place. Part of the resulting beam goes to the photodetector (see Figure 2.1). The beam splitter has reflection and transmission coefficients denoted by r_s and t_s, respectively. In an idealistic case where mirrors do not have losses, the reflection and transmission factors must satisfy $r^2 + t^2 = 1$. In reality, there are losses represented by p, the loss coefficient, which accounts for the absorption in the coating of the mirrors and the scattering into higher-order modes. The power balance is thus $r^2 + t^2 = 1 - p$. In Virgo's mirrors p has been measured and it is about 1ppm [46]. The reflectivities of the end mirrors are given by r_1 and r_2. Under nominal conditions, i.e.: when no sources of noise exist, the length of each arm is L. Mirrors in GW detectors are suspended and can be treated as free-falling masses. For that reason, in the detector frame, the passage of a GW will displace the mirrors. Under the assumption that noise exists, the end mirrors will displace and so the length of each arm will be denoted by a and b (see Figure 2.1). For a field entering the interferometer with amplitude A, the outgoing field reaching the photodetector has an amplitude

$$B = r_s t_s A(r_1 e^{2ik_L a} + r_2 e^{2ik_L b}), \tag{2.1}$$

where $k_L \equiv 2\pi/\lambda_L$ is the wave number and λ_L is the laser wavelength. From Eq. (2.1) the power that can be detected exiting the interferometer is given by

$$B\bar{B} = r_s^2 t_s^2 A\bar{A}(r_1^2 + r_2^2 + 2r_1 r_2 \cos[2k_L(a - b)]). \tag{2.2}$$
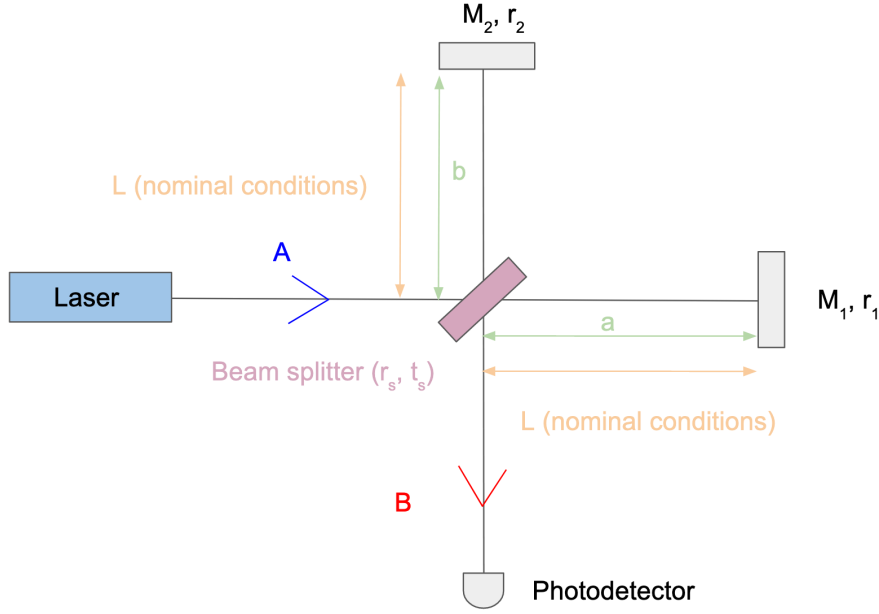
Figure 2.1: Schematic representation of a simple Michelson interferometer. It is composed by a source (a laser in this case), a beam splitter (pink rectangle) with reflectivity and transmissivity factors r_s and t_s, respectively, and two mirrors M_1 and M_2.

The Eq. (2.2) implies that any variation in length in the interferometer (IFO) will be detected as a variation in the power detected at the output photodetector. Let us assume a small variation of the length of the arm is to be measured. Given the length of one arm is $a = a_o + x(t)$, where $x(t) << \lambda_L$ represents a very small displacement of mirror M_1 (see Figure 2.1), the outgoing power of the interferometer P_{DC} is modified by a time varying component of the power $\Delta P(t) = r_1 r_2 P_o k_L x(t) \sin(\alpha)$ as $P(t) = P_{DC} + \Delta P(t)$, where P_o is the average value of P_{DC}. P_{DC} is the power under nominal conditions and is given by [46]

$$P_{DC} = \frac{1}{4} P_o(r_1^2 + r_2^2 + 2r_1 r_2 \cos(\alpha)), \tag{2.3}$$

where $\alpha \equiv 2k(a-b)$ is known as the *static tuning* of the interferometer. In the case that the displacement is zero, $x(t) = 0$, the outgoing power is controlled by α. There are two scenarios. If alpha is an integer number of 2π, $\alpha = 2n\pi$, the nominal power is given by

$$P_{DC,b} = \frac{(r_1 + r_2)^2}{4} P_o. \tag{2.4}$$

In such a case, the interferometer (IFO) is said to be tuned at a *bright fringe*. For $r_1 \sim r_2 \sim 1$ then the value of the output power is close to P_o. In the case that $\alpha = (2n+1)\pi$, the power is given by

$$P_{DC,d} = \frac{(r_1 - r_2)^2}{4} P_o. \tag{2.5}$$

In this case, the IFO is said to be tuned at a *dark fringe*. The motivation to have the IFO tuned at dark fringe and with $P_{DC,d} = 0$ will be explained in subsequent sections. The minimum displacement x that can be detected is determined from the signal to noise ratio, defined as

$$\text{SNR(f)} = \frac{S_{\Delta P}(f)}{S_P(f)}, \tag{2.6}$$

where $S_P(f)$ is the spectral density of the power equivalent to shot noise, which will be described in section 2.3.

22

2.1.1 Effect of a GW in the light propagating within the IFO in the TT frame

Let us consider a light ray propagating in the x,y directions of a Michelson IFO, i.e.: x and y arms. In vacuum the light follows null geodesics

$$g_{\mu\nu}dx^\mu dx^\nu = 0, \tag{2.7}$$

where $g_{\mu\nu}$ is the metric ($\eta_{\mu\nu} + h_{\mu\nu}$) and dx^μ is the space time elementary vector separating two events encountered by the light ray. Using Eq. (1.20) and the null geodesic equation, Eq. (2.7), the latter can be written as

$$0 = c^2dt^2 - dx^2 - dy^2 - dz^2 + 2h_x dx dy + h_+(dx^2 - dy^2). \tag{2.8}$$

The interaction with the GW does not modify the direction of propagation of the light ray. The only effect is a phase change in the light that will be derived in what follows. For a light ray only propagating in the x direction, Eq. (2.8) can be simplified

$$0 = c^2dt^2 - dx^2 + h_+dx^2 \Rightarrow dx = \pm cdt\Big[1 + \frac{1}{2}h_+(t)\Big], \tag{2.9}$$

where the second equation is obtained with an expansion of $\frac{1}{\sqrt{1-h_+}}$ on h_+ since $h_+ << 1$. The plus sign represents forward propagation (beam splitter to mirror) and the minus sign represents the return trip (mirror to beam splitter). Eq. (2.9) is solved for a round trip experiment in which light is emitted from the origin of coordinates at t_o and received at $x = L$ at t_1. Integrating Eq. (2.9) thus results in

$$L = c(t_1 - t_o) + \frac{1}{2}c\int_{t_o}^{t_1} h_+(u)du. \tag{2.10}$$

Light at $x = L$ is then reflected back and reaches the origin of coordinates at t_2. Since it is backward propagation according to the convention set in Eq. (2.9), the integration leads to

$$- L = c(-t_2 + t_1) - \frac{1}{2}c\int_{t_1}^{t_2} h_+(u)du. \tag{2.11}$$

Deducting Eq. (2.10) from Eq. (2.11) results in

$$2L = t_2 - t_o + \frac{1}{2}c\int_{t_o}^{t_2} h_+(u)du \tag{2.12}$$

If t_2 is rewritten as t, which denotes the detection time, and $t_o \equiv t_r$, where t_r is called the retarded time, then Eq. (2.12) can be rewritten as

$$t_r = t - \frac{2L}{c} + \frac{1}{2}\int_{t_r=t-2L/c}^{t} h_+(u)du. \tag{2.13}$$

The time t_r is that at which the light was initially emitted, which is given by the detection time t minus the time it takes the light to do a round trips, i.e.: $2L/c$. Hence, the lower limit of the integral in Eq. (2.13) can be substituted by $t - 2L/c$. For a monochromatic GW of frequency $\nu_g = \Omega/(2\pi)$, i.e.: $h_+(t) = h\cos(\Omega t)$, the solution to Eq. (2.13) is [46]

$$t_r = t - \frac{2L}{c} + h\frac{L}{c}\text{sinc}\Big(\frac{\Omega L}{c}\Big)\cos\Big(\Omega(t - L/c)\Big). \tag{2.14}$$

In the case that the light's path lies in the y direction, a similar expression is obtained

$$t_r = t - \frac{2L}{c} - h\frac{L}{c}\text{sinc}\Big(\frac{\Omega L}{c}\Big)\cos\Big(\Omega(t - L/c)\Big). \tag{2.15}$$

This method of measuring the times of emission of light and detection could be used for detecting GWs according to the excess delay between t_r and t. Let us now denote t_r by $t_r^{(x)}$ in Eq. (2.14) and t_r by $t_r^{(y)}$ in Eq. (2.15). The field that reaches the beam splitter at t from arm x is given by

$$E^{(x)}(t) = -\frac{1}{2}E_o e^{-i\omega_L t_r^{(x)}} = -\frac{1}{2}E_o e^{-i\omega_L(t-2L/c)+i\Delta\phi_x}, \tag{2.16}$$

where $\Delta\phi_x$ is the phase shift the light has acquired due to the trip along the x arm, given by

$$\Delta\phi_x(t) = -h\frac{\omega_L L}{c}\text{sinc}\Big(\frac{\Omega L}{c}\Big)\cos\Big(\Omega(t - L/c)\Big). \tag{2.17}$$

Similarly, the field reaching from arm y will be given by

$$E^{(y)}(t) = \frac{1}{2}E_o e^{-i\omega_L t_r^{(y)}} = \frac{1}{2}E_o e^{-i\omega_L(t-2L/c)+i\Delta\phi_y}, \tag{2.18}$$

where $\Delta\phi_y$ is the phase shift the light has acquired due to the trip along the y arm, given by

$$\Delta\phi_y(t) = h\frac{\omega_L L}{c}\text{sinc}\Big(\frac{\Omega L}{c}\Big)\cos\Big(\Omega(t - L/c)\Big). \tag{2.19}$$

Hence, $\Delta\phi_y = -\Delta\phi_x$ and the total phase difference acquired by the light in the detector due to a GW passing through is

$$\Delta\phi_{\text{Mich}} \equiv \Delta\phi_x - \Delta\phi_y = 2\Delta\phi_x. \tag{2.20}$$

The total field reaching the output of the interferometer is given by

$$E_{\text{tot}}(t) = E^{(x)}(t) + E^{(y)}(t) = -iE_o e^{-i\omega_L(t-2L/c)}\sin[\Delta\phi_x(t)]. \tag{2.21}$$

The power detected at the output photodetector is

$$P = |E_{\text{tot}}|^2 = P_o\sin^2[\Delta\phi_x(t)], \tag{2.22}$$

where $P_o \equiv |E_o|^2$. The result in Eq. (2.22) shows that the power detected at the end of the IFO is proportional to the laser power P_o. We need to have $\Delta\phi_x(t)$ as large as possible so that we can recover the value of h (see Eq. (2.19)). From Eq. (2.17) it can be seen that $\Delta\phi_x(t)$ is maximized for $\Omega L/c = \pi/2$. Hence, the optimal value of L is $L_{\text{optimal}} = \pi c/(2\Omega)$. Given than $\Omega = 2\pi f_{GW}$, where f_{GW} is the frequency of the GW, the optimal length can be expressed as

$$L_{\text{optimal}} = \frac{c}{4f_{GW}} \sim 74948km\frac{1Hz}{f_{GW}} \sim 750km\frac{100Hz}{f_{GW}}. \tag{2.23}$$

For a GW with a frequency of 100Hz the length of the arm required would be technologically and financially impossible to build. Hence the need to find an alternative way of making the optical path length very large. This is achieved with a Fabry–Pérot resonant cavity, which is introduced in the next section.

2.2 Fabry–Pérot resonant cavity

A Fabry–Pérot (FP) cavity is made of two parallel mirrors (see Figure 2.2). In the ground-based interferometers, the mirrors are referred to as input test mass (ITM) and end test mass (ETM). When light enters the cavity through ITM, it is partially reflected E_{ref} and partially transmitted E_o. The transmitted wave is reflected by ETM, E_2 and so it returns to ITM, where it recombines with the incoming wave E_o. Part of the light reaching ITM will be transmitted, E_{out}.
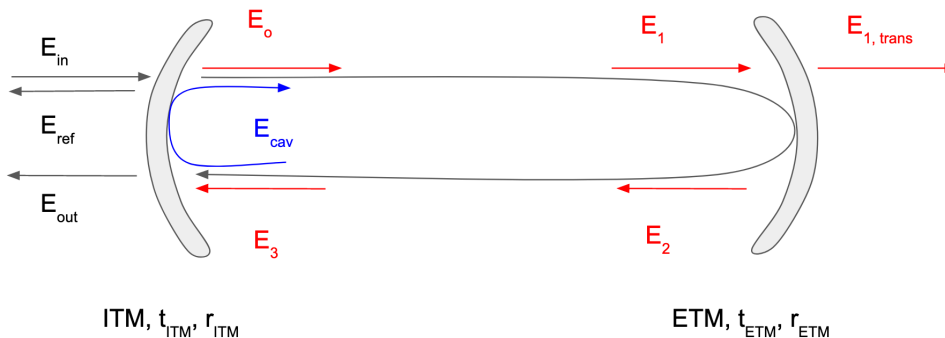
Figure 2.2: Schematic representation of the field stored within a FP cavity with input mirror denoted by ITM and end mirror by ETM. Their transmissivities and reflectivities are represented by $t_{\text{mirrorname}}$ and $r_{\text{mirrorname}}$, respectively.

We now set the conventions needed to derive the field that can be stored in an FP cavity, denoted by E_{cav}. Let us assume an ideal monochromatic source of light with frequency ω_L. The field is chosen such that the field at location x is given by

$$E(t, x) = E(x)e^{-i\omega_L t}. \tag{2.24}$$

The propagation along a path of length L in vacuum is represented by a phase factor that modifies the amplitude as $E(x + L) = e^{ik_L L}E(x)$. The amplitudes of the reflected and transmitted fields are given in terms of the amplitude of the input field E_{in}

$$E_{ref} = rE_{in}; \quad E_{trans} = tE_{in}. \tag{2.25}$$

If the phase after a round trip in the cavity is an integer number of the incoming phase, then the interference between E_3 and E_o will be constructive and a strong intra-cavity field E_{cav} will build up. In this scenario, the cavity is said to be in resonance. The cavity field is derived in Appendix B and is given by

$$E_{cav} = \frac{t_1}{1 - r_1 r_2 e^{-2ikL}} E_{in}. \tag{2.26}$$

A resonance will thus occur when the intracavity power in maximised, which happens for $2kL = 2\pi n \Rightarrow e^{-2ikL} = 1$, where n is an integer. Resonance can be achieved by fixing the length of the cavity to L and tuning the frequency of light. There are a series of resonant frequencies

$$\nu_n = \left(n + \frac{1}{2}\right)\frac{c}{2L}, \tag{2.27}$$

where n is an integer number. The resonances are plotted in Figure 2.3 as a function of $2kL$.
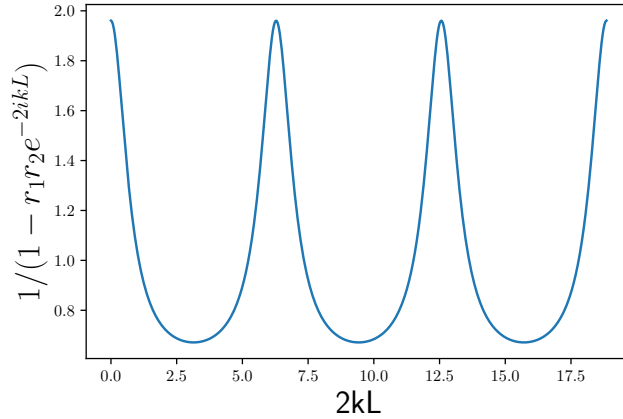
Figure 2.3: Resonances in a FP cavity with $r_{ITM} \simeq r_{ETM} = 0.7$, as a function of $2kL$. The distance between maxima is given by the free spectral range (FSR), given by Eq. (2.28).

The spacing between two successive resonances (see Figure 2.3) is called the Free Spectral Range (FSR) and is

$$\Delta\nu_{FSR} = \frac{c}{2L}. \tag{2.28}$$

The ratio between $E_{cav}/E_{in} \equiv S$ is known as the surtension factor, which has as maximum value $S_{max} = t_1/(1 - r_1 r_2)$. In a realistic FP cavity with losses p_1 (associated to the first mirror) and p_2 (associated to the second mirror), the value of r_1 for which S_{max} is maximum is $r_{opt} = (1 - p_1)r_2$. The value of the surtension factor in this case is thus

$$S_{opt} = \frac{1 - p_1}{1 - (1 - p_1)(1 - p_2)} \simeq \frac{1}{p_1 + p_2}. \tag{2.29}$$

25

The width of the resonance line can be evaluated assuming the frequency ν is close to a resonance: $\nu = \nu_n + \delta\nu$, where $\delta\nu << \Delta\nu_{FSR}$. Then, $2kL = (2n+1)\pi + 2\pi\frac{\delta\nu}{\Delta\nu_{\text{FSR}}}$. The surtension coefficient is thus

$$S = \frac{t_1}{1 - r_1 r_2 e^{2i\pi\frac{\delta\nu}{\Delta\nu_{\text{FSR}}}}}. \tag{2.30}$$

The square of Eq. (2.30) is the ratio of intensities

$$|S|^2 = \frac{t_1^2}{(1 - r_1 r_2)^2 + 4r_1 r_2 \sin(\pi\delta\nu/\Delta\nu_{\text{FSR}})} = S_{\max}^2 \frac{1}{1 + \left[\frac{2\sqrt{r_1 r_2}}{1 - r_{12}}(\pi\delta\nu/\Delta\nu_{\text{FSR}})\right]}, \tag{2.31}$$

where in the last equality the simplification $\sin(\pi\delta\nu/\Delta\nu_{\text{FSR}}) \simeq \pi\delta\nu/\Delta\nu_{\text{FSR}}$ has been used, given that the width of the resonance is much smaller than the distance between resonances, $\delta\nu << \Delta\nu_{\text{FSR}}$. Eq. (2.31) can be further simplified by defining the Finesse of the cavity as

$$\mathcal{F} = \frac{\pi\sqrt{r_1 r_2}}{1 - r_1 r_2}. \tag{2.32}$$

It can be shown that the average time a photon remains within a FP cavity is large for large finesse cavities [9]. Finally, the ratio between the intensity of the cavity field and the intensity of the incoming field is given by

$$|S|^2 = S_{\max}^2 \frac{1}{1 + \left[2\mathcal{F}\delta\nu/\Delta\nu_{\text{FSR}}\right]^2}. \tag{2.33}$$

The values of $\delta\nu$ that make the surtension factor be half its maximum are $\delta\nu = \pm\Delta\nu_{\text{FSR}}/(2\mathcal{F})$. With this values the full width at half maximum (FWHM) of the resonance can be calculated $\delta\nu_{\text{FWHM}} = \pm\Delta\nu_{\text{FSR}}/(\mathcal{F})$. The expression for the resonance is thus

$$|S|^2/S_{\max}^2 = \frac{1}{1 + \left[\frac{2\mathcal{F}}{\pi}\sin(\delta\nu/\Delta\nu_{\text{FSR}})\right]^2}. \tag{2.34}$$

The wave reflected off the cavity is derived in appendix B and is given by

$$E_{\text{out}} = r_{\text{ITM}}E_{\text{in}} + t_{\text{ITM}}E_3 = r_{\text{ITM}}E_{\text{in}} - t_{\text{ITM}}e^{-2ik_L L}E_{\text{cav}}. \tag{2.35}$$

The phase of the reflected wave undergoes a transition of 2π (see Figure 2.4(right)) when crossing the resonance (see Figure 2.4(left)). A detailed derivation of the procedure carried out to achieve the resonant condition in the IFO is provided in Appendix C.
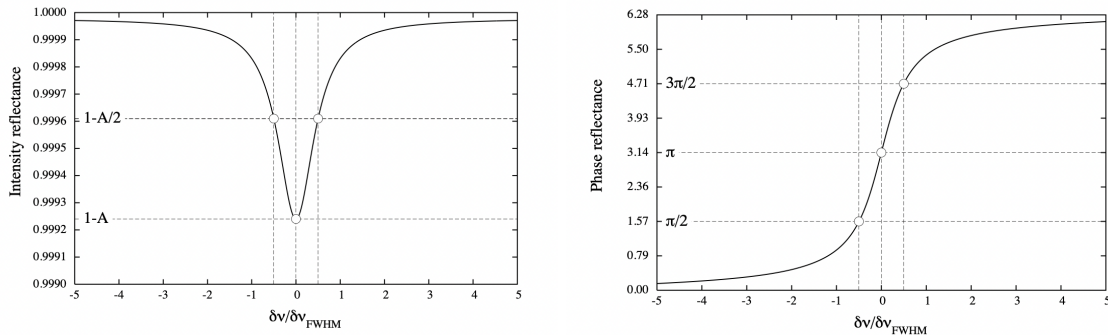
Figure 2.4: Figures retrieved from Ref. [46]. **Left** Absorption line of a FP cavity with $r_1 = 0.85$ and $r_2 = 0.99998$. A is the maximum of absorption. **Right** Phase reflectance of a FP cavity with $r_1 = 0.85$ and $r_2 = 0.99998$.

2.2.1 GW signal extraction from a FP cavity

We have seen that the passage of a GW through an IFO has the effect of introducing a phase shift $\Delta\phi_{\mathrm{GW}}(t)$ in the light propagating within the IFO. This phase shift is not trivial to detect. In a Michelson IFO, we have seen the power at the output photodetector is given by Eq. (2.22). At the output photodetector of the IFO, all that is measured is the power, which makes it hard to determine whether a variation in the power is due to a GW passing by or a fluctuation in the laser power. For that reason, a null instrument could be a solution, i.e.: an IFO whose output power equals zero when no GW is passing by. Thus, the best working point would be that represented by a red dot in Figure 2.5, in which the output power is normalized by the input power. However, at this working point, $\partial P/\partial \phi$ is also null. Since $\Delta\phi_{\mathrm{GW}}(t) \propto \mathcal{O}(h)$ (see Eq. (2.19)), then at the dark fringe the variations in power will be of the order of $\Delta P = \mathcal{O}(h)$. For signals with a strain of about $h = 10^{-21}$, it would imply that the detector should be capable of measuring a power variation of the order of 10^{-42}, which is very difficult. For this reason, an alternative is needed.
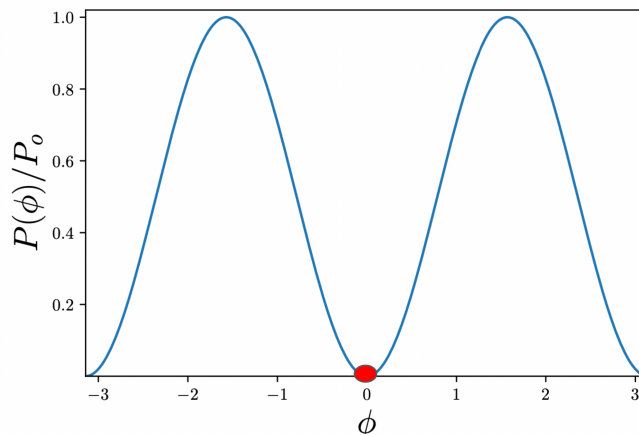
Figure 2.5: Output power of the Michelson IFO normalized by the input power as a function of the phase. The red spot, where P=0, represents a working point where the IFO would be a null instrument, i.e.: detecting power only when a GW passes by.

The alternative is phase modulating the input laser light at a frequency Ω_{mod}. This is achieved by passing the beam through a crystal or a block of dielectric material with an index of refraction dependent on an electric field $E_{\mathrm{applied}} = |E_{\mathrm{applied}}| \cos(\Omega_{\mathrm{mod}}t)$ [9]. The amplitude of the field entering the cavity is

$$E(t) = E_o e^{-i(\omega_L t + \Gamma \sin(\Omega_{\mathrm{mod}}t))}, \tag{2.36}$$

where ω_L is the frequency of the laser, i.e.: the variable to be servoed. Γ is the modulation depth (or modulation index) and $\Gamma << 1$ so E(t) can be expanded in Fourier modes

$$E(t) = E_o[J_o(\Gamma)e^{-i\omega_L t} + J_1(\Gamma)e^{-i(\omega_L+\Omega_{\mathrm{mod}})t} - J_1(\Gamma)e^{-i(\omega_L-\Omega_{\mathrm{mod}})t} + \mathcal{O}(e^{-i\omega_L \pm 2\Omega_{\mathrm{mod}}})], \tag{2.37}$$

where J_n are Bessel functions. Therefore, the phase modulation creates sidebands with frequencies $\omega_L \pm \Omega_{mod}$. In Eq. (2.37), $E_o J_o(\Gamma)e^{-i\omega_L t}$ is known as the *carrier field* and the other two terms are the two *sideband fields* added by the modulator. The carrier and sidebands are reflected differently by the FP cavity. The reflected field's amplitude is

$$B(t) = E_o \left[Re^{-i\omega_L t} + i\frac{\Gamma}{2}R_+ e^{-i(\omega_L+\Omega_{\mathrm{mod}})t} + i\frac{\Gamma}{2}R_- e^{-i(\omega_L-\Omega_{\mathrm{mod}})t} \right], \tag{2.38}$$

where R is the reflectance of the cavity for the carrier field, and R_+, R_- the reflectances of the cavity for the sidebands. It can be shown [9] that the output field of the carrier is proportional to $\sin\left(2\pi\frac{a-b}{\lambda_L}\right)$ and the output field of the sidebands proportional to $\sin\left(2\pi\frac{a-b}{\lambda_L} \pm 2\pi\frac{a-b}{\lambda_{\mathrm{mod}}}\right)$. For $a - b = n\lambda_L$, where n is an integer, the carrier is in the dark fringe while the sidebands are not. When a GW passes

by, the output field of the carrier is proportional to $\sin\left(2\pi\frac{a-b+Lh(t)}{\lambda_L}\right)$, while that of the sidebands to $\sin\left(2\pi\frac{a-b+Lh(t)}{\lambda_L} \pm 2\pi\frac{a-b+Lh(t)}{\lambda_{mod}}\right)$. As a consequence, the carrier is no longer in dark fringe. The total power the photodetector can measure has three terms. One of them is not relevant as it is of order $\mathcal{O}(h^2)$, another one is not dependent on h and the third term is linear on h and oscillates with a frequency Ω_{mod}, which is the one that is extracted. The very same procedure is generalized to a FP cavity.

2.2.2 A133 algebra

Section 2.1.1 shows what the phase shift due to the passage of a GW is in a Michelson IFO. The procedure can be generalized to a real GW detector, for which an algebra is introduced to ease the calculations. Let us assume the same monochromatic GW as in previous sections does a round trip in an FP cavity. B(t) is the amplitude of the field propagating within the cavity at the end of the round trip and E(t) is the amplitude at the beginning

$$B(t) = E(t_r) \quad / \quad E(t) = Ee^{-i\omega_L t}. \tag{2.39}$$

Substituting the retarded time, Eq. (2.14), in Eq. (2.39) results in two sidebands of frequencies $\omega_L \pm \Omega$ in the incoming field

$$B(t) = Ee^{-i\omega_L t}e^{2i\omega_L L/c} + \frac{\mathrm{i}}{2}\mathrm{hE}\frac{\omega_\mathrm{L}\mathrm{L}}{\mathrm{c}}\mathrm{sinc}\left(\frac{\Omega\mathrm{L}}{\mathrm{c}}\right)\mathrm{e}^{2i\omega_\mathrm{L}\mathrm{L}/\mathrm{c}}\mathrm{e}^{\mathrm{i}\Omega\mathrm{L}/\mathrm{c}}\mathrm{e}^{-\mathrm{i}(\omega_\mathrm{L}+\Omega)\mathrm{t}} +$$
$$+ \frac{\mathrm{i}}{2}\mathrm{hE}\frac{\omega_\mathrm{L}\mathrm{L}}{\mathrm{c}}\mathrm{sinc}\left(\frac{\Omega\mathrm{L}}{\mathrm{c}}\right)\mathrm{e}^{2i\omega_\mathrm{L}\mathrm{L}/\mathrm{c}}\mathrm{e}^{-\mathrm{i}\Omega\mathrm{L}/\mathrm{c}}\mathrm{e}^{-\mathrm{i}(\omega_\mathrm{L}-\Omega)\mathrm{t}}, \tag{2.40}$$

as shown in previous sections. In the case that the incoming field E(t) was already modulated and had 2 sidebands with amplitudes E_1 and E_2 (this is the case in real GW detectors, as described in section C), the input field would be expressed as

$$E(t) = \left(E_o + \frac{1}{2}hE_1 e^{-i\Omega t} + \frac{1}{2}hE_2 e^{i\Omega t}\right)e^{-i\omega_L t}. \tag{2.41}$$

The output field's amplitude after a roundtrip will thus be

$$B(t) = E(t_r) = \left(B_o + \frac{1}{2}hB_1 e^{-i\Omega t} + \frac{1}{2}hB_2 e^{i\Omega t}\right)e^{-i\omega_L t}. \tag{2.42}$$

The coefficients B_o, B_1 and B_2 are given by [46]

$$B_o = e^{2i\xi}E_o,$$
$$B_1 = e^{2i(\xi+\eta)}E_1 - i\epsilon\xi sinc(\eta)e^{i(2\xi+\eta)}E_o,$$
$$B_2 = e^{2i(\xi-\eta)}E_2 - i\epsilon\xi sinc(\eta)e^{i(2\xi-\eta)}E_o, \tag{2.43}$$

where two definitions have been used $\xi \equiv \omega_L L/c$ and $\eta \equiv \Omega L/c$. Eq. (2.42) can be written in matrix form as

$$\mathcal{B} = \mathbf{X}\mathcal{E} \quad / \quad \mathcal{E} = (E_o, E_1, E_2), \mathcal{B} = (B_o, B_1, B_2), \tag{2.44}$$

where $\mathbf{X}$ is given by

$$\mathbf{X} = \begin{pmatrix} e^{2i\xi} & 0 & 0 \\ -\mathrm{i}\epsilon\xi\mathrm{sinc}(\eta)\mathrm{e}^{\mathrm{i}(2\xi+\eta)} & e^{2i(\xi+\eta)} & 0 \\ -\mathrm{i}\epsilon\xi sinc(\eta)e^{i(2\xi-\eta)} & 0 & e^{2i(\xi-\eta)}. \end{pmatrix} \tag{2.45}$$

The diagonal terms describe the free propagation of the carrier and sidebands. The other two off-diagonal non-null terms describe that a round trip of the carrier produces more contributions to the sidebands. $\mathbf{X}$ is an operator of the form

$$\mathbf{O} = \begin{pmatrix} O_{oo} & 0 & 0 \\ O_{10} & O_{11} & 0 \\ O_{20} & 0 & O_{22} \end{pmatrix}, \tag{2.46}$$

that satisfies the following operations

- The sum: $(\mathbf{A} + \mathbf{B})_{ij} = \mathbf{A}_{ij} + \mathbf{B}_{ij}$.

- The product: $(\mathbf{AB})_{ii} = \mathbf{A}_{ii}\mathbf{B}_{ii}$; $(\mathbf{AB})_{i0} = \mathbf{A}_{i0}\mathbf{B}_{00} + \mathbf{A}_{ii}\mathbf{B}_{i0}$.

- The inverse: $(\mathbf{A}^{-1})_{ii} = \frac{1}{\mathbf{A}_{ii}}$; $(\mathbf{A}^{-1})_{i0} = -\frac{\mathbf{A}_{i0}}{\mathbf{A}_{00}\mathbf{A}_{ii}}$.

All the operators of the form Eq. (2.46) satisfying the previous algebraic operations form an algebra known as A133. Optical elements can be characterized by operators from the A133 algebra. For instance, the operator corresponding to a FP cavity is the generalization of the single roundtrip operator described above, Eq. (2.45). For many roundtrips in the FP cavity, the A133 operator is given by

$$\mathcal{F} = \begin{pmatrix} F & 0 & 0 \\ G_+ & + & 0 \\ - & 0 & - \end{pmatrix}, \tag{2.47}$$

where F is the reflectance of the FP cavity to the carrier and $F_\pm$ the reflectance of the FP to the sidebands. F, $F_\pm$ and $G_\pm$ are given in terms of the reduced gravitational frequency $f_g \equiv \nu_g / \delta \nu_{FWHM}$ as

$$F = -\frac{1 - \sigma + 2i\Delta f}{1 - 2i\Delta f} \tag{2.48}$$

$$F_\pm = -\frac{1 - \sigma + 2i(\Delta f \pm f_g)}{1 - 2i(\Delta f \pm f_g)} \tag{2.49}$$

$$G_\pm = i\epsilon \frac{2\mathcal{F}L}{\lambda} \frac{2 - \sigma}{(1 - 2i\Delta f)[1 - 2i(\Delta f \pm f_g)]}. \tag{2.50}$$

2.2.3 Signal to noise ratio

The A133 algebra also allows to compute the signal-to-noise ratio of a GW signal passing through any optical system. Let us assume a pure monochromatic wave $\mathcal{E}_{in} = (E, 0, 0)$ propagating through an optical system characterized by an operator from the A133 algebra denoted by $\mathbf{S}$. The output field is given by

$$\mathcal{E}_{out} = E\left[S_{00} + \frac{h}{2}S_{10}e^{-i\Omega t} + \frac{h}{2}S_{20}e^{i\Omega t}\right]e^{-i\omega t}, \tag{2.51}$$

where S_{ij} are the matrix elements of S. The power that will be detected at the output of the system is

$$P(t) = \mathcal{E}_{out}\bar{\mathcal{E}}_{out} = P_{in}\left[|S_{00}|^2 + \frac{h}{2}(S_{10}\bar{S}_{00} + \bar{S}_{20}S_{00})e^{-i\Omega t} + \frac{h}{2}(S_{20}\bar{S}_{00} + \bar{S}_{10}S_{00})e^{i\Omega t}\right], \tag{2.52}$$

where the signal amplitude is given by $S(\nu_g) = |S_{10}\bar{S}_{00} + \bar{S}_{20}S_{00}|$[1]. The DC component of the output is proportional to $|S_{00}|^2$, so the SNR is given by

$$SNR(\nu_g) = \sqrt{\frac{P_{in}}{2h_P\nu}}||S_{10}| + |\bar{S}_{20}|e^{i(\phi_{10} + \phi_{20} - 2\phi_{00})}|h(\nu_g), \tag{2.53}$$

where ϕ_{ij} are the arguments of S_{ij} . The SNR is proportional to the input power of the laser.

2.2.4 Michelson interferometer with FP cavities

As already mentioned, the real GW interferometer is a classical Michelson IFO in which the end mirrors have been replaced by FP cavities (see Figure 2.6) to increase the effective length of the arms.

---

[1]Reminder: $\nu_g \equiv \Omega/(2\pi)$
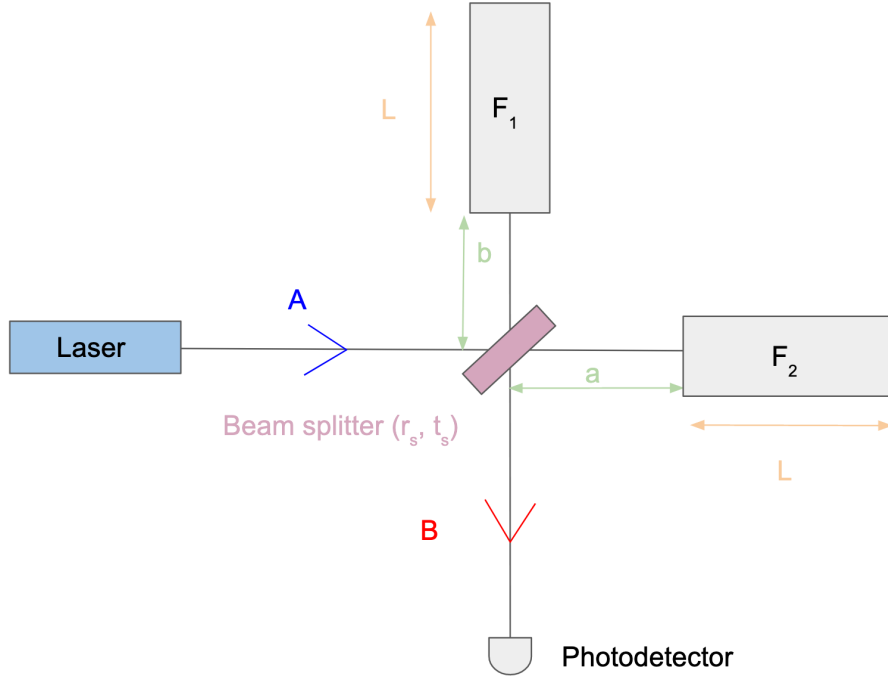
Figure 2.6: Schematic representation of a real GW interferometer, composed by a Michelson interferometer in which the end mirrors have been replaced by FP cavities. These cavities are represented by operators from the A133 algebra denoted by F_1 and F_2.

The FP cavities are represented by the operator from Eq. (2.47). In the case of the x arm, the operator is exactly Eq. (2.47) and denoted by $\mathcal{F}_1$, while for the y arm the sign of the terms F_{10} and F_{20} is changed and the operator is denoted by $\mathcal{F}_2$

$$\mathcal{F}_1 = \begin{pmatrix} F & 0 & 0 \\ G_+ & F_+ & 0 \\ G_- & 0 & F_- \end{pmatrix} \quad , \quad \mathcal{F}_2 = \begin{pmatrix} F & 0 & 0 \\ -G_+ & F_+ & 0 \\ -G_- & 0 & F_- \end{pmatrix}. \tag{2.54}$$

For this IFO, the transmittance, T, and reflectance, R, operators can be obtained from $\mathcal{F}_1$ and $\mathcal{F}_2$, leading to these operators

$$T = (1-p_s)e^{ik(a+b)} \begin{pmatrix} 0 & 0 & 0 \\ -iG_+ & 0 & 0 \\ -iG_- & 0 & 0 \end{pmatrix} \quad , \quad R = (1-p_s)e^{ik(a+b)} \begin{pmatrix} iF & 0 & 0 \\ 0 & iF_+ & 0 \\ 0 & 0 & iF_- \end{pmatrix}, \tag{2.55}$$

where p_s are the losses of the beam splitter. Therefore, with these operators the SNR is obtained in Ref. [46] and given by

$$\mathrm{SNR}(\mathrm{f_g}) = \frac{8\mathcal{F}\mathrm{L}}{\lambda} \frac{1-\sigma/2}{\sqrt{1+4\mathrm{f_g^2}}} \sqrt{\frac{\mathrm{P_L}}{2\mathrm{h_P}\nu}} \mathrm{h}(\mathrm{f_g}). \tag{2.56}$$

Eq. (2.56) shows that the SNR increases with the length of the arm, L, and the power of the laser, P_L, as Eq. (2.22) already implied.

2.2.5 Improvements for the GW interferometers: recycling mirror and signal recycling

In GW interferometers, in order to enhance the cavity power, a system composed of an FP inside another FP is used. If it was not for this setup, given that the IFO is tuned at dark fringe, when no GW is passing by all the power coming from the arms would be transmitted by the beam splitter towards the laser and hence wasted. This setup is known as a *power recycling cavity* and is built by

adding an extra mirror between the laser and the beam splitter called *power recycling mirror* (see Figure 2.7).

Figure 2.7: Schematic representation of a GW interferometer with a recycling mirror, placed between the laser and the beam splitter. The Michelson interferometer acts as a mirror on its own. The cavity composed of the recycling mirror and the Michelson is known as the recycling cavity which can be tuned to increase the SNR.

The *power recycling cavity* is composed by three mirrors, M_1, M_2 and M_3. These mirrors are represented by red blocks in Figure 2.7. In Figure 2.8 a simpler drawing of the *power recycling cavity* is shown, since it will be relevant for our calculations. The distance between M_1 and M_2 is l and is much smaller than the one between M_2 and M_3, L (see Figure 2.8). The reflectivity factors of M_1 and M_2 are r_1 and r_2, respectively, while that of M_3 is assumed to be 1. Hence, the transmissivities of M_1 and M_2 are t_1 and t_2, respectively, while that of M_3 is 0.
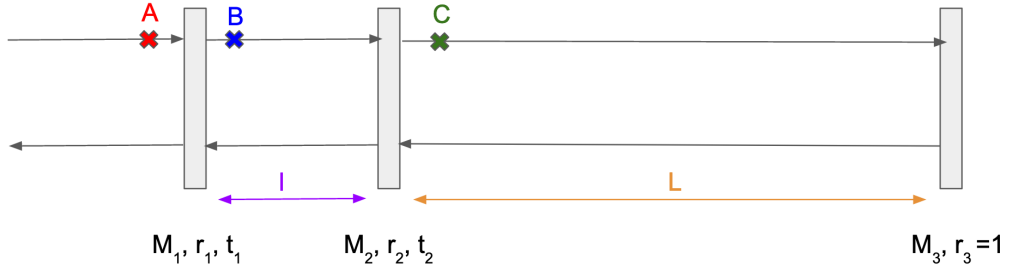
Figure 2.8: Schematic representation of the power recycling cavity, which has the aim of enhancing the cavity power. It is composed by the mirrors, M_1, M_2 and M_3. The distance between M_1 and M_2 is l and is much smaller than the one between M_2 and M_3, L. The cavity is assumed to be ideal, so the reflectivity of M_3 is assumed to be 1.

The amplitude transmitted through M_2 in absence of M_3 defines the transmittance

$$\mathcal{T} = \frac{t_1 t_2 e^{ik_L L}}{1 + r_1 r_2 e^{2ik_L L}}.$$
(2.57)

The reflectance is given by

$$\mathcal{R} = \frac{r_2 + r_1 e^{2ik_L L}}{1 + r_1 r_2 e^{2ik_L L}}.$$
(2.58)

31

The amplitude of the field in point C (see Figure 2.8) can be calculated assuming a single FP cavity with a virtual mirror of parameters $\mathcal{T}$ and $\mathcal{R}$ and an end mirror [46], which results in

$$C = \frac{\mathcal{T}}{1 + \mathcal{R}e^{2ikL}} A = \frac{t_1 t_2 e^{ik_L L}}{1 + r_1 r_2 e^{2ik_L L} + e^{2ikL}(r_2 + r_1 e^{2ik_L L})} A, \tag{2.59}$$

where A is the amplitude of the input field to the compound cavity. The maximum value of C is obtained for $2k_L l = 0$ and $2k_L L = \pi$, which implies the short cavity (the one formed by M_1 and M_2) is in antiresonance and the large cavity (the one formed by M_2 and M_3) is in resonance. In this case, the power is given by

$$|C|^2 = \frac{t_1^2 t_2^2}{(1 - r_1)^2 (1 - r_2)^2} |A|^2. \tag{2.60}$$

The result can be written as a global surtension factor [46]

$$S_o = \left[\frac{|C^2|}{|A|^2} \right]_{\text{resonance}} = \frac{(1 + r_1)(1 + r_2)}{(1 - r_1)(1 - r_2)}. \tag{2.61}$$

A cavity at antiresonance is more reflective than any of its mirrors, so under the assumptions that the mirror's reflectivity factors are given by $r_1 = 1 - \epsilon_1$ and $r_2 = 1 - \epsilon_2$, where $\epsilon_1, \epsilon_2 << 1$, then the reflectance of the cavity is given by

$$\mathcal{R}_{\text{antiresonance}} = \mathcal{R}_o = \frac{r_1 + r_2}{1 + r_1 r_2} \sim 1 - \frac{\epsilon_1 \epsilon_2}{2}. \tag{2.62}$$

Since $L >> l$, the relation between the spectral ranges is $\Delta_L << \Delta_l$. It can be checked that the phase of the reflectance changes very little: $2kl = 2\pi \delta\nu/\Delta_l$, so the reflectance can be written as

$$\mathcal{R} = \mathcal{R}_o \left[1 + 2i\pi \frac{\delta\nu}{\Delta_L} \left[\frac{r_1(1 - r_2^2)}{(r_1 + r_2)(1 + r_1 r_2)} \right] \right]. \tag{2.63}$$

The quantity $2k_L L$ is $2k_L L \equiv \pi + 2\pi \delta\nu/\Delta_L$ and the surtension factor is derived in Ref. [46] as

$$S = \frac{|C|^2}{|A|^2} = S_o \left[1 + \frac{4\mathcal{R}\sin^2(\pi\delta\nu/\Delta_L)}{(1 - \mathcal{R})^2} \right]^{-1} = S_o \frac{1}{1 + (2\mathcal{F}_{super}\delta\nu/\Delta_L)^2}, \tag{2.64}$$

where $\mathcal{F}_{super} \equiv \frac{\pi\sqrt{\mathcal{R}}}{1 - \mathcal{R}}$ is the surperfinesse. The linewidth is thus $\delta_L = \Delta_L/\mathcal{F}_{super}$. The optimal SNR in this optical system is derived in Ref. [46] and is given by

$$\text{SNR}(\nu_g) = \frac{4\pi L}{\sqrt{2}\lambda} \frac{1}{P} \frac{\sqrt{\sigma}(2 - \sigma)}{\sqrt{1 + 2\pi\nu_g\sigma/(P\Delta\nu_{\text{FSR}})^2}} \sqrt{\frac{P_L}{2h_P\nu}} h(\nu_g). \tag{2.65}$$

Controlling the resonance of this *recycling cavity* allows to get a higher power to reach the beam splitter and thus the SNR increases as well.

Another recent development is the signal recycling cavity, formed by adding one more mirror after the output port of the IFO (see Figure 2.9) to store the sidebands generated by the GW. The dark fringe port plus the signal recycling mirror form a resonant cavity whose reflectivity can be tuned. The gravitational frequencies creating a sideband for which the signal cavity is antiresonant are enhanced. This allows to modify the sensitivity curve and have a gain factor of $2\mathcal{F}/\pi$ at a given frequency range of special interest [47].
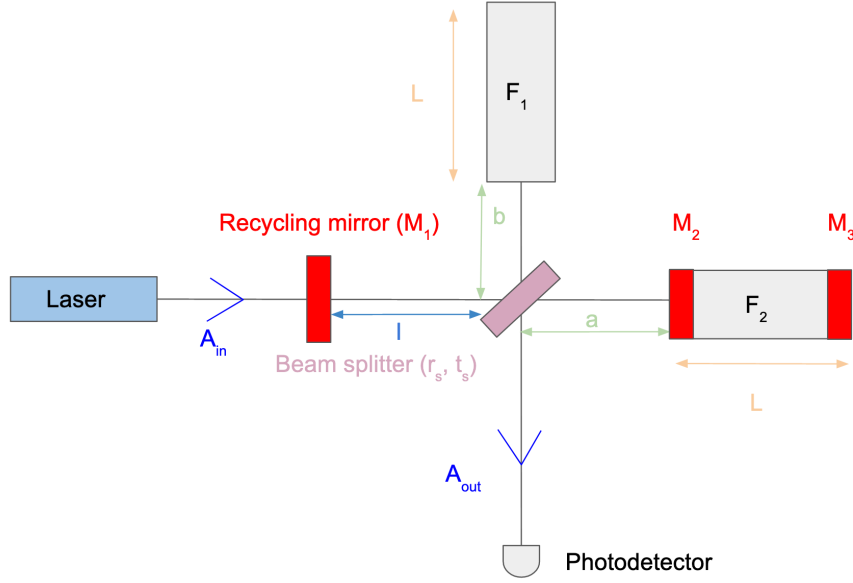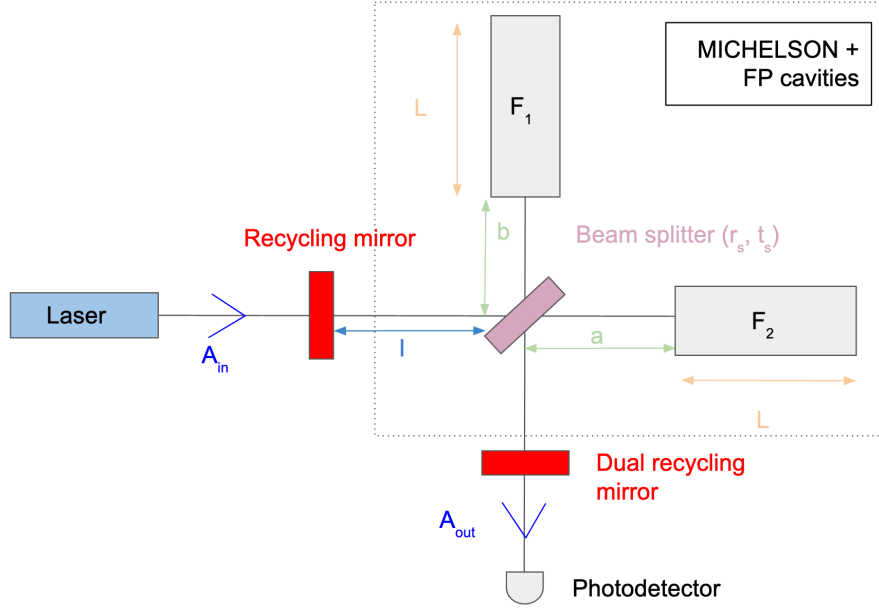
Figure 2.9: Schematic representation of a GW interferometer with a dual recycling mirror, placed between the beam splitter and the output port.

2.3 Types of noise and noise sources in GW interferometers

As shown in Eq. (1.50), the proper distance between two free masses changes as GWs pass by an amount $\Delta L = \frac{1}{2}h_+ L$, where $L \equiv x_2 - x_1$. This is the length change in the arm of an interferometer when a GW passes by (in the detector frame). Consequently, for a burst signal with strain amplitude $h_+ \sim 10^{-21}$ and an IFO with arm length of 3km, the variation in length of the arm is $\Delta L \sim 1.499 \cdot 10^{-18}$m. This implies that for a signal whose strain is of the order of $h_o \sim 10^{-21}$, an IFO has to be sensitive enough to detect a displacement of the order of 10^{-18}m. In terms of phase shift, we aim at $\Delta\phi_{Mich} = \frac{4\pi}{\lambda_L}h_o L \simeq 3.54 \cdot 10^{-11}$rad. However, this value is higher in the case of a Michelson with FP cavities. In this case, a gain of $2\mathcal{F}/\pi$ is achieved in the phase shift. For instance, if the FP cavities have a finesse of ~ 200, then the gain is about 130 and thus the phase shift: $\Delta\phi_{Mich} \simeq 4.607 \cdot 10^{-9}$rad. Nevertheless, there are many sources of noise in the IFO that make this task more difficult. In what follows, a summary of some of the noise sources is given as well as how they affect the sensitivity of the IFO, expressed in terms of the strain sensitivity, $S_n^{1/2}(f)$. The strain sensitivity is the square root of the *noise spectral density*, $S_n(f)$, which is derived in terms of the noise in a detector, denoted by $n(t)$. If the noise is stationary, the Fourier components are uncorrelated and so their ensemble average is [9]

$$\langle \tilde{n}^*(f)\tilde{n}(f') \rangle = \delta(f - f')\frac{1}{2}S_n(f). \tag{2.66}$$

Given that the noise is a real function, then $S_n(-f) = S_n(f)$. For $f = f'$, the right hand side of Eq. (2.66) diverges. Hence, we restrict the time interval to $-T/2 < t < T/2$, where T is the observation time. The delta is then evaluated

$$\delta(f = 0) \to \left[\int_{-T/2}^{T/2} dt\, e^{i2\pi ft} \right]|_{f=0} = T. \tag{2.67}$$

Hence, Eq. (2.66) results in

$$\langle |\tilde{n}(f)|^2 \rangle = \frac{1}{2}S_n(f)T, \tag{2.68}$$

where the 1/2 factor is a convention that is added so that $S_n(f)$ is obtained integrating only over physical frequencies, i.e.: f>0.

Noise sources can be classified according to different criteria. The first criterion is stationarity. If a noise's statistical properties do not vary much over time, the noise is said to be *stationary*. Another criterion is the origin of the noise. There are *fundamental noises*, which are those intrinsic to the detector, such as shot noise, radiation pressure, and seismic noise. Noises introduced in the system or amplified by control loops used to maintain the IFO in a correct working point are called *control noises*. *Technical noises* are those coming from the implementation of the IFO, such as power noises. There are also many *environmental noises*, such as magnetic fields that couple to the detector [48] or scattered light.

In this section an explanation on fundamental noises is provided. Control noises and technical noises will not be explained in this thesis. For a detailed description of these, the reader is referred to Ref. [49]. Two types of environmental noise, scattered light and Schumann resonances, are explained in detail in Chapter 4 and Chapter 6, respectively.

2.3.1 Shot noise

Shot noise is due to the fact that the laser light is discrete, i.e.: it comes as photons. After each observation time T, the number of photons reaching the photodetector, N_γ, will be different. The fluctuation in the number of photons is given by $\Delta N_\gamma = \sqrt{N_\gamma}$. It thus produces a fluctuation in the power observed given by [9]

$$(\Delta P)_{\text{shot}} = \frac{1}{T}\sqrt{N_\gamma}\hbar\omega_L = \sqrt{\frac{\hbar\omega_L}{T}P}, \tag{2.69}$$

where P is the average power measured at the photodetector and ω_L the frequency of the laser. The fluctuation of power in the laser has to be compared with the power fluctuations a GW would induce. A periodic GW with frequency f and plus polarization produces a power fluctuation given by [9]

$$(\Delta P)_{GW} = \frac{P_o}{2}|\sin(2\phi_o)|\frac{4\pi L}{\lambda_L}h_o, \tag{2.70}$$

where P_o is the input power to the IFO, which relates to the output power by $P = P_o \sin^2(\phi_o)$. The signal to noise ratio (SNR) is thus given by

$$\frac{S}{N} = \frac{(\Delta P)_{GW}}{(\Delta P)_{shot}} = \sqrt{\frac{P_o T}{\hbar\omega_L}}\frac{4\pi L}{\lambda_L}h_o|\cos(2\phi_o)|. \tag{2.71}$$

For $\cos(\phi_o) = 1/\sqrt{2}$, the SNR simplifies to

$$\frac{S}{N} = \frac{(\Delta P)_{GW}}{(\Delta P)_{\text{shot}}} = \sqrt{\frac{P_o T}{\hbar\omega_L}}\frac{4\pi L}{\lambda_L}h_o. \tag{2.72}$$

Also, for a periodic GW of frequency f, the SNR can be written in terms of the strain sensitivity $S_n^{1/2}(f)$ as

$$\frac{S}{N} = \left(\frac{T}{S_n(f)}\right)^{1/2}h_o \tag{2.73}$$

By equating Eqs. (2.72) and (2.73) the strain sensitivity due to shot noise is obtained

$$S_n^{1/2}(f)|_{\text{shot}} = \frac{\lambda_L}{4\pi L}\sqrt{\frac{2\hbar\omega_L}{P_o}}. \tag{2.74}$$

In a realistic GW detector, where there exists a power recycling, the efficiency of the photodetector is accounted for and there is dependence on the GW frequency, the strain sensitivity due to shot noise is

$$S_n^{1/2}(f)|_{\text{shot}} = \frac{1}{8\mathcal{F}L}\sqrt{\frac{4\pi\hbar\lambda_L c}{\eta P_{bs}}}\sqrt{1 + \left(\frac{f}{f_p}\right)^2}. \tag{2.75}$$

The parameter η is the efficiency of the photodetector, P_{bs} the power on the beam splitter after recycling and f_p is the pole frequency, defined as $f_p = c/(4\mathcal{F}L)$. A way of reducing the shot noise is achieving an increase in the power reaching the beam splitter P_{bs}, which can be achieved with a *power recycling cavity*, as described in section 2.2.5.

2.3.2 Radiation pressure

Radiation pressure is exerted by the light impinging in the mirrors and then reflecting back. Since the number of photons fluctuates as $\Delta N_\gamma = \sqrt{N_\gamma}$, the radiation pressure will also fluctuate. This fluctuation generates a force that shakes the mirrors and grows as $\sqrt{P_{bs}}$. Hence, the solution provided in the previous subsection for decreasing the shot noise would in fact increase the radiation pressure. The fluctuations of the force exerted by a laser beam with power P during an observation time T are given by [9]

$$\Delta F = 2\sqrt{\frac{\hbar\omega_L P}{c^2 T}}. \tag{2.76}$$

The spectral density of the force is thus given by [9]

$$S_F^{1/2} = 2\sqrt{\frac{\hbar\omega_L P}{c^2}}, \tag{2.77}$$

which can also be expressed as the spectral density of the displacement of the mirror of mass M as

$$S_x^{1/2}(f) = \frac{2}{M(2\pi f)^2}\sqrt{\frac{\hbar\omega_L P}{c^2}}. \tag{2.78}$$

The strain sensitivity due to radiation pressure is

$$S_n^{1/2}(f)|_{\text{rad pressure}} = \frac{4}{ML(2\pi f)^2}\sqrt{\frac{\hbar\omega_L P}{c^2}} \tag{2.79}$$

It can be shown that for a Michelson IFO plus FP cavities the strain sensitivity due to radiation pressure is given by [9]

$$S_n^{1/2}(f)|_{\text{rad pressure}} = \frac{16\sqrt{2}\mathcal{F}}{ML(2\pi f)^2}\sqrt{\frac{\hbar P_{bs}}{2\pi\lambda_L c}}\frac{1}{\sqrt{1+(f/f_p)^2}}. \tag{2.80}$$

2.3.3 Standard quantum limit

The combined effect of shot noise and radiation pressure is known as the *optical read-out noise*. Its spectral density is obtained by adding linearly the independent spectral densities

$$S_n(f)|_{\text{opt}} = S_n(f)|_{\text{shot}} + S_n(f)|_{\text{rad}}, \tag{2.81}$$

which can thus be expressed as

$$S_n^{1/2}(f)|_{\text{opt}} = \frac{1}{L\pi f_o}\sqrt{\frac{\hbar}{M}}\left[1+(f/f_p)^2+(f/f_p)^4\frac{1}{1+(f/f_p)^2}\right]^{1/2}, \tag{2.82}$$

where f_o is defined as $f_o = \frac{8\mathcal{F}}{2\pi}\sqrt{\frac{P_{bs}}{\pi\lambda_L cM}}$. The optimal value of f_o is that for which the shot noise and radiation pressure contributions are equal: $1+f^2/f_p = (f_o/f)^2$. The corresponding optimal value of $S_n^{1/2}(f)$ defines the *standard quantum limit* (SQL)

$$S_{\text{SQL}}^{1/2}(f) = \frac{1}{2\pi f L}\sqrt{\frac{8\pi}{M}}. \tag{2.83}$$

The limiting value of $S_{\text{SQL}}(f)$ is a manifestation of the Heisenberg uncertainty principle. However, the detector sensitivity can be improved beyond its quantum noise limit by using squeezed light technology. This technology consists of injecting squeezed states of light into the measurement output (dark port) of the interferometer. Even though no light enters the interferometer through the dark port, the quantum fluctuations of the vacuum field of the light do enter the dark port and superimpose with the output electromagnetic field of the interferometer, which contains the GW signal. If these vacuum fluctuations are replaced by a continuous injection of squeezed vacuum states of light, the measurement uncertainty can be controlled [50].

The effect of the quantum noise in the sensitivity of Virgo is seen in Figure 2.10 represented by a purple solid line. In Figure 2.10 the contributions from the different noise sources mentioned in the following sections are plotted against the overall Virgo sensitivity (black solid line). The narrow lines in the sensitivity are due to various sources. The lines at 50Hz and harmonics are due to the power mains. The frequencies of resonance of the fibers used to suspend the mirrors are called violin modes and are also visible in the sensitivity curve.
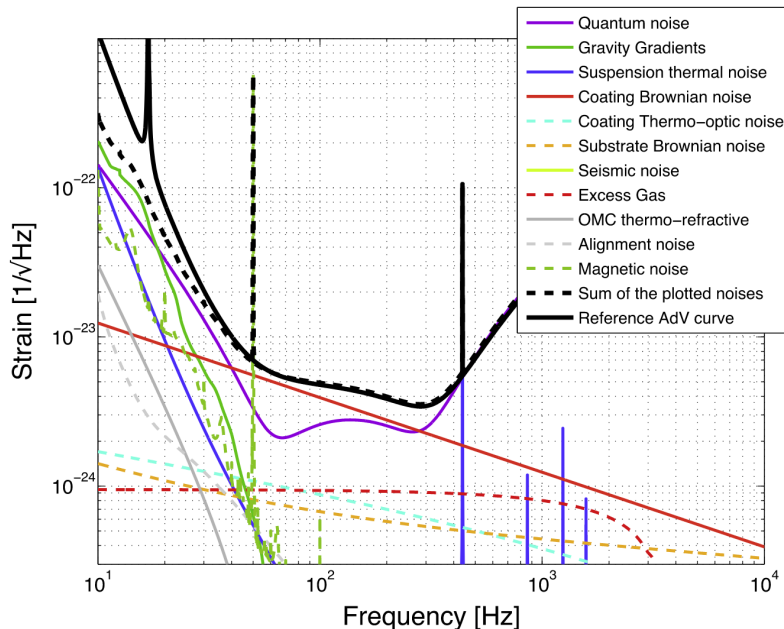
Figure 2.10: Figure retrieved from Ref. [51]. Strain sensitivity of the different noises in Virgo. The black curve represents the estimated sensitivity curve for Advanced Virgo. The worst limiting noise for frequencies below 40Hz and above 300Hz is quantum noise (solid purple line). The Brownian noise in the coating of mirrors (solid red line) is the limiting noise in the region between 40-300Hz. Seismic noise (green solid line) has a very big impact at frequencies below 40Hz. At 50Hz, the peak visible is due to the mains in electronics, which takes this value in Europe. Other peaks above 300Hz are due to the suspension thermal noise.

2.3.4 Displacement noise

The laser light is not the only source of noise that moves the test masses. Other effects or sources unrelated to the laser are known as *displacement noise*. Displacement noise is characterized by a strain spectral density of the displacement which is denoted by $x(f)$. A GW passing by an FP cavity modifies the cavity length by $\Delta L = hL$. Thus, if the length of the cavity changes by Δx due to the displacement noises, the corresponding equivalent GW amplitude is $\Delta x/L$.

Seismic motion

The Earth's ground is in constant motion. Human activity (means of transport, walking, daily activities,...) and weather conditions such as winds affect the sensitivity of the IFO in the region between 1-10Hz. There is also a micro-seismic background which shakes the suspension mechanisms and thus the mirrors. Its strain sensitivity has the form

$$x(f) \simeq A\left(\frac{1Hz}{f^\nu}\right)mH^{-1/2}. \tag{2.84}$$

For frequencies above 1 Hz, the values of ν and A are $\nu \simeq 2$ and $A \simeq 10^{-7}$. Dividing by the arm length of the IFO results in a noise strain at least ten orders of magnitude larger than the values to detect GWs. The seismic noise must therefore be attenuated by a huge factor. This is achieved with a set of pendulums in cascade. This device is commonly known as *superattenuator* in Virgo. One

single pendulum with normal mode f_o has its suspension point moving in the horizontal direction with a frequency f such that $f > f_o$. This oscillation is transmitted with an attenuation proportional to $(f_o/f)^2$ to a mass suspended from the pendulum. For a chain of pendula, the oscillation will be transmitted with an attenuation proportional to f^{-2n}, where n is the number of pendula [52, 53]. This is the working principle of the superattenuator, represented in Figure 2.11.

The effect of the seismic noise is seen in Figure 2.10 represented by a bright green solid line.
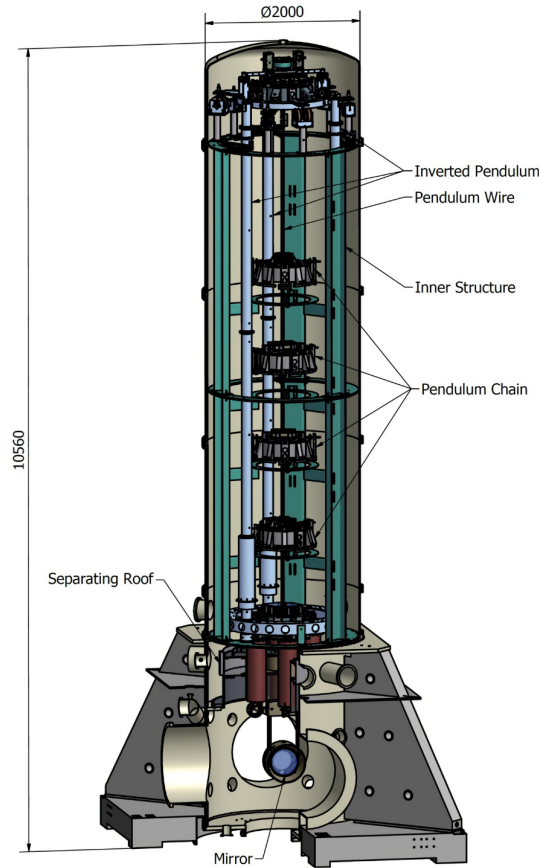
Figure 2.11: Figure retrieved from Ref. [53]. Virgo superatenuator. It is composed by a chain of n pendula that reduces the seismic motion of the test mass as f^{-2n}, where f is the frequency with which a single pendulum's suspension point moves in the horizontal direction.

Newtonian noise

The Newtonian noise (NN) is also known as *gravity gradient noise* and is due to the Newtonian gravitational forces of objects that are moving. For instance, the test masses in the IFO are subject to gravity perturbations due to the propagation of seismic waves, atmospheric changes, ... [54]. In order to properly model the NN curve, the local seismic field nearby the test masses is monitored, which is done with seismometers and tiltmeter data. This movement of test masses results in a time-varying gravitational force that cannot be screened out from the detectors, though the noise can be reduced. Using seismic sensors' data can be used as a coherent cancellation of Newtonian noise [54].

The effect of the Newtonian noise in the sensitivity of Virgo is seen in Figure 2.10 represented by a green solid line.

Thermal noise

Thermal noise induces vibrations in the mirrors and the suspensions. The displacement spectral density of the force responsible for thermal fluctuations in a system at temperature T is [9]

37

$$x(\omega) = \frac{1}{\omega|Z(\omega)|}[4kTRe(Z(\omega))]^{1/2}, \tag{2.85}$$

where $Z(\omega)$ is the impedance of the system and ω is the frequency of the characteristic mode of the system. The most important thermal noises are

- Suspension thermal noise. Any vibration induced in the suspension of the test masses results in a displacement noise. The effect of the suspension thermal noise is seen in Figure 2.10 represented by a blue solid line.

  - Pendulum thermal fluctuations induce a swinging motion in the suspensions and thus a horizontal displacement of the mirrors. This is the dominant noise between a few Hz to about 50Hz.

  - Vertical thermal fluctuations. Thermal noise also induces a vertical motion of the suspensions.

  - Violin modes are vibrations that can be described in terms of fluctuations of the normal modes of the wires holding the mirrors. These are very narrow peaks.

- Test mass thermal noise are thermal fluctuations within the test masses themselves.

  - Brownian motion. The atoms of a mirror at temperature T have Brownian motion due to their kinetic energy, which leads to thermal noise. This is the dominant source of noise between a few tens to a few hundreds of Hz. The effect of the Brownian motion is seen in Figure 2.10 represented by a red solid line.

  - Thermo-elastic fluctuations. In a finite volume, the temperature fluctuates, which generates displacement noise through the expansion of the material. This takes place both in the bulk and coating of the mirrors.

  - Thermo-refractive fluctuations. The refractive index of the coatings is a function of the temperature. The same temperature fluctuations that lead to thermo-elastic fluctuations also induce fluctuations in the refraction index.

Scattered light

A very harmful source of noise in GW detectors is scattered light. A detailed description of scattered light is provided in Chapter 4. Scattered light can be mitigated by different means, and one of them consists of using devices called *baffles* that absorb part of the scattered light. Baffles are described in Chapter 4.

2.3.5 Search for noise sources and methods to clean data

The search for sources of noise is a laborious on-site work called *noise hunting* that consists of tracking down each noise source and understanding the conversion mechanism between the source and the output signal of the interferometer. To achieve this task, the GW detectors are equipped with many sensors (seismometers, magnetometers, photodiodes, ...) whose signals are used to monitor external disturbances to determine whether a candidate GW event is such or whether it was a fake signal produced by instrumental or environmental noise.

The noise hunting process starts by identifying transient noise events (*glitches*, due to sudden malfunctioning of the IFO components affected by environmental noise that cannot be mitigated) or spectral lines. Then, the events must be correlated with unusual detector behaviors or environmental disturbances. If there is no correlation, a series of experiments are performed. They start by injecting fake noise around noise source candidates. The effect of this injection in the environmental noise detectors around the point of injection is correlated to an effect in the sensitivity curve. Each type of noise is searched for differently. For instance, in the case that there was a feature in the sensitivity curve looking like scattered light, the first task is injecting noise in the form of seismic motion in sensitive areas of the IFO. The seismic motion will be transmitted due to different processes such as backscattering to the propagating beam. The sensitivity curve will see the effect of this noise injection

in the form of an increase of the already existing feature if the noise source candidate is indeed the culprit. This task will be repeated until the source is found. Actions to mitigate the noise will follow according to the type of noise source.

An example of the use of these noise-hunting activities is explained for the case of environmental magnetic fields produced by electronic boards, pumps, motors, lights, or electrical power circuits, which are also worrying because they can affect the coils that act on the test masses to position them. These sources are studied with magnetic injections from a driving coil we built [48]. Placing the coil in different locations and after several injections, we could estimate the transfer function (TF) that converts the magnetic noise into strain sensitivity [48]. This TF is the one used in studies of the effect of correlated magnetic noise in gravitational-wave background searches [21], introduced in Chapter 6.

Not all the noise sources can be mitigated or understood, so data analysis techniques have been developed to "clean" the data and not bias the results of the analysis. As mentioned above, some lines such as the power mains or the violin modes (see Figure 2.10) are very well known and narrow in the frequency domain, so they are *notched* from the data, i.e.: they are removed from the data and substituted by zeroes. Some sources of glitches are also not well understood and hence the period when these glitches appeared is excluded, which is an action known as *vetoing* [55].

These mitigation actions were not enough in O3, and the search for a gravitational wave background was affected by a large rate of very loud glitches. For this reason, a new technique was developed called *gating*, which consists of substituting by zeroes the glitches. Before applying this technique, other data quality tests were performed, such as non-stationarity cuts (see section 6.4 for further details) or inverse noise weighting, but they were not successful in removing the effect of these glitches. Hence the need for a new technique. The effect of analyzing data with zeros is small, as shown in Ref. [56], and gating does not add extra lines in frequency domain to the data nor remove real GW events.

Chapter 3

Simulations

In this chapter a simulation tool used to determine the distribution of light in optical elements of the interferometers is introduced. To do this, the physical concepts the simulation tool uses are first explained. These are the theory of diffraction and the paraxial approximation.

3.1   Brief summary of the theory of diffraction

All real optical systems have finite apertures, with boundaries or edges. For this reason, it is important to have an insight into the physical diffraction effects and the analytical techniques used to describe them. It is essential to have theoretical models for light propagation. The Scalar Diffraction Theory (SDT) is assumed, which is based on the Kirchhoff equation, derived in what follows.

The vector $\mathcal{E}(\mathbf{r}, t)$ is a component of the electric field which, in a medium with refractive index n, obeys the wave equation

$$\left(\nabla^2 - \frac{n^2}{c^2}\frac{\partial^2}{\partial t^2}\right)\mathcal{E}(\mathbf{r}, t) = 0\,. \tag{3.1}$$

Light from a laser can be considered as a pure monochromatic wave and is given by

$$\mathcal{E}(\mathbf{r}, t) = \frac{1}{2}\Big[E(\mathbf{r})e^{-i\omega t} + \bar{E}(\mathbf{r})e^{i\omega t}\Big]. \tag{3.2}$$

The vector $E(\mathbf{r})$ is the amplitude of the electric field and ω is the angular frequency, given by $\omega = 2\pi\nu$, with ν the frequency. Applying the wave equation over the monochromatic wave in Eq. (3.2) leads to the Helmholtz equation

$$(\nabla + k^2)E(\mathbf{r}) = 0, \tag{3.3}$$

where $k \equiv n\omega/c$ is the wavenumber. The Helmholtz equation can be solved resorting to the Green's theorem, which results in the Kirchhoff equation,

$$E(\mathbf{r}) = \int\int_{z=0} E(\mathbf{r}')\mathbf{n}' \cdot \nabla'G(\mathbf{r}, \mathbf{r}')dx'dy'. \tag{3.4}$$

The Green's function $G(\mathbf{r}, \mathbf{r}')$ is fully derived in Ref. [46] and results in

$$G(\mathbf{r}, \mathbf{r}') = \frac{e^{ik|\mathbf{r}-\mathbf{r}'|}}{|\mathbf{r}-\mathbf{r}'|} - \frac{e^{ik|\mathbf{r}-\mathbf{r}''|}}{|\mathbf{r}-\mathbf{r}''|}. \tag{3.5}$$

Given a surface with an aperture of diameter D, and a propagating field, the Kirchhoff equation relates the incoming field with the field after passing through the aperture. This process is represented in Figure 3.1. The field to the left of the aperture is $E_1(\mathbf{r})$. Right after trespassing the aperture at $z = 0$, the field for radii smaller than $D/2$ is equal to $E_1(\mathbf{x}, \mathbf{y}; \mathbf{0})$, while for radii larger than $D/2$ the field is zero. The field at a distance $\mathbf{r}$ from the centre of the aperture is denoted by $E_2(\mathbf{r})$, and given by the Kirchhoff equation, Eq. (3.6).
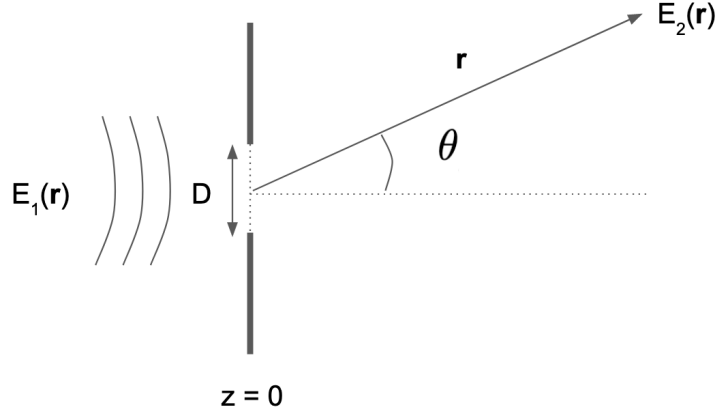
Figure 3.1: Field $E_1(\mathbf{r})$ trespassing an aperture at z=0 with diameter D. Right after trespassing the aperture at z=0, the field for radii smaller than $D/2$ is equal to $E_1(\mathbf{x}, \mathbf{y}; \mathbf{0})$ $/(x^2 + y^2) < (D/2)^2$, while for radii larger than $D/2$ the field is zero. The field at a distance $\mathbf{r}$ from the centre of the aperture is denoted by $E_2(\mathbf{r})$. θ is the angle under which the aperture is seen from the observation point, placed at $\mathbf{r}$ from the centre of the aperture.

$$E_2(\mathbf{r}) = -\frac{i}{\lambda} \int \int_D E_1(\mathbf{r}')\mathbf{n}' \cdot \nabla' G(\mathbf{r}, \mathbf{r}') dx' dy' \tag{3.6}$$

In Eq. (3.6), the factor $\mathbf{n}' \cdot \nabla' G(\mathbf{r}, \mathbf{r}')$ is known as the diffraction kernel, given by

$$\mathbf{n}' \cdot \nabla' G(\mathbf{r}, \mathbf{r}') = -\frac{i}{\lambda} \frac{e^{ik\rho}}{\rho} (1 + \frac{i}{k\rho}) \frac{z}{\rho} \tag{3.7}$$

The parameter ρ is the distance between the source and the observation point, and is given by $\rho \equiv \sqrt{(x - x')^2 + (y - y')^2 + z^2}$. With the explicit expression of the diffraction Kernel, the Kirchhoff equation can be rewritten as

$$E_2(\mathbf{r}) = -\frac{i}{\lambda} \int \int_D E_1(\mathbf{r}')\frac{e^{ik\rho}}{\rho} (1 + \frac{i}{k\rho}) \frac{z}{\rho} dx' dy' \,. \tag{3.8}$$

As the distance z between the aperture and the observation plane becomes larger, the factor $1/(k\rho) \to 0$. Eq. (3.6) can thus be rewritten as

$$E_2(\mathbf{r}) = -\frac{i}{\lambda} \oint_D E_1(\mathbf{r}')\frac{e^{ik\rho}}{\rho} \cos(\theta) ds' \,, \tag{3.9}$$

known as the Huygens Fresnel equation. The angle θ is that under which the aperture is seen (represented in Figure 3.1) [46]. If $\theta << 1$, the paraxial approximation can be applied, which neglects terms of second order and above of $\sqrt{(x - x')^2 + (y - y')^2}/z$. As a consequence, $\rho \equiv \sqrt{(x - x')^2 + (y - y')^2 + z^2} \simeq z + \frac{(x-x')^2 + (y-y')^2}{2z}$. This leads to the paraxial diffraction integral

$$E_2(\mathbf{r}) = -\frac{i}{\lambda z}e^{ikz} \int \int_D E_1(x', y', 0)e^{ik\frac{(x-x')^2 + (y-y')^2}{2z}} dx' dy' \,. \tag{3.10}$$

Solving the integral in Eq. (3.10) is a cumbersome procedure, so an equivalent equation known as the paraxial diffraction equation (PDE) is derived

$$(2ik\partial_z + \partial_x^2 + \partial_y^2)E = 0 \,, \tag{3.11}$$

where the field E is given by

$$E_2(\mathbf{r}) = E(\mathbf{r})e^{ikz}. \tag{3.12}$$

To obtain Eq. (3.11), it has been assummed that E varies so slowly with z that its second derivative $\partial_z^2 E$ can be neglected [57]. As mentioned above, the paraxial diffraction equation, Eq. (3.11), and

paraxial diffraction integral Eq. (3.10) are equivalent. It will be seen that the FFT simulation tool introduced in this chapter uses Eq. (3.10), instead of solving the differential equation Eq. (3.11).

This derivation has been performed for an aperture with diameter D. This aperture can be thought of as that of a test mass from an FP cavity, leading to the same PDE.

3.1.1 Fundamental TEM mode

In this section, the PDE is solved for an axially symmetric geometry. It will be shown that the solution is a set of modes called Transverse Electromagnetic Modes.

The PDE can be solved for an axially symmetric geometry using two unknown functions dependent on z, $A(z)$ and $q(z)$. The function $A(z)$ represents a complex phase shift which is associated with the propagation of the light beam. The function $q(z)$ is a complex beam parameter which describes the variation in intensity of the field with the distance r from the optical axis, as well as the curvature of the phase front which is spherical near the axis [57]. A hypothetical solution given by a function dependent on r and z is

$$\Psi(r, z) = e^{A(z)} e^{ikr^2/(2q(z))}, \tag{3.13}$$

which is substituted in Eq. (3.11), leading to the system of equations

$$\frac{dq}{dz} = 1; \quad \frac{dA}{dz} = -\frac{1}{q(z)}. \tag{3.14}$$

The differential equation $dq/dz = 1$ has solution $q(z) = q_o + z$[1]. The parameter q_o must be chosen so that at $z = 0$ the wave is a real Gaussian function with parameter w_o, i.e.: proportional to e^{-r^2/w_o^2}. The parameter w_o is the minimum beam radius and at that abscissa, the phase front is plane [57]. Consequently, $q_o = -i\frac{kw_o^2}{2}$, which is usually rewritten using the Rayleigh range,

$$b = \frac{kw_o^2}{2}, \tag{3.15}$$

as $q_o = -ib$. The function $q(z)$ can thus be rewritten as $q(z) = z - ib$, which leads to $dA/dz = -1/(z - ib)$. This differential equation has solution $A(z) = ln\left(\frac{1}{z - ib}\right) + C$. The constant C is chosen so that $A(0) = 0$, which leads to $C = -ln\left(-\frac{1}{ib}\right)$. Finally, $A(z)$ can be written as $A(z) = ln\left(\frac{1}{\sqrt{1 + (z/b)^2}}\right) - i\arctan(z/b)$. The real part of A(z) represents a phase shift difference between the Gaussian beam and an ideal plane wave. The imaginary part of A(z) implies that the intensity of the beam on the axis decreases due to the propagation [57]. The exponent $ik/(2q(z))$ in Eq. (3.13) can be separated into real and imaginary parts: $\frac{ik}{2q(z)} = \frac{1}{z + b^2/z} + \frac{i}{b + z^2/b}$. It can be rewritten in terms of the beam half width at the abscissa z, defined as $w(z) \equiv w_o\sqrt{1 + z^2/b^2}$ and the radius of curvature of the beam at the abscissa z, defined as $R(z) \equiv z(1 + b^2/z^2)$. The functions w(z) and R(z) contain the same information as q(z), which is known as the complex curvature radius. The beam radius w is represented in Figure 3.2.

---

[1]Given an optical system with input and output plane separated by z, $q(z) = q_o + z$ relates the beam parameter $q(z)$ in the output plane to the parameter q_o in the input plane
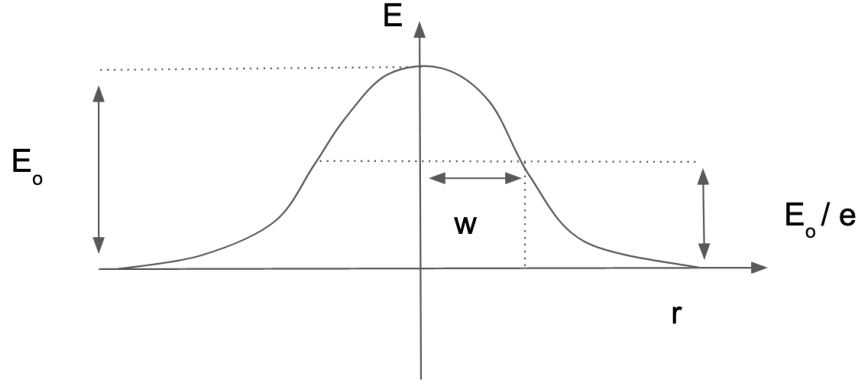
Figure 3.2: $w(z)$ is a measure of the decrease of the field amplitude E with the distance from the axis. The beam radius w depends on the amplitude of the beam E_o, and it is the distance at which the amplitude is 1/e times smaller than that on the propagation axis.

Finally, $1/q(z)$ can be expressed as $\frac{ik}{2q(z)} = -\frac{1}{w^2(z)} + \frac{ik}{2R(z)}$ and the complete solution for the PDE is given by

$$\Psi(r,z) = \frac{1}{\sqrt{1+z^2/b^2}} e^{-r^2/w^2(z)} e^{ikr^2/(2R(z))} e^{-i\arctan(z/b)}. \tag{3.16}$$

Eq. (3.16) is commonly known as the fundamental Transverse Electromagnetic Mode, or the TEM 00. The quantity $\arctan(z/b)$ is called the Gouy phase. A coherent light beam with a Gaussian intensity profile, Eq. (3.16), is not the only solution of the PDE. The other solutions are the Transverse Electromagnetic Modes, labeled by two indices m and n, TEM(m,n), commonly referred to as *Higher Order Modes (HOMs)*. They form a complete and orthogonal set of functions called the "modes of propagation". The most used are the Hermite Gauss (HG) and Laguerre Gauss (LG) modes, represented by HG(m,n) and LG(m,n), respectively. The HG modes are used when the coordinates of the problem are Cartesian, while in the case of polar coordinates LG modes are more convenient. The TEM 00 mode coincides in the two basis $\text{TEM}(0,0)(x,y;z) = \text{HG}(0,0)(x,y;z) = \text{LG}(0,0)(x,y;z)$ and is given by Eq. (3.16). More details on these two bases are provided in Appendix D. The beam widens as it propagates and the Gaussian aperture angle is given by $\theta_g = \lambda/(\pi w_o)$, represented in Figure 3.3.

3.1.2 Stable optical resonator

The Transverse Electromagnetic Modes have two very relevant properties. A TEM(m,n) mode has a finite transverse extension and it has a surface with the same phase at every point (equiphase surface). This allows to make mirrors with curvature and shape adapted to the equiphase surface of the TEM(m,n) mode so that this mode reflects on the mirrors [46]. Let us assume a Gaussian beam with a waist w_o, or Rayleigh range $z_R \equiv \pi w_o^2/\lambda$, propagating in a Fabry Perot cavity with two curved mirrors. If the beam is fitted to the mirrors, the mirrors will form an optical resonator. The Fabry Perot cavity has an input mirror M_1 and an end mirror M_2 with radii of curvature R_1 and R_2, respectively. The length of the cavity is L (see Figure 3.3) and the mirrors are located at positions z_1 and z_2. For the cavity mode to be matched with the mirrors, the wavefront curvature $R(z)$ of the beam must match R_1 and R_2 at each mirror. This results in three equations

$$R(z_1) = z_1 + z_R^2/z_1 = -R_1,$$
$$R(z_2) = z_2 + z_R^2/z_2 = R_2,$$
$$L = z_2 - z_1, \tag{3.17}$$

where the sign of the wavefront is chosen such that it is positive for a diverging beam and negative for a converging beam. It is customary to define the resonator g parameters, g_1 and g_2, given by

$$g_1 \equiv 1 - \frac{L}{R_1} \quad , \quad g_2 \equiv 1 - \frac{L}{R_2}. \tag{3.18}$$

The Rayleigh range is then derived from the system of Eqs. (3.17) and using the g parameters it can be expressed as [58]

$$z_R^2 = \frac{g_1 g_2 (1 - g_1 g_2)}{(g_1 + g_2 - 2g_1 g_2)^2} L^2. \tag{3.19}$$

The location of the mirrors with respect to the Gaussian beam waist is given by [58]

$$z_1 = \frac{g_2(1 - g_1)L}{g_1 + g_2 - 2g_1 g_2} \quad , \quad z_2 = \frac{g_1(1 - g_2)L}{g_1 + g_2 - 2g_1 g_2}. \tag{3.20}$$

By inspecting Eqs. (3.19) and (3.20), for the Gaussian beam parameters to have real and finite solutions, the product of the g parameters must be confined to this stability range [58]

$$0 \leq g_1 g_2 \leq L \tag{3.21}$$
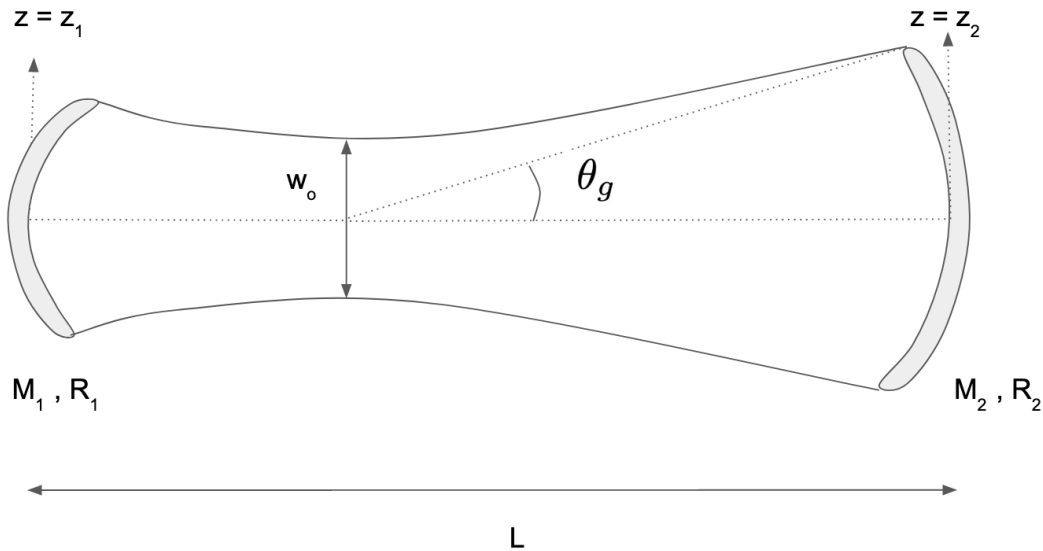
Figure 3.3: Fabry-Perot cavity of length L with an input mirror M_1 and an end mirror M_2 with radii of curvature R_1 and R_2, respectively. The waist of the beam is w_o and it represents the minimum width the beam acquires during its propagation. θ_g is the Gaussian aperture angle.

If the stability condition of the cavity is fulfilled, the cavity will be able to store certain TEM(m,n) modes for a fixed cavity length. The resonance condition is $2\pi L/\lambda + (n + m + 1)\text{gouy00} = N\pi$, so only selected modes are resonant for a given length.

3.1.3 Numerical methods

In previous sections the propagation of light through real optical elements has been described. As mentioned above, solving Eq. (3.10) is a cumbersome procedure, so numerical methods are needed. In this section, the numerical methods used in the FFT simulation tool that will be introduced in this chapter are explained.

There are different ways of representing a light beam numerically. A beam can be represented numerically by sampling its complex amplitude in a Cartesian grid. It can also be mapped onto a polar mesh with sampling points characterized by polar coordinates (r, ϕ). The beam can also be expanded in terms of a discrete basis, such as the HG or LG modes, see Appendix D. The latter approach is recommended to study the field within a system with small perturbations such as displacements of the

beam, tilts, or misalignments of the mirrors.

When a beam's complex amplitude is sampled in a Cartesian grid with equally spaced sampling points, a discrete two-dimensional Fourier transform (DFT) can be used to propagate the field. The DFT is a crude approach to the numerical Fourier transform of any function $\phi(t)$ which is zero outside the interval [0,T]. The Fourier transform (FT) of a function $\Phi(t)$ is

$$\tilde{\Phi}(f) = \int_0^T e^{2i\pi f t} \Phi(t) dt \,.$$

Numerically, $\tilde{\Phi}$(f) can be obtained by numerical integration, done by dividing the interval [0,T] in N slices of width $\Delta t = T/n$,

$$\tilde{\Phi}(f) = \frac{T}{N} \sum_{j=0}^{N-1} e^{2i\pi f j T/N} \Phi(jT/N) \,.$$

The function can then be sampled in the frequency domain. The smallest frequency interval is given in terms of the length of the interval $\Delta f = 1/T$. As a consequence, the sampling frequency is $f_m = m/T$ and the samples of the Fourier transform are given by the DFT

$$\tilde{\Phi}_m = \tilde{\Phi}\left(\frac{m}{T}\right) = \frac{1}{N} \sum_{j=0}^{N-1} e^{2i\pi m j N} \Phi_j \,,$$

where $\Phi_j \equiv \Phi(jT/N)$. The result of a DFT is not a sampling of the result of the continuous transformation. The integration will converge as the number of slices increases, $N \to \infty$.

In many simulations, a fast Fourier transform (FFT) is used to propagate the field defined in a grid. An FFT is an algorithm that computes the Discrete Fourier transform (DFT) of a matrix and can reduce the computational time from $\mathcal{O}(N^2)$ to $\mathcal{O}(N \log N)$, where N is the data size [59]. This procedure consists of applying an FFT over the array a(i,j) of size N x N containing the complex amplitude of the field. The result is then multiplied by a propagator that represents the optical elements or free space the beam needs to go through. Finally, an inverse FFT is applied over the array. This procedure is schematically represented in Figure 3.6.
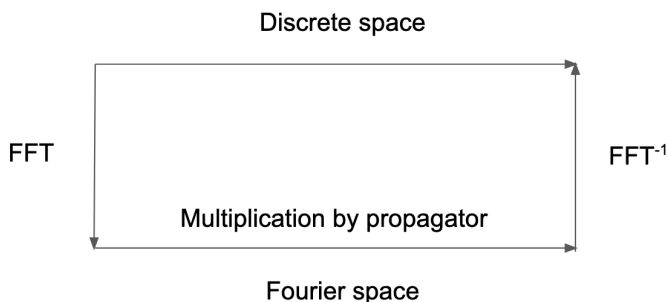
Figure 3.4: Propagation of a complex field via an FFT algorithm. The field's complex amplitude is represented by an NxN matrix a(i,j). An FFT is applied over this matrix. The result is then multiplied by a propagator that represents the optical elements or free space the beam needs to go through. Finally, an inverse FFT is applied over the array.

3.2 Stationary Interferometer Simulation

The Stationary Interferometer Simulation (SIS) is an FFT-based simulation package used to calculate fields in a stationary interferometer under various configurations. SIS was designed and is developed by Hiro Yamamoto[2]. SIS was originally developed to design the optical configuration of the Advanced LIGO Interferometer. SIS calculates fields in optical systems by taking into account realistic details of

---

[2]Hiro Yamamoto is a researcher in Caltech. His e-mail address is: hiroy@caltech.edu

optical components, like macroscopic shapes and microscopic surface phasemaps [60, 61].

SIS also serves as an analysis tool of optical system characteristics. For instance, after stationary state fields are calculated, mode analysis can be done to check the mode matching. Gaussian fitting can also be done to calculate the effective beam size and curvature.

SIS was originally developed using C++, based on an object-oriented architecture. SIS then integrated an FFT-based simulation package known as FOG (Fast Fourier Transform Optical Simulation of Gravitation Wave Interferometer), designed and developed by Richard Day[3] and written using Matlab. Richard Day analyzed the details of the FFT-based simulation framework and improved the acceleration algorithm of the field calculations in complex optical systems [62] alongside Gabriele Vajente[4]. SIS was fully rewritten in Matlab when the original SIS package and FOG were integrated into one simulation environment.

SIS is like a toolbox for building optical systems. This toolbox consists of elements to build an IFO simulation setup, and of algorithms to combine these parts for arbitrary configurations. By combining tools, any optical configuration could be built and simulated. However, the user has to assemble parts to build the setup for a specific optical configuration and various parameters have to be calculated and set by hand. SIS consists of three parts, building optical systems, setting up fields, and analyzing them.

The details of the optics can also be included in the simulation, as well as components such as baffles and ring heaters. Any measured optics data in common data formats can be used in the simulation without any prior conversion to a specific format.

The mode analysis of the entire IFO is done to set up various parameters necessary for the FFT-based calculation. The field calculation uses actual parameters and aberrations. One of the important parameters calculated using the mode analysis is the beam size on each optic. As explained in subsection 3.1.3, in FFT-based calculations the fields are defined in grids with a fixed number points (`Nfft`) in a finite area. The area, FFT window size (`Wfft`), is chosen so that it is large enough to cover the optic of interest, and the resolution, `Wfft` / `Nfft`, needs to be small enough to recognize the variation of the field and the aberration structure of optics. When the modal parameters for all fields are calculated, the optimal values of `Wfft` and `Nfft` are calculated. The number of grid points, `Nfft`, does not change from optic to optic, while `Wfft` is adjusted proportionally to the beam size on each optic (see Figure 3.5). The field propagation is done taking this scaling into account. After the window sizes are chosen, one value of `Nfft` is calculated so that the resolutions are enough at all optics. The default resolution is 1/16 of the beam size. When the user specifies resolutions for some optics, these are included to calculate the tightest constraint to specify `Nfft`. After `Nfft` and all `Wfft`s are chosen, transmission, reflection, and propagation maps are calculated alongside other support parameters, using all information of the optical setup. These maps are matrices of dimensions `Nfft` x `Nfft`, and incoming fields are multiplied by these matrices to calculate outgoing fields. These maps are calculated using actual parameters specified in `setHRfiles`. When the surface aberration is specified in `setHRfiles`, the reflection matrix has this information included, and the field is disturbed when the incoming field is multiplied by the reflection map [61].

---

[3]Richard Day was working at the European Gravitational Observatory (EGO) at that time. His e-mail address is: r.arthur.day@gmail.com

[4]The email address of Gabriele Vajente is: vajente@caltech.edu
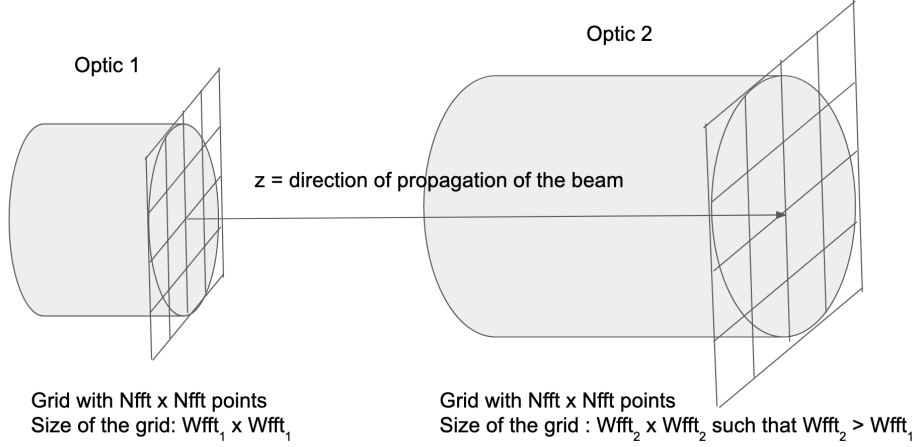
Figure 3.5: Fields are defined in grids of Nfft x Nfft points. The number of points per grid does not change as the beam propagates. The size of the grid is Wfft x Wfft and it does change depending on the size of the optical elements.

3.2.1 Propagation of fields in SIS, interaction with optics, and round-trip losses.

In SIS, the interaction between fields and optics is done in the spatial domain. The propagation of fields is done via Eq. (3.10) in the frequency domain, and it is performed with the following steps

1. An FFT is applied to convert the field at $\mathbf{r}'$ in Eq. (3.9) to a distribution in frequency domain.

2. Then, the resulting field is multiplied by the diffraction kernel, Eq. (3.7), in the frequency domain.

3. An inverse FFT is then applied to convert the field in the frequency domain back to the spatial domain.

4. Finally, the result is multiplied by the longitudinal propagation phase, $e^{-ik\Delta z}$, where $\Delta z = z - z'$.

If the propagation takes place within a substrate with refractive index n, the wavenumber k is replaced by kn, which modifies Eq. (3.10). Also, the dependence on $z - z'$ becomes $(z - z')/n$ [63]. A graphical representation of this procedure is in Figure 3.6. Even though ABCD matrices (see appendix E) are not used in SIS, they have been used separately to check the results obtained with the method used in SIS. It has been proved that both methods lead to the same results [63].
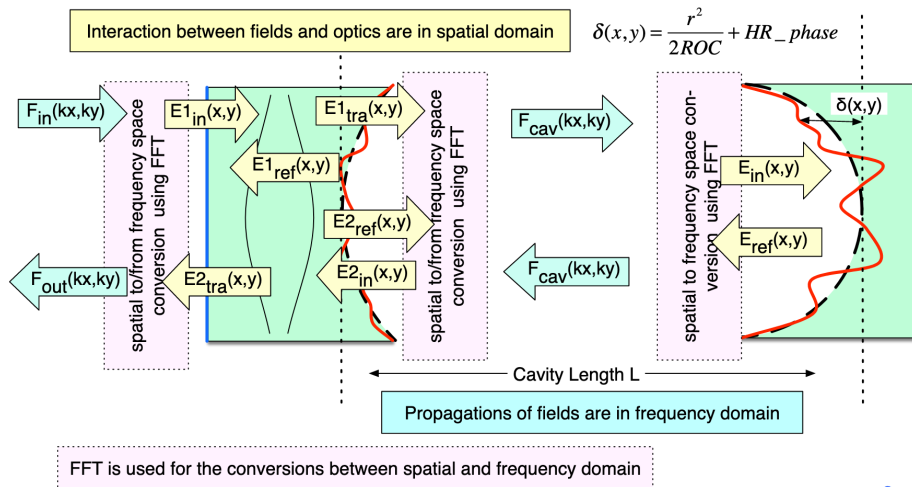
Figure 3.6: Figure retrieved from Ref. [63]. Propagation of fields within a FP cavity. In SIS, the interaction between fields and optics is done in spatial domain, while the propagation is in frequency domain. The FFT algorithm is used to convert back and forth from spatial to frequency domain.

Given a field E_{in} entering a FP cavity, the stationary field within the cavity E_4 (see Figure 3.7 for a graphical representation) is calculated numerically by iteration. This calculation includes the effect of the mode coupling of the input field and the cavity mode, as well as other sources that degrade the power in the cavity. The round trip loss (RTL) is defined as the total losses of light there are after one trip of the beam within the Fabry Perot cavity. Mathematically, the RTL can be expressed as $E_4 = E_{in}t_{ITM}/(1 - r_{ITM}r_{ETM}\sqrt{1 - RTL})$. The stationary field can also be expanded as

$$E_4 = \frac{E_{in}t_{ITM}}{1 - r_{ITM}r_{ETM}\sqrt{1 - RTL}} \sim \frac{E_{in}t_{ITM}}{1 - r_{ITM}r_{ETM}}\left(1 - \frac{RTL}{2(1 - r_{ITM}r_{ETM})}\right). \qquad (3.22)$$

The total loss L_{total} is defined by $P_{cav}(RTL) = (1 - L_{total})P_{cav}(RTL = 0)$, which allows to relate it to the RTL as $L_{total} = 1/(1 - r_{ITM}r_{ETM})RTL$.
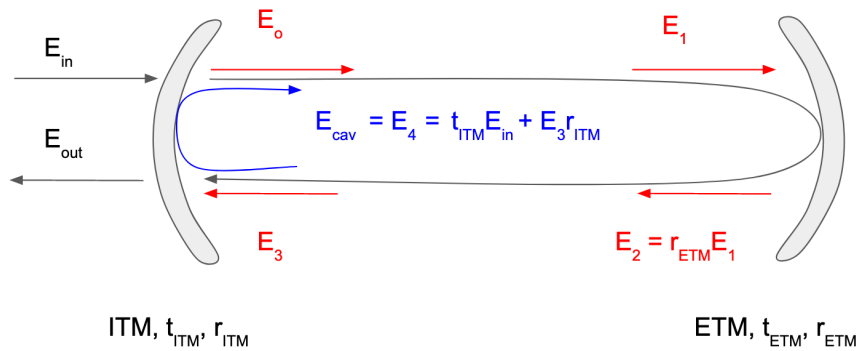
Figure 3.7: Schematic representation of the propagation of light within a FP cavity with input mirror denoted by ITM and end mirror by ETM. Their transmissivities and reflectivities are represented by $t_{mirrorname}$ and $r_{mirrorname}$, respectively.

3.2.2 Thermal deformations of optics

The heating of mirrors occurs both by absorption in the substrate and by dissipation in the coating, leading to temperature gradients in the optics. These temperature gradients affect the optical properties of the mirrors, so it is essential to include these effects in the simulations. SIS includes an explicit analytical model of the uniform coating absorption derived by Patrice Hello and Jean-Yves Vinet in Ref. [64], and of the deformation by point absorbers calculated by Wenxuan Jia in Ref. [65]. In this section, details of the implementation of the uniform coating absorption are discussed according to Ref. [64].

Mirrors are considered to be cylindrical blocks of pure silica with a high reflectance coating (HR) and an anti-reflecting coating (AR). They are assumed to have radii r = a and thickness h (Figure 3.8). The power of light is expected to dissipate by bulk absorption in the silica substrate and by the coating losses. Mirrors are also suspended in a vacuum vessel, so heat losses are only due to thermal radiation.
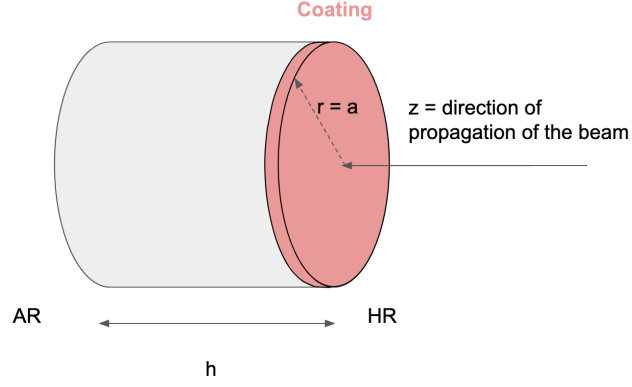
Figure 3.8: Schematic representation of the mirror assumed for the derivations in Ref. [64]. It is a cylindrical block of pure silica with a high reflectance coating (HR) and an antireflecting coating (AR). It is assumed to have radii r = a and thickness h.

The equation describing the temperature T(z,r) in the mirror after heating up by absorption of power in the coating in the steady-state is given by [64]

$$T(r,z) = \sum_m \frac{\epsilon p_m a}{K} e^{-\zeta_m h/(2a)} \frac{(\zeta_m - \tau)e^{-\zeta_m(h-z)/a} + (\zeta_m + \tau)e^{-\zeta_m z/a}}{(\zeta_m + \tau)^2 - (\zeta_m - \tau)^2 e^{-2\zeta_m h/a}} J_o\left(\zeta_m \frac{1}{a}\right) \quad (3.23)$$

The density of silica is ρ, K its thermal conductivity, and C its specific heat. The parameter ζ_m is the mth solution of $xJ_1(x) - \tau J_o(x) = 0$. The functions $J_o(z)$ and $J_1(z)$ are Bessel functions [66, 67] of 0th and 1st order, respectively. They are represented in Figure 3.9.
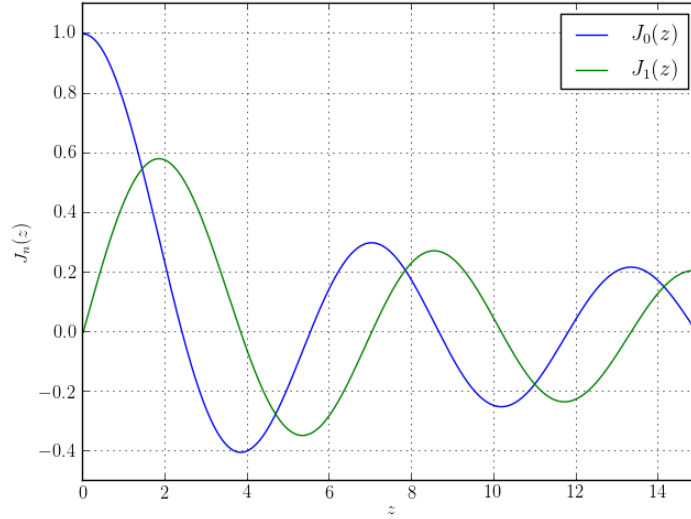
Figure 3.9: Bessel functions of 0th and 1st order. Bessel functions are the solution to the differential equation $z^2 \frac{d^2 w}{dz^2} + z \frac{dw}{dz} + (z^2 - v^2)w = 0$. Bessel functions are functions of z with order v, $J_{\pm v}(z)$. They are regular throughout the z plane cut along the negative real axis [66].

In Eq. (3.23), τ is he reduced radiation constant, given by

$$\tau \equiv \frac{4\sigma' T_{ext}^3 a}{K}, \quad (3.24)$$

where T_{ext} is the temperature of the environment surrounding the mirror and σ' is the Stefan-Boltzmann constant corrected for emissivity. For a Gaussian beam with waist w and power P reaching the mirror, the intensity is given by $I(r) = 2P/(\pi w^2)e^{-2r^2/w^2}$. In this case, the coefficients p_m in Eq. (3.23) are

given by

$$p_m = \frac{2\zeta_m^2}{\zeta_m^2 + \tau^2} - \frac{1}{J_o(\zeta_m)^2} \frac{1}{a} \int_0^a I(r) J_o\left(\zeta_m \frac{r}{a}\right) r dr \,. \tag{3.25}$$

In Eq. (3.23) the coefficient ϵ represents the efficiency of the conversion of light into heat power in the coating. To determine the equation governing the temperature gradient in the bulk, some assumptions need to be made. The light beam is assumed to cross a transparent disk with a weak distributed attenuation characterized by the parameter α, instead of the coating layer. The final result for a steady-state is

$$T(r,z) = \frac{\alpha a^2}{K^2} \sum_m \frac{p_m}{\zeta_m^2} \left[1 - \frac{2\tau \cosh\left(\zeta_m z/a\right)}{(\zeta_m + \tau)e^{\zeta_m h/(2a)} - (\zeta_m - \tau)e^{\zeta_m h/(2a)}} J_o\left(\zeta_m \frac{r}{a}\right)\right]. \tag{3.26}$$

Both of these effects combined affect the curvature of mirrors. An example produced with SIS is shown in Figure 3.10. In this case, a FP cavity is simulated with two mirrors with an aperture of 0.3m separated by 3km. The input test mass has a radius of curvature of 1420 m, while the end test mass has a radius of curvature of 1683 m. Both mirrors have a coating surface with an absorbing power of 100 mW and a substrate absorbing power of 1 mW. The blue line in Figure 3.10 (left) represents the profile of the surface map of the input test mass in the cold state, i.e.: when a light beam is not impinging on the mirrors. The red line represents the profile of the surface map of the input test mass in the hot state, i.e.: when a light beam is impinging on the mirrors. Figure 3.10 (right) represents the profiles of the cold and hot maps of the end test mass.
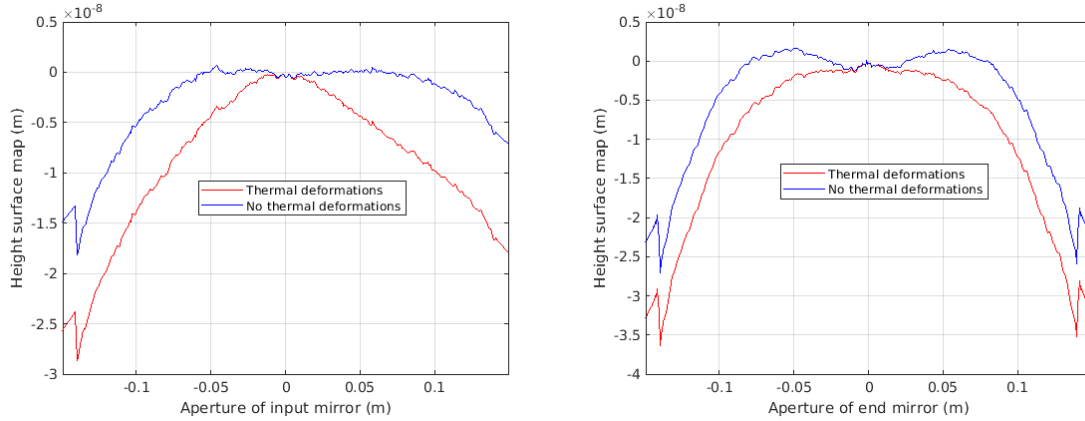
Figure 3.10: Profiles of the surface maps of the test masses in a FP cavity with two mirrors with aperture 0.3m separated 3km. The input test mass has a radius of curvature of 1420 m, while the end test mass has a radius of curvature of 1683 m. Both mirrors have a coating surface with an absorbing power of 100 mW and a substrate absorbing power of 1 mW. Red curves represent the hot state . Blue curves represent the cold state **Left** Profile of the hot and cold maps of the input test mass. **Right** Profile of the hot and cold maps of the end test mass.

During the hot state, the curvature of the mirrors is affected by the heating of the coating and substrate. This would lead to a mismatch between the main resonating mode and the mirrors. For this reason, a ring heater has to be introduced. A ring heater is, as the name indicates, an annulus in front of the edges of the mirrors that compensate for the deformation of the center of the mirror by heating up the edges of the mirror. In SIS, the effect of the ring heater is simulated. Figure 3.11 shows the same surface maps as in Figure 3.10, though having applied the equivalent to the ring heater in SIS.
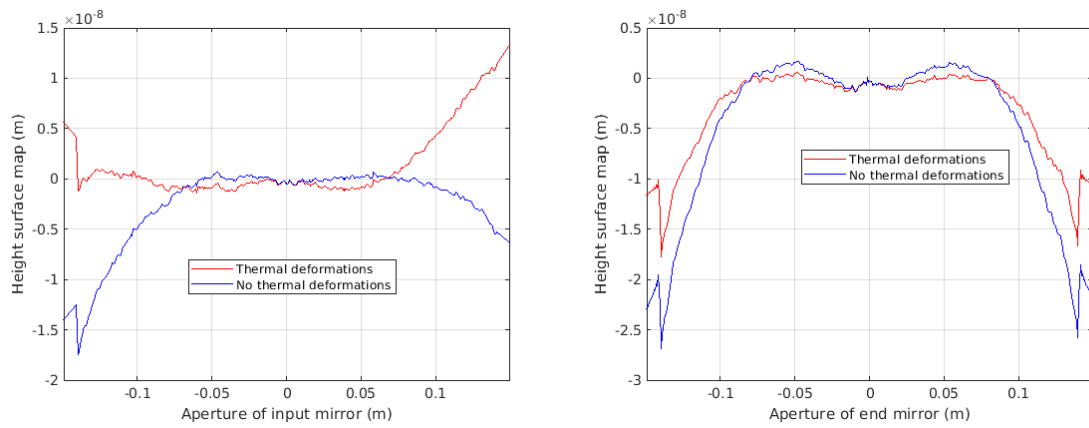
Figure 3.11: Profiles of the surface maps of the test masses in an FP cavity with two mirrors with aperture 0.3m separated 3km. The input test mass has a radius of curvature of 1420 m, while the end test mass has a radius of curvature of 1683 m. Both mirrors have a coating surface with an absorbing power of 100 mW and a substrate absorbing power of 1 mW. Red curves represent the hot state when the equivalent to the TCS in SIS is applied. Blue curves represent the cold state **Left** Profiles of the hot and cold surface maps of the input test mass when the ring heater is applied. **Right** Profiles of the hot and cold surface maps of the end test mass when the ring heater is applied.

In this case, even though the edges of the maps do not match between the cold and hot state, the central area does. The majority of light reaches the central area, so the ring heater applied fixes the problem of the mismatch between the cavity mode and the mirrors due to the heating of the optics.

Chapter 4

Instrumented baffles

In this chapter, scattered light is introduced as one of the major sources of noise in the GW detectors. To absorb the scattered light, mechanical instruments known as baffles are used. The group at IFAE has worked on the design and construction of baffles instrumented with photodiodes. The results from the simulations performed to help in the design of the distribution of photodiodes are also presented in this chapter.

4.1 Scattered light

In the framework of the interferometer experiment, scattered light, also known as *stray light*, is the light coming from the laser that does not follow the designed path in the optical system. There are many sources of scattered light. One of them is the imperfections in the surface of the coating over mirrors, which make them not just reflect light and dissipate part of it into heat, but also scatter light in all directions. These imperfections can be, for instance, point absorbers. Scattered light can also be seen as secondary beams (spurious reflections) due to a non-ideal anti-reflective coating. Also, optical components with a limited aperture can lead to diffraction, which is scattered light. The total losses in the mirrors in the current interferometers are very low. This means the amplitude of the scattered light is just a few parts per million. The scattered light may backscatter and recouple to the main cavity mode, introducing a shift in the phase of the main mode. The phase modulation introduced by the coupled back-scattered light is due to the extra path the scattered light has traveled and the possible vibration of optical elements it may have encountered in its path. In the current interferometers, the most usual scenario is light scattered by the main test masses that reflects in the walls of the vacuum pipe close to the mirrors. The seismic motion of the pipe phase modulates the scattered light. In the case that this scattered light backscatters and recouples to the main cavity mode, the main cavity mode will be polluted. For this reason, models of scattering are highly necessary. The first thorough analysis of noise due to scattered light in GW interferometers was done by Kip Thorne [68]. In what follows a brief mathematical description of scattered light is provided.

The mirrors in the interferometers have a roughness of a few nanometers, which is three orders of magnitude below the laser wavelength (1064 nm). The departure of a mirror from its ideal shape is represented by a 2-dimensional stationary stochastic process [69], function $f(\mathbf{x})$, where $\mathbf{x}$ are the coordinates in the plane where the surface is projected, see Figure 4.1. This process has an associated standard deviation of σ.
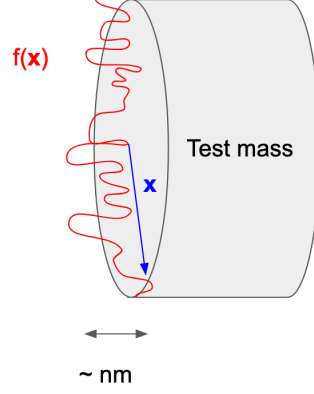
Figure 4.1: The roughness of the coating of a test mass is described by a 2-dimensional function $f(\mathbf{x})$, where $\mathbf{x}$ are the coordinates in the plane where the surface is projected.

As mentioned above, roughness can be thought of as a random process, so it can be assumed to be zero on average $\langle f \rangle = 0$. Also, the roughness is stationary, so $\langle f^2 \rangle = \sigma^2$ [69]. The relevant statistics is the auto-correlation function, defined as

$$C(\mathbf{x} - \mathbf{x'}) = \langle f(\mathbf{x}) \cdot f(\mathbf{x'}) \rangle / \sigma^2 \,. \tag{4.1}$$

Given that the roughness is isotropic, the autocorrelation function depends only on the length of the separation vector $C(\mathbf{x} - \mathbf{x'}) = C(||\mathbf{x} - \mathbf{x'}||)$.

Given a light beam with amplitude $\phi(\mathbf{r})$ impinging normally on the high reflective surface of a mirror, the reflected beam's amplitude is given by

$$\psi(\mathbf{x}) = e^{2ikf(\mathbf{x})}\phi(\mathbf{r}) \,, \tag{4.2}$$

where $k \equiv 2\pi/\lambda$. The Fourier transform of $\psi(\mathbf{x})$ is given by

$$|\tilde{\psi}(\mathbf{p})|^2 = \int e^{i\mathbf{p}(\mathbf{x} - \mathbf{x'})} e^{2ik[f(\mathbf{x}) - f(\mathbf{x'})]} \phi_o(\mathbf{x})\phi_o^*(\mathbf{x'}) d\mathbf{x} d\mathbf{x'} \,. \tag{4.3}$$

Given that the amplitude of the random process describing the scattering $f(\mathbf{x})$ is much smaller than the laser wavelength, the exponential dependent on $f(\mathbf{x})$ in Eq. (4.3) can be Taylor expanded [69]

$$|\tilde{\psi}(\mathbf{p})|^2 = \int e^{i\mathbf{p}(\mathbf{x} - \mathbf{x'})} \Big[1 + 2ik[f(\mathbf{x}) - f(\mathbf{x'})] - 2k^2[f(\mathbf{x})^2 + f(\mathbf{x'})^2 - 2f(\mathbf{x})f(\mathbf{x'})] \Big] \phi_o(\mathbf{x})\phi_o^*(\mathbf{x'}) d\mathbf{x} d\mathbf{x'} \,. \tag{4.4}$$

The expectation value of Eq. (4.4) is derived in Ref. [69] and the result obtained is

$$\langle |\tilde{\psi}(\mathbf{p})|^2 \rangle = (1 - 4k^2\sigma^2)|\phi(\mathbf{p})|^2 + 4k^2\sigma^2 \frac{1}{4\pi^2} \int \tilde{C}(\mathbf{q}) \cdot |\tilde{\phi}(\mathbf{p} - \mathbf{q})|^2 d\mathbf{q} \,. \tag{4.5}$$

Some remarks need to be made. The function $|\tilde{\psi}(\mathbf{p})|^2$ is sharply peaked, so it can be simplified as $|\tilde{\psi}(\mathbf{p})|^2 = 2\pi w_o^2 e^{-p^2 w_o^2/2}$ [69]. Also, the Fourier transform of the autocorrelation function (the power spectral density) does not vary on angles of the order of the angular width of the beam. The beam function can thus be treated as a Dirac delta and the integral simplified, leading to this expression of the expectation value

$$\langle |\tilde{\psi}(\mathbf{p})|^2 \rangle = (1 - 4k^2\sigma^2)|\phi(\mathbf{p})|^2 + 4k^2\sigma^2 \tilde{C}(\mathbf{p}) \,. \tag{4.6}$$

The reflected light is thus the sum of two contributions. The term $(1 - 4k^2\sigma^2)|\phi(\mathbf{p})|^2$ has the same angular distribution as the incoming beam, meaning it is a specularly reflected beam. The other term $4k^2\sigma^2\tilde{C}(\mathbf{p})$ has an angular distribution given by the properties of the surface. This is known as the power spectral density of f. This contribution represents the scattered light. The incoming power is shared between the specularly reflected light and the scattered light. The scattering losses are given

by $P_{\mathrm{scatt}}/P_{\mathrm{in}} = 4k^2\sigma^2 \equiv \epsilon$, where P_{in} is the light power of the stored wave. The ratio between the specularly reflected power and the input power is $P_{\mathrm{spec}}/P_{\mathrm{in}} = 1 - \epsilon$. The distribution of scattered light is given by

$$\frac{1}{P_{\mathrm{in}}}\frac{dP_{\mathrm{scatt}}}{d\mathbf{p}} = \frac{\epsilon}{4\pi^2}\tilde{C}(\mathbf{p}).\qquad(4.7)$$

4.1.1 Bidirectional scatter distribution function and total integrated scattering

The light scattered by optical components can fill the entire sphere centered on the scatterer. The distribution of scattered light is a function of the incident angle, wavelength, power, transmittance of the scatterer, and its absorption, among others. The bidirectional scatter distribution function (BSDF) is commonly used to describe scattered light patterns. The terms BRDF, BTDF, and BVDF, used for reflective, transmissive, and volume samples, respectively, are subsets of the more-generic BSDF [70]. The BRDF was firstly derived in Ref. [71]. It is defined as the surface radiance divided by the incident surface irradiance. The surface irradiance is the light flux (in Watts) incident on the surface per unit illuminated surface area. The scattered surface radiance is the light flux scattered through a solid angle Ω (see Figure 4.2) per unit illuminated surface area per unit projected solid angle [70]. The projected solid angle is obtained by multiplying the solid angle Ω by $\cos(\theta)$ (see Figure 4.2).
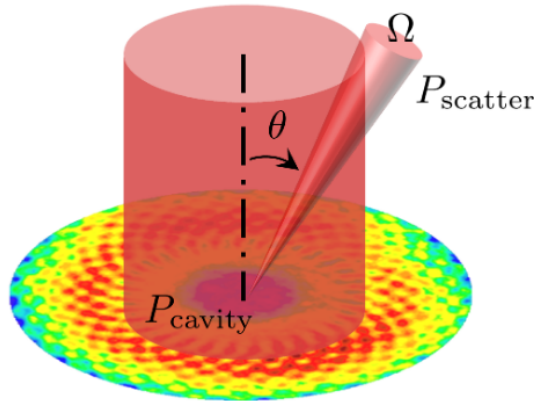
Figure 4.2: Figure retrieved from Ref. [72]. Graphical representation of the light scattered by a test mass (colorful disk). The red cylinder is the main beam propagating in a FP cavity, which carries a power denoted by P_{cavity}. The scattered light is represented by the cone of solid angle Ω and tilted by θ with respect to the beam propagation direction. The scattered light carries a power denoted by P_{scatter}. These variables are the ones needed to define the Bidirectional Reflective Distribution Function (BRDF).

Resorting to the definition and Figure 4.2, the BRDF can be mathematically expressed as

$$\mathrm{BRDF} = \frac{\mathrm{differential\ \ radiance}}{\mathrm{differential\ \ irradiance}} \simeq \frac{\mathrm{dP_{scatter}}/\mathrm{d}\Omega}{\mathrm{P_{cavity}}\cos(\theta)} \simeq \frac{\mathrm{P_{scatter}}/\Omega}{\mathrm{P_{cavity}}\cos(\theta)}.\qquad(4.8)$$

This definition of BRDF is valid for all incident and scattering angles. The first devices that would try to measure scattered light could not measure the BSDF as a function of the incident angles. They would integrate the light scattered into a hemisphere in front of the scatterer and then re-direct it towards a single detector. The measured scatter power would then be normalized by the reflected specular power leading to the definition of the total integrated scattering (TIS) [70]. The measurement of the TIS is currently used as an important scatter specification and it is related to the BRDF by Eq. (4.9). Integrating spheres have the purpose of measuring the TIS.

$$\mathrm{TIS} = \int_0^\pi \mathrm{BRDF}(\theta)\cos(\theta)2\pi\sin(\theta)\mathrm{d}\theta\qquad(4.9)$$

4.2 Instrumented baffles

To mitigate the effect of stray light in the interferometer, many different solutions can be taken. One of them is controlling the displacement of a potential scatterer. Also, the coupling factor or amount of scattered light recombining can be minimized. Another solution is resorting to baffles and diaphragms, which obscure roughnesses and discontinuities from the line of sight of the core optics [51]. They are designed in such a way that they can intercept and absorb as much stray light as possible. For these reasons, their reflectivity must be very low. Also, to avoid the baffles from seismic motion that could be transmitted to the scattered light, some of them are suspended. The distribution of baffles in LIGO is schematically represented in Figure 4.3. The Virgo interferometer has a similar distribution of baffles.
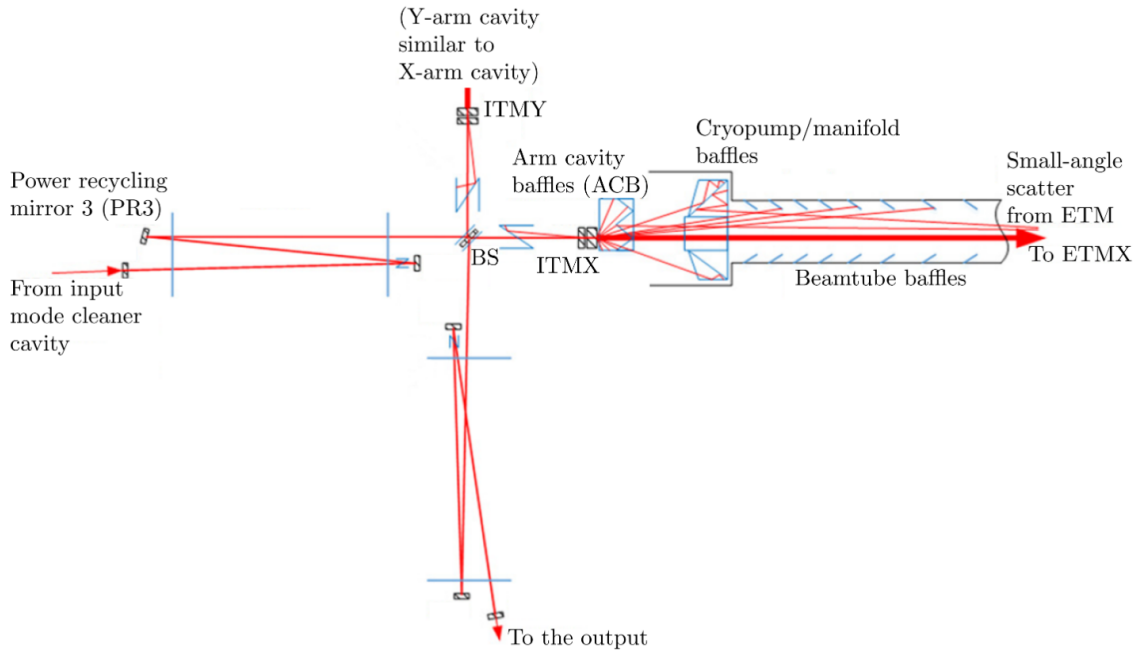
Figure 4.3: Figure retrieved from Ref. [73]. Distribution of baffles placed in LIGO for the control of scattered photons (low scattering angle) with a noisy extra phase that could re-couple to the main cavity mode.

One improvement for the second phase of Advanced Virgo Plus (AdV+/Phase II) [1] is the installation of baffles instrumented with photosensors surrounding the main test masses. The signal measured by the photosensors will help to better understand the scattered light distribution at low angles in the interferometer. It will also help in the detection of higher-order modes (HOMs) that may arise within the cavity. Contamination in the mirrors leads to scattered light at low angles, so this contamination could be monitored with the aid of the signal detected by the photosensors. Finally, the photosensors could also help in a more efficient pre-alignment and fine-tuning of the parameters of the interferometer after shutdowns and during operations. These instrumented baffles have been designed and built by the Virgo group at IFAE. A prototype was made for the Phase I upgrade. The reason is that the end-mirror of the input mode cleaner (IMC) and the payload holding it were replaced. This also motivated the replacement of the old un-instrumented baffle (Figure 4.4) with a new one instrumented with photodiodes (PDs). This prototype serves as a demonstrator of the new technology, which is ultra-high vacuum compatible. Also, it will help to gain experience with the technology and how to operate the instrumented baffles to be installed in the main arms.

---

[1] Advanced Virgo Plus (AdV+) is the next upgrade of Virgo and will occur in two phases. The first phase, or Phase I, is currently taking place between the O3 and O4 observation runs, while Phase II will take place between the O4 and O5 observation runs [74].
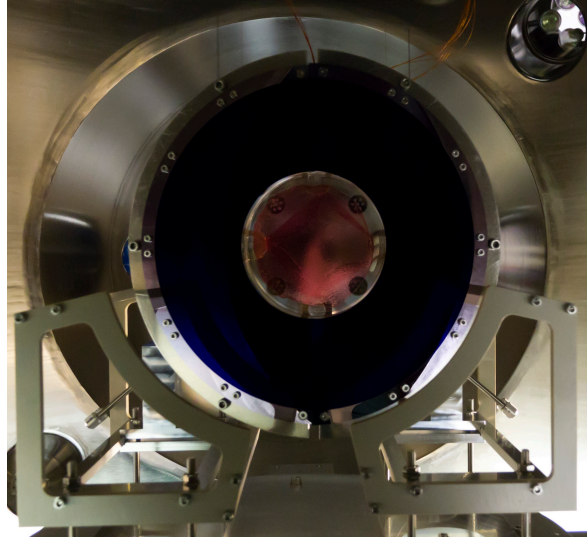
Figure 4.4: Figure retrieved from Ref. [75]. Old baffle installed around the end test mass of the input mode cleaner. This baffle was not instrumented.

In what follows, a description of the instrumented baffles' technology is provided. The instrumented baffle that has been built has an inner radius of 7 cm, an outer radius of 17.5 cm and it is made of mirror-polished stainless steel. It is divided into two halves, each tilted 9 degrees with respect to the normal to the direction of propagation of the beam (see Figure 4.5(left)). This allows to avoid back reflections in the cavity. Each half has 76 conical holes of 4mm in diameter that cover the edges of 76 new Silicon-based photosensors developed by Hamamatsu. This conical shape avoids that light resolves the sensor edge and minimizes the scattering of light. The photosensors have an area of 7.37×7.37 mm^2, though their photosensitive area is 6.97×6.97 mm^2. The photosensors are mounted on two large gold-plated polyamide-based printed circuit boards (PCBs). The baffle and the photosensors' surface include an anti-reflecting coating for the laser wavelength, 1064nm. The baffle and all its components are ultra-high vacuum compatible [76].
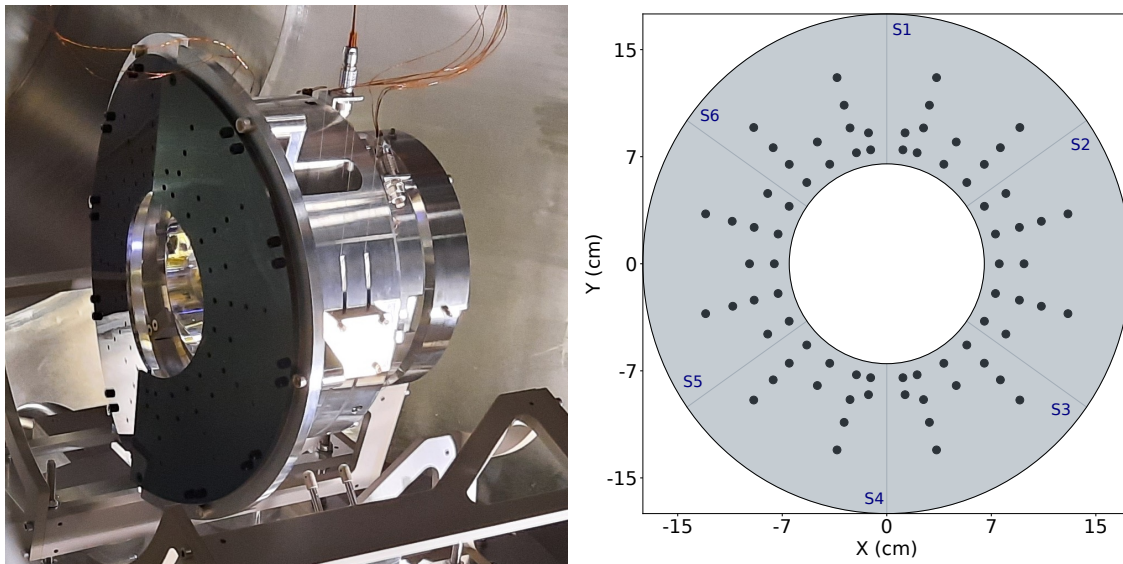
Figure 4.5: Figures retrieved from Ref. [76]. **Left** Photo of the instrumented baffle installed around the end test mass of the Input Mode Cleaner (IMC) cavity. The baffle is divided in two halves and has an inner radius of 7cm and an outer radius of 17.5cm. Each halve is tilted 9 degrees with respect to the normal to the direction of propagation of the beam. **Right** Distribution of photosensors in the two halves of the baffle, represented by black dots in each sextant.

The 76 photosensors are symmetrically placed with respect to the y axis as shown in Figure 4.5(right).

The majority is located in two concentric rings at radii of 8.8 and 9.8cm. Additional sensors are placed at larger radii and different azimuthal angles. The signals measured by the photosensors are processed by 16 analog-to-digital converters (ADCs). Each half baffle contains 8 ADCs which average each of the sensor signals over 500 ms, implying a baffle readout rate of 2 Hz. The calibration of the photosensors shows good linear behavior and all the 76 sensors agree in their measurements with an error of 3%. The absolute calibration is 4.6μW/ADC counts, with an error of 5%. Each ADC has a temperature sensor and the whole system operates with a limited voltage of 3.3V [76].

4.3 Input mode cleaner

As mentioned above, a prototype of the instrumented baffles to be installed around the main test masses in AdV+/Phase II has already been built and installed around the end test mass of the Input Mode Cleaner (IMC). The IMC cavity is an in-vacuum triangular cavity used for modal and frequency filtering of the laser beam before entering the main cavity of the interferometer. A schematic representation of the IMC cavity is in Figure 4.6. The IMC also reduces the beam's amplitude and the beam- pointing fluctuations before entering the interferometer [51]. It is composed of three suspended mirrors. Two of them are part of a dihedron and are referred to as MC1 and MC3. The so-called MC1 is the input mirror of the IMC cavity and MC3 is the output mirror. MC1 and MC3 are flat mirrors. The third mirror is the end mirror of the cavity, referred to as MC2. The end mirror has a radius of curvature of 187m.
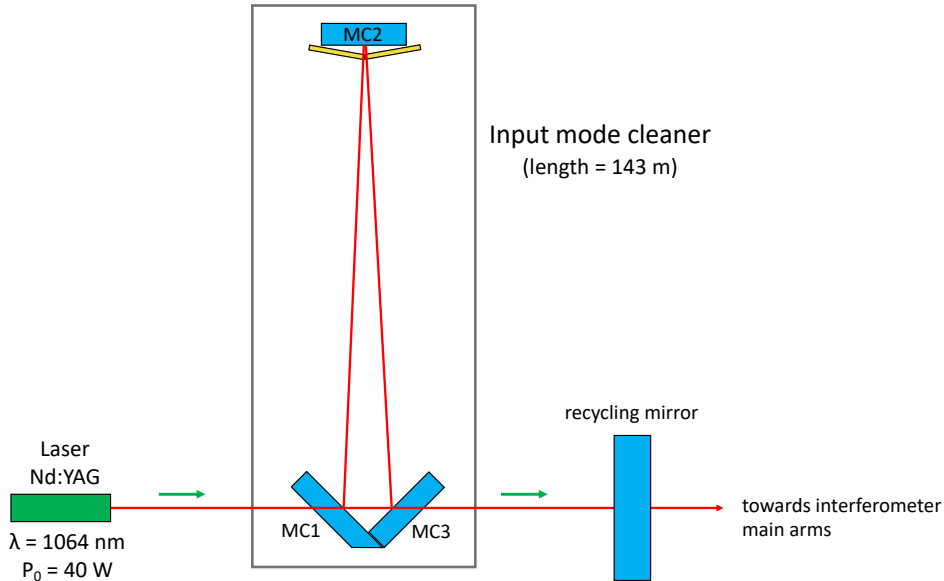
Figure 4.6: Figure retrieved from Ref. [75]. Schematic representation of the Input Mode Cleaner (IMC) cavity. It is a triangular cavity with a dihedron and an end mirror. The dihedron is composed of two flat mirrors, input (MC1) and output (MC3). The end mirror is curved and is commonly named MC2. The half roundtrip length of the IMC cavity is ~ 143 m.

The half roundtrip length of the IMC cavity is ~ 143 m and its finesse of 1200 [51]. Figure 4.4 shows the end mirror of the IMC and the old baffle surrounding it, which was not instrumented. Figure 4.7 shows the forward and backwards propagation of light within the IMC cavity. The nominal propagation is the forward one, represented by yellow in Figure 4.7. The backscattered light (represented in green in Figure 4.7) is also resonant inside the IMC. For this reason, the IMC is equivalent to a flat mirror, and its effective reflectivity, $R_{\rm eff}$, can be calculated with the backscattering reflectivity of the curved end mirror for an angle of incidence of 300 μrad, R_{ϵ}, and the recycling gain G, as $R_{\rm eff} = G^2 R_{\epsilon}$. Consequently, for a gain of about 800 the effective reflectivity of the IMC cavity is $R_{\rm eff} \simeq 10^{-8}$ [77].
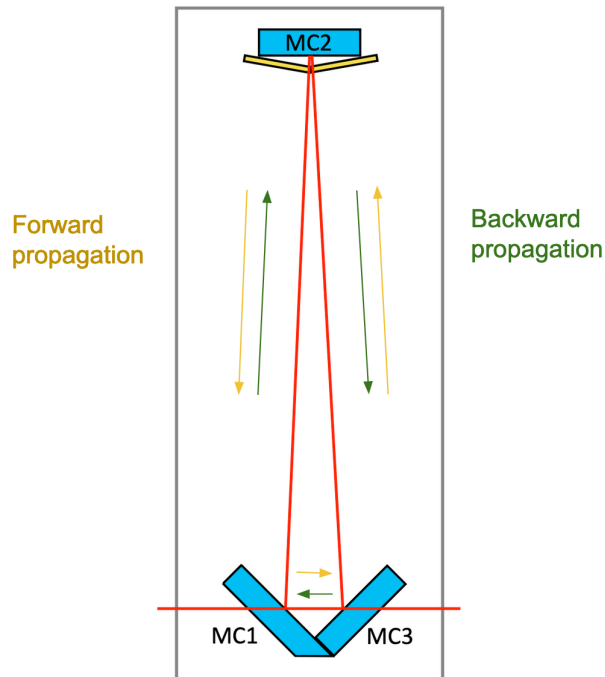
Figure 4.7: Schematic representation of the beam propagation within the IMC cavity. The nominal propagation is the forward propagation (represented in yellow). However, the end mirror of the IMC has roughness that makes the light propagating in one direction to backscatter in the opposite direction. This leads to the backward propagation (represented in green). This beam is also resonant in the cavity.

4.4 Simulation results

As mentioned in the previous chapter, a simulation tool (SIS, see section 3.2) has been used to design the distribution of photodiodes (PDs) in the instrumented baffle [78]. SIS was also used to determine the light exposure of the PDs under different scenarios of the interferometer operations. This last task was essential to assess whether the photodiodes would keep their integrity under all the different scenarios. Furthermore, now that the prototype instrumented baffle is installed around the end test mass of the IMC, SIS is being used to comprehend the data retrieved by the PDs.

4.4.1 Aiding the design of the PDs layout and assessing their integrity under different scenarios of the IMC cavity

In this section, the results obtained from simulating the IMC cavity under different configurations to assess the amount of light reaching the PDs are presented. Four scenarios are simulated with an input power of 40W. Firstly, the IMC cavity is assumed to be in resonance and perfectly aligned. Then, a small misalignment of the end mirror is applied, though still keeping the resonance in the cavity. These two scenarios are studied with SIS. The third scenario analyzed is the cavity being out of resonance due to a complete misalignment. The final scenario is that in which the cavity loses resonance due to a sudden cavity misalignment because of transient noise. These last two scenarios cannot be simulated, so they are analyzed analytically. In each analysis, the amount of power reaching each PD is determined. This allows to assess the capability of the PDs to detect misalignments in the system and the risk the PDs could potentially be exposed to.

Firstly, the IMC is considered in resonance (locked) and perfectly aligned. In this steady-state, the laser beam hits the center of the end-mirror of the IMC. The power light distribution in the ensemble mirror plus baffle can be seen in Figure 4.8 (left), obtained with SIS. The total power reaching the mirror and the baffle is of the order of 1.35×10^4 W [75]. It is obtained by integrating the differential distribution of the power over the mirror and baffle areas. The power reaching the baffle surface is

only 0.21 W, 1.6×10^{-5} of the total power. The power distribution in the baffle area can be seen in Figure 4.8 (right), also obtained with SIS. A PD placed in the region in the baffle exposed to the highest power would receive a maximum dose of about 3.2×10^{-3} W [75]. A PD located in the outer part of the baffle, at a radius of 17 cm from the center of the mirror, would be exposed to a power of the order of 3.2×10^{-5} W [75]. The dark current of each PD in the baffle, at the level of 50 to 5000 pA, will allow detecting light power as low as 10^{-5} W with more than three orders of magnitude of margin in the signal to noise ratio.
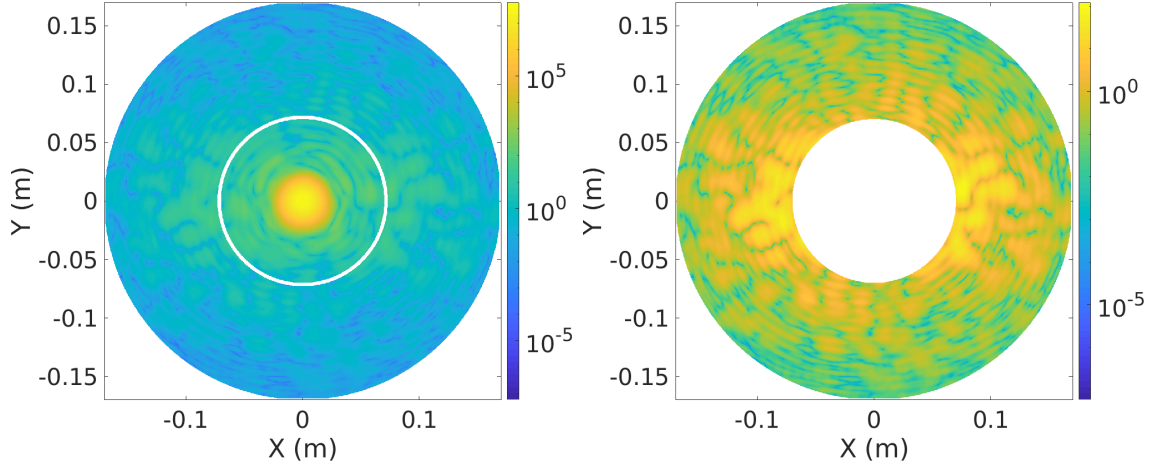
Figure 4.8: Figures retrieved from Ref. [75]. **Left** Power light distribution in the ensemble mirror plus baffle, obtained with SIS. A fine white line shows the outer edge of the end mirror. The total power reaching the mirror and the baffle is of the order of 1.35×10^4 W. **Right** Power distribution in the baffle surrounding the end test mass of the IMC. The power reaching the baffle surface only is 0.21 W, only 1.6×10^{-5} of the total power.

In the case of a misalignment of 10μrad of the cavity, the same analysis was performed. In SIS, the misalignment is implemented via a tilt of the end mirror with respect to its nominal position. Figure 4.9 shows the power in the IMC cavity as a function of the misalignment. The power decreases with increasing tilt. The analysis is done for a tilt of 10μrad because it is small enough to maintain the IMC cavity in resonance. The IMC cavity remains resonant as long as the tilt does not reduce the cavity power by 3/4. Tilts leading to cavity powers lower than 3.5 kW are larger than ~ 30 μrad.
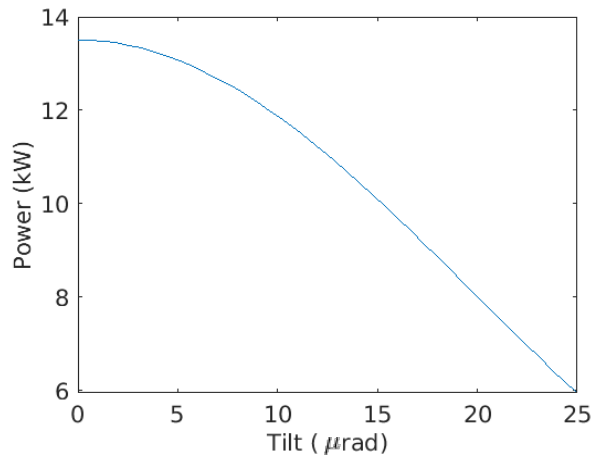
Figure 4.9: Figure retrieved from Ref. [75]. Power reaching the end mirror of the IMC plus the baffle as a function of the tilt of the end mirror.

In this scenario with a small misalignment of the MC2, the power light distribution in the ensemble mirror plus baffle is shown in Figure (4.10)(left). The total power reaching this area is 1.19×10^4 W.

Only 0.17 W (1.4×10^{-5} of the total cavity power) illuminate the baffle area, and they're distributed as seen in Figure (4.10)(right). The power reaching a PD placed in the area of the baffle with the highest light exposure would receive 3.0×10^{-3} W.
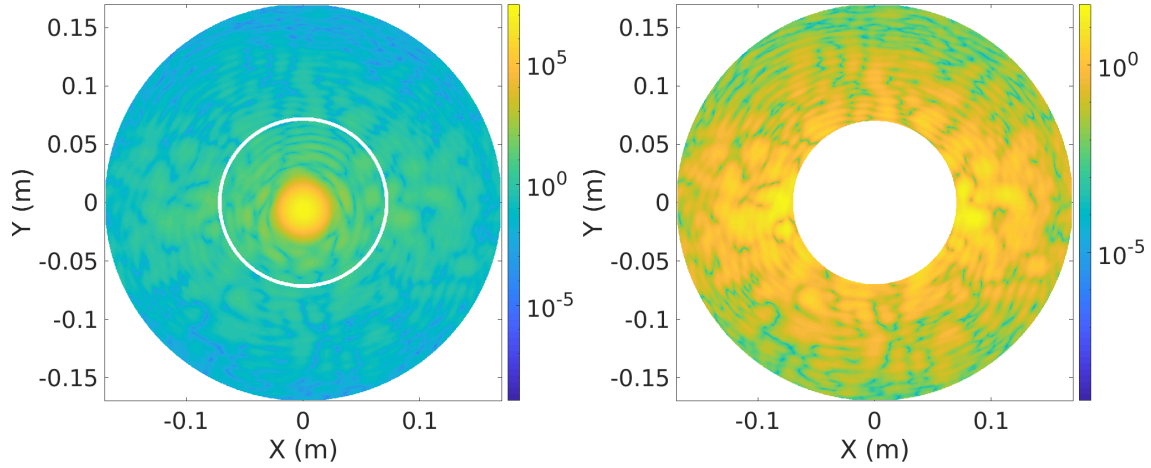
Figure 4.10: Figures retrieved from Ref. [75]. **Left** Power light distribution in the ensemble mirror plus baffle, obtained with SIS for an IMC cavity with a misalignment of 10μrad. A fine white line shows the outer edge of the end mirror. The total power reaching the mirror and the baffle is of the order of 1.19×10^4 W. **Right** Power distribution in the baffle surrounding the end test mass of the IMC for a misalignment of the cavity of 10μrad. The power reaching the baffle surface only is 0.17 W (1.4×10^{-5} of the total cavity power).

For both scenarios, the aligned and misaligned case, the radial distribution of power in the vertical axis in the mirror plus baffle ensemble is represented in Figure (4.11)(left). The radial distribution of power in the horizontal axis is presented in Figure (4.11)(right). The blue vertical line represents the inner radius of the baffle. Both figures show that the distribution of light close to the centre of the mirror is nearly Gaussian. However, for larger radii the light distribution departs from a Gaussian behaviour and it shows some "wiggles". These structures are due to diffraction effects from the finite aperture of the test masses. The distributions at $\theta = 0$ (see Figure 4.12) and $\theta = \pi$ are not equal, though quite similar. This is due to the fact that the mirror does not have perfect circular symmetry.
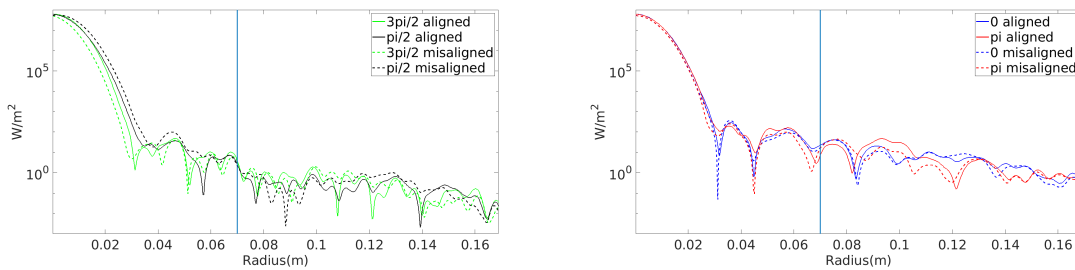
Figure 4.11: Figures retrieved from Ref. [75]. **Left** Radial distribution of power over the MC2 plus baffle ensemble in the vertical axis. The black solid (dashed) line represents the radial distribution of light intensity for $\theta = \pi/2$ in the aligned (misaligned) case. The green solid (dashed) line represents the radial distribution of light intensity for $\theta = 3\pi/2$ in the aligned (misaligned) case. **Right** Radial distribution of power over the MC2 plus baffle ensemble in the horizontal axis. The blue solid (dashed) line represents the radial distribution of light intensity for $\theta = 0$ in the aligned (misaligned) case. The red solid (dashed) line represents the radial distribution of light intensity for $\theta = \pi$ in the aligned (misaligned) case.
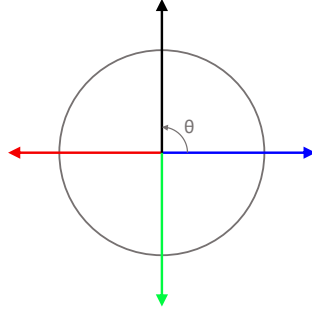
Figure 4.12: Figure retrieved from Ref. [75]. Definition of theta in our analysis. The colour code of each axis is associated with the lines in Figure 4.11.

In the previous two scenarios the IMC cavity was locked and, as mentioned before, the analysis could be done with SIS. However, in the next two scenarios, the IMC cavity is out of resonance. Hence, the analysis can only be done analytically.

For a completely misaligned IMC cavity, resonance is lost. In order to determine the light exposure of a PD in such configuration, an analytical calculation is performed based on the transmissivities and reflectivities of the mirrors of the IMC cavity [79]. For a beam size of 0.01 m at the end-mirror of the IMC the intensity reaching the mirror, I_{MC2}, is evaluated as

$$I_{\text{MC2}} = P_{\text{in}} \times T_{\text{in}} \times R_{\text{out}}/A_{\text{beam}},. \tag{4.10}$$

The parameter $T_{\text{in}} \simeq 2.5 \times 10^{-3}$ is the transmissivity of MC1 and $R_{\text{out}} \simeq 1$ is the reflectivity of MC3, leading to $I_{\text{MC2}} = 1.3 \times 10^3 \ W/m^2$. For a Gaussian beam illuminating a PD directly, the maximum light exposure is 2.1×10^{-2} W [75]. Laser-induced damage-threshold tests indicate that the PDs have a light power tolerance at least two orders of magnitude larger than the light dose expected to reach the sensors in each lock loss.

Finally, the scenario in which there is a sudden cavity misalignment due to transient noise is studied. This transient noise would lead to a mechanical drift that could potentially result in exposing the PDs for a short period to the energy stored in the cavity. The total energy stored in the cavity in nominal conditions can be expressed as $E_{\text{TOT}} = P_{\text{in}} \times g \times \tau$ [79], where P_{in} is the input power and g is the gain of the cavity. The gain is defined in terms of the finesse of the cavity (F) as $g = \frac{2F}{\pi}$. The parameter τ is the decay time of the cavity, which is the average time that a photon stays within the cavity. It is computed as $\tau = \frac{F}{2\pi\text{FSR}}$, where FSR denotes the IMC free spectral range. For the IMC cavity, $F = 1005$ and FSR $= 1.04 \times 10^6$ Hz, leading to values $g \sim 640$, $\tau = 153 \ \mu$s, and $E_{\text{TOT}} = 3.9$ J. The total power illuminating the baffle is obtained resorting to the time response of the payload and suspension systems. The payload and suspension feedback systems will need 10 ms to apply measures to correct the misalignment. This recovers the power illuminating the baffle in the aligned case. However, during the 10 ms reaction time, the baffle is potentially exposed to a power not exceeding 400 W. The power that would reach a PD during this transient by assuming a laser beam, of Gaussian transverse profile with an amplitude of 390 W and beam size of 1 cm at the end mirror, is estimated. Given a PD with an area of 0.49 cm^2, it would be exposed to about 130 W [75] during 10 ms.

In what follows an estimation of the power that could potentially reach the PDs of the baffles installed in the main arms of the interferometer is done. In the current long-arm Fabry-Perot cavities of AdV, the energy stored is of the order of 170 J with a beam radius at the test masses of $\sim 5cm$. In a Fabry-Perot arm, the stored energy is calculated through the gain of the power recycling cavity (RG = 35) and the beam splitter transmission (BS$_t$ = 0.5) as follows: E$_{\text{cav}}$ = P$_{\text{in}}$ × RG × BS$_t$ × g × t$_{\text{cav}}$, where P_{in} = 20 W, the decay time of the arm cavities is $t_{\text{cav}} = 1.7$ ms and the gain $g = 2 \times 450\pi = 286.5$, where 450 is the finesse of the cavity. An average power not exceeding 170 $J/10 \ ms = 1.70 \times 10^5$ W, can potentially hit the baffle, meaning an intensity of $2.2 \times 10^6 \ W/m^2$, much larger than that in the IMC cavity. Laboratory characterization has shown the laser-induced damage threshold of the payload

baffles to be roughly 0.5 MW/m^2. Nonetheless, no damage has been noticed on the baffles attached to the payloads, so these are hints that the above upper limit for the IMC is greatly conservative.

4.4.2 Analysis after installation

After the installation of the instrumented baffles around the end test mass of the input mode cleaner, a campaign to analyze the data retrieved by the photodiodes started. The results are compared with those obtained from simulations, leading to a better understanding of what sources could be generating the patterns of scattered light detected.

The baffle shows a good performance in the absence of light inside the IMC cavity and has a noise level of up to 0.01-0.16 counts (root mean square). The signal-to-noise ratio with light reaches values over 10. The raw signal detected by the photosensors averaged over a period of one hour is shown if Figure 4.13 for two different datasets. Figure 4.13 shows that the highest amount of light is concentrated at low radius and sensors detect more than 100 counts. Data show a left-right asymmetry, with more power in the half baffle with negative x values. Data also suggest the power is concentrated in a plane tilted about 15 degrees in the θ direction (see Figure 4.12) with respect to the nominal x-z plane of the IMC cavity. This effect is persistent in all the data analysed [76].
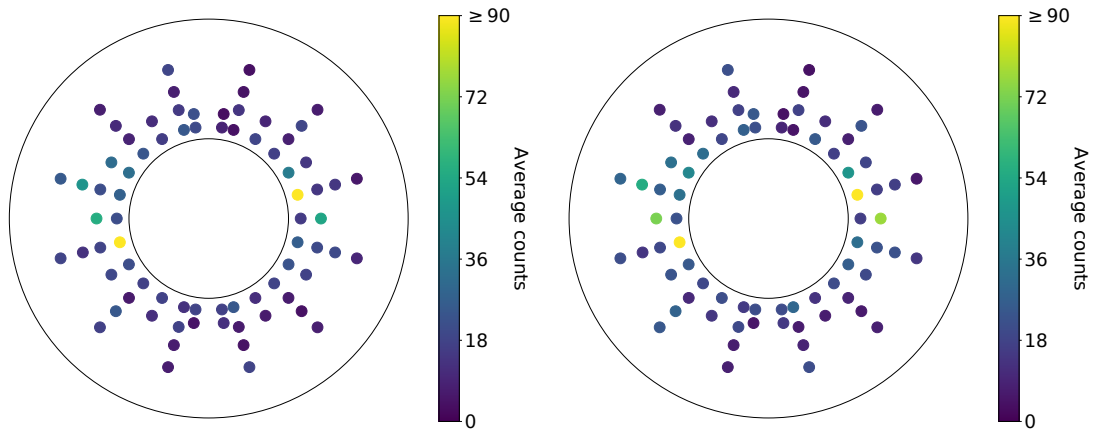
Figure 4.13: Figures retrieved from Ref. [76]. **Left** Raw signal detected by the photosensors averaged over a period of one hour (dataset 1). Data show the power is concentrated in a plane tilted about 15 degrees in the θ direction with respect to the nominal x-z plane of the IMC cavity. **Right** Raw signal detected by the photosensors averaged over a period of one hour (dataset 2). The same behaviour is seen as for the data shown in subfigure (a).

This measured data is compared to the results obtained with simulations of the light inside the IMC cavity, performed with SIS. For that purpose, data had to be calibrated by subtracting from the data per photosensor the average noise pedestal from each photosensor. The simulation is similar to the one used in Ref. [75], where a locked and perfectly aligned IMC cavity is assumed. The input power, in this case, is 28.5 $\pm$ 0.1 W. The results from running the simulation are in Figure 4.14, expressed in terms of energy density, or light intensity (W/m^2). Qualitatively, the results from the simulation are very similar to the real data, since they also show the highest amount of power in a plane tilted 15 degrees in the θ direction (see Figure 4.12).
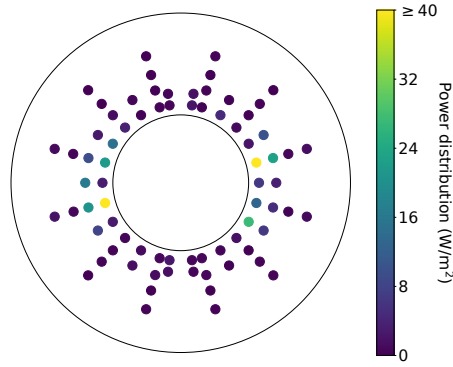
Figure 4.14: Figure retrieved from Ref. [76]. Energy density per photodiode obtained by running the same simulation as in Ref. [75] for an input power of 28.5 ± 0.1 W. The highest amount of power is in a plane tilted 15 degrees in the ϕ direction.

A comparison of the measured data and the results of the simulation is shown in Figure 4.15 for the four different concentric rings of photosensors in the baffle. Figure 4.15 shows the light intensity reaching the photosensors as a function of θ (see definition of θ in Figure 4.12). Data show a strong radial dependence, with the power concentrated in the inner-most ring of photosensors. The light intensity varies between 1.1W/m^2 to 53.3W/m^2 for small radii and between 0.4W/m^2 to 9.6W/m^2 for larger radii. As shown in Figures 4.13 and 4.14, data in the inner and second rings show more power for a plane tilted 15 degrees in the θ direction. This is seen in Figure 4.15 in the peaks at $\theta \sim 0$ and $\theta \sim \pi$. There were two potential causes for this tilt, one was a misalignment in any of the optics in the IMC, and another one was the surface maps of the optics. The former was discarded after repeating the simulation assuming different combinations of misalignments of the different mirrors. It was then proved that the cause for the excess power in the plane tilted 15 degrees are the roughness of the mirrors. The simulation was repeated assuming a perfectly aligned cavity without real surface maps of the dihedron. This led to the disappearance of the peaks in Figure 4.15 at $\theta \sim 0$ and $\theta \sim \pi$. The distribution of power around the end test mass of the IMC is plotted in Figure 4.16. Each subplot represents the distribution with different combinations of maps. It can be seen that the highest amount of power around the MC2 is achieved when the MC1 and MC3 surface maps are present. This indicates that the distribution of power around MC2 is highly dependent on the maps of the dihedron mirrors. When the MC3 mirror map is present, the tilt in θ at 15º measured by the data is recovered.
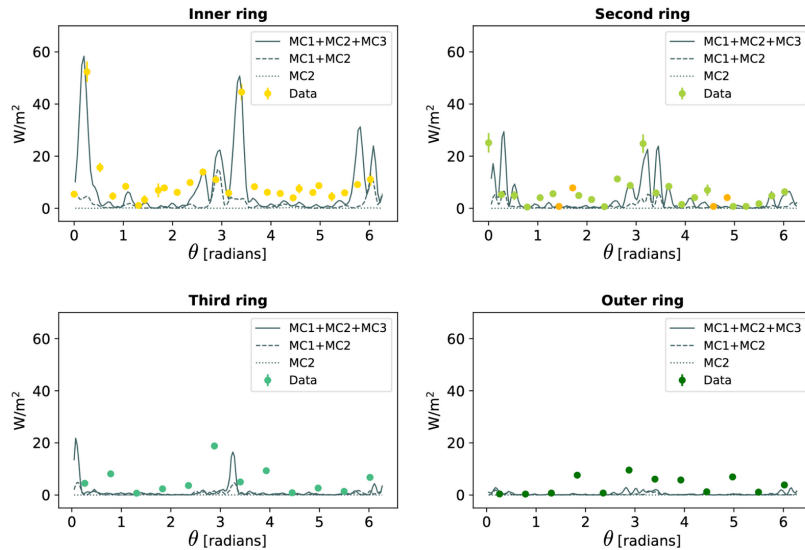
Figure 4.15: Figure retrieved from Ref. [76]. Comparison of the measured data and the results of the simulation for the four different concentric rings of photosensors in the baffle. Light intensity is shown as a function of θ (location of each photosensor). Power is concentrated in the inner-most ring of photosensors. Data in the inner and second rings show more power at $\theta \sim 0$ and $\theta \sim \pi$.
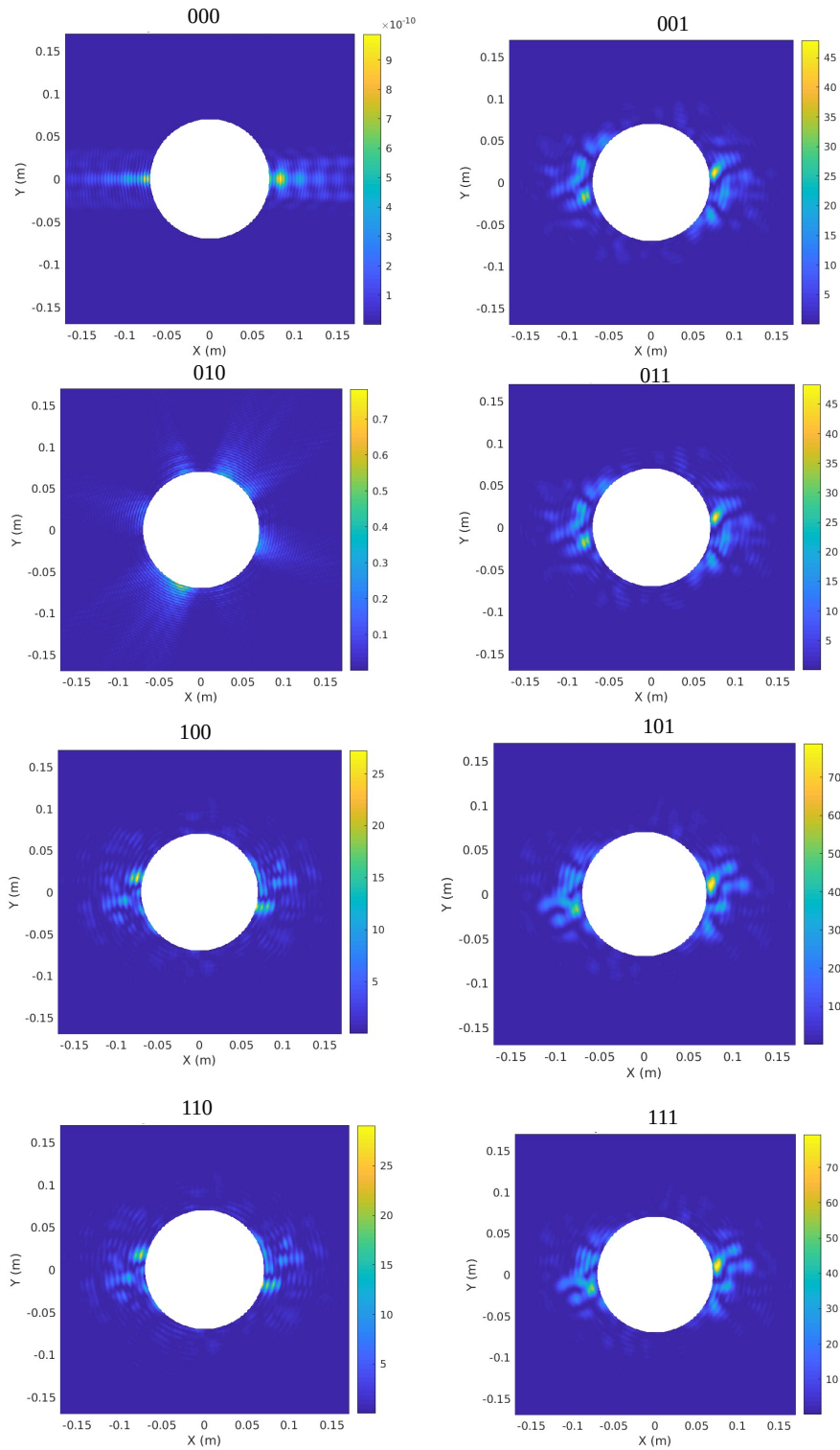
Figure 4.16: Distribution of power (in W) around the end test mass of the IMC cavity. Each subplot represents the power with different combinations of mirror maps, i.e.: the plot labeled by 000 indicates there were no mirror maps; the plot labeled by 001 was obtained with no surface maps over the MC1 and MC2, and only the surface map of MC3. The subplot labeled 101 shows the distribution of power when only the surface maps of MC1 and MC3 are used.

Chapter 5

Statistical methods

In this chapter, a description of the frequentist and Bayesian approaches to statistics is provided. Both approaches will be introduced because in searches for the gravitational wave background, the framework used is a hybrid of the frequentist and Bayesian approaches.

Classical inference is usually called frequentist inference. Many analyses are not purely frequentist or Bayesian, but a combination of both. The difference between the two approaches is how they interpret probability. In the frequentist approach, probabilities are related to the frequency of events. In the Bayesian approach, probabilities are related to knowledge about an event. For instance, when inferring the mass of a star, in the frequentist approach the star has a true, fixed mass, denoted by "m". The uncertainty is intrinsic to the data, denoted by "d", and the relevant probability is that of observing the data given the star has a mass "m". This is known as the likelihood, represented by $p(d|m)$. However, in the Bayesian approach data are known and the mass of the star is the variable with uncertainty. The relevant probability is that the mass has a certain value, given the data. This probability distribution is the posterior, $p(m|d)$ [80]. The likelihood and the posterior distribution are related by the Bayes' theorem, given by

$$p(m|d) = \frac{p(d|m)p(m)}{p(d)},$$ (5.1)

where $p(m)$ is the prior probability distribution for the mass m. The prior represents the knowledge about the range and distribution of the parameter in the model (mass in this example). The normalization factor $p(d)$ is the marginalised likelihood or evidence, obtained by integrating over the model parameters, m in this case, $p(d) = \int p(d|m)p(m)dm$ [80].

5.1 Frequentist statistics

In the frequentist approach the probability is the relative number of occurrences of an event in a set of identical experiments. The measured data are drawn from an underlying distribution known as the likelihood. The likelihood represents the change in knowledge acquired by carrying out an experiment. To make a statistical inference, knowledge of the probability distribution of the statistic is required. Given a statistic and its sampling distribution (likelihood), confidence intervals for parameter estimation or p-values for hypothesis testing can be calculated (these concepts are introduced later on in the chapter).

An example is used to explain how to test a hypothesis with the frequentist approach. Given the hypothesis H_1 that data contains a GW signal with an amplitude $a > 0$ and the null hypothesis H_o that data does not contain a GW signal, a statistic Λ is constructed. The statistical test will be based on Λ. The likelihood for Λ can be calculated either analytically or with simulations [1] assuming H_o is

---

[1] As more parameters are included in the model and thus the dimensionality of the likelihood increases, techniques such as Markov-chain Monte Carlo [81] or nested sampling [82] are needed to efficiently calculate confidence intervals on

true and is denoted by $p(\Lambda|H_o)$ [80]. If the observed value of Λ, Λ_{obs}, in the data lies far out in the tails of the distribution, then the null hypothesis H_o is discarded at a probability of p at the percent level. The p-value is the significance of the test, given by [80]

$$p \equiv \text{Prob}(\Lambda > \Lambda_{\text{obs}}|H_0) \equiv \int_{\Lambda_{obs}}^{\infty} p(\Lambda|H_0) \, d\Lambda. \tag{5.2}$$

Graphically, the value of p is the area under the likelihood $p(\Lambda|H_o)$ for $\Lambda \gtrsim \Lambda_{obs}$, Figure (5.1). The p-value required to reject H_o determines a threshold Λ_*, above which H_o is discarded and H_1 accepted. That is, for $\Lambda_{obs} \gtrsim \Lambda_*$ a detection can be claimed.
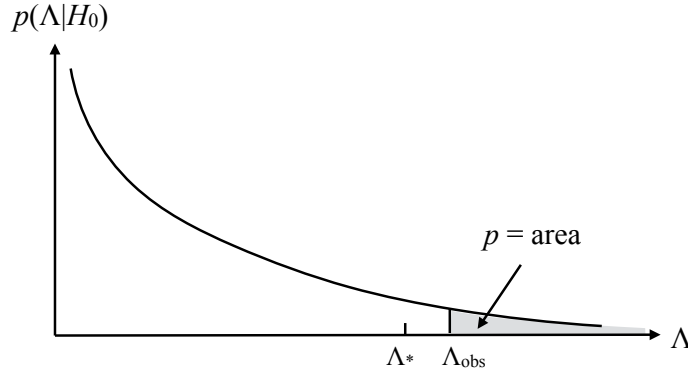
Figure 5.1: Figure retrieved from Ref. [80]. Graphical representation of the p-value, given by Eq. (5.2). It is the area under the likelihood $p(\Lambda|H_o)$ for $\Lambda \gtrsim \Lambda_{obs}$.

Every statistical test can have two types of errors, the false alarm error α and false dismissal error $\beta(\alpha)$, given by

$$\alpha \equiv \text{Prob}(\Lambda > \Lambda_*|H_0)\,,$$
$$\beta(a) \equiv \text{Prob}(\Lambda < \Lambda_*|H_a). \tag{5.3}$$

The false alarm error happens when H_o is rejected while in reality, it is true. The false dismissal error happens when H_o is accepted despite being false in reality. The false dismissal error, $\beta(\alpha)$, is calculated with the sampling distribution of the test statistic assuming the hypothesis that there is a signal with amplitude "a" H_a. The desired result is having α as low as possible. The false dismissal probability allows defining the frequentist detection probability, defined as $1 - \beta(\alpha)$. It represents the fraction of times that the test statistic Λ correctly identifies the presence of a GW signal of amplitude a in the data, for a fixed false alarm error α. It is common to use plots of the frequentist detection probability vs the signal strength (Figure 5.2) to show how strong a signal needs to be detected with a probability $1 - \beta(\alpha)$ [80].

When no detection is done, bounds (or upper limits) can still be set on the strength of the signal. The upper limit (UL) depends on Λ_{obs} and a choice of confidence level (CL). For instance, the UL at 90% CL, $a^{90\%,UL}$, represents the minimum value of a for which $\Lambda \gtrsim \Lambda_{\text{obs}}$ at least 90% of the times. Mathematically it can be expressed as $\text{Prob}(\Lambda \geq \Lambda_{\text{obs}}|a \geq a^{90\%,UL}, H_a) \geq 0.90$. If $a \gtrsim a^{90\%,UL}$ the signal would have been detected at least in 90% of the repeated observations. Figure 5.3 represents the frequentist UL at 90% confidence level on the parameter a [80].

5.1.1 Frequentist paramater estimation

To perform parameter estimation (PE) with the frequentist approach, the first step is constructing a statistic (estimator) $\hat{a}$ of the parameter of interest a. Then, the likelihood $p(\hat{a}|a, H_a)$ must be calculated. It must be kept in mind than in the frequentist approach, $\text{Prob}(\hat{a} - \Delta < a < \hat{a} + \Delta) = 0.95$ is not the

the model parameters [83].
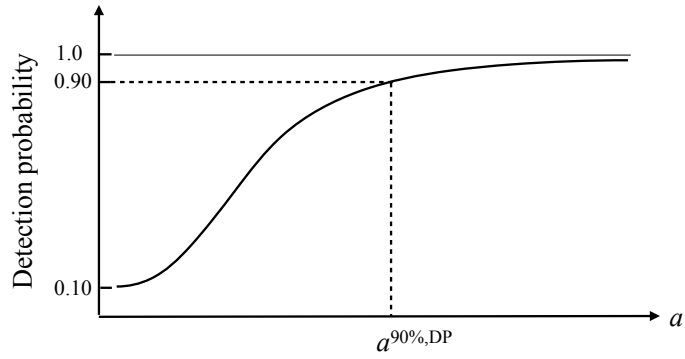
Figure 5.2: Figure retrieved from Ref. [80]. Frequentist detection probability vs the signal amplitude. This plot represents how strong a signal needs to be in order to detect it with probability $1 - \beta(\alpha)$, where $\beta(\alpha)$ is the false dismisal error. In this case, α, the false alarm error, is fixed to 0.1 and the value of a that is required for the signal to be detected with a 90% probability is denoted by $a^{90\%,DP}$.
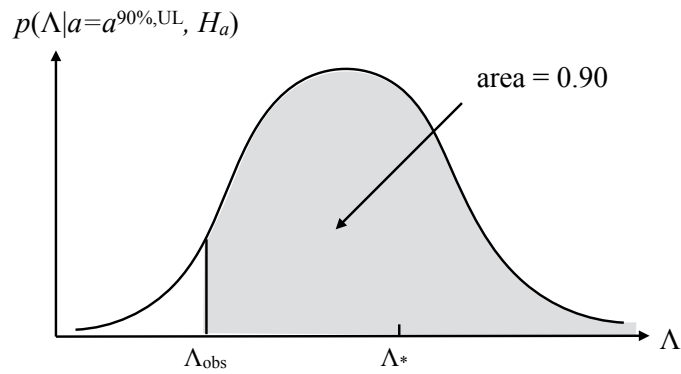
Figure 5.3: Figure retrieved from Ref. [80]. Graphical representation of the frequentist UL at 90% confidence level, given by $Prob(\Lambda \geq \Lambda_{obs} | a \geq a^{90\%,UL}, H_a) \geq 0.90$. It is the area under the likelihood $p(\Lambda | a = a^{90\%,UL}, H_a)$ when $\Lambda \gtrsim \Lambda_{obs}$ at least 90% of the times, which corresponds to $a = a^{90\%,UL}$.

probability of parameter "a" lying within the interval $[\hat{a} - \Delta, \hat{a} + \Delta]$. Instead, 0.95 is the fraction of the intervals that will contain the true value of "a" in a set of many experiments. Each interval in this set of intervals $\{[\hat{a} - \Delta, \hat{a} + \Delta]\}$ is the 95% frequentist confidence interval [80].

The estimator $\hat{a}$ could take un-physical values. To avoid them, a procedure introduced in Ref. [84] can be followed. It consists of introducing a new "ordering" of the values of the variable "a" to include in the acceptance intervals for an unknown parameter. The task starts by choosing the credible interval $[\hat{a}_1, \hat{a}_2]$ such that it satisfies

$$\text{Prob}(\hat{a}_1 < \hat{a} < \hat{a}_2) \equiv \int_{\hat{a}_1}^{\hat{a}_2} p(\hat{a}|a, H_a) \, d\hat{a} = \text{CL} \equiv \text{confidence} \quad \text{level} \tag{5.4}$$

for each a. The "ordering" of the values of a is based on the ranking function

$$R(\hat{a}|a) \equiv \frac{p(\hat{a}|a, H_a)}{p(\hat{a}|a, H_a)\big|_{a=a_{best}}}. \tag{5.5}$$

The value a_{best} is the one that maximizes the likelihood $p(\hat{a}|a, H_a)$. The credible interval $[\hat{a}_1, \hat{a}_2]$ must also satisfy $R(\hat{a}_1|a) = R(\hat{a}_2|a)$ [80].

5.2 Bayesian approach

In the Bayesian approach a parameter "a" is estimated in terms of its posterior distribution $p(a|d)$, which contains all the information about "a". Even though all the information is encoded in the posterior, the posterior mean and probability intervals are concise ways of expressing the results of an analysis. A Bayesian confidence interval (CI)[2] is the degree of belief about an event [80]. It is defined in terms of the area below the posterior between two parameter values. This definition is represented in Figure 5.4 for the case of a 95% credible interval.
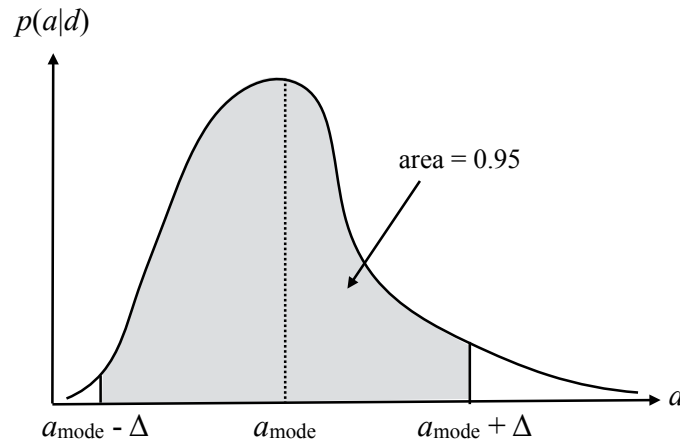
Figure 5.4: Figure retrieved from Ref. [80]. Graphical representation of a Bayesian 95% credible interval (CI). The area below the posterior $p(a|d)$ comprised between $a_{mode} - \Delta$ and $a_{mode} + \Delta$ is the credible interval, which coincides with a 95% of the total area below the posterior. a_{mode} is the peak of the posterior.

If the posterior is dependent on two parameters "a" and "b", the posterior only for "a" can be obtained by marginalizing the joint posterior over "b"

$$p(a|d) = \int db \, p(a, b|d) = \int db \, p(a|b, d)p(b), \tag{5.6}$$

where the relation $p(a|b, d)p(b) = p(a, b|d)$ has been used [80]. This is done when there is no interest in parameter "b", which is an example of the so-called *nuisance parameters*. According to the Bayes' theorem, the prior knowledge on "a" is updated by what is learned from the data, "d", as measured

---

[2]The confidence interval is also referred to as credible interval (CI).

by the likelihood, which results in the posterior distribution of "a". In this process, the amount of information gained is given by

$$I = \int da\, p(a|d) \log\left(\frac{p(a|d)}{p(a)}\right).$$ (5.7)

A Bayesian upper limit (UL) on "a" is a Bayesian credible interval for a with the lower end point of the interval set to the smallest value that the parameter can take. For instance, the UL on "a" at 90% CI is defined by

$$\text{Prob}(0 < a < a^{90\%,UL}|d) = 0.90,$$ (5.8)

where probability is the degree of belief that "a" has a real value in the credible interval. This UL is represented graphically in Figure 5.5[3].
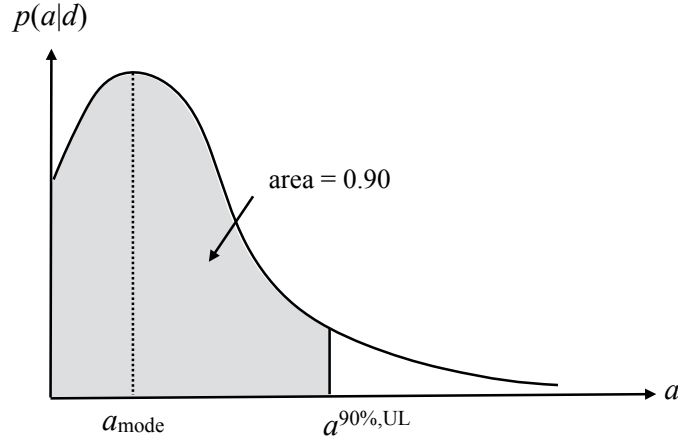
Figure 5.5: Figure retrieved from Ref. [80]. Graphical representation of the Bayesian upper limit (UL) on a at 90% credible interval, denoted by $a^{90\%,UL}$. It is a Bayesian credible interval where the lowest value of the interval coincides with the lowest possible value a can take. In the case of a being the amplitude of the GW signal, this lower-end value is 0.

To choose between different hypotheses or models, $\mathcal{M}_\alpha$, with parameters $\underline{\theta}_\alpha$, the Bayes factor is used. We shall use the index α to denote the different hypotheses or models. To define the Bayes factor, we shall start with the joint posterior distribution, which is given by

$$p(\underline{\theta}_\alpha|d, \mathcal{M}_\alpha) = \frac{p(d|\underline{\theta}_\alpha, \mathcal{M}_\alpha)p(\underline{\theta}_\alpha|\mathcal{M}_\alpha)}{p(d|\mathcal{M}_\alpha)}.$$ (5.9)

The quantity $p(d|\mathcal{M}_\alpha)$ is the model evidence, given by

$$p(d|\mathcal{M}_\alpha) = \int p(d|\underline{\theta}_\alpha, \mathcal{M}_\alpha)p(\underline{\theta}_\alpha|\mathcal{M}_\alpha)\,d\underline{\theta}_\alpha,$$ (5.10)

and it is obtained by marginalizing over the model parameters $\underline{\theta}_\alpha$. The posterior for model $\mathcal{M}_\alpha$ is given by the Bayes' theorem

$$p(\mathcal{M}_\alpha|d) = \frac{p(d|\mathcal{M}_\alpha)p(\mathcal{M}_\alpha)}{p(d)},$$ (5.11)

where $p(d)$ is given by

$$p(d) = \sum_\alpha p(d|\mathcal{M}_\alpha)p(\mathcal{M}_\alpha).$$ (5.12)

The posterior odds ratio between two models $\mathcal{M}_\alpha$ and $\mathcal{M}_\beta$ is given by

---

[3]All the upper limits in this thesis are Bayesian upper limits. Practically speaking, these ULs are obtained by integrating the posterior on a parameter until an xx% of the area of the posterior is achieved. The value of the parameter for which this happens will be the UL on the parameter at xx% confidence level.

$$\mathcal{O}_{\alpha\beta}(d) = \frac{p(\mathcal{M}_\alpha|d)}{p(\mathcal{M}_\beta|d)} = \frac{p(\mathcal{M}_\alpha)}{p(\mathcal{M}_\beta)} \frac{p(d|\mathcal{M}_\alpha)}{p(d|\mathcal{M}_\beta)}. \tag{5.13}$$

After the last equality, the first ratio is the prior odds for models $\mathcal{M}_\alpha$ and $\mathcal{M}_\beta$, and the second ratio is defined as the Bayes factor $\mathcal{B}_{\alpha\beta}(d)$. The Bayes factor,

$$\mathcal{B}_{\alpha\beta}(d) \equiv \frac{p(d|\mathcal{M}_\alpha)}{p(d|\mathcal{M}_\beta)}, \tag{5.14}$$

indicates a preference for one model over the other. Usually, the value quoted in searches is $\log \mathcal{B}_{\alpha\beta}(d)$. A positive log-Bayes factor indicates that model $\mathcal{M}_\alpha$ fits the data better than model $\mathcal{M}_\beta$, while if negative it indicates the opposite. It is commonly assumed that for a log Bayes factor of ~ 8 there is a statistically significant preference for one hypothesis over the other [85, 86].

5.3 Relation between frequentist and Bayesian approach

It is important to compare the hypothesis selection or testing between the two approaches. For that purpose, an example is introduced, where $\mathcal{M}_o$ indicates there is only noise, denoted by "n", in the data and $\mathcal{M}_1$ indicates there is noise and a GW signal, denoted by "h", in the data. The model $\mathcal{M}_o$ has associated parameters $\underline{\theta}_n$ and $\mathcal{M}_1$ has parameters $\{\underline{\theta}_n, \underline{\theta}_h\}$. The frequentist detection statistic is defined as the ratio of the maxima of the likelihoods for the two models, given by [80]

$$\Lambda_{ML}(d) \equiv \frac{\max_{\underline{\theta}_n} \max_{\underline{\theta}_h} p(d|\underline{\theta}_n, \underline{\theta}_h, \mathcal{M}_1)}{\max_{\underline{\theta}'_n} p(d|\underline{\theta}'_n, \mathcal{M}_0)}. \tag{5.15}$$

The Bayesian model selection uses the Bayes factor given by

$$\mathcal{B}_{10}(d) = \frac{\int d\underline{\theta}_n \int d\underline{\theta}_h \, p(d|\underline{\theta}_n, \underline{\theta}_h, \mathcal{M}_1) p(\underline{\theta}_n, \underline{\theta}_h|\mathcal{M}_1)}{\int d\underline{\theta}'_n \, p(d|\underline{\theta}'_n, \mathcal{M}_0) p(\underline{\theta}'_n|\mathcal{M}_0)}. \tag{5.16}$$

Eqs. (5.15) and (5.16) can be related using Laplace's approximation. For a model $\mathcal{M}$ with parameters $\underline{\theta}$, the Laplace approximation is given by [80, 87]

$$\int d\underline{\theta} \, p(d|\underline{\theta}, \mathcal{M}) p(\underline{\theta}|\mathcal{M}) \simeq p(d|\underline{\theta}_{ML}, \mathcal{M}) \frac{\Delta V_{\mathcal{M}}}{V_{\mathcal{M}}}. \tag{5.17}$$

The quantity $\Delta V_{\mathcal{M}}$ is the spread of the likelihood around its peak and $V_{\mathcal{M}}$ is the total parameter space volume of the model parameters. Applying Laplace's approximation, the Bayes factor $\mathcal{B}_{10}$ and the frequentist detection statistic Λ_{ML} are related by

$$2 \ln \mathcal{B}_{10}(d) \simeq 2 \ln (\Lambda_{ML}(d)) + 2 \ln \left(\frac{\Delta V_1/V_1}{\Delta V_0/V_0} \right). \tag{5.18}$$

The first term in Eq. (5.18) is the square of the signal-to-noise-ratio, which indicates the SNR^2 is an alternative frequentist detection statistic. The second term is a penalty factor. For two models that fit the data equally, this penalty factor will favor the simplest model.

5.4 Paramater estimation, model selection and choice of priors in GW searches

To define the likelihood function, the interferometer response and its noise have to be well understood. For ground-based interferometers, the data comes from the error signal in the differential arm length control system.

Given that the signal and noise $n(t)$ are uncorrelated, the data is $d(t) = h(t) + n(t)$, where $h(t)$ represents the GW metric perturbation $h_{ab}(t, \underline{x})$ convolved with the interferometer response. The likelihood of observing $d(t)$ can be found demanding that the residual $r(t) \equiv d(t) - \bar{h}(t)$ is consistent with a draw from the noise distribution

$$p(d(t)|\bar{h}(t)) = p_n(r(t)) = p_n(d(t) - \bar{h}(t)) \,, \tag{5.19}$$

where $\bar{h}(t)$ is the model describing the GW signal. For discretely sampled data $d \equiv \{d_1, d_2, \cdots, d_N\}$, where d_i is the data at time t_i, $d_i \equiv d(t_i)$, the likelihood can be generalized as $p(d|\bar{h}) = p_n(r)$. The quantities $r \equiv \{r_1, r_2, \cdots, r_N\}$, where $r_i \equiv r(t_i)$, are the residuals per data sample. Noise is due to many individual sources, so from the central limit theorem the likelihood can be approximated by [80]

$$p(d|\bar{h}) = \frac{1}{\sqrt{det(2\pi C_n)}} \, e^{-\frac{1}{2} \sum_{i,j} r_i \left(C_n^{-1}\right)_{ij} r_j} \,, \tag{5.20}$$

where C_n is the noise correlation matrix, with components $(C_n)_{ij} = \langle n_i n_j \rangle - \langle n_i \rangle \langle n_j \rangle$. The indices "i", "j" label different data samples, taken at times, t_i and t_j. In the case of stationary noise, the noise correlation matrix is only dependent on the time difference $|t_i - t_j|$, which implies the likelihood can be rewritten for a network of interferometers [80] as

$$p(d|\bar{h}) = \frac{1}{\sqrt{det(2\pi C_n)}} e^{-\frac{1}{2} \sum_{Ii,Jj} r_{Ii} \left(C_n^{-1}\right)_{Ii,Jj} r_{Jj}} \,. \tag{5.21}$$

The indices "i" and "j" label the discrete-time or frequency sample for each detector, denoted by I and J. In Bayesian inference, a model $\mathcal{M}$ has to be chosen, which implies placing a prior on the samples h_i. If the model is well known, the prior can be expressed as

$$p(\bar{h}|\mathcal{M}) = \delta(\bar{h} - \bar{h}(\underline{\theta}, \mathcal{M})) \, p(\underline{\theta}|\mathcal{M}) \,, \tag{5.22}$$

where $\underline{\theta}$ are the model parameters. The isotropic SGWB has a prior given by

$$p(\bar{h}|\mathcal{M}) = \frac{1}{2\pi S_h} e^{-(\bar{h}_+^2(\hat{n}) + \bar{h}_\times^2(\hat{n}))/2S_h} \,, \tag{5.23}$$

where S_h is the power spectrum of the GWB. This prior corresponds to a signal $\bar{h} = (\bar{h}_+(\hat{n}), \bar{h}_\times(\hat{n}))$ coming from direction $\hat{n}$.

All of these concepts will become relevant in Chapters 6 and 7, where the Bayesian-frequentist approach is used on the search for a GWB and to set upper limits over model parameters of the GWB.

Chapter 6

Gravitational wave background

In this chapter the gravitational wave background is introduced, characterized statistically and the method used for the detection of the GWB is explained, as well as the data analysis techniques used in LIGO-Virgo. With this foundation, the analysis performed and results obtained after the third observational run in LIGO-Virgo are presented for an unpolarized background. Finally, polarized GWBs and GWBs with non-GR polarizations are briefly introduced.

6.1   Energy density spectrum in gravitational waves

The GWB is a superposition of a large number of weak, independent, and unresolved GW sources [88, 89]. The GWB is a persistent and incoherent signal, meaning it is always present and the lack of knowledge about the source forces us to treat the phase as random [90]. It is commonly referred to as 'stochastic' GWB because it can only be characterized statistically [88]. The sources can either be cosmological or astrophysical (see section 1.5.4). This thesis focuses on an isotropic and unpolarized GWB, meaning the GWB has no preference for a particular direction in the sky and it has no preference for the cross or plus polarization.

The large number of sources composing the GWB are assumed random and hence the components of the plane wave expansion $h_A(f,\hat{\Omega})$ are considered as random variables. Resorting to the central limit theorem, the GWB can thus be assumed to be Gaussian distributed. This simplifies the problem of specifying an entire probability density function to just specifying the first two moments of $h_A(f,\hat{\Omega})$, $\langle h_A(f,\hat{\Omega})\rangle$ and $\langle h_A^*(f,\hat{\Omega})h_{A'}(f',\hat{\Omega}')\rangle$, where $\hat{\Omega}$ is a particular direction in the sky and A represents the polarization of the GWB, + or x. The first two moments are the mean and standard deviation of the distribution. As mentioned above, the GWB will be assumed to be isotropic. This assumption is an extrapolation of the fact that the CMB is isotropic [91]. Finally, given that the age of the Universe is about 20 orders of magnitude larger than the typical period of the GWs, the GWB is assumed to be stationary, meaning the 2-point correlation function[1] of the GW strain depends on the different times and not the time origin [88, 91] [2]. The GWB has zero mean, i.e.: the expectation value of the amplitude over time is zero $\langle h_A(f,\hat{\Omega})\rangle = 0$. The reason for the mean being zero is derived in Ref. [90]. Since $h_A(f,\hat{\Omega})$ is a complex number, it can be expressed in terms of an amplitude $A_A(f,\hat{\Omega})$ and a phase $\Phi(f,\hat{\Omega})$ uniformly distributed on $(0,2\pi)$ as $h_A(f,\hat{\Omega}) = A_A(f,\hat{\Omega})e^{i\Phi(f,\hat{\Omega})}$. The amplitude and phase are statistically independent, so the first moment of the component of the plane wave expansion

---

[1]The moments of the components $h_A(f,\hat{\Omega})$ mentioned above are also known as correlation functions. A correlation function between two random variables provides the statistical correlation between them. The correlation function between random variables representing the same quantity at different points is called the autocorrelation function. The correlation function between different random variables is known as the cross-correlation function. In the text, we will use the term n-point correlation function for $n = \{2, 3, 4\}$, which implies the correlation is being calculated between n random variables. According to Isserlis' theorem [92], given a set of Gaussian random variables, all the higher-order moments (3-point correlation function and higher) are trivial.

[2]Note that the noise of the detectors is not stationary, posing a problem for the data analysis. This issue will be dealt with in the following sections.

vanishes [90]

$$\langle h_A(f, \hat{\Omega}) \rangle = \langle A_A(f, \hat{\Omega}) \rangle \langle e^{i\Phi(f, \hat{\Omega})} \rangle = 0. \tag{6.1}$$

Even though the mean over time is zero, at each time there is a small amplitude of the background that will make the detection possible with future detectors. The GWB, being Gaussian with zero mean, isotropic, unpolarized, and stationary allows writing the 2-point correlation function as

$$\langle h_A^*(f, \hat{\Omega}) h_{A'}(f', \hat{\Omega}') \rangle = \delta_{AA'} \delta(f - f') \delta^2(\hat{\Omega}, \hat{\Omega}') H(f), \tag{6.2}$$

where H(f) is the strain power spectrum at the frequency f, related to the strain power spectral density $S_h(f)$ as $H(f) = S_h(f)/(16\pi)$. GWs composing the GWB carry energy which is characterized by the dimensionless energy density in gravitational waves spectrum,

$$\Omega_{GW} = \frac{1}{\rho_{c,o}} \frac{d\rho_{GW}}{d(\ln f)}. \tag{6.3}$$

The function ρ_{GW} is the energy density in GWs, normalized by $\rho_{c,o}$, the critical energy density of the universe today, $\rho_{c,o} = 3H_o^2 c^2/(8\pi G)$, given in terms of the Hubble parameter today[3]. This spectrum fully characterizes the GWB alongside with the assumptions mentioned above. The energy density in GWs ρ_{GW} is expressed in terms of the 2-point correlation function of the time derivative of the perturbation in the Minkowski metric, $h_{\mu\nu}$,

$$\rho_{GW} = \frac{c^2}{32\pi G} \langle \dot{h}_{ab}(t, \mathbf{x}) \dot{h}^{ab}(t, \mathbf{x}) \rangle. \tag{6.4}$$

The indices a and b correspond to spatial indices (x, y, z). As derived in section 1.2, the perturbation $h_{ab}(t, \mathbf{x})$ can be expressed as a superposition of plane waves

$$h_{ab}(t, \mathbf{x}) = \sum_{A=+,x} \int_{-\infty}^{\infty} df \int d\hat{\Omega} h_A(f, \hat{\Omega}) e^{2\pi i f(t - \hat{\Omega} \cdot \mathbf{x}/c)} e_{ab}^A(\hat{\Omega}), \tag{6.5}$$

with a frequency f and propagating in the direction $\hat{\Omega}$. Each plane wave is characterized by the amplitude $h_A(f, \hat{\Omega})$ and the phase $2\pi i f(t - \hat{\Omega} \cdot \mathbf{x}/c)$[4]. The tensors $e_{ab}^A(\hat{\Omega})$ are the polarization tensors, introduced in appendix A. The component $h_{ab}(t, \mathbf{x})$ is real, so the plane wave components satisfy $h_A(-f, \hat{\Omega}) = h_A^*(f, \hat{\Omega})$. The above mentioned assumptions can be used to express the energy density in GWs as a function of the strain power spectrum $H(f)$. In order to derive this relation, we start with the energy density spectrum in GWs, given by Eq. (6.3). Using Eqs. (6.4) and (6.5), Ω_{GW} can be expressed as

$$\Omega_{GW}(f) = \frac{f}{\rho_{c,o}} \frac{c^2}{32\pi G} \frac{d}{df} \langle \dot{h}_{ab} \dot{h}^{ab} \rangle. \tag{6.6}$$

Taking the time derivative of h_{ab} and the frequency derivative of the expectation value of $\dot{h}_{ab} \dot{h}^{ab}$, Eq. (6.6) can be rewritten as

$$\Omega_{GW}(f) = \frac{f}{32\pi G \rho_{c,o}} \sum_{A,A'=+,x} \int_{-\infty}^{\infty} df' \int_{S^2} d\hat{\Omega} d\hat{\Omega}' \langle h_A^*(f, \hat{\Omega}) h_{A'}(f, \hat{\Omega}) \rangle$$
$$4\pi^2 f f' e^{-2\pi i f(t - \hat{\Omega} \cdot \mathbf{x}/c)} e^{2\pi i f'(t - \hat{\Omega}' \cdot \mathbf{x}'/c)} e_{ab}^A(\hat{\Omega}) e_{A',ab}(\hat{\Omega}'). \tag{6.7}$$

Frequency is a positive quantity, so the integral in frequency turns into $2 \int_0^{\infty} df'$. Assuming that the GWB is isotropic and unpolarized, Eq. (6.7) can be re-written as

$$\Omega_{GW}(f) = \frac{8fc^2\pi}{32G\rho_{c,o}} \sum_{A,A'=+,x} \int_0^{\infty} df' \int_{S^2} d\hat{\Omega} d\hat{\Omega}' \delta_{A,A'} \delta(f - f') \delta^2(\hat{\Omega}, \hat{\Omega}') H(f)$$
$$f f' e^{-2\pi i f(t - \hat{\Omega} \cdot \mathbf{x}/c)} e^{2\pi i f'(t - \hat{\Omega}' \cdot \mathbf{x}'/c)} e_{ab}^A(\hat{\Omega}) e_{A',ab}(\hat{\Omega}'). \tag{6.8}$$

---

[3]Measured from type IA supernovae and Cosmic Microwave Background (CMB) experiments.

[4]This phase is written as such from the dispersion relation, where the wavenumber $k = 2\pi f/c$. In 3-dimensions, it can be generalized to $\mathbf{k} = \frac{2\pi f}{c} \hat{\Omega}$.

The polarization tensor contracted with itself is 2, and because of the + and x polarizations, $e_{ab}^A(\hat{\Omega})e_{A,ab}(\hat{\Omega}) = 4$. Furthermore, the integral in the sky position is independent on the integrand, so Eq. (6.8) leads to

$$\Omega_{GW}(f) = \frac{\pi c f^3}{4G\rho_{c,o}} \int_{S^2} d\hat{\Omega} H(f) = \frac{32\pi^3}{3H_o^2} f^3 H(f). \tag{6.9}$$

Eq. (6.9) has deep implications in the GWB searches. Detectors that work at lower frequencies are more sensitive to the energy density in GWs given the f^3 dependence. Let us explain this concept in more detail. For the same strain $H(f)$, for smaller frequencies, the detector will be sensitive to a smaller value of $\Omega_{\text{GW}}(f)$. For instance, if the detector's highest sensitivity was 2 orders of magnitude in frequency below the current one, because of f^3, we would be nearly acquiring an extra order of magnitude in sensitivity to $\Omega_{\text{GW}}(f)$. Furthermore, given the sensitivity curve of a detector, it is straightforward to know which is the level of Ω_{GW} detectable by the detector. It is usual to rewrite Eq. (6.9) in terms of the strain power spectral density. Hence, Eq. (6.9) is then interchangeably used with this equation

$$\Omega_{GW}(f) = \frac{2\pi^2}{3H_o^2} f^3 S_h(f). \tag{6.10}$$

In addition to $S_h(f)$ and $\Omega_{GW}(f)$, the strength of the GWB is also expressed in terms of the characteristic strain amplitude $h_c(f) \equiv \sqrt{fS_h(f)}$. Now that the energy density spectrum has been introduced, Figure 6.1 shows examples of the spectrum of the GWB from different cosmological models in comparison with the best upper limits and future expected GW detector sensitivities. The astrophysical background (dashed grey band) may mask the primordial background in a wide range of frequencies ranging from 10^{-3} to 10^3 Hz. The current ground based detectors do not have enough sensitivity to probe the models in Figure 6.1, though future detectors such as LISA and the 3G detectors could probe some sources such as cosmic string and phase transitions.
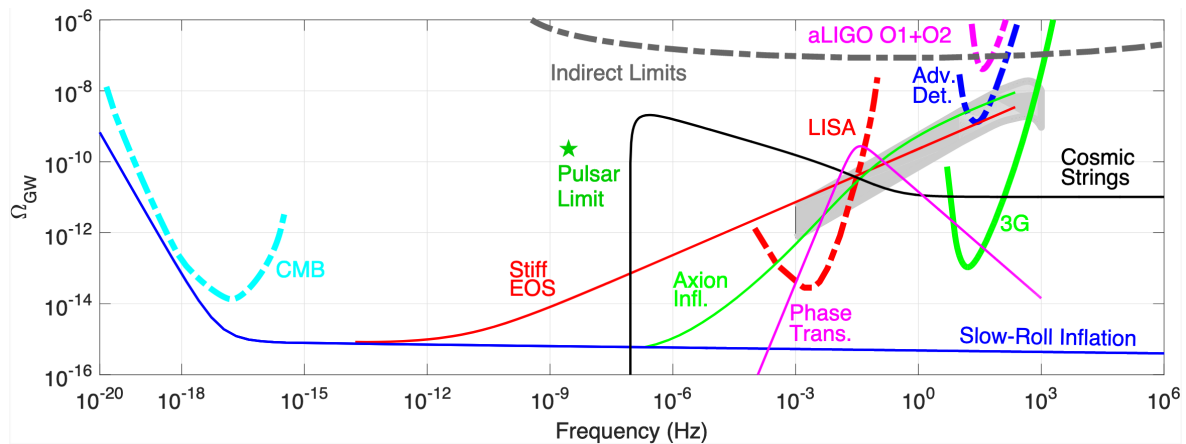
Figure 6.1: Figure retrieved from Ref. [93]. GWB spectra for several cosmological models (solid lines) compared to past measurements (Advanced LIGO upper limit [94], constraints based on the big bang nucleosynthesis and cosmic microwave background (CMB) observations, low-l CMB observations, and pulsar timing [95]), and future expected sensitivities [96] (the final sensitivity of Advanced LIGO [97], Cosmic Explorer [98], and LISA, all assuming 1 year of exposure [99]). The gray shaded band indicates the expected amplitude of the GWB due to the cosmic population of CBC mergers, based on the observed coalescieng binary systems [100].

6.2   Isotropic detection method. Cross correlation technique.

In this section, the framework for the detection of a GWB is introduced in some detail. Given the random nature of a GWB, distinguishing between a signal and local detector noise is difficult. For that reason, searches for a GWB involve cross-correlating data from pairs of interferometers assuming that correlated noise between interferometers is negligible. This search technique was first introduced by B. Allen and J. Romano [88]. The Eq. (6.9) shows that if the detected $\Omega_{GW}(f)$, converted to strain units,

was higher than $\sim 10^{-22}$, then one single detector should be capable of making a detection. However, the strain amplitude of a GWB is below 10^{-25}, and hence the need to use an alternative detection technique. This cross correlation method is equivalent to computing the 2-point correlation function of the metric (see Eq. (1.29)), which is related to the energy density spectrum, Eqs. (6.3) and (6.4). The output of a detector $s_i(t)$ is the sum of the detector's noise $n_i(t)$ and a signal $h_i(t)$,

$$
\begin{aligned}
s_1(t) =& n_1(t) + h_1(t), \\
s_2(t) =& n_2(t) + h_2(t).
\end{aligned}
\tag{6.11}
$$

The noise of a detector is dominated by Gaussian processes, so it can be assumed to be zero over time $\langle n_i(t) \rangle = 0$. The noise between two detectors is uncorrelated [5] $\langle n_i(t)n_j(t) = \delta_{ij}$. The GW signal $h_i(t)$ depends on the metric and how the signal couples to a detector at a particular time, which may vary over time. Nevertheless, the signal is Gaussian, as stated above, so on average $\langle h_i(t) \rangle = 0$. Consequently, $s_i(t)$ is also Gaussian $\langle s_i(t) \rangle = 0$.

The cross-correlation estimator for an observation period T is defined as

$$
Y = \int_{-T/2}^{T/2} dt \int_{-T/2}^{T/2} dt' s_1(t) s_2(t) Q(t,t').
\tag{6.12}
$$

The function $Q(t,t')$ is known as *filter* and it maximises the SNR (see derivation below). The noise and the GWB are assumed to be stationary during the observation time T, so the time origin is not important but the time difference. Consequently, the filter can be written as $Q(t-t')$ [6].

In order to obtain the SNR, defined as $\mathrm{SNR}^2 := \langle Y \rangle^2 / \sigma_Y^2$, in terms of $\Omega_{GW}(f)$, the point estimate Y will be expanded in Fourier domain. Given the properties of the filter $Q(t,t')$, one of the integrals in Eq. (6.12) can be extended from $-\infty$ to ∞, getting

$$
\begin{aligned}
Y &= \int_{-T/2}^{T/2} dt \int_{-\infty}^{\infty} dt' \int_{-\infty}^{\infty} df df' df'' s_1^*(f) e^{-2\pi i f t} s_2(f') e^{2\pi i f' t'} Q(f'') e^{-2\pi i f''(t-t')} \\
&= \int_{-T/2}^{T/2} dt \int_{-\infty}^{\infty} df df' df'' s_1^*(f) s_2(f') Q(f'') e^{-2\pi i (f-f'')t} \int_{-\infty}^{\infty} dt' e^{2\pi i (f'-f'')t'} \\
&= \int_{-\infty}^{\infty} df df' s_1^*(f) s_2(f') Q(f') \int_{-T/2}^{T/2} dt e^{-2\pi i (f-f')t},
\end{aligned}
\tag{6.13}
$$

where the last equality is obtained by integrating over t' the delta function $\int_{-\infty}^{\infty} dt' e^{2\pi i (f'-f'')t'} = \delta(f'-f'')$. In Eq. (6.13), the last term is a finite time approximation to a delta function, whose solution is

$$
\delta_T(f-f') = \int_{-T/2}^{T/2} dt e^{-2\pi i (f-f')t} = \frac{\sin(\pi T(f-f'))}{\pi(f-f')}.
\tag{6.14}
$$

For $f = f' \Rightarrow \delta_T(0) \to T$, which tends to a usual Dirac delta function for $T \to \infty$. The cross power spectral density is the product of $s_1^*(f)s_2(f')$ and the observation time,

$$
\hat{C}_{12} \equiv \frac{T}{2} s_1^*(f) s_2(f').
\tag{6.15}
$$

As seen in Eq. (6.13), to recover Y the optimal filtering has to be applied to $\hat{C}_{12}$, meaning the function $Q(f')$ that maximizes the SNR has to be applied. The next steps are calculating the expectation value of the cross correlation estimator $\langle Y \rangle$ and determining the optimal filter $Q(f')$. The former is proportional to $\langle s_1^*(f)s_2(f') \rangle$. Using Eqs. (6.11), this expectation value can be expanded as in

---

[5] In reality there are sources of noise that are correlated (see section on Schumann resonances 6.4.1)

[6] Note that the cross-correlation will be maximum when two detectors are co-located and co-aligned, which translates into $t = t'$ and the filter Q will peak. In the limit in which the detectors are infinitely separated, $|t - t'| \to \infty$ and the cross-correlation will be null, so $Q(t - t') \to 0$. This implies that $Q(t - t') \to \delta(t - t')$.

$$\langle s_1^*(f)s_2(f')\rangle = \langle (n_1(f) + h_1(f))^*(n_2(f') + h_2(f'))\rangle \simeq \langle h_1^*(f)h_2(f')\rangle, \tag{6.16}$$

where the last equality is obtained under the assumptions that the noise between interferometers is uncorrelated $\langle n_i^*(f)n_j(f')\rangle = \delta_{ij}$ and the noise is uncorrelated with the signal $\langle n_i^*(f)h_j(f')\rangle = 0$. The signal at detector i can be expressed as the contraction between the metric (see Eq. (1.29)) and the detector $h_i(t) = h_{ab}(t, \mathbf{x}_i)d^{ab}(t, \mathbf{x}_i)$, where $\mathbf{x}_i$ is the location of the detector. The vector $d^{ab}(t, \mathbf{x}_i)$ denotes the response of the detector i located at $\mathbf{x}_i$. It can be expressed in terms of the unit vectors along the x and y arms of the detector, $\hat{X}(t, \mathbf{x}_i)$ and $\hat{Y}(t, \mathbf{x}_i)$, respectively, as

$$d^{ab}(t, \mathbf{x}_i) = \frac{1}{2}\Big(\hat{X}^a(t, \mathbf{x}_i)\hat{X}^b(t, \mathbf{x}_i) - \hat{Y}^a(t, \mathbf{x}_i)\hat{Y}^b(t, \mathbf{x}_i)\Big). \tag{6.17}$$

In order to calculate the expectation value in Eq. (6.16), $h_i(t)$ is expanded in frequency domain resorting to the plane wave expansion,

$$h_i(f;t) = \sum_{A=+,x} \int d\hat{\Omega} h_A(f, \hat{\Omega})e^{-2\pi i f\hat{\Omega}\cdot\mathbf{x}_i/c}e_{ab}^A(\hat{\Omega})d^{ab}(t, \mathbf{x}_i), \tag{6.18}$$

where the t index is kept to emphasize the fact that the analysis is done per segment of time. The last term captures the contraction of the polarization tensor with the detector response tensor at location $\mathbf{x}_i$ and time t, and can be expressed as $F_i^A(\hat{\Omega}, t) := e_{ab}^A(\hat{\Omega})d^{ab}(t, \mathbf{x}_i)$, known as the *detector pattern functions*. Eq. (6.16) is now expressed as

$$\begin{aligned}
\langle s_1^*(f)s_2(f')\rangle &= \sum_{A,A'=+,x} \int d\hat{\Omega} \int d\hat{\Omega}' \langle h_A^*(f, \hat{\Omega})h_{A'}(f', \hat{\Omega}')\rangle e^{2\pi i\hat{\Omega}\cdot\mathbf{x}_1/c}e^{-2\pi i\hat{\Omega}\cdot\mathbf{x}/c}F_1^A(\hat{\Omega}, t)F_2^{A'}(\hat{\Omega}', t') \\
&= \sum_{A,A'=+,x} \int d\hat{\Omega} \int d\hat{\Omega}'\delta_{AA'}\delta(f - f')\delta^2(\hat{\Omega}, \hat{\Omega}')H(f)e^{2\pi i\hat{\Omega}\cdot\mathbf{x}_1/c}e^{-2\pi i\hat{\Omega}\cdot\mathbf{x}/c}F_1^A(\hat{\Omega}, t)F_2^{A'}(\hat{\Omega}', t') \\
&= \sum_A \int d\hat{\Omega}\delta(f - f')H(f)e^{2\pi i f\hat{\Omega}\cdot\Delta\mathbf{x}/c}F_1^A(\hat{\Omega}, t)F_2^{A'}(\hat{\Omega}', t') \\
&= \frac{3H_o^2}{32\pi f^3}\Omega_{GW}(f)\delta(f - f')\sum_A \int d\hat{\Omega}e^{2\pi i f\hat{\Omega}\cdot\Delta\mathbf{x}/c}F_1^A(\hat{\Omega}, t)F_2^{A'}(\hat{\Omega}', t') \\
&= \frac{3H_o^2}{20\pi^2 f^3}\Omega_{GW}(f)\delta(f - f')\gamma_{12}(f),
\end{aligned} \tag{6.19}$$

where $\Delta\mathbf{x} := \mathbf{x}_1 - \mathbf{x}_2$ and $\gamma_{12}(f)$ is a purely geometrical quantity known as the overlap reduction function (ORF), given by

$$\gamma_{12}(f) = \frac{5}{8\pi}\sum_A \int d\hat{\Omega}e^{2\pi i f\hat{\Omega}\cdot\Delta\mathbf{x}/c}F_1^A(\hat{\Omega}, t)F_2^{A'}(\hat{\Omega}', t'). \tag{6.20}$$

The pre-factor $\frac{5}{8\pi}$ in Eq. (6.20) is chosen so that $\gamma_{12}(t) = 1$ for co-aligned and co-located detectors. Furthermore, in the fourth equality of Eq. (6.19), Eq. (6.9) has been substituted. The final result of Eq. (6.19) is important because it shows that the expected value of cross-correlating two detectors' time series, is related to $\Omega_{GW}(f)$. The expectation value of Y can be calculated using the result from Eq. (6.19)

$$\begin{aligned}
\langle Y\rangle &= \int_{-\infty}^{\infty} df df' \langle s_1^*(f)s_2^*(f')\rangle Q(f')\delta_T(f - f') \\
&= \frac{3H_o^2}{20\pi^2} \int_{-\infty}^{\infty} df df' \frac{\Omega_{GW}}{f^3}\delta(f - f')\gamma_{12}(f)Q(f')\delta_T(f - f') \\
&= \frac{3H_o^2 T}{20\pi^2} \int_{-\infty}^{\infty} df \frac{\Omega_{GW}}{f^3}\delta(f - f')\gamma_{12}(f)Q(f').
\end{aligned} \tag{6.21}$$

In the last equality of Eq. (6.21), $\delta_T(0) = T$ has been used. The expectation value of Y, $\langle Y \rangle$, has an associated error or variance given by $\sigma_Y^2 = \langle Y^2 \rangle - \langle Y \rangle^2$. Assuming the detector noise is much larger than the GWB, the approximation $\sigma_Y^2 \simeq \langle Y^2 \rangle$ can be used. The expectation value of Y^2 is proportional to terms like $\langle n_i(f)h_j(f') \rangle$, $\langle n_i(f)n_j(f') \rangle$, $\langle n_i(f)...h_N(f') \rangle$, for N odd, that will all be zero under the assumptions that noise between interferometers is uncorrelated and has no correlation with the signal. For these reasons, σ_Y^2 can be approximated by

$$
\begin{aligned}
\sigma_Y^2 &\simeq \int_{-\infty}^{\infty} df df' dk dk' \langle n_1^*(f)n_2(f')n_1^*(k)n_2(k') \rangle \delta_T(f-f')\delta_T(k-k')Q(f')Q(k') \\
&= \int_{-\infty}^{\infty} df df' dk dk' \langle n_1^*(f)n_1(-k)n_2^*(-f')n_2(k') \rangle \delta_T(f-f')\delta_T(k-k')Q(f')Q(k'),
\end{aligned}
\tag{6.22}
$$

where in the last equality the reality of the noise is used $n_i^*(k) = n_i(-k)$. The n_i values are statistically independent, so the 4-point correlation function in Eq. (6.22) can be expressed in terms of the 2-point correlation function

$$
\begin{aligned}
\sigma_Y^2 &\simeq \int_{-\infty}^{\infty} df df' dk dk' \langle n_1^*(f)n_1(-k) \rangle \langle n_2^*(f')n_1(k') \rangle \delta_T(f-f')\delta_T(k-k')Q(f')Q(k') \\
&= \int_{-\infty}^{\infty} df df' dk dk' \frac{1}{2}\delta(f+k)\frac{1}{2}\delta(f'+k')Q(f')Q(k') \\
&= \frac{1}{4} \int_{-\infty}^{\infty} df df' P_1(|f|)P_2(|f'|)\delta_T^2(f-f')Q^2(f') \\
&\simeq \frac{T}{4} \int_{-\infty}^{\infty} df P_1(|f|)P_2(|f'|)Q^2(f),
\end{aligned}
\tag{6.23}
$$

where the definition of noise power spectrum $\langle n_i^*(f)n_i(f') \rangle = \frac{1}{2}\delta(f-f')P_i(|f|)$ has been used[7]. In the last equality of Eq. (6.23), $\delta_T(0) = T$ is used. In order to express the SNR, an inner product between functions $A(f)$ and $B(f)$ is defined

$$
(A, B) = \int_{-\infty}^{\infty} df A^*(f)B(f)P_1(|f|)P_2(|f|).
\tag{6.24}
$$

Making use of this inner product, the expectation value of the cross correlation estimator in Eq. (6.21) can be written as

$$
\langle Y \rangle = \frac{3H_o^2 T}{20\pi^2} \Big(Q(|f|), \frac{\Omega_{GW}(|f|)\gamma_{12}(|f|)}{f^3 P_1(|f|)P_2(|f|)} \Big).
\tag{6.25}
$$

Similarly, using the inner product defined in Eq. (6.24), the variance of Y, Eq. (6.23), can be written as

$$
\sigma_Y^2 = \frac{T}{4}(Q(|f|), Q(|f|)).
\tag{6.26}
$$

The SNR can then be written as

$$
\mathrm{SNR}^2 = \frac{\langle Y \rangle^2}{\sigma_Y^2} = \Big(\frac{3H_o^2}{10\pi^2} \Big)^2 T \frac{\Big(Q(|f|), \frac{\Omega_{GW}(|f|)\gamma_{12}(|f|)}{f^3 P_1(|f|)P_2(|f|)} \Big)^2}{(Q(|f|), Q(|f|))}.
\tag{6.27}
$$

The filter $Q(|f|)$ will be chosen such that the SNR is maximized. This happens when $Q(|f|)$ is defined as

$$
Q(f) = \lambda \frac{\Omega_{GW}(f)\gamma_{12}(f)}{f^3 P_1(f)P_2(f)},
\tag{6.28}
$$

---

[7]Frequencies are positive, leading to a factor of $1/2$ in the definition of the noise power spectrum. The absolute value over f is used to emphasize $f \in \mathcal{R}^+$.

where λ is a scaling factor. The scaling factor in Eq. (6.28) is chosen such that $\langle Y \rangle = T\Omega_\alpha$, where Ω_α is the amplitude of the GWB. Substituting Eq. (6.28) in Eq. (6.27) leads to

$$\text{SNR} = \frac{3\text{H}_\text{o}^2\sqrt{\text{T}}}{10\pi^2}\left(\int_{-\infty}^{\infty} \text{df}\, \frac{\Omega_{\text{GW}}^2(|\text{f}|)\gamma_{12}^2(\text{f})}{|\text{f}|^6 \text{P}_1(|\text{f}|)\text{P}_2(|\text{f}|)} \right)^{1/2}. \tag{6.29}$$

This equation has major implications in the analysis. The SNR increases with the square root of the observing time T, so long observational periods, of the order of a year, are preferable. The power spectra $P_i(|f|)$ in the denominator naturally suppress noisy frequencies from the analysis. Furthermore, as the detector sensitivity increases, $P_i(|f|)$ drops, leading to an increase in the SNR. As stated above, the presence of the f^6 factor in the denominator implies a higher sensitivity to the GWB at lower frequencies. Finally, $\Omega_{GW}(|f|)$ appears in Eq.(6.29), so to do the analysis, an assumption of the shape of the spectra needs to be taken. It is common to use a simple power law

$$\Omega_{GW}(f) = \Omega_{ref}\Big(\frac{f}{f_{ref}}\Big)^\alpha, \tag{6.30}$$

where α is the spectral index, f_{ref} the reference frequency and Ω_{ref} is the amplitude of the GWB at f_{ref}. Here, f_{ref} is usually chosen to be 25Hz since that is the frequency where the LIGO-Virgo network has the highest sensitivity. Depending on the source being searched for, the spectral index α can take values 0, 2/3, or 3. The value $\alpha = 0$ characterizes cosmic strings [29, 36] and slow-roll inflation [45] in the LIGO-Virgo band. The value $\alpha = 2/3$ represents the inspiral phase of a CBC [101][8]. The CBCs are believed to be the main source of the GWB [100], so whenever searching for other sources, CBCs have to be simultaneously fitted using this spectrum

$$\Omega_{\text{CBC}}(f) = \Omega_{2/3}\Big(\frac{f}{f_{\text{ref}}}\Big)^{2/3}. \tag{6.31}$$

Finally, $\alpha = 3$ describes some astrophysical sources such as supernova [103] and it leads to a frequency-independent or flat strain power.

6.2.1 Overlap reduction function

The ORF has been derived in Eq. (6.20). It quantifies the reduction in sensitivity of the cross correlation between data of two interferometers to a GWB due to the response of the detectors as well as their separation and orientation [80]. From Eq. (6.19) and using the relation in Eq. (6.10), we obtain

$$\langle s_1^*(f)s_2(f')\rangle = \frac{S_h(f)}{10}\delta(f - f')\gamma_{12}. \tag{6.32}$$

From Eq. (6.15), $\langle \hat{C}_{12}\rangle \propto \gamma_{12}S_h(f)$, which implies the ORF is the transfer function between the GW strain power $S_h(f)$ and the detector response cross-spectral density [80]. The ORF between the LIGO interferometers and other major detectors can be seen in Figure 6.2, retrieved from Ref. [88]. There are some features to note. The cases in which the ORF is negative as $f \to 0$ are due to the fact that the two interferometers considered for the calculation are rotated by 90º with respect to each other [80]. Note that the ORF with the most distant detectors have their first zero at lower frequencies than those for nearby detectors 6.2. This implies that the further apart the detectors in a pair are from each other, the least sensitive the pair will be to the low-frequency content of a GWB.

---

[8]The spectrum with $\alpha = 2/3$ will no longer be applicable for future detectors, and the contributions from the merger and ringdown phases will have to be included [102]. For a single population of CBCs, the spectrum behaves as $f^{2/3}$ within a certain frequency range. However, beyond that frequency range, the spectrum will be governed by the equation of state of the CBC. The current frequency region of the high sensitivity of LIGO-Virgo coincides with that in which the spectral shape looks like $f^{2/3}$. However, with future detectors, the sensitivity at higher frequencies could increase and hence they will become sensitive to the region where the spectral shape does not behave like $f^{2/3}$. Restricting the analysis to about 100 Hz would be ok to keep the 2/3 behavior.
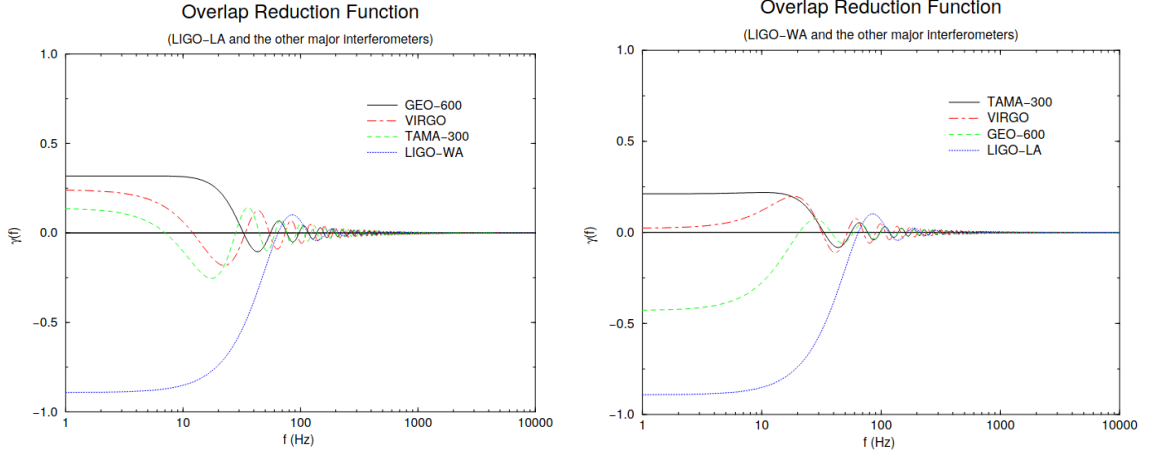
Figure 6.2: Figures retrieved from Ref. [88]. **Left** ORF between the LIGO-Livingstone detector and other interferometers. In dotted blue, the ORF with LIGO-Hanford and in dashed red with Virgo. **Right** ORF between the LIGO-Livingstone detector and other interferometers. In dotted blue, the ORF with GEO and in dashed red with Virgo.

6.2.2 Narrowband analysis

In practical terms, the analysis of data is not done for a continuous set of frequencies, as presented in section 6.2 (*broadband analysis*). Instead, measured data is discretely sampled, so the analysis is performed in discrete bins of frequency. This analysis is known as *narrowband analysis* [104, 80]. The narrowband definition of Y can be obtained from Eq. (6.13) by reducing the bandwidth of the analysis to just δf. For $f = f'$ and reducing the bandwidth to δf, Eq. (6.13) can be written as

$$Y_\alpha(f) = \delta f Re[s_1^*(f)s_2(f)]Q_\alpha(f)T \,, \tag{6.33}$$

The function $Q_\alpha(f)$ is the optimal filter, Eq. (6.28), which, for a spectrum given by a simple power law, Eq. (6.30), can be written as

$$Q_\alpha(f) = \lambda_\alpha \frac{(f/f_{ref})^\alpha \gamma_{12}(f)}{f^3 P_1(f) P_2(f)} \,. \tag{6.34}$$

Note that the index α indicates what spectral index has been used in the spectrum describing the GWB. The expectation value of Y_α, $\langle Y_\alpha \rangle$, is given by Eq. (6.21) which, for a power law, can be written as

$$\langle Y_\alpha \rangle = \frac{3H_o^2 T}{20\pi^2} \int_{-\infty}^{\infty} df \frac{\Omega_\alpha (f/f_{ref})^\alpha}{f^3} \gamma_{12}(f) Q_\alpha(f') \,. \tag{6.35}$$

Substituting Eq. (6.34) into Eq. (6.35) and then equating the result to Ω_α results in

$$\Omega_\alpha = \frac{3H_o^2 T}{20\pi^2} \int_{-\infty}^{\infty} df \frac{\Omega_\alpha (f/f_{ref})^\alpha}{f^3} \gamma_{12}(f) \lambda_\alpha \frac{(f/f_{ref})^\alpha \gamma_{12}(f)}{f^3 P_1(f) P_2(f)} \Rightarrow$$
$$\Rightarrow \lambda_\alpha^{-1} = \frac{3H_o^2 T}{20\pi^2} \int_{-\infty}^{\infty} df \frac{(f/f_{ref})^{2\alpha} \gamma_{12}^2(f)}{f^6 P_1(f) P_2(f)} \rightarrow \lambda_\alpha^{-1} = \delta f \frac{3H_o^2 T}{20\pi^2} \frac{(f/f_{ref})^{2\alpha} \gamma_{12}^2(f)}{f^6 P_1(f) P_2(f)} \,, \tag{6.36}$$

where the integral in df has been substituted by δf because of reducing the bandwidth of the analysis to just δf. The final definition of the cross correlation estimator for a narrowband search is given by

$$\hat{Y}_\alpha(f) \equiv \frac{2}{T} \frac{Re[s_1^*(f)s_2(f)]}{\gamma_{12}(f)S_\alpha} \,, \tag{6.37}$$

obtained by substituting the results in Eqs. (6.36) and (6.34) in Eq. (6.33). The associated variance is given by [80, 105]

$$\sigma_{\hat{Y}_\alpha}^2(f) \simeq \frac{1}{2T\Delta f} \frac{P_1(f)P_2(f)}{\gamma_{12}^2 S_\alpha^2}, \tag{6.38}$$

where S_α is the assumed spectral shape, which is related to the spectrum as $S_\alpha \equiv \frac{3H_o^2}{10\pi^2} \frac{1}{f^3} \left(\frac{f}{f_{ref}}\right)^\alpha$. The full broadband statistics can be expressed in terms of the narrowband statistics by combining frequency bins as if they were independent measurements of Y_α [105].

$$\hat{Y}_\alpha \equiv \frac{\sum_f \sigma_{\hat{Y}_\alpha}^{-2} \hat{Y}_\alpha(f)}{\sum_f' \sigma_{\hat{Y}_\alpha}^{-2}}, \tag{6.39}$$

$$\sigma_{\hat{Y}_\alpha}^{-2} \equiv \sum_f \sigma_{\hat{Y}_\alpha}^{-2}(f). \tag{6.40}$$

The two most important outputs from the usual GWB search pipeline are the sensitivity integrand $S_\alpha(f)$ [105] and the point estimate $p(f)$, which are defined as

$$S_\alpha(f) = \frac{2T\gamma_{12}^2 S_\alpha^2}{P_1(f)P_2(f)}, \tag{6.41}$$

$$p(f) = \frac{Q_\alpha(f)T}{2} Re[s_1^*(f)s_2^*(f)]. \tag{6.42}$$

Hence, Eqs. (6.37) and (6.38) can be re-written in terms of the sensitivity integrand and the point estimate as

$$Y_\alpha(f) = \frac{2}{\sigma_{\hat{Y}_\alpha}^2} Re[p(f)/S_\alpha(f)], \tag{6.43}$$

$$\sigma_{\hat{Y}_\alpha}(f) = \frac{1}{\sqrt{S_\alpha(f)\Delta f}}. \tag{6.44}$$

6.2.3 Combination of different sets of measurements

The power spectra of the noise of the detectors change over time. For this reason, it is convenient to combine the analysis of different sets of measurements taken with the same duration T. The way in which these measurements are combined is explained in what follows. Let us assume m different sets of measurements $^iS_1, ^iS_2, ...^iS_{n_i}$ where i denotes each measurement and thus takes values from 1 to m. Each measurement has mean $^i\mu := \langle ^iS \rangle$[9] and variance $^i\sigma^2 := \langle ^iS^2 \rangle - \langle ^iS \rangle^2$. The sample mean, or estimator, can be defined as [88] [10].

$$^i\hat{Y} := \frac{1}{n_i} \sum_{j=1}^{n_i} {}^iS_j. \tag{6.45}$$

This estimator has mean $\mu_i := \langle ^i\hat{Y} \rangle = \mu$ and variance $\sigma_i^2 := \langle ^i\hat{Y}^2 \rangle - \langle ^i\hat{Y} \rangle^2 = \frac{^i\sigma^2}{n_i^2}$. The combination of all measurements is done so that the SNR is maximised. This is done with the weighted average, given by

$$\hat{Y} := \frac{\sum_{i=1}^m \lambda_i {}^i\hat{Y}}{\sum_{j=1}^m \lambda_j} \quad /\lambda_j > 0. \tag{6.46}$$

The SNR is maximized when $\lambda_i \propto \sigma_i^{-2}$, as shown in Ref. [88]. Physically, this averaging is reasonable, since the larger the variance, i.e.: the more noisy the interferometer was during data taking, the smaller the weight associated with the data from that period is. For $\lambda_i = \sigma_i^{-2}$, the variance and SNR of the optimal estimator $\hat{Y}_{\text{optimal}} := \hat{Y}|_{\lambda_i = \sigma_i^{-2}}$ are given by

---

[9]The mean can be assumed to be the same for all measurements, $^i\mu := \langle ^iS \rangle \equiv \mu$

[10]In the literature, different notations are used. It is usual to denote to the cross correlation estimator Y, Eq. (6.12), as S. The expectation value $\langle Y \rangle$, Eq. (6.21), is sometimes denoted by $\mu \equiv \langle S \rangle = \langle Y \rangle$.

$$\sigma_{\text{optimal}}^{-2} = \sum_{i=1}^{m} \sigma_i^{-2} = \sum_{i=1}^{m} n_i^i \sigma^{-2} \quad ; \quad \text{SNR}_{\text{optimal}}^2 = \sum_{i=1}^{m} \text{SNR}_i^2 = \sum_{i=1}^{m} n_i^i \text{SNR}^2, \qquad (6.47)$$

where $\text{SNR}_i := \frac{Y_i}{\sigma_i} = \frac{\mu}{\sigma_i}$ and $^i\text{SNR} := \frac{^iY}{^i\sigma} = \frac{\mu}{^i\sigma}$. Then, the squared SNR of the optimal estimator is a sum of the squared SNR for each measurement ^iS, after n_i observation periods that last T each [88].

6.2.4 Combination of measurements from different detector pairs

In order to increase the sensitivity to the detection of a GWB, measurements from multiple detector pairs are combined[11]. The procedure is described in Ref [80]. We will denote by I and J each interferometer in each pair. For multiple detector pairs IJ, n_{IJ} different measurements are represented by the optimally filtered cross correlations, $^{(IJ)}S_1$, $^{(IJ)}S_2$, $\cdots$, $^{(IJ)}S_{n_{IJ}}$. Each measurement has an associated estimator $\hat{C}_{IJ} := \frac{1}{n_{IJ}} \sum_{k=1}^{n_{IJ}} {}^{(IJ)}S_k$ and error σ_{IJ}. The estimators from different detector pairs are combined as

$$\hat{C} := \frac{\sum_I \sum_J \sigma_{IJ}^{-2} \hat{C}_{IJ}}{\sum_I \sum_J \sigma_{IJ}^{-2}} . \qquad (6.48)$$

The inverse variance for the optimal estimator, defined as $\hat{C}_{\text{optimal}} := \hat{C}\big|_{\sigma_{IJ}^{-2}}$, is given by

$$\sigma_{\text{optimal}}^{-2} = \sum_I \sum_J \sigma_{IJ}^{-2} . \qquad (6.49)$$

Finally, the optimal SNR is the sum of the SNR per pair of interferometers

$$\text{SNR}_{\text{optimal}}^2 = \sum_I \sum_J n_{IJ} \, {}^{(IJ)}\text{SNR}^2 . \qquad (6.50)$$

Similarly to the case in which different analyzed segments are combined, the SNR of the optimal estimator obtained from combining measurements from different baselines is a sum of the squared SNR for each measurement $^{(IJ)}S_i$, after n_{IJ} observation periods of duration T.

6.2.5 Likelihood in searches for the GWB

An alternative to the usual GWB cross-correlation detection method is the hybrid frequentist-Bayesian framework described in Chapter 5. It can be more advantageous because it gives the possibility to deal with arbitrary spectra of the GWB, Ω_{GW}. It is also used to corroborate results from the cross-correlation technique. The ultimate goal of this hybrid framework for GWB searches is to obtain the posterior density function (PDF).

A reduced form of the likelihood in Eq. (5.20) can be used to search for a GWB. In Ref. [106] a detailed derivation of this reduced form of the likelihood is done. The final result is given by [83]

$$L(\hat{Y}_i, \sigma_i | \underline{\theta}) \propto \exp\left[-\frac{1}{2} \sum_i \frac{(\hat{Y}_i - \Omega_M(f_i; \underline{\theta}))^2}{\sigma_i^2} \right], \qquad (6.51)$$

where the sum is run over frequency bins f_i[12]. The quantities $\hat{Y}_i$ and σ_i^2 are the estimator and variance in the frequency bin f_i, given by Eqs. (6.37) and (6.38), respectively.

In our searches we always compute the Bayes factor between the hypothesis of having a signal and the hypothesis of only having noise in the data. To obtain this Bayes factor, the likelihood for the noise-only case is required. As introduced in Ref. [107], this likelihood is given by

---

[11]These measurements have the same duration T.

[12]The analysis of the data in the cross correlation technique (see section 6.4) implies breaking the data into n segments of length $T << T_{obs}$ and carrying out the discrete Fourier transform of each segment. Each segment is thus labelled by f_i.

$$L(\hat{Y}_i, \sigma_i | \underline{\theta}) \propto \exp\left[-\frac{1}{2}\sum_i \frac{(\hat{Y}_i)^2}{\sigma_i^2}\right]. \tag{6.52}$$

The point estimate $\hat{Y}_i$ and the variance σ_i^2 are approximate sufficient statistics for ground-based searches for a GWB, as shown in Ref. [106]. Sufficient statistics is defined as the combination of data in terms of which the likelihood can be re-written without loss of information. The use of sufficient statistics can lead to a significant increase in efficiency when sampling from posteriors. Also, using the likelihood in Eq. (6.51) does not lead to an information loss compared to using the full Gaussian likelihood, Eq. (5.20).

Calibration uncertainties in the search for the GWB

Data from ground based GW detectors has to be calibrated to convert the digital output of the detector into a relative displacement of the test masses in the detectors. The calibration process has associated statistical uncertainties and systematic errors that need to be accounted for in the data analysis [108]. The systematic errors are defined as the deviation of the estimated detector response to the dimensionless strain h from the true detector response. The error is estimated by propagating the measured error of each response component of the IFO through the whole response of the IFO. The reader is referred to Ref. [109] for a detailed discussion on calibration uncertainties.

The estimation of the upper limits over the energy density in the gravitational waves spectrum has to account for the calibration uncertainties [110], as mentioned above. An optimal combination x of cross-correlated measurements provides a point estimate Y with an associated error σ. x is an estimator of λY, where λ is an unknown calibration factor described by an uncertainty ε. The likelihood is thus given by

$$p(x|Y,\lambda) = \frac{1}{\sigma\sqrt{2\pi}}\,\exp\left[-\frac{(x-\lambda Y)^2}{2\sigma^2}\right] \tag{6.53}$$

and the posterior is obtained by marginalizing over λ,

$$p(x|Y) = \int d\lambda\,p(x|Y,\lambda)p(\lambda). \tag{6.54}$$

In the case that the distribution of λ is Gaussian, the posterior is given by

$$p(x|Y) = \frac{1}{\sqrt{2\pi(\sigma^2 + \varepsilon^2 Y^2)}}\,\exp\left[-\frac{1}{2}\frac{(x-Y)^2}{(\sigma^2 + \varepsilon^2 Y^2)}\right]. \tag{6.55}$$

The calibration uncertainty varies from pair of detectors and observational runs. In O1 and O2, the calibration uncertainties were 0.072 and 0.046, respectively. In O3a, the HL pair had an associated calibration uncertainty of 0.094, the HV pair 0.089 and the LV pair 0.081. In O3b, the calibration uncertainties were 0.148, 0.123 and 0.108 for HL, HV and LV pairs, respectively.

The final result in GWB searches is the combination of the results for individual pairs of interferometers (see section 6.2.4). Each pair of interferometers has an unknown calibration factor λ_α, where α labels each detector pair. The statistical errors for each pair of interferometers are independent, so the combined likelihood is obtained by multiplying the individual likelihood for a pair of interferometers,

$$p(\mathbf{x}|Y,\boldsymbol{\lambda}) = \prod_\alpha \left\{\frac{1}{\sigma_\alpha\sqrt{2\pi}}\,\exp\left[-\frac{(x_\alpha - \lambda_\alpha Y)^2}{2\sigma_\alpha^2}\right]\right\}, \tag{6.56}$$

where Y_α and σ_α^2 are the point estimate and variance per pair of interferometers, respectively.

6.3 Power law integrated sensitivity curves

There are different methods used to describe the sensitivity of a GW detector and the strength of a GW source. As we have seen, it is common to summarise this information on a sensitivity curve plot [111], since it provides a visual indicator of the sensitivity of an instrument to potential GW sources. The simplest type of sensitivity curve is a plot of the power spectral density of the detector noise $P_n(f)$, or its amplitude spectral density, given by the square root $\sqrt{P_n(f)}$. However, these plots can be misleading, as they do not take into account the frequency dependent response to GWs [80]. A better quantity to plot is the sky and polarization-averaged amplitude spectral density $h_{\text{eff}} \equiv \sqrt{fS_{\text{eff}}(f)} = \sqrt{fP_n(f)/R(f)}$, where $R(f)$ is the response to a GW. The most common form of sensitivity curve for a GWB compares predictions of $\Omega_{GW}(f)$ to the equivalent noise energy density $\Omega_n \equiv 2\pi^2 f^3 S_n(f)/(3H_o^2)$. However, these plots do not fully capture the boost that comes from integrating over frequencies. An alternative form of sensitivity curve uses the envelope of limits that can be placed on power-law GWBs, these are the power-law integrated (PI) sensitivity curves.

The characteristic strain of a signal, $h_c(f) \equiv \sqrt{fS_h(f)}$, is compared with the PI sensitivity curve, and when it lies above the sensitivity curve, the signal is said to have an SNR>1. However, this comparison is not enough for searches of the GWB, and hence why Bayesian searches are carried out, as explained in chapter 5.

In order to explain the steps needed to obtain the PI sensitivity curves, the effective strain needs to be related to the SNR. The effective strain of a signal is related to $\Omega_{GW}(f)$ via

$$\Omega_{GW}(f) = \frac{2\pi^2}{3H_o^2} f^2 h_c^2(f), \tag{6.57}$$

obtained from substituting $h_c(f) = \sqrt{fS_h(f)}$ into Eq. (6.10). For a power law spectrum of the form $\Omega_{GW}(f) = \Omega_\beta(f/f_{ref})^\beta$, Eq. (6.57) can be written as

$$h_c^2(f) = \frac{3H_o^2}{2\pi^2} \Omega_\beta f^{\beta-2} f_{ref}^{-\beta} = A_\alpha^2 \left(\frac{f}{f_{ref}}\right)^\alpha, \tag{6.58}$$

where $A_\alpha^2 = \frac{3H_o^2}{2\pi^2} \Omega_\beta f_{ref}^{-2}$ and $\alpha = (\beta - 2)/2$, where β is the spectral index. The SNR is given by Eq. (6.29), and using Eq. (6.57) it can be expressed in terms of the GW power spectral density $S_h(f)$,

$$
\begin{aligned}
\text{SNR} =& \frac{3H_o^2\sqrt{T}}{10\pi^2} \left(\int_{-\infty}^{\infty} df \frac{\Omega_{GW}^2(|f|)\gamma_{12}^2(f)}{|f|^6 P_1(|f|)P_2(|f|)} \right)^{1/2} \\
=& \frac{3H_o^2\sqrt{T}}{10\pi^2} \cdot \frac{2\pi^2}{3H_o^2} \left(\int_{-\infty}^{\infty} df \frac{f^4 h_c^4 \gamma_{12}^2(f)}{|f|^6 P_1(|f|)P_2(|f|)} \right)^{1/2} = \frac{\sqrt{T}}{5} \left(\int_{-\infty}^{\infty} df \frac{S_h^2 \gamma_{12}^2(f)}{P_1(|f|)P_2(|f|)} \right)^{1/2},
\end{aligned}
\tag{6.59}
$$

where in the last equality this relation has been substituted $h_c^2 = fS_h$. For a network of detectors, Eq. (6.59) can be generalized to

$$
\begin{aligned}
\text{SNR} =& \frac{\sqrt{T}}{5} \left(\int_{-\infty}^{\infty} df \sum_{I=1}^{M} \sum_{J}^{M} \frac{S_h^2 \gamma_{IJ}^2(f)}{P_I(|f|)P_J(|f|)} \right)^{1/2} \\
=& \frac{\sqrt{T}}{5} \left(\int_{-\infty}^{\infty} df S_{eff}^{-2}(f)S_h^2(f) \right)^{1/2} = \frac{\sqrt{T}}{5} \left(\int_{-\infty}^{\infty} df f^2 h_{eff}^{-4} S_h^2 \right)^{1/2},
\end{aligned}
\tag{6.60}
$$

where the second equality is obtained substituting the effective strain, defined as

$$S_{\text{eff}}^{-2}(f) \equiv \sum_{I=1}^{M} \sum_{J}^{M} \frac{\gamma_{IJ}^2(f)}{P_{nI}(|f|)P_{nJ}(|f|)}. \tag{6.61}$$

The third equality in Eq. (6.60) is obtained substituting the effective strain noise amplitude $h_{\text{eff}} \equiv \sqrt{fS_{\text{eff}}(f)}$. In what follows the construction method of the PI sensitivity curves is described according to Ref. [112].

1. Considering Eq. (6.10) and the definition of the effective strain power spectral density, Eq. (6.61), $\Omega_{eff}(f)$ is defined as

$$\Omega_{eff}(f) = f^3 \frac{2\pi^2}{3H_o^2} \left(\sum_{I=1}^{M} \sum_{J}^{M} \frac{\gamma_{12}^2(f)}{P_1(|f|)P_2(|f|)} \right)^{1/2}. \tag{6.62}$$

2. An observation time T is chosen.

3. For a set of spectral indices $\beta = \{-8, -7, ...7, 8\}$ and a chosen reference frequency, Ω_β must be computed. The condition SNR=1 must be satisfied using the following equation

$$SNR = \frac{3H_o^2\sqrt{T}}{10\pi^2} \left(\int_{-\infty}^{\infty} df \sum_{I=1}^{M} \sum_{J}^{M} \frac{\Omega_\beta (f/f_{ref})^{2\beta} \gamma_{IJ}^2(f)}{f^6 P_{nI}(|f|)P_{nJ}(|f|)} \right)^{1/2} \Rightarrow \Omega_\beta = \frac{SNR \cdot 10\pi^2}{3H_o^2\sqrt{T}} \left(\int_{-\infty}^{\infty} df \frac{(f/f_{ref})^{2\beta}}{f^6 S_{eff}^2} \right)^{-1/2}$$

$$\Omega_\beta = \frac{SNR \cdot 5}{\sqrt{T}} \left(\int_{-\infty}^{\infty} df \frac{(f/f_{ref})^{2\beta}}{\Omega_{eff}^2} \right)^{-1/2}$$

$$\tag{6.63}$$

4. For each pair $\{\beta, \Omega_\beta\}$, $\Omega_{GW}(f) = \Omega_\beta (f/f_{ref})^\beta$ is plotted as a function of frequency. These lines are plotted in solid black in Figure 6.3, retrieved from Ref. [112].

5. The envelope of the curves obtained in step 4 is the PI sensitivity curve. It can be seen in solid blue in Figure 6.3.
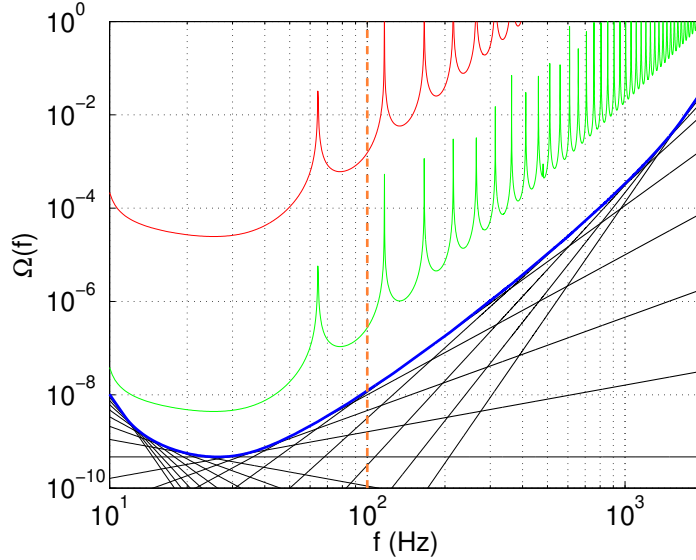
Figure 6.3: Figure retrieved from Ref. [112]. Sensitivity curves in a LIGO Hanford - LIGO Livingstone correlation search for a GWB described by a simple power law. The red curve shows the sensitivity of the pair of detectors to a GWB, where the spikes are due to zeros in the ORF of this pair. Said otherwise, it shows the effective energy density spectrum, Eq. (6.62), for the detector pair. The green curve shows the improvement in sensitivity achieved by integrating over an observation time of 1 year for a frequency bin size of 0.25Hz, i.e.: it is the red curve normalized by one year of observation. The set of black lines is obtained by integrating over frequency for different spectral indices in the power law describing the background, assuming an SNR = 1. The blue solid line is the PI sensitivity curve for T=1 year and $f_{\text{ref}} = 100Hz$, obtained as an envelope of the black solid lines. The orange dashed line represents the reference frequency.

Any spectrum tangent to the PI sensitivity curve (in log-log scale) corresponds to a GWB with SNR=1. If the spectrum lies above the PI sensitivity curve, the GWB associated has an SNR>1. More specifically, it will be observed with an SNR = $\Omega_\beta^{\text{pred}}/\Omega_\beta > 1$.

6.4 Data analysis

In this section the methodology used for the analysis of LIGO/Virgo data for the search of a GWB is detailed. The objective of a search is to obtain a point estimate, Y_α (Eq. 6.39) and an associated error, σ_α (Eq. 6.40) from which the SNR of a signal can be determined. Raw data is firstly pre-processed, which consists of downsampling the data and removing the low-frequency content. Then, to ease the computational load, data is split into intervals and these into segments over time. Then, the analysis continues in the frequency domain, where the cross-correlator is computed. Applying an optimal filter and the appropriate ORFs, the point estimate and error can finally be obtained.

The raw data measured at detector I, i.e.: data measured by detector I that has not been processed, is denoted by $s_I(t_k)$, where t_k are discrete times given by $t_k \equiv k\delta t$. The values of k are positive integers and δt is the sampling period, which is $1/(16384 \text{ Hz})$. The raw data from the two interferometers are down-sampled to 4096Hz, implying a Nyquist frequency of $f_{\text{Nyquist}} = 2048$ Hz. The Nyquist frequency is the highest frequency that can be coded at a given sampling rate to be able to fully reconstruct the signal. This means that data cannot be probed or studied above 2048Hz. This is not a limitation, since most models of sources of the GWB predict signals peaking at lower frequencies. Furthermore, the low-frequency content of the spectrum (below 10Hz) is louder than the frequencies of interest (between 20-1726Hz [21]) due to quantum and Newtonian noise (see section 2.3). For this reason, frequencies below 11Hz are removed from the data. It is customary to say that data is high pass filtered. At this point, data is said to be pre-processed (see Figure 6.4).
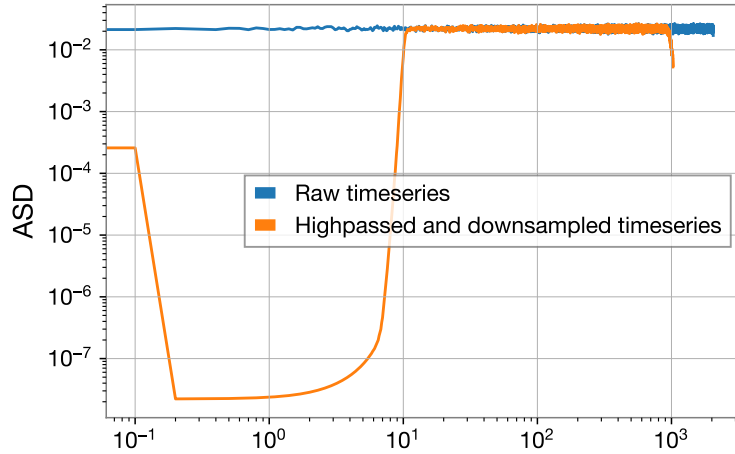
Figure 6.4: Comparison between the raw data (blue solid line) and the preprocessed data (orange solid line). Preprocessing consists on downsampling the data to 4096Hz and then removing the low frequency content, below 10Hz.

The next step consists of preparing the data to compute the cross-correlation between the data from two interferometers. Data is split into intervals and within each interval, it is split into segments over time to deal with the detector non-stationarity (see Figure 6.5). Given that the detection method described in previous sections assumes a stationary background, splitting the data into small segments allows to maintain an approximate stationarity. The segment duration must be much larger than the light travel time between interferometers but short enough to yield a sufficient number of cross-correlation measurements within each interval. In O3 each segment's length was 192s. The interval duration is dependent on the detector status, i.e.: whether it is taking data or not and whether there are glitches (noise that could mimic a GW). After these periods are removed from the analysis, the intervals' durations are set, which do not necessarily have to be of the same length. The combination of different segments is done with a weighted average (see Eq. (6.39)), with inverse variances as weights, and hence the difference in length between segments does not pose a problem for the analysis.
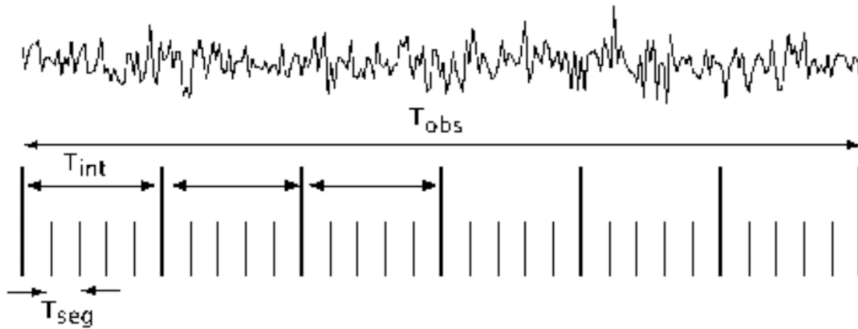
Figure 6.5: Figure retrieved from Ref. [113]. Example of data stream and how it is split to perform the cross correlation. The entire observation period is represented by T_{obs}. The data is then divided into intervals of duration T_{int} to ease the computational load. Each interval is then divided into segments of duration T_{seg}. In the O3 isotropic analysis, the values of T_{seg} was 192s.

The analysis then proceeds in the Fourier domain. To do this, a discrete Fourier transform of each segment is performed. However, large deviations of the data from a mean value could lead to spectral leakage in the Fourier transform. The FFT takes a signal and breaks it down into sine waves of different amplitudes and frequencies. However, the FFT has limitations. The FFT assumes a continuous spectrum that is one period of a periodic signal. In this case, the FFT turns out fine. Nevertheless, on most occasions, the signal is not an integer number of periods. Therefore, the finiteness of the signal results in a truncated waveform with different characteristics from the original signal and sharp transition changes. These sharp transitions are discontinuities that appear in the FFT as high-frequency components not present in the original signal. It appears as though energy at one frequency leaks into other frequencies, hence why this phenomenon is known as *spectral leakage*. To avoid these artifacts, each segment is Hann-windowed, which zeroes the beginning and end of the segment. The "windowing" method consists of multiplying the signal by a function (*window*) whose amplitude decreases slowly towards zero at the edges. This will effectively reduce the amplitude of the discontinuities in the signal. There are different types of windows. The most commonly used is the Hann window since it works when the nature of the signal is unknown. This procedure loses part of the data, so an overlap of 50% between segments is performed, which tapers to zero for roughly half of the data in a segment. For this reason, to avoid losing the first 25% and last 25% of the data from a segment due to windowing, we compensate by overlapping the segments by 50%. Now that each segment from the data is Fourier transformed, a cross-correlation estimator per segment can be computed according to Eq. (6.33). The optimal filter, $Q_\alpha(f)$, is calculated according to Eq. (6.34).

Then, before computing the final point estimate and associated error, some data quality cuts are performed, both in the time and frequency domain. These cuts allow discarding segments that show non-stationarity or extremely loud glitches. In the time domain, the power fluctuations or σ_Y between segments are compared. It is imposed that the difference in σ_Y between adjacent segments is lower than 20%. If the difference is larger, the middle segment is discarded from the analysis. Effectively, the condition that segment J needs to satisfy in order to be discarded is $[(\sigma_J - \sigma_{J-1}) + (\sigma_J - \sigma_{J+1})]/(2\sigma_J) > 0.2$. This is a way of detecting glitches that may impact the data and removing the corresponding segments. This non-stationarity cut is commonly known as the *delta sigma cut*. With this cut, about 4-5% of the data is lost. This non-stationarity cut is repeated for different spectral indices since each power law is sensitive to a different frequency band. More specifically, $\alpha = \{-5, 0, 3, 5\}$. The delta sigma cut checks for noise fluctuations at high frequencies for the high positive index 5, and is therefore complementary to the delta sigma cut that uses a smaller index, such as 0 or -5, which checks for fluctuations at lower frequencies, see Figure 6.6. Studies have been performed that show that using only $\alpha = \{0, 3\}$ is not enough to remove high SNR lines at low frequencies, below 30Hz[13]. However, $\alpha = -5$ does remove them. A union of all the segments discarded for each α is done leading to a full list of segments to discard from the analysis.

---

[13]Work described in the following internal reference: https://stochastic-alog.ligo.org/aLOG/index.php?callRep=339959
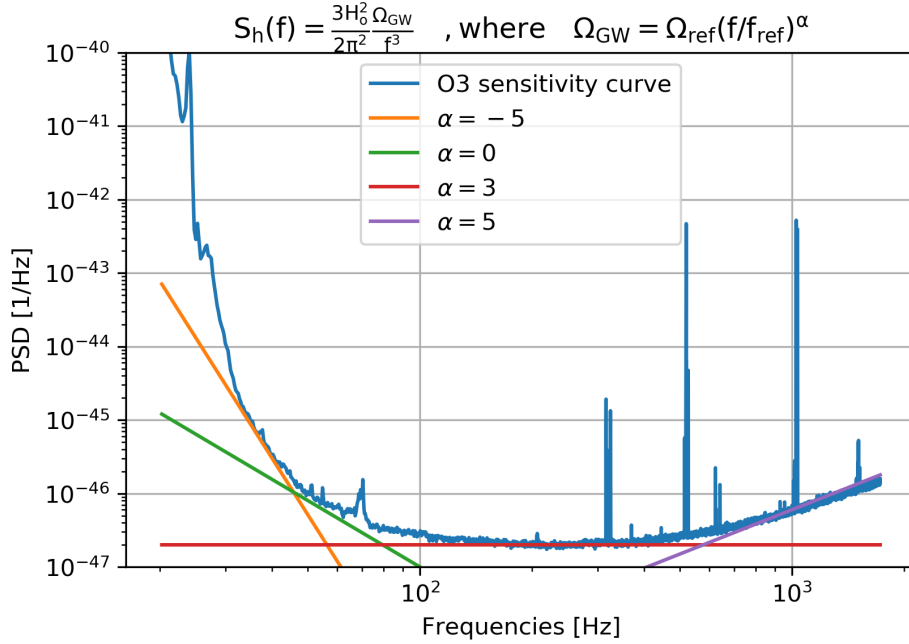
Figure 6.6: In this plot, different power laws are compared to the O3 sensitivity curve of LIGO-Livingstone. Each power law is sensitive to a different frequency band. This makes necessary repeating the delta sigma cut for different α. The O3 sensitivity curve for LIGO-Livingstone was retrieved from Ref. [114].

In the frequency domain, peaks in the spectrum due to different sources of noise are removed from the analysis (see section 2.3). This procedure is known as *notching*, and it removes about 10% of the data. To identify these correlated instrumental lines in frequency domain, a time shifted analysis is performed, which consists on shifting by one second the time-series output of one detector relative to that of the other before doing the cross correlation analysis. This way, broadband GW correlations are eliminated while preserving narrowband noise features [11]. In O3, a high rate of very loud broadband glitches appeared in the data. Using the delta sigma cut would have removed them, but more than 50% of the data would have been lost [56]. For this reason, an alternative method was used, called gating [56, 115]. Gating consists of substituting stretches of data with excess noise by zeroes [56]. Further information on the method is provided in Ref. [115]. In Ref. [56] we analyzed whether the effect of analyzing data with zeros is small. Then we checked whether this method introduced artifacts in the data such as frequency lines. Finally, we made sure that the gating procedure does not remove real GW events. Our stochastic analysis of non-gated data versus gated data shows that there is only a difference within one sigma in the estimated point estimate and the error bar only shifts about 1%. Also, we checked that none of the GW events detected in the first half of O3 [116] were gated.

The final point estimate is obtained by combining the point estimates per segment, Eq. 6.39, and the associated error is obtained by also combining the errors per segment, Eq. 6.40. From these results, the SNR can be obtained, which will help in the decision of whether to claim a signal.

6.4.1 Correlated noise: Schumann resonances

Correlated noise is a limitation to the detection of stochastic signals given that their detection is based on a correlation method. If the spectral shape of either, or both, the noise and the signal were known, it would be possible to separate them. There are some sources of correlated noise, such as correlations between the electronics mains (60Hz in LIGO and 50Hz in Virgo) and correlations from the fact data sampling is referenced to clocks of the GPS system [80]. The most worrying cause of correlated noise is Schumann resonances. They are caused by lightning strikes that remain within the ionosphere of the Earth and thus become common for all IFOs. Schumann resonances are electromagnetic excitations at

low frequencies (<50Hz) [117]. These resonances can produce coherent oscillations in magnetometer readings at the GW ground-based detectors. They are expected to couple via the mirror suspension systems, electric cables, and electronics.

In order to estimate the potential presence of Schumann resonances in the LIGO-Virgo data from the first three observing runs, the methodology from Refs. [118, 119] has been followed, where a noise budget for the magnetic correlations was created [21]

$$\hat{C}_{\text{mag},IJ}(f) = \frac{2}{T} \frac{|T_I(f)||T_J(f)|\text{Re}[\tilde{m}_I^\star(f)\tilde{m}_J(f)]}{\gamma_{IJ}(f)S_0(f)}. \tag{6.64}$$

The functions $\tilde{m}_I(f)$ are Fourier transforms of the magnetometer channels, the functions $T_I(f)$ are the magnetic coupling functions, and γ_{IJ} is the ORF between interferometers I and J. The magnetic coupling functions were estimated by injecting an oscillating magnetic field of a known frequency and amplitude at different locations near each detector and measuring the effect in the GW strain channel [21]. Figure 6.7 shows an estimate of the correlated magnetic noise compared to the O3 sensitivity curve. The red band shows the combined budget obtained from weekly magnetic coupling function measurements. It is compared with the O3 power-law integrated curve (red solid line) introduced in section 6.3. The black dotted line shows the upper range of the magnetic budget. If compared with the black solid line, which shows the sensitivity to a GWB in every frequency bin, it is way below. This implies that measurements show no evidence for correlated magnetic noise.
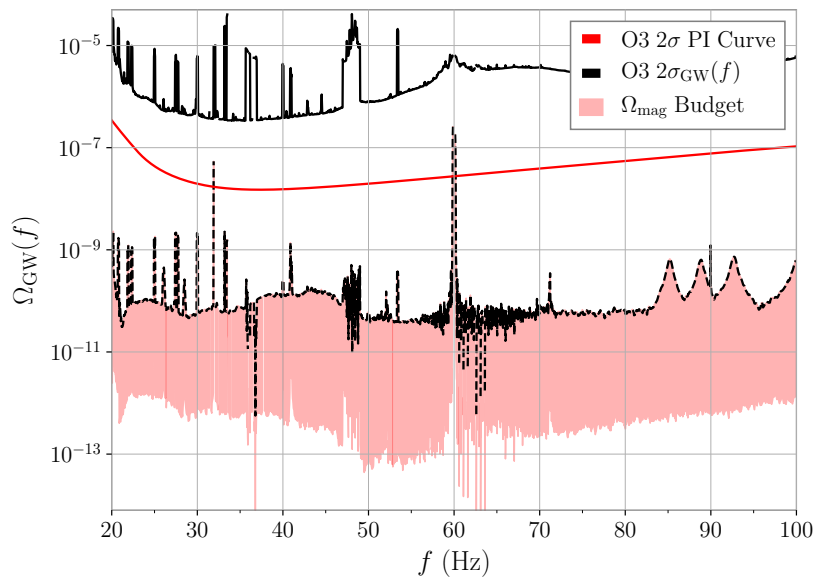
Figure 6.7: Image retrieved from Ref. [21]. The red band is an estimate of the correlated magnetic noise compared to the O3 sensitivity curve (black solid line). This magnetic budget is obtained from weekly magnetic coupling function measurements. It is compared with the O3 power-law integrated curve (red solid line). The black dotted line shows the upper range of the magnetic budget, which lies below the black solid line (sensitivity to a GWB in every frequency bin).

However, the estimated spectrum from Schumann resonances is above the design sensitivity and hence the need to develop a robust method by which to distinguish in future runs whether a potential correlated signal is due to Schumann resonances or is indeed a GWB signal. This method has already been developed, gravitational wave geodesy, and is explained in what follows.

Gravitational wave geodesy

A tool for separating spurious and/or terrestrial signals from a stochastic background is the gravitational wave geodesy (GW-geodesy) [120]. It is based on the same idea as radio geodesy: a true GW detection allows to infer the position and orientation of an interferometer, so by demanding

that a GW background detection is consistent with the well-known geometry of the interferometer, the spurious signals can be separated from the real GW background. There are some sources of noise that can be correlated between interferometers, such as Schumann resonances (described in the previous subsection) and the synchronization of electronics (placed in each interferometer) to GPS time.

The expectation value of the cross-correlation spectrum is given by the energy density spectrum times the overlap reduction function (ORF), which contains information on a detector baseline geometry. Consequently, cross-correlation measurements between data from two detectors can give information about the baseline's geometry. If the estimated geometry is not the right one, this implies that the data is polluted by correlated noise. Given a potential detection, a way of determining whether it is polluted is by computing the Bayes factor between the hypothesis that the measured cross-correlation is consistent with the baseline's geometry against the hypothesis that it is not consistent. For each hypothesis, the model used is a simple power law times the true ORF, and an ORF dependent on parameters defining possible geometries of the baseline, respectively. This method can be used not just to discard correlated noise but also to bolster the confidence of a gravitational wave background detection. In Refs. [120, 121], the authors probe the validity of the method, which will prove crucial, once the GWB is detected, to differentiate between a real signal and correlated noise.

6.5   Isotropic analysis

The LIGO-Virgo Collaboration has previously placed upper limits on the isotropic GWB using data from the first two observing runs [122]. In the O3 isotropic analysis [21] we do the same but include O3 data and an extra interferometer, Virgo. In the past, only one baseline was used, HL, while now three baselines enter the analysis, HL, HV, and LV. O1 and O2 are considered as two datasets, while O3 was divided into two periods. The period from the 1st of April 2019 to the 1st of October 2019 is known as O3a. O3b is the period from the 1st of November 2019 to the 27th of March 2020. The cross-correlation technique introduced in section 6.2 was used to compute the cross-correlation spectrum. For cross-correlation to be applied, both detectors must be in science mode and no critical issues must exist.

The optimal estimator for a given signal includes both, auto-correlation (the noise power spectral densities used to compute the point estimate $\hat{Y}$, Eq. (6.43), are computed by auto-correlating the noise of each detector) and cross-correlation. However, in the isotropic search only the cross correlation is used, since the noise power spectral density is not well known so as to be subtracted accurately. An optimal estimator to search for a GWB is obtained by combining the cross correlation spectra from different frequency bins,

$$
\begin{aligned}
\hat{C}^{IJ} &= \frac{\sum_k w(f_k)\hat{C}^{IJ}(f_k)\sigma_{IJ}^{-2}(f_k)}{\sum_k w(f_k)^2 \sigma_{IJ}^{-2}(f_k)}, \\
\sigma_{IJ}^{-2} &= \sum_k w(f_k)^2 \sigma_{IJ}^{-2}(f_k),
\end{aligned}
\tag{6.65}
$$

with appropriate weights given by

$$
w(f) = \frac{\Omega_{GW}(f)}{\Omega_{GW}(f_{\text{ref}})}.
\tag{6.66}
$$

The values f_k are a discrete set of frequencies. The reference frequency is $f_{\text{ref}} = 25 Hz$ because that is approximately the beginning of the sensitive band for the isotropic search in the LIGO-Virgo interferometers. Eq. (6.66) shows that the analysis can be done for any choice of the spectrum. In the O3 isotropic search, the GWB is described by the simple power law in Eq. (6.30). Finally, information from all three baselines is optimally combined in the correlator defined in Eq. (6.48) with associated variance given by Eq. (6.49).

The vetoes introduced in Ref [123] were applied on the data. With these vetoes, stretches of data containing instrumental features and artifacts that could affect the estimated SNR were removed from the analysis. It must be noted that the observed CBCs were not removed from the data, even though they contribute to the cross-correlation. The reason is that in Ref. [21] it has been calculated that the strength of the background is lower than 10^{-10}, which is way below the O3 sensitivity curve. This value was estimated by using the median values for the masses and redshifts in O3a from Ref. [116], the livetime for O3a and the inspiral approximation in Eq.(16) from Ref. [124].

Then, the analysis described in section 6.4 was performed. Figure 6.8 shows the estimated cross correlation as a function of frequency in the range of study mentioned in section 6.4 (20-1726Hz). This correlation is represented by the blue line, and it has an associated error plotted by the solid black lines. It can be seen that the point estimate (or cross correlator) fluctuates roughly symmetrically around zero, which is consistent with what is expected from Gaussian noise, and hence indicating no GWB is detected. At 60Hz the correlation is very high due to the existence of the power mains in the US, which affect LIGO-Hanford and LIGO-Livingston.
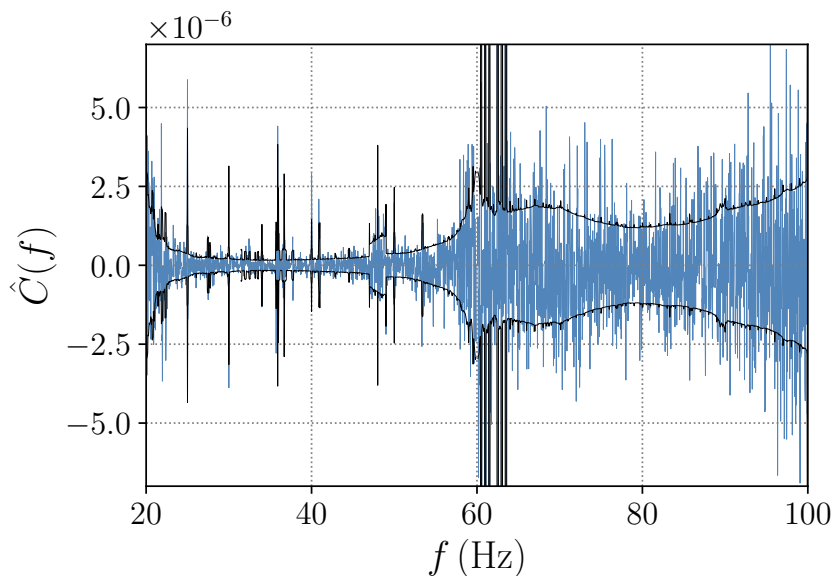
Figure 6.8: Image retrieved from Ref. [21]. Cross correlation estimator obtained by combining the data from the three baselines in O3 and data from the HL baseline in O1 and O2.

Given that the estimated cross correlator shows no evidence for a signal, upper limits were set on the strength of the background. The hybrid Bayesian-frequentist framework introduced in chapter 5 was used to compute the ULs without fitting for an extra contribution from Schumann resonances. The ULs at 95% CL were obtained for different priors on Ω_{ref} and α [14]. The priors on Ω_{ref} are uniform and log uniform. A log uniform prior gives equal weights to different orders of magnitude of Ω_{ref} and it is agnostic on α. A uniform prior leads to more conservative ULs, so that is why results using this prior are also presented. The lower bound in the prior on Ω_{ref} is chosen to be 10^{-13}, following Ref. [122]. The priors on α are fixed values $\{0, 2/3, 3\}$ or Gaussian with zero mean and standard deviation given by the width of the prior divided by 2, which results in 3.5.

The posteriors on Ω_{ref} and α for a log uniform prior in Ω_{ref} and a Gaussian prior on α are in Figure 6.9.

---

[14]To perform model selection and parameter estimation, in our searches we use `pyMultinest` [125], a Python-based software that uses `MultiNest` [126], an implementation of the nested sampling algorithm [82]. `MultiNest` allows introducing several model parameters and the number of live points to sample the prior volume. The optimal number of live points we use in different searches is 2000 [107]. `pyMultinest` also estimates the error associated with the evidences.

The posterior on α keeps the Gaussian shape of the prior. The posterior on Ω_{ref} allows to obtain the UL at 95% CL shown in Table 6.1, 6.6×10^{-9}.
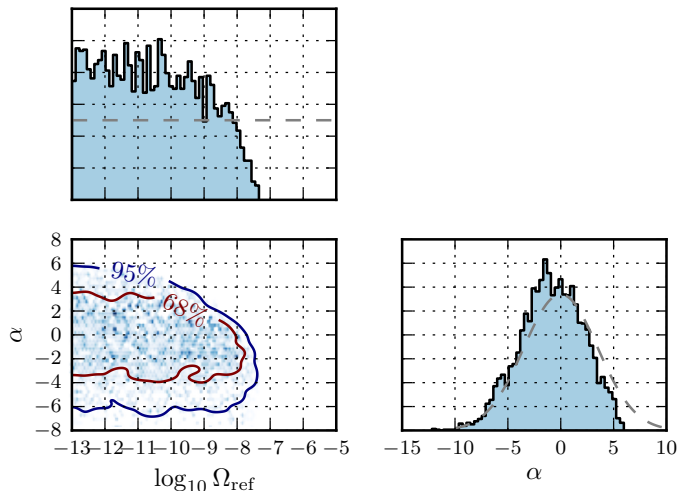
Figure 6.9: Image retrieved from Ref. [21]. Posteriors distributions on Ω_{ref} and α for a log uniform prior in Ω_{ref} and a Gaussian prior on α. The posterior on α keeps the shape of the prior. The posterior on Ω_{ref} allows to obtain the UL shown in Table 6.1

Table 6.1 also contains the ULs for all the other runs. The last two columns show the improvement in the ULs with respect to those set from the first two observing runs [122]. The overall improvement in all runs of O3 is due to the addition of another interferometer, Virgo. The big improvement of 13 in the UL obtained for a prior in $\alpha = 3$ is due to the improved high-frequency sensitivity in O3.

Upper limits at 95% CL over the strength of the GWB for a reference frequency of 25Hz				
	Log uniform prior on Ω_{ref}	Uniform prior on Ω_{ref}	UL O3/ UL O2 (Log uniform)	UL O3/ UL O2 (Uniform)
Delta prior on $\alpha = 0$	5.8×10^{-9}	1.7×10^{-8}	6.0	3.6
Delta prior on $\alpha = 2/3$	3.4×10^{-9}	1.2×10^{-8}	8.8	4.0
Delta prior on $\alpha = 3$	3.9×10^{-10}	1.3×10^{-9}	13.1	5.9
Gaussian prior on α	6.6×10^{-9}	2.7×10^{-8}	5.1	4.1

Table 6.1: Upper limit at 95% CL over Ω_{ref} for different priors on Ω_{ref} and α. The last two columns show the improvement in the ULs obtained with respect to the analysis done in O2 [122].

The formalism introduced in chapter 5 was again used to search for a GWB in addition to correlated magnetic noise. The resulting Bayes factor between a model hypothesis containing magnetic noise and a hypothesis of only Gaussian noise is $\log \mathcal{B}_{\mathrm{Gaussian}}^{\mathrm{Magnetic}} = 0.03$, which shows no evidence for correlated magnetic noise.

The ULs on the GWB amplitude have implications in the GWB due to CBCs. The three classes of CBCs are considered, BBHs, BNSs and NSBHs and the energy density spectra from each of these contributions is computed, $\Omega_{\mathrm{BBH}}(f)$, $\Omega_{\mathrm{BNS}}(f)$ and $\Omega_{\mathrm{NSBH}}(f)$, respectively (the reader is referred to Ref. [21] for further details). The estimate of $\Omega_{\mathrm{BBH}}(f)$ is shown in green in Figure 6.10. It was found that at the reference frequency of 25Hz $\Omega_{\mathrm{BBH}}(25\mathrm{Hz}) = 5.0^{+1.7}_{-1.4} \times 10^{-10}$. The estimate of the BNS GWB is shown in red in Figure 6.10 and the value at 25Hz is $\Omega_{\mathrm{BNS}}(25Hz) = 2.1^{+2.9}_{-1.6} \times 10^{-10}$. Finally, no NSBH has been detected yet, so an UL on $\Omega_{\mathrm{NSBH}}(f) \leq 8.4 \times 10^{-10}$ is set and is shown as a dashed black line in Figure 6.10. In the right-hand side of Figure 6.10 the estimate of the combined GWB due to BBH and BNS mergers is presented. At 25Hz $\Omega_{\mathrm{BBH+BBS}}(25\mathrm{Hz}) = 7.2^{+3.3}_{-2.3} \times 10^{-10}$. By combining the ULs on $\Omega_{\mathrm{NSBH}}(f)$ with the ULs at 95% CL from BBH and BNS mergers, an overall UL over the

total expected GWB from CBCs is set to $\Omega_{\mathrm{CBC}}(25\mathrm{Hz}) = 1.9 \times 10^{-9}$. The PI curve (see section 6.3) for O3 is shown (solid black line in the plot to the right of Figure 6.10) at 2σ as well as the projection for the 2 years of Advanced LIGO-Virgo at design sensitivity (dashed grey line) and the expected A+ design sensitivity after 2 years. The plot to the right of Figure 6.10 shows that if the detector reached the A+ design sensitivity, part of the parameter space of the GWB from CBCs could be probed.
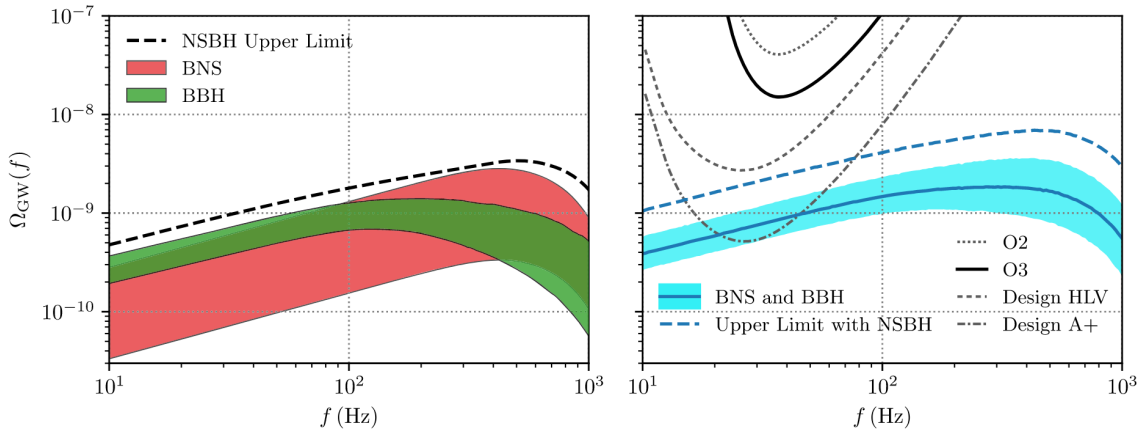

Figure 6.10: Image retrieved from Ref. [21]. Fiducial model predictions for the GWB from BBHs, BNSs, and NSBHs, compared to the current and projected sensitivity curves. **Left** 90% credible bands for the GWB contributions from BNS (pink) and BBH (green) mergers. The pink band shows the statistical uncertainties in the BNS merger rate. The green band not only shows the uncertainty in the BBH merger rate but also includes systematic uncertainties in the binary mass distribution. Given that no detections of NSBH systems have been made, an upper limit on their possible contribution is set (black dashed line). **Right** Comparison of the energy density spectra from BBHs and BNSs (shaded blue region) with the PI sensitivity curves from O2 (dotted grey line), O3 (black solid line), and the expected design sensitivity curves. The solid blue line shows the median estimate of $\Omega_{\mathrm{BBH+BNS}}(f)$ and the shaded blue region shows the 90% credible uncertainties. The dashed blue line represents the projected upper limit on the total GWB.

Another important feature of the cross-correlation analysis is that it provides indirect information on the CBC population at large redshifts z. It is complementary to the information from population analysis using individually detectable events. Constraints on the merger rate as a function of redshift for binary black holes (BBHs) were obtained [21]. By combining direct detections of CBCs (from the GWTC-2 catalog [116]) with the UL on the GWB from CBCs seen in Figure 6.10, the BBH merger rate $R_{\mathrm{BBH}}(z)$ can be measured. The result of the analysis is plotted in Figure 6.11. The constraints at 90% CL on the BBH merger rate as a function of redshift is represented by the grey solid line. From O1 and O2 data, the UL on the BBH merger rate was $\sim 10^4 \mathrm{Gpc}^3\mathrm{yr}^{-1}$ beyond $z \simeq 2$ at 90% credibility [127], meaning that the O3 analysis has improved this limit by a factor of approximately ten [21].

6.5.1 Polarized GWB

Some cosmological sources can create a parity violation, leading to the generation of circularly polarized GWs. Some examples of these are the Chern-Simons gravitational term [128], axion inflation [129] and turbulences from FOPTs [130]. The circular polarization degree describes the asymmetry between the amplitude of the right and left-handed GWs, and measuring this degree in the GWB could lead to the detection of parity violation [131]. The basis for the transverse traceless tensor is given by $\{e^+, e^x\}$ (see Appendix A), expressed in terms of the unit vectors $\hat{e}_\theta$ and $\hat{e}_\phi$, perpendicular to $\hat{n}$, the direction of propagation of the wave. Alternatively, another basis given in terms of the right and left-handed polarization can be used $\{e_R \equiv (e^+ + ie^x)/\sqrt{2}, e_L \equiv (e^+ - ie^x)/\sqrt{2}\}$. The corresponding amplitudes of the GW are given by

$$h_R = \frac{h_+ - ih_x}{\sqrt{2}} \quad ; \quad h_L = \frac{h_+ + ih_x}{\sqrt{2}}. \tag{6.67}$$

The 2-point correlation function for right and left-handed waves is given by [132]
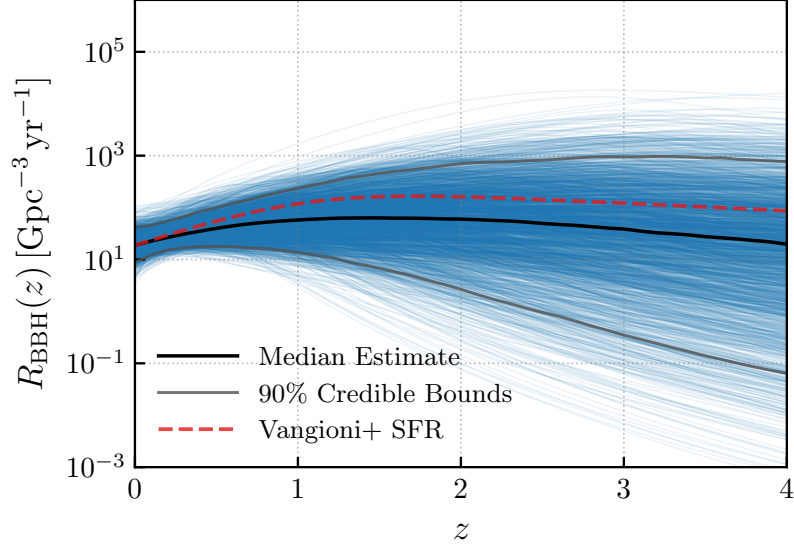
Figure 6.11: Figure retrieved from Ref. [21]. BBH merger rate $R_{BBH}(z)$ measured by combining direct detections of CBCs (GWTC-2 catalog [116]) with the UL on the GWB from CBCs. The constraints at 90% CL is represented by the grey solid line. Each blue line is a draw from the posterior on the BBH mass distribution and merger rate history. The median is represented by the black solid line.

$$\begin{pmatrix} \langle h_R(f,\hat{\Omega})h_R^*(f',\hat{\Omega}')\rangle \\ \langle h_L(f,\hat{\Omega})h_L^*(f',\hat{\Omega}')\rangle \end{pmatrix} = \frac{\delta(f-f')\delta(\hat{\Omega}-\hat{\Omega}')}{4\pi} \begin{pmatrix} I(f,\hat{\Omega}) + V(f,\hat{\Omega}) \\ I(f,\hat{\Omega}) - V(f,\hat{\Omega}) \end{pmatrix}. \tag{6.68}$$

For two right polarized waves, the strain power will be higher than for two left ones [133]. The real function V characterizes the asymmetry between the two amplitudes h_R and h_L, while I, positive definite, represents their total amplitude. A similar procedure to the one followed in section 6.1 is followed to obtain the expression for the energy density in GWs with circular polarization [133]

$$\Omega_{GW}(f) = \frac{f}{\rho_{c,o}} \cdot \frac{d\rho_{GW}}{df} = \frac{\pi f^3}{G\rho_{c,o}} I(f). \tag{6.69}$$

Note that the energy density spectrum is only dependent on I(f). The expectation value of the cross correlation estimator for a polarized background is

$$\langle \hat{Y} \rangle = \frac{3H_o^2 T}{10\pi^2} \int_0^\infty \frac{\Omega'_{GW}(f)\gamma_I(f)Q(f)}{f^3}, \tag{6.70}$$

obtained following a similar procedure to the one in section 6.2 [133]. The expectation value $\langle \hat{Y} \rangle$ has an associated variance given by

$$\sigma^2 = \frac{T}{4} \int_0^\infty df P_1(|f|)P_2(|f|)|Q(f)|^2. \tag{6.71}$$

The optimal filter is given by $Q(f_i) = \mathcal{N} \frac{\gamma_I(f_i)}{f_i^3 P_1(f_i)P_2(f_i)}$, where i represents each frequency bin from the analysis and $\mathcal{N}$ is chosen so that $\langle \hat{Y}_i \rangle = \Omega_o$. [15]

In Eq. (6.70), $\Omega'_{GW}(f)$ is given by

$$\Omega'_{GW}(f) = \frac{\Omega_{GW}(f)}{\gamma_I(f)}[\gamma_I(f) + \Pi(f)\gamma_V(f)], \tag{6.72}$$

where $\Pi(f) \equiv V(f)/I(f)$, and the ORFs are given by [131]

---

[15] This is assuming a constant energy density spectrum $\Omega_{GW}(f) = \Omega_o$.

$$\gamma_I(f) = \frac{5}{8\pi} \int d\hat{\Omega}[F_1^+(F_2^+)^* + F_1^x(F_2^x)^*]e^{2\pi i f\hat{\Omega}\cdot\Delta\mathbf{x}/c},$$
$$\gamma_V(f) = -\frac{5}{8\pi} \int d\hat{\Omega}i[F_1^+(F_2^x)^* + F_1^x(F_2^+)^*]e^{2\pi i f\hat{\Omega}\cdot\Delta\mathbf{x}/c}. \tag{6.73}$$

The spectrum $\Omega'_{GW}(f)$ can be thought of as the usual energy density spectrum distorted by the parity violation corrected ORF, $1 + \Pi(f)\gamma_V(f)/\gamma_I(f)$. The function $\Pi(f)$ has values within $[-1, 1]$, being $\Pi(f) = 1$ for a right fully polarized background and $\Pi(f) = -1$ for a left fully polarized one. The ORF $\gamma_I(f)$ coincides with the ORF in the non-polarized case, Eq. (6.20). In the case that there is no circular polarization, that is, there is no asymmetry between h_R and h_L, $V(f) = 0$. This way, the non-polarized equations are recovered; Eq. (6.70) turns into Eq. (6.21) and $\Omega'_{GW}(f)$ into $\Omega_{GW}(f)$. Eqs. (6.73) are plotted for different baselines in Figure 6.12 (left), obtained from Ref. [133]. γ_V differs from γ_I in amplitude at low frequencies.
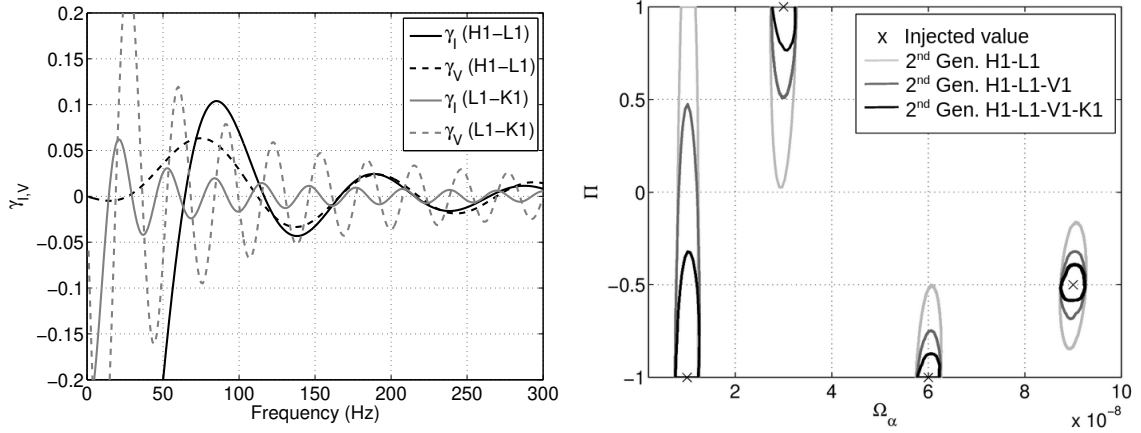
Figure 6.12: Figures retrieved from [133]. **Left** Polarized overlap reduction function for H1-L1 (black lines) and L1-K1 (grey lines). The solid lines represent γ_I and dashed lines γ_V. **Right** Recovery of a polarized injected GWB in the $\Pi - \Omega_\alpha$ plane. The lightest-gray line shows the recovery with a confidence interval of 95% with the H1-L1 baseline, the medium-gray line to the recovery with H1-L1-V1, and the black line to the recovery with H1-L1-V1-K1 [133]

In this polarized case, $\langle\hat{Y}\rangle$ is interpreted as the energy density modified by the polarized ORF. For this reason, when running a Bayesian search, the likelihood in Eq. (6.51) is modified to [133]

$$L(\hat{Y}_i, \sigma_i|\vec{\theta}) \propto \exp\left[-\frac{1}{2}\sum_i \frac{(\hat{Y}_i - \Omega'_M(f_i;\vec{\theta}))^2}{\sigma_i^2}\right], \tag{6.74}$$

where the model used is given by the energy density in GWs modified by the parity violation corrected ORF, $1 + \Pi(f)\gamma_V(f)/\gamma_I(f)$. Parameter estimation will be more accurate as the network of interferometers increases. Figure 6.12(right) shows how the credible level at 95% reduces in size as new detectors are added to the network.

6.5.2 GWB with non-GR polarizations

The GWB can be used as a test of GR. As explained in Chapter 1, GWs are predicted to have two tensor polarizations, cross and plus. However, a more general metric theory of gravity could have up to six polarizations. The extra polarizations are two vectors, x and y, and two scalar polarizations, breathing and longitudinal [107]. Figure 6.13, retrieved from Ref. [107], shows the effect of all six polarizations on a ring of freely-falling test particles. The existence of six polarizations would recquire a network of at least six IFOs to uniquely determine the polarization of the GWB.

Some sources are believed to be capable of generating a GWB with extra polarizations, such as core-collapse supernovae [134], CBCs [135], cosmic strings [136] and bubble walls from FOPTs [137].

Figure 6.13: Figure retrieved from Ref. [107]. Effect of all six polarizations on a ring of freely-falling test particles. Each wave propagates in the z direction. GR allows for two tensor polarizations, plus and cross, while more general theories allow for four extra polarizations. These are two vector polarizations, x and y, and two scalar polarizations, breathing and longitudinal.

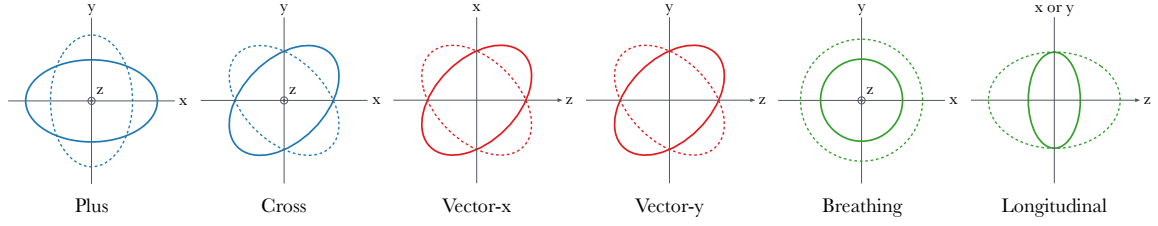Discovering non-tensorial modes would imply that gravity is not only explained by GR. Not detecting the extra polarizations could help to experimentally constrain general metric theories of gravity. The current detectors are limited to determining the polarization of transient GWs directly. However, the GWB would allow to directly measure the polarization of the GWs. Searches for a non-tensor polarized GWB have been performed in recent years following the methods from Ref. [107]. The tensor, vector, and scalar polarizations are assumed to be uncorrelated and individually unpolarized. For this reason, the average of the cross-correlation estimator $\langle \hat{C}(f) \rangle \propto \langle \tilde{s}_1^*(f) \tilde{s}_2^*(f) \rangle$ can be expressed as a sum of three terms due to each polarization mode

$$\langle \hat{C}(f) \rangle = \sum_{a=\{T,V,S\}} \delta(f - f') \gamma_a(f) H^a(f), \tag{6.75}$$

where $H^a(f)$ is the spectral shape of the GWB for each polarization mode and $\gamma_a(f)$ is the ORF for each polarization, i.e.: the response each baseline has for each polarization mode. The cross correlation statistic is normalized such that $\langle \hat{C}(f) \rangle = \sum_{a=\{T,V,S\}} \gamma_a(f) \Omega^a(f)$ and the variance is $\sigma^2(f) = \frac{1}{2Tdf} \left(\frac{10\pi^2}{3H_0^2} \right)^2 f^6 P_1(f) P_2(f)$. Combining these results, it can be shown that the SNR is given by [107]

$$\mathrm{SNR}^2 = \frac{\left(\hat{C} \,|\, \gamma_a \Omega_M^a \right)^2}{\left(\gamma_b \Omega_M^b \,|\, \gamma_c \Omega_M^c \right)}, \tag{6.76}$$

where $\Omega_M^a(f)$ is the chosen model for the energy density spectrum in GWs, which is usually a simple power law (Eq. (6.30)). The inner product defined by Eq. (6.24) is used in Eq. (6.76). The SNR is maximised when $\Omega_M^a(f)$ coincides with the true GWB's energy density spectrum

$$\mathrm{SNR}^2_{\mathrm{OPT}} = (\gamma_a \Omega^a \,|\, \gamma_b \Omega^b). \tag{6.77}$$

Following the Bayesian search introduced in Ref. [107] and described in chapter 5, we set upper limits over the energy density spectrum in GWBs for different polarizations. We assume different scenarios. First of all, the GWB is assumed to be composed of one single polarization mode. It is described by a simple power-law with a reference frequency $f_{\mathrm{ref}} = 25\mathrm{Hz}$. The parameters of each model are the amplitude of the background at the reference frequency Ω^a_{ref} and the spectral index α_a, where a represents each of the polarizations, $a = \{T, V, S\}$. A log uniform prior over the energy density spectrum is used, ranging from 10^{-13} to 10^{-5}. A Gaussian prior centered in 0 over α is used. The standard deviation is $7/2$, following the choice introduced in section 6.5. The one single polarization mode cases are:

- Only tensor polarized GWB: $\Omega_T(f) = \Omega^T_{ref} \left(\frac{f}{f_{ref}} \right)^{\alpha_T}$. The resulting posterior distributions on the parameters $\{ \Omega^T_{ref}, \alpha_T \}$ are in Figure 6.14. The posterior on the energy density spectrum allows to obtain an upper limit at 95% CL of 7.66×10^{-9}.

- Only vector polarized GWB: $\Omega_V(f) = \Omega^V_{ref} \left(\frac{f}{f_{ref}} \right)^{\alpha_V}$. The resulting posterior distributions on the parameters $\{ \Omega^V_{ref}, \alpha_V \}$ are in Figure 6.15(left). The posterior on the energy density spectrum allows to obtain an upper limit at 95% CL of $\Omega^V_{\mathrm{ref}} = 6.13 \times 10^{-9}$.

- Only scalar polarized GWB: $\Omega_S(f) = \Omega_{ref}^S \left(\frac{f}{f_{ref}} \right)^{\alpha_S}$. The resulting posterior distributions on the parameters $\{\Omega_{ref}^S, \alpha_S\}$ are in Figure 6.15(right). The posterior on the energy density spectrum allows to obtain an upper limit at 95% CL of $\Omega_{ref}^S = 1.68 \times 10^{-8}$.

Figure 6.14: Posterior distributions of the parameters from the tensor polarized model $\{\Omega_{ref}^T, \alpha_T\}$. The 95% and 68% CL contours are shown in the $\Omega_{ref}^T - \alpha_T$ plane. The recovered posterior on alpha is very similar to the prior used.
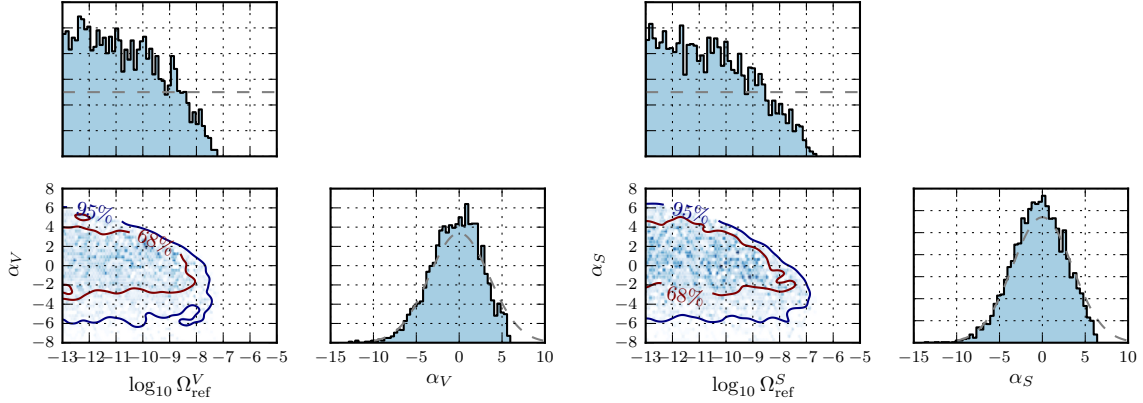
Figure 6.15: **Left** Posterior distributions of the parameters from the vector polarized model $\{\Omega_{ref}^V, \alpha_V\}$. The 95% and 68% CL contours are shown in the $\Omega_{ref}^V - \alpha_V$ plane. The recovered posterior on alpha is very similar to the prior used. **Right** Posterior distributions of the parameters from the scalar polarized model $\{\Omega_{ref}^S, \alpha_S\}$. The 95% and 68% CL contours are shown in the $\Omega_{ref}^S - \alpha_S$ plane. The recovered posterior on alpha is very similar to the prior used.

Then, we assume the GWB is composed by a mix of two polarizations. They are uncorrelated and individually polarized, e.g.: for the tensor polarized case, both the plus and cross polarizations have the same power. For this reason, each contribution to the energy density spectrum can be expressed as a simple power law:

- Vector and tensor polarized GWB: $\Omega_{VT}(f) = \Omega_{ref}^T \left(\frac{f}{f_{ref}} \right)^{\alpha_T} + \Omega_{ref}^V \left(\frac{f}{f_{ref}} \right)^{\alpha_V}$. The resulting posterior distributions on the parameters $\{\Omega_{ref}^T, \alpha_T, \Omega_{ref}^V, \alpha_V\}$ are in Figure 6.16. The posteriors on the energy density spectra allow to obtain an UL at 95% CL of $\Omega_{ref}^T = 8.10 \times 10^{-9}$ and $\Omega_{ref}^V = 7.31 \times 10^{-9}$

- Vector and scalar polarized GWB: $\Omega_{VS}(f) = \Omega_{ref}^S \left(\frac{f}{f_{ref}} \right)^{\alpha_S} + \Omega_{ref}^V \left(\frac{f}{f_{ref}} \right)^{\alpha_V}$. The resulting

posterior distributions on the parameters $\{\Omega^S_{ref}, \alpha_S, \Omega^V_{ref}, \alpha_V\}$ are in Figure 6.17. The posteriors on the energy density spectra allow to obtain an UL at 95% CL of $\Omega^V_{ref} = 7.90 \times 10^{-9}$ and $\Omega^S_{ref} = 1.83 \times 10^{-8}$.

- Scalar and tensor polarized GWB: $\Omega_{TS}(f) = \Omega^S_{ref}\left(\frac{f}{f_{ref}}\right)^{\alpha_S} + \Omega^T_{ref}\left(\frac{f}{f_{ref}}\right)^{\alpha_T}$. The resulting posterior distributions on the parameters $\{\Omega^T_{ref}, \alpha_T, \Omega^S_{ref}, \alpha_S\}$ are in Figure 6.18. The posteriors on the energy density spectra allow to obtain an UL at 95% CL of $\Omega^T_{ref} = 6.47 \times 10^{-9}$ and $\Omega^S_{ref} = 2.10 \times 10^{-8}$.
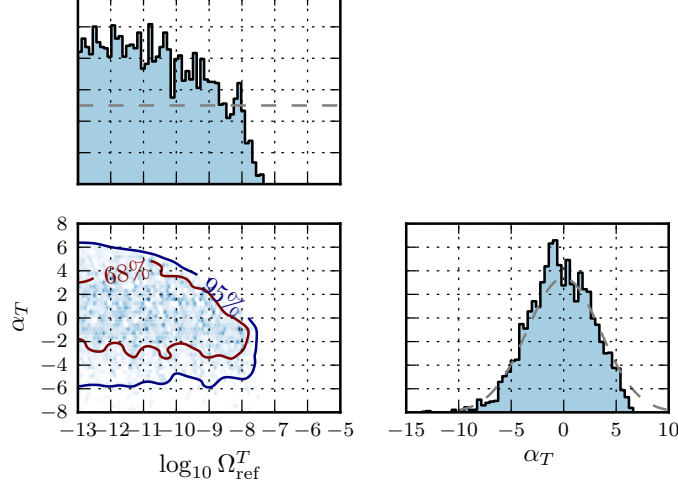

Figure 6.16: Posterior distributions of the parameters from the tensor and vector polarized model $\{\Omega^T_{ref}, \alpha_T, \Omega^V_{ref}, \alpha_V\}$. The 95% and 68% CL contours are shown for combinations of different posteriors. The recovered posterior on the spectral indices is very similar to the prior used.

Figure 6.17: Posterior distributions of the parameters from the scalar and vector polarized model $\{\Omega_{\mathrm{ref}}^{\mathrm{S}}, \alpha_{\mathrm{S}}, \Omega_{\mathrm{ref}}^{\mathrm{V}}, \alpha_{\mathrm{V}}\}$. The 95% and 68% CL contours are shown for combinations of different posteriors. The recovered posterior on the spectral indices is very similar to the prior used.
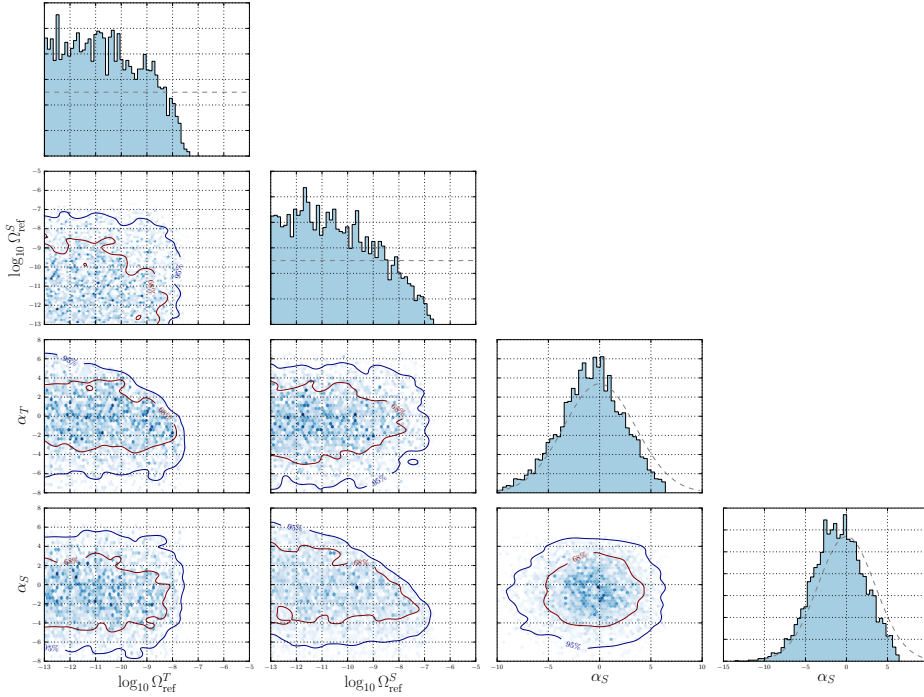
Figure 6.18: Posterior distributions of the parameters from the tensor and scalar polarized model $\{\Omega_{\mathrm{ref}}^{\mathrm{T}}, \alpha_{\mathrm{T}}, \Omega_{\mathrm{ref}}^{\mathrm{S}}, \alpha_{\mathrm{S}}\}$. The 95% and 68% CL contours are shown for combinations of different posteriors. The recovered posterior on the spectral indices is very similar to the prior used.

Finally, the GWB is assummed to be a mix of the three polarizations. Given the assumptions mentioned above, the energy density spectrum can be expressed as a superposition of simple power laws:

- Vector, scalar and tensor polarized GWB: $\Omega_{\text{TVS}}(f) = \Omega_{ref}^T \left(\frac{f}{f_{ref}} \right)^{\alpha_T} + \Omega_{ref}^V \left(\frac{f}{f_{ref}} \right)^{\alpha_V} + \Omega_{ref}^S \left(\frac{f}{f_0} \right)^{\alpha_S}$,

The posteriors over the parameters of this model are in Figure (6.19), where the posteriors on the energy density spectra allow to obtain an UL at 95% CL of $\Omega_{ref}^T = 6.45 \times 10^{-9}$, $\Omega_{ref}^V = 7.91 \times 10^{-9}$, $\Omega_{ref}^S = 2.06 \times 10^{-8}$.
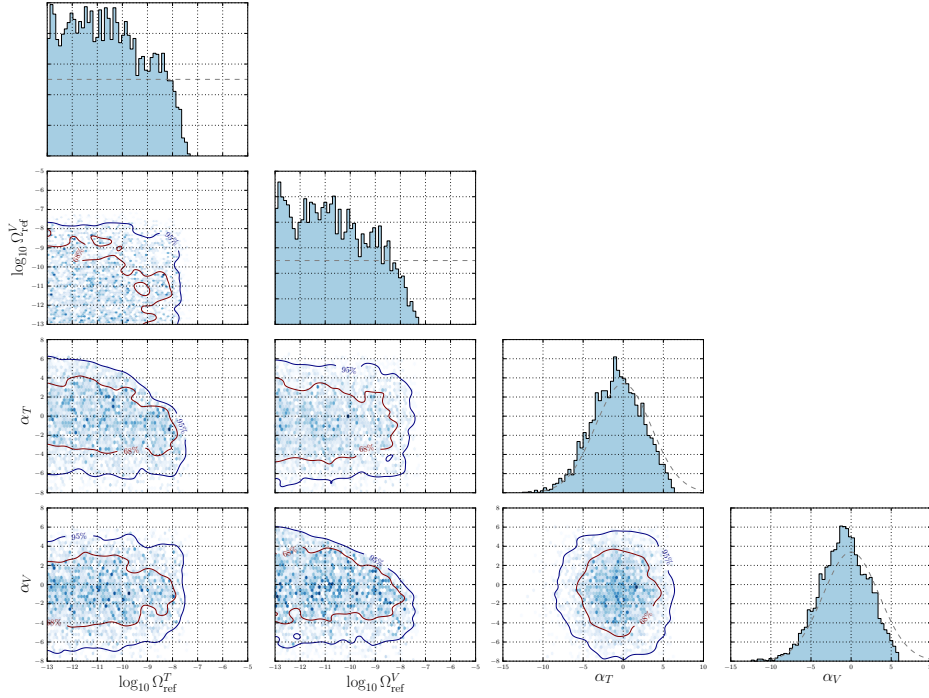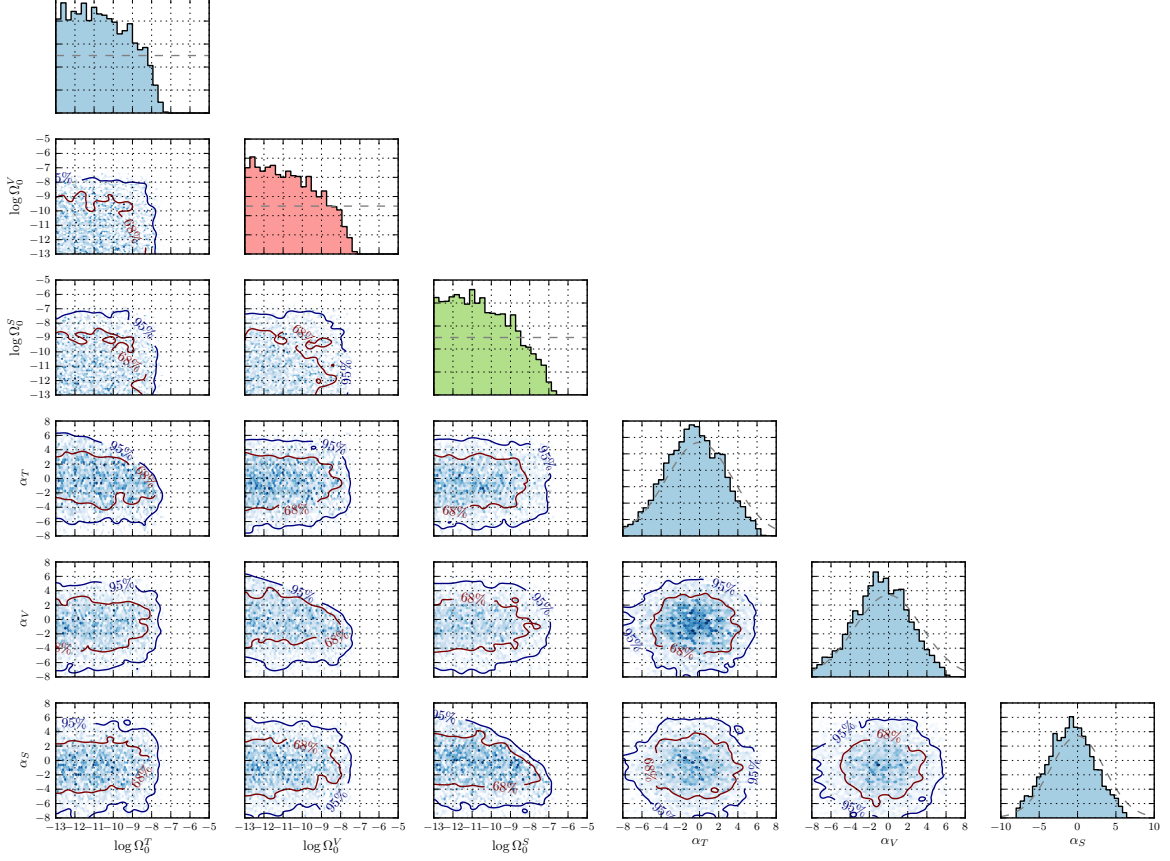

Figure 6.19: Posterior distributions of the parameters from the tensor and vector polarized model $\{\Omega_{ref}^T, \alpha_T, \Omega_{ref}^V, \alpha_V\}$. The 95% and 68% CL contours are shown for combinations of different posteriors. The recovered posterior on the spectral indices is very similar to the prior used.

In the Bayesian search, each $\Omega_a(f)$ for $a = \{T, V, S\}$ is multiplied by the corresponding ORF γ_a in order to obtain the expectation value of the cross correlation estimator $\langle \hat{C}(f) \rangle$, Eq. (6.75). The response of the H1-L1 and H1-V1 baselines to a GWB with different polarizations can be seen in Figure 6.20.

The upper limit at 95% CL over the energy density spectrum for each hypothesis can be seen in Table 6.2. Our search is less sensitive to the scalar polarization mode. The upper limit over Ω_{ref}^T is more constraining as more polarization modes are added to the model describing the GWB. The opposite applies to Ω_{ref}^V.
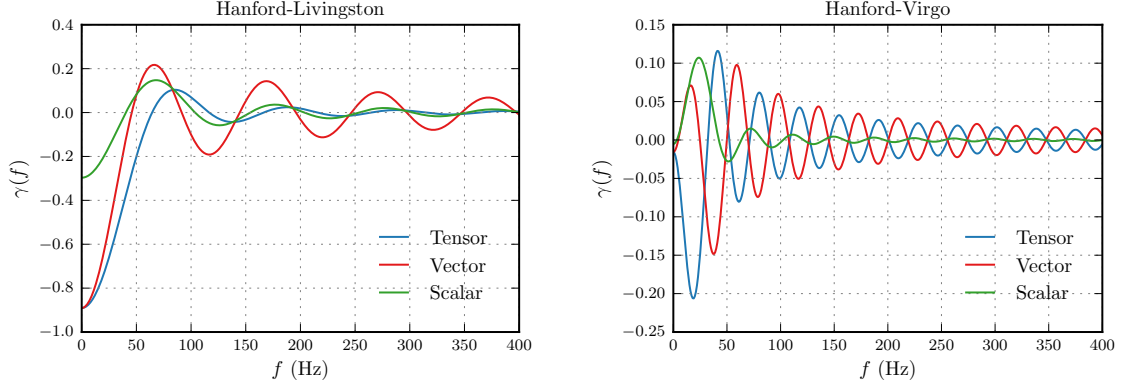
Figure 6.20: Figures retrieved from Ref. [107]. **Left** ORF of the H1-L1 baseline to a GWB with tensor (solid blue), vector (solid green) and scalar (solid red) polarization. **Right** ORF of the H1-V1 baseline to a GWB with tensor (solid blue), vector (solid green) and scalar (solid red) polarization.

Upper limits at 95% CL over the model parameters			
	$\Omega_{ref}^{T}(\times 10^{-9})$	$\Omega_{ref}^{V}(\times 10^{-9})$	$\Omega_{ref}^{S}(\times 10^{-8})$
T-polarized GWB	7.66	–	–
V-polarized GWB	–	6.13	–
S-polarized GWB	–	–	1.68
TV-polarized GWB	8.10	7.31	–
TS-polarized GWB	6.47	–	2.10
VS-polarized GWB	–	7.90	1.83
TVS-polarized GWB	6.45	7.91	2.06

Table 6.2: Upper limit at 95% CL over the model parameters for all the types of polarized GWBs studied.

Chapter 7

Interpretations of the Gravitational Wave Background

7.1 Motivation

As already discussed, the usual searches for an isotropic GWB are agnostic in terms of the model describing the background. A simple power law, Eq.(6.30), is used as the spectrum of the background. However, recent searches have reinterpreted the background as being sourced by cosmic strings [31]. We perform a similar search assuming the GWB is sourced by either First Order Phase Transitions or the formation of Primordial Black Holes alongside a non-negligible contribution from Compact Binary Coalescences (CBCs).

Many models Beyond The Standard Model (BSM) predict strong phase transitions, such as grand unification models [138], supersymmetric models [139] and models with an extended Higgs sector [140], among others. Such models predict new phenomena at very large energy scales that can only be partially tested at colliders given the limited center-of-mass energy in the collisions. For this reason, much attention is being put on searches for phase transitions leading to GWs and the GWB signals at high frequency, testing very large temperatures. There may be symmetries spontaneously broken through a FOPT, such as the Peccei-Quinn symmetry [141], the B-L symmetry [142] or the left-right symmetry [143]. The predicted temperature of the transition in different models spans a wide range. The peak frequency of the spectrum is related to the temperature, so the contribution to the GWB from FOPTs spans a wide range of frequencies[1]. The frequency band of interest in the LIGO-Virgo network is approximately between 1-100Hz. This band corresponds to temperatures in the range $10^7 - 10^{10}$GeV, which are supported by the Peccei Quinn axion model [145]. The Peccei-Quinn model solves the strong CP problem and provides a dark matter candidate, the axion [146].

PBHs are of great interest as they could be a dark matter (DM) candidate. PBHs may not exist at all, but if they did, they would have formed before the end of the radiation-dominated era. Furthermore, evaporating PBHs could explain the extragalactic and galactic γ-ray backgrounds, antimatter in cosmic rays [147] and some short period γ-ray bursts [148] among others (for further details see Ref. [149]). Setting constraints on the number of PBHs of a given mass sets constraints on the cosmological models that would generate them.

7.2 First Order Phase Transitions

In the Standard Model of Cosmology, after inflation, the Universe heats up during the reheating period [2]. It then progressively expands, cooling down until acquiring the current temperature. In this

---

[1]More specifically, the peak frequency is determined by the typical length scale at the transition, the mean bubble separation R_{pt} and the amount of redshifting determined by T_{pt} and the cosmic history [144]

[2]During inflation the Universe is cold and lacking thermal entropy. By the end of inflation, the energy density of the inflaton (scalar field of the inflationary period) is released leading to an increase in the temperature of the Universe.

process, many models BSM predict first, second, or cross-over phase transitions (PTs). PTs are very violent events that can lead to the generation of particles, defects, magnetic fields, baryonic asymmetry, and GWs that will be part of the GWB [150]. The time scale of the entire phase transition is much shorter than the Hubble time [3]. The Physics responsible for PTs can occur at scales ranging from 0.1 to 10^{15}GeV. Two PTs are believed to have occurred in the history of the Universe. One is the QCD transition between a quark-gluon plasma and a hadron gas. The other is the electroweak (EW) transition. At this point, the EW symmetry was spontaneously broken, allowing the SM particles to acquire Gauge invariant mass. This led to the baryon asymmetry via the EW baryogenesis mechanism. Both PTs are believed to have left an imprint in the GWB [150].

In quantum field theory (QFT), a phase transition (PT) is the transition between one vacuum state to another with lower energy. At the end of the reheating period, when temperatures are very high, the thermal Higgs-like potential has only one minimum (see the potential at temperature T_o in Figure 7.2). As the Universe cools down, a new ground state generates (see the potential at temperature T_c in Figure 7.2). Both minima are separated by a potential barrier. When the temperature reaches a critical value T_c, both minima are degenerate, i.e.: they have the same pressure and can thus coexist. Eventually, $T < T_c$ and from this point, it is thermodynamically favorable for the Higgs-like field to occupy the new minimum. However, the Higgs-like field has to cross the potential barrier. This can either be done by quantum tunneling [151, 152] or by thermal fluctuations [153]. The former procedure happens in regions in space called bubbles. These bubbles are the ones containing the absolute ground state, also known as true vacuum (see Figure 7.1(left)). These bubbles expand and eventually coalesce in a medium that is the local minimum or false vacuum (see Figure 7.1(right)). While these bubbles expand, they expel heat into their surrounding, heating the false vacuum (FV) until acquiring the temperature mentioned above T_c. At this point, the pressure of the FV prevents further expansion of the bubbles containing the true vacuum (TV). As the universe expands, the bubbles containing the TV expand. During this process, the temperature of the Universe remains constant, T_c, until the full latent heat (difference between the two phases) is eliminated. When the TV bubbles occupy 30-50% of the total volume they collide. Once the bubbles start colliding, the motion of the fluid and the production of gravitational waves is described with numerical simulations [154, 155].
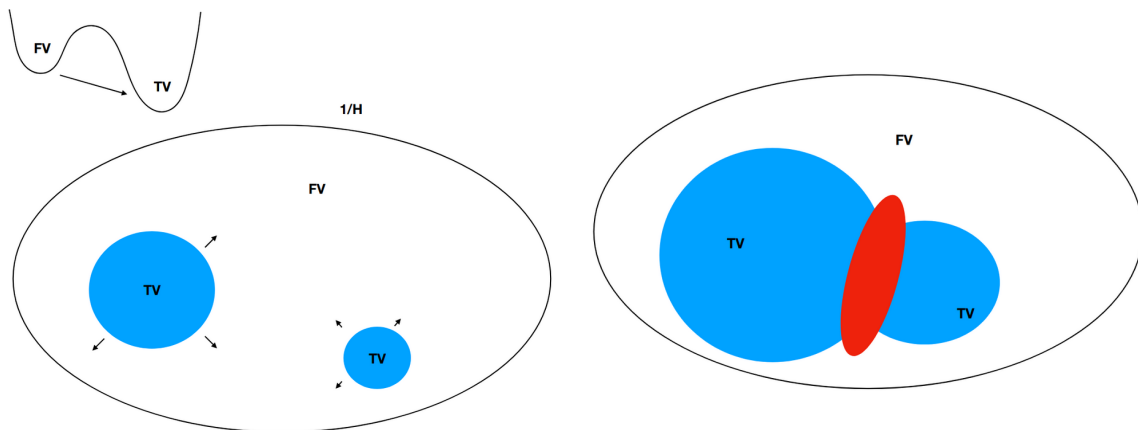
Figure 7.1: Schematic representation of a FOPT. **Left** The ground state or true vacuum (TV) is contained by bubbles embedded in a medium less energetically favourable, the false vacuum (FV). **Right** These bubbles expand in the medium and eventually coalesce. Images generated by O. Pujolás.

Numerical simulations show that there are three stages in which GWs can be produced. Firstly, the stage in which the bubbles collide and merge is of short duration and subdominant compared to the subsequent stages of production of GWs, unless the bubbles grow up to the Hubble length. The Hubble length is given by cH_o^{-1}, where H_o is the Hubble constant, which is the constant of proportionality between recession speed v and distance d in the expanding Universe, i.e.: $v = H_o d$. The contribution

---

[3]The inverse of the Hubble constant is known as the Hubble time. It is the time since the Big Bang origin of the expansion, assuming that a deceleration is negligible. It does not coincide with the age of the Universe. The Hubble time is the age the Universe would have if its expansion had been linear, which is not the case.

from bubble collisions (BC) is denoted by Ω_{coll}. Secondly, the shells of fluid kinetic energy continue expanding, which generates compression waves that propagate into the plasma as sound waves (SW). These waves overlap and source GWs. The power spectrum sourced by this stage is denoted by Ω_{sw}. Finally, the intrinsic non-linearity in the fluid equations becomes important. Due to these non-linearities, the previous stages might produce vorticity and turbulence, and the SW could develop shocks. The spectrum of this phase is denoted by Ω_{turb}. These three sources are relevant on different length scales and at different time scales. For this reason, the contribution from FOPTs to the GWB can be modelled as the sum of the three contributions $\Omega_{\text{GW}}(f)h^2 = \Omega_{\text{coll}}(f)h^2 + \Omega_{\text{sw}}(f)h^2 + \Omega_{\text{turb}}(f)h^2$ [156].

7.2.1 Parameters of a First Order Phase Transition

The derivation of the production of GWs by FOPTs is very involved. For a complete derivation, we refer the reader to Ref. [156]. In this section, we describe the parameters of the FOPT that can be inferred from the GWB. The parameters we will introduce are the temperature at which the TV bubbles appear, the velocity at which they expand, the total number of bubbles, the fraction of TV volume, the duration, and the speed of the transition.

For a generic scalar field ϕ and a potential $V(\phi)$, the action of the tunneling solution from a false vacuum ϕ_{false} to a true vacuum ϕ_{true} is [157]

$$S = 4\pi \int dr r^2 \Big(\frac{\dot{\phi}^2}{2} + V(\phi)\Big). \tag{7.1}$$

To find the field profile $\phi = \phi(r)$ one needs to solve the equation of motion of the scalar field ϕ [150] numerically

$$\frac{d^2\phi}{dr^2} + \frac{2}{r}\frac{d\phi}{dr} = \frac{dV}{d\phi}. \tag{7.2}$$

The boundary conditions satisfy that the field is equal to the FV at infinity $\phi(\infty) \sim \phi_{\text{false}}$, and equal to the TV in the vicinity $\phi(0) \sim \phi_{\text{true}}$. The transition takes place when within one Hubble time about one bubble nucleates inside the Hubble volume [4], which defines the transition time t_* and transition temperature T_* [157]

$$\int_0^{t_*} \frac{\Gamma}{H^3} dt = \int_{T_c}^{T_*} \frac{dT}{T} \frac{\Gamma}{H^4} = 1, \tag{7.3}$$

where the lower integration limit in the second equality is the critical temperature T_c defined above, and Γ is the tunneling rate, given in terms of the action, Eq. (7.1), $\Gamma(T) = A(T)e^{-S(T)/T}$, where $A(T)$ is a factor of order T^4 [159]. The temperature T_* can be approximated by the nucleation temperature T_N. After a bubble nucleates, it expands creating a larger region of the TV. This expansion leads to more particles in the plasma acquiring mass. Near the bubble wall, the equilibrium distribution of particles in the plasma is perturbed. This is energetically costly, which leads to resistance to the bubble expansion. If the friction is large enough, the bubble wall may not move at ultra-relativistic speeds. When the volume fraction of the FV is negligible, the FOPT finishes. At this point, the temperature is denoted by T_f, as seen in Figure 7.2.

The inverse duration of the transition is denoted by β and is given in terms of the action S, $\beta = -\frac{dS}{dt}|_{t=t_*} \simeq \frac{\dot{\Gamma}}{\Gamma}$. It usually is normalized by the Hubble parameter at the time of the transition H_{pt}. The ratio β/H_{pt} is a very important parameter that controls the energy density of the GW signal [160]. The smaller β/H_{pt}, the stronger the FOPT as well as the produced GW signal. In typical transitions, the temperature of the thermal bath at time t_*, is approximately equal to the nucleation temperature $T_* \simeq T_N$. With this approximation, the ratio can be expressed as $\beta/H_{pt} = T_* \frac{dS}{dT}|_{T_*}$ [161].

The strength of a FOPT is denoted by α, and is given by the energy density going into the bubbles over the thermal energy density of the surrounding plasma $\alpha = \frac{\rho_{vac}}{\rho_{rad}^*}$, where $\rho_{rad}^* = g_* \pi^2 T_*^4/30$. This

---

[4]A Hubble volume is a spherical region of the observable universe for an observer (located in the center of the sphere) beyond which objects should recede faster than the speed of light so as to be causally connected (due to the expansion of the Universe [158]), which is not possible.
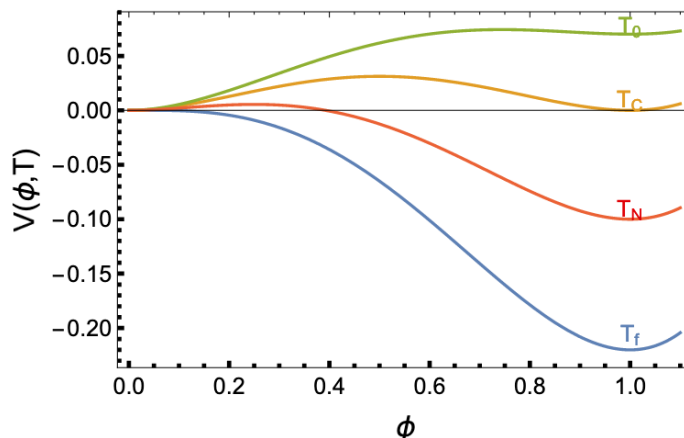
Figure 7.2: Image retrieved from Ref. [150]. Evolution of the scalar potential for different temperatures. The temperature when a new minimum appears is T_0. When the two minima are degenerate, the temperature is critical T_c. The temperature when there is at least one critical bubble per Hubble volume is the nucleation temperature T_N. The transition finishes at a temperature T_f.

quantity is related to the duration of a FOPT. For weak FOPTs (small α), the lifetime of the soundwaves τ_{SW} is short compared to a Hubble time. However, very strong FOPTs do last longer, $H\tau_{SW} \gtrsim 1$ [157].

The bubble wall velocity is determined by the interaction of the bubbles with the surrounding plasma. The plasma exerts friction that slows down the propagation of the walls of the bubbles. In strong FOPTs, the pressure difference across the bubble walls dominates over the friction exerted by the plasma, which makes bubble walls speed up. In this case, $v_w \to 1$. Weaker FOPTs have bubble walls with a speed close to the speed of sound $v_w \to 1/\sqrt{3}$ [145].

An isolated bubble does not generate GWs as it has no quadrupole moment. However, bubble collisions do generate GWs. When a collision takes place, the latent heat is converted into a bulk flow of the plasma which leads to the commonly known as GWs from soundwaves. Also, the latent heat is converted into kinetic energy of the scalar field. The efficiency of converting vacuum energy into scalar field gradient energy is denoted by κ_ϕ and given by $\kappa_\phi = \frac{\rho_\phi}{\rho_{vac}}$, where ρ_ϕ is the energy density of the scalar field and ρ_{vac} that of the vacuum. The efficiency is usually small since the contribution from bubble collisions is subdominant [162]. The fraction of the latent heat which goes into the bulk motion, i.e.: the fraction of vacuum energy converted into the kinetic energy of the bulk flow, is given by $\kappa_{sw} = \frac{\rho_V}{\rho_{vac}}$. This efficiency is dependent on the strength of the transition α and the bubble wall velocity v_w. The motion of the plasma will be important to determine the efficiency of the sound waves in a FOPT, so we now review the aspects of the plasma hydrodynamics in the presence of expanding bubbles from a FOPT [157]. The derivations are done under the assumption that there is only one expanding bubble interacting with the plasma, which behaves as a perfect fluid. Also, the bubble is assumed to be spherically symmetric, so that the fluid spatial dependence is given in terms of the radial coordinate r from the center of the bubble [157]. As the bubble wall velocity increases, the plasma profile may behave in three different ways, deflagrations, hybrid, and detonation. For a known v_w, these three solutions to the hydrodynamic equations of the transition are schematically represented in Fig. 7.3, retrieved from Ref. [163].

- Detonations. The PT wall moves at a supersonic speed, $v_w > c_s$, and the strength of the transition is weak enough $\alpha < \alpha_{max}^{det} = \frac{(1-\sqrt{3}v_w)^2}{3(1-v_w^2)}$[157]. If this condition is not satisfied, the solution is hybrid. In detonations, the plasma shell follows the expansion of the bubble wall with speed v_w [163].

- Deflagrations. The plasma is at rest inside the wall, so the velocity is $v_w < c_s$. However, the wall pushes the plasma shell around it [157].
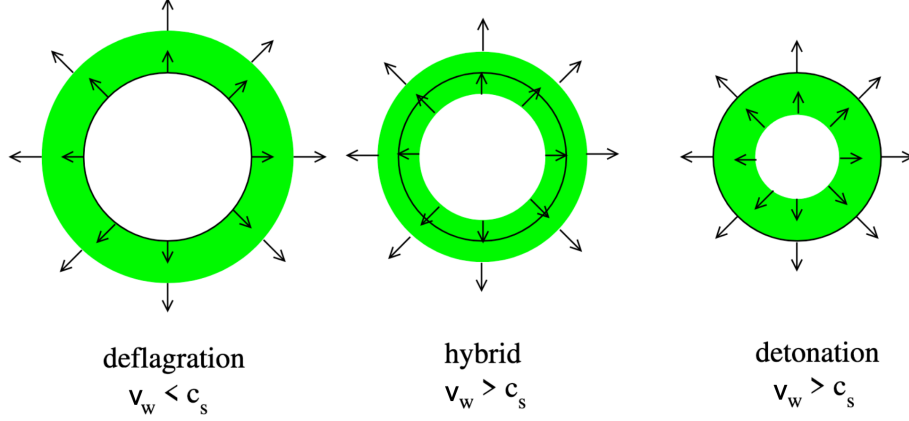
Figure 7.3: Image retrieved from Ref. [163]. Solutions to the hydrodynamic equations of a phase transition. For subsonic v_w the bubble expansion takes place through deflagrations. For supersonic v_w, the solution is either detonations, for weak enough transitions, or hybrid, in stronger transitions.

- Hybrids. The detonation and deflagration solutions are combined to obtain a new velocity profile. This is a Physical scenario since supersonic deflagrations are not stable but develop a detonation-like profile. In this case, $v_w > c_s$ in the plasma, and there exists a strong interaction with the plasma [157].

As a summary, for subsonic v_w the bubble expansion takes place through deflagrations. For supersonic v_w, the solution is either detonations, for weak enough transitions or hybrid, in stronger transitions. As mentioned above, the efficiency of the sound waves in the transition is dependent on the solution to the plasma equations of motion, deflagrations, hybrid, and detonation. More information is provided in appendix F.

7.3 Implications for First Order Phase Transitions from the three LIGO-Virgo observing runs

As already mentioned, no detection of a GWB has been made, but with the current sensitivity, we can set upper limits over the parameters of strong FOPT taking place at temperatures between $10^7 - 10^{10}$GeV. In our study, we did not account for turbulences, since they are subdominant and their spectrum is the least well understood [161].

The energy density in GWs for the contribution from SWs is given by [161, 144]

$$\Omega_{\text{sw}}(f)h^2 = 2.65 \times 10^{-6} \left(\frac{H_{pt}}{\beta}\right) \left(\frac{\kappa_{sw}\alpha}{1+\alpha}\right)^2 \left(\frac{100}{g_*}\right)^{1/3} \times v_w \left(\frac{f}{f_{\text{sw}}}\right)^3 \left(\frac{7}{4+3(f/f_{\text{sw}})^2}\right)^{7/2} \Upsilon(\tau_{\text{sw}}) ,$$
(7.4)

where f_{sw} is the peak frequency, given by

$$f_{\text{sw}} = 19 \frac{1}{v_w} \left(\frac{\beta}{H_{pt}}\right) \left(\frac{T_{pt}}{100\text{GeV}}\right) \left(\frac{g_*}{100}\right)^{\frac{1}{6}} \mu\text{Hz}.$$
(7.5)

The parameter $\Upsilon = 1 - (1 + 2\tau_{\text{sw}}H_{pt})^{-1/2}$ is a suppression factor introduced in Ref. [164] and it is due to the finite lifetime, τ_{sw}, of sound waves. The spectrum of the contribution from sound waves, Eq. (7.4), is shown in Figure 7.4 for different combinations of parameters compared to the O3 PI sensitivity curve (solid blue line). It is assumed that the GWB is only sourced by sound waves. From Figure 7.4 we can make some qualitative statements. Large temperatures correspond to high peak frequencies. Also, the change in α affects the amplitude of the spectrum. For larger α, the amplitude of the spectrum increases. Finally, The change of β/H_{pt} affects both the peak frequency and amplitude
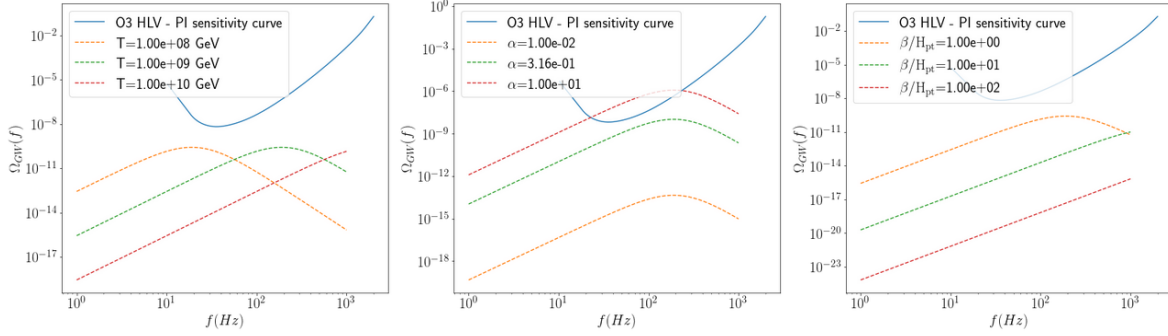
105

Figure 7.4: Spectra from the contribution of SW to the GWB compared to the PI curve for O3 (blue solid line). It is assumed that the GWB is only sourced by sound waves, and the bubble wall is equal to the speed of light $v_w = 1$. **Left** Spectra corresponding to $\alpha = 0.1$ and $\beta/H_{pt} = 1$. Each dashed line corresponds to the spectrum at different temperature. Large temperatures correspond to large peak frequencies. **Centre** Spectra corresponding to $T = 10^9\ GeV$ and $\beta/H_{pt} = 1$. Each dashed line corresponds to the spectrum for different strengths. For larger α, the amplitude of the spectrum increases. **Right** Spectra corresponding to $\alpha = 0.1$ and $T = 10^9\ GeV$. Each dashed line corresponds to the spectrum with different β/H_{pt}. Larger β/H_{pt} correspond to higher peak frequencies and smaller amplitudes of the spectra.

of the signal. Larger β/H_{pt} correspond to higher peak frequencies and smaller amplitudes of the spectra.

When SW are highly suppressed, BC become dominant. The contribution from BCs is described in Refs. [165, 166] and given by

$$\Omega_{\text{coll}}(f)h^2 = 1.67 \times 10^{-5} \Delta \left(\frac{H_{pt}}{\beta} \right)^2 \left(\frac{\kappa_\phi \alpha}{1 + \alpha} \right)^2 \times \left(\frac{100}{g_*} \right)^{1/3} S_{\text{env}}(f), \tag{7.6}$$

where the amplitude Δ is given by $\Delta(v_w) = 0.48 v_w^3 / (1 + 5.3 v_w^2 + 5 v_w^4)$. The function S_{env} is the spectral shape, given by $S_{\text{env}} = 1/(c_l \tilde{f}^{-3} + (1 - c_l - c_h) \tilde{f}^{-1} + c_h \tilde{f})$, where $c_l = 0.064$, $c_h = 0.48$, obtained from numerical fits to simulated power spectra in Ref. [167], and $\tilde{f} = f/f_{\text{env}}$. The quantity f_{env} is the present peak frequency, given by

$$f_{\text{env}} = 16.5 \left(\frac{f_{bc}}{\beta} \right) \left(\frac{\beta}{H_{pt}} \right) \left(\frac{T_{pt}}{100\ \text{GeV}} \right) \left(\frac{g_*}{100} \right)^{\frac{1}{6}} \mu\text{Hz}, \tag{7.7}$$

where f_{bc} is the peak frequency right after the transition $f_{bc} = 0.35\beta/(1 + 0.069 v_w + 0.69 v_w^4)$. Eq. (7.6) was obtained with the envelope approximation [168], which assumes infinitely thin walls of the bubbles. The spectrum of the contribution from bubble collisions, Eq. (7.6), is shown in Figure 7.5 for different combinations of parameters. It is assumed that the GWB is only sourced by bubble collisions, $\kappa_{bc} = 1$. From Figure 7.5 we can make some qualitative statements. Large temperatures correspond to large peak frequencies. For larger α, the amplitude of the spectrum increases. The change of β/H_{pt} affects both the peak frequency and amplitude of the signal. Larger β/H_{pt} correspond to higher peak frequencies and smaller amplitudes of the spectra. It can be noticed that the amplitude of the spectra from BC is larger than those from SW for the same set of parameters.

In reality, the contribution from CBCs to the GWB is non-negligible. Assuming a reference amplitude of $\Omega_{ref}(f) = 10^{-9}$ and using Eq. (6.31), a spectrum for the CBC contribution is obtained. It is then added to the spectra from Figures 7.4 and 7.5, resulting in Figures 7.6 and 7.7, respectively.

According to the definition of the PI curve in section 6.3, any spectrum above the PI curve will have an SNR above a given threshold. In the isotropic searches, the threshold is 3. No detection of a GWB has been made, so the combination of parameters leading to a spectrum above the PI curve is discarded. Discarding parameters case by case in a two-dimensional plot is not accurate since this approach does not account for systematics, so a Bayesian search was performed to set upper limits over the parameters of the models. We ran the Bayesian search over the isotropic correlated data from the three first observing runs[5]. Two sets of models were used to describe the contribution of GWs

---

[5]This data is publicly available at: https://dcc.ligo.org/LIGO-G2001287
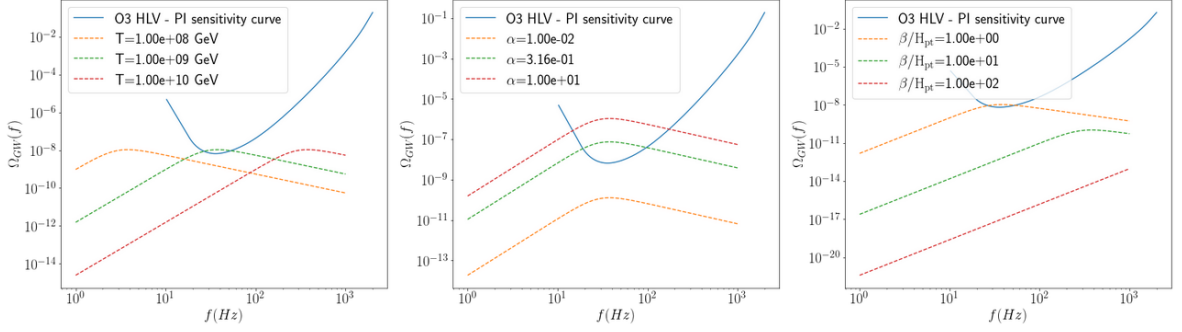
Figure 7.5: Spectra of the contribution from bubble collisions to the GWB. They are compared with the PI sensitivity curve for O3 (blue dashed line). **Left** Spectra corresponding to $\alpha = 0.1$ and $\beta/H_{pt} = 1$. Large temperatures correspond to large peak frequencies. **Centre** Spectra corresponding to $T = 10^9 \ GeV$ and $\beta/H_{pt} = 1$. For larger α, the amplitude of the spectrum increases. **Right** Spectra corresponding to $\alpha = 0.1$ and $T = 10^9 \ GeV$. Larger β/H_{pt} correspond to higher peak frequencies and smaller amplitudes of the spectra.

Figure 7.6: Spectra from the contribution of SW and CBCs to the GWB compared to the PI curve for O3 (blue solid line). The parameters for each spectrum are the sames as in Figure 7.4 and a CBC contribution with $\Omega_{ref}(f) = 10^{-9}$ has been added.
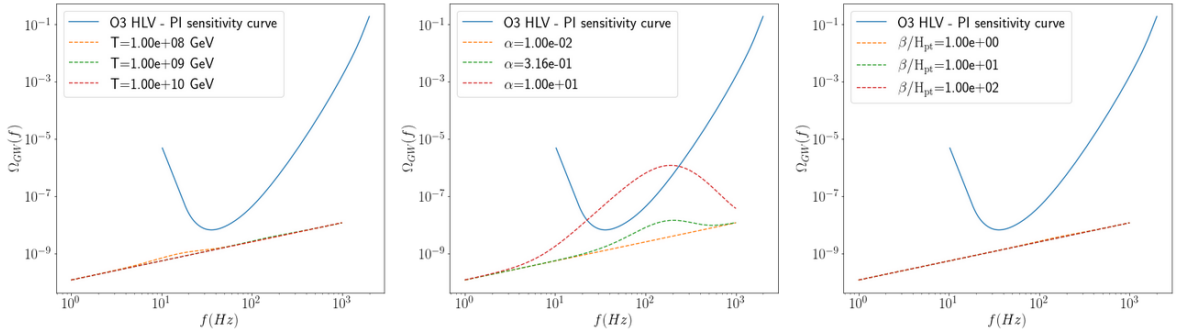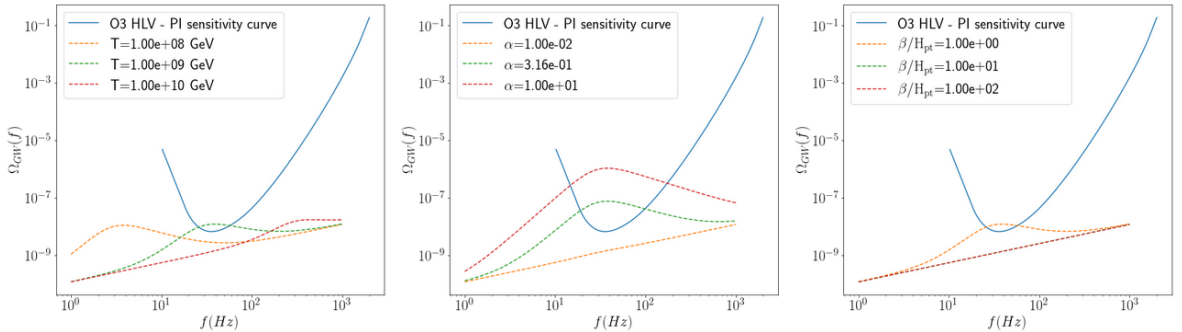

Figure 7.7: Spectra from the contribution of BC and CBCs to the GWB compared to the PI curve for O3 (blue solid line). The parameters for each spectrum are the sames as in Figure 7.5 and a CBC contribution with $\Omega_{ref}(f) = 10^{-9}$ has been added.

107

from FOPTs to the GWB. Firstly, a broken power law (BPL) was used. Secondly, a phenomenological model was used with spectra given by Eqs. (7.4) and (7.6). In both cases, the contribution from the CBC background was included using the spectrum from Eq. (6.31). A contribution from Schumann resonances (see section 6.4.1) was neglected.

The BPL is given by

$$\Omega_{\mathrm{bpl}}(f) = \Omega_* \left(\frac{f}{f_*}\right)^{n_1} \left[1 + \left(\frac{f}{f_*}\right)^{\Delta}\right]^{(n_2-n_1)/\Delta}, \tag{7.8}$$

where f_* is the peak frequency. In our search, the prior on f_* is uniform and contains the region of highest sensitivity in the LIGO-Virgo network. In Eq. (7.8), the spectral index n_1 is set to 3 from causality. As discussed in Ref. [169], the power spectrum at large scales is that of white noise (flat in frequency) and since Ω_{GW} is proportional to k^3 times the power spectrum, then it grows as k^3. Hence, the energy density spectrum behaves like f^3 and thus the choice of $n_1 = 3$. The other spectral index n_2 takes the values -4 or -1 depending on which is the main source of GWs, sound waves, or bubble collisions, respectively. However, in our search, we chose a uniform prior from -8 to 0, which includes both of these extreme cases. The parameter Δ is set to 2 for SW and 4 for BC. The prior on the amplitude of the contribution from FOPTs to the GWB, Ω_*, is log uniform, same as the one for Ω_{ref}. Consequently, the model fitted to the data is $\Omega_{GW}(f, \underline{\theta}_{GW})$, where $\underline{\theta}_{GW} = (\Omega_{ref}, \Omega_*, f_*, n_2)$. The priors on these parameters are summarized in Table 7.1.

Broken power law model		
Parameter	Prior type	Prior range
Ω_{ref}	LogUniform	$(10^{-10}, 10^{-7})$
Ω_*	LogUniform	$(10^{-9}, 10^{-4})$
f_*	Uniform	(0, 256 Hz)
n_1	–	3
n_2	Uniform	(-8,0)
Δ	–	2

Table 7.1: Priors used for the parameters of the BPL+CBC model in the Bayesian search. The spectral index $n_1 = 3$ from causality. The parameter $\Delta = 2$ corresponds to SW dominating the production of GWs and it leads to more conservative upper limits than with $\Delta = 4$. The prior for f_* is uniform and contains the region of highest sensitivity in the LIGO-Virgo network. The narrow prior on Ω_{ref} stems from previous estimates of the CBC background [100].

This analysis led to a Bayes factor of $\log \mathcal{B}_{\mathrm{noise}}^{\mathrm{CBC+BPL}} = -1.4$, which shows no evidence for a signal described by the BPL and CBC model. The posterior distributions obtained are in Figure 7.8. The posterior on Ω_{ref} allows obtaining an upper limit at 95% CL of 6.1×10^{-9}, consistent with the UL from the O3 isotropic search [21]. Similarly, an upper limit at 95% CL is obtained for $\Omega_* = 5.6 \times 10^{-7}$. From this upper limit, assuming a reference frequency of 25Hz and choosing individual posterior samples for f_* and n_2, the UL at 95% CL on Ω_{BPL} is 4.4×10^{-9}. The wide posteriors on n_2 and f_* show no preference for any particular value.

The Bayesian search was repeated using delta priors over n_2 and f_* to obtain upper limits at 95% CL on Ω_*. The values chosen for f_* are 1Hz (below the LIGO-Virgo sensitivity range of frequencies), 25 Hz (the region where LIGO-Virgo have the highest sensitivity), and 200Hz (above the sensitivity region). The spectral index n_2 takes values corresponding to the case in which only BCs source the GWB or the case with only SW, -1, or -4, respectively. The results from these searches are in Table 7.2. The most constraining upper limits on $\Omega_*^{95\%}$ are obtained for $f_* = 25$ Hz. This is expected given that it is the region with the highest sensitivity in the LIGO-Virgo network. For $f_* = 1$ Hz, the faster the decay, i.e.: the smaller n_2, the less stringent ULs.

A similar methodology was then used using the phenomenological model instead of the BPL. Two benchmark cases were studied, one where the only source of GWs are BCs and other in which only SWs contribute to the GWB. In the case of only BCs, the spectrum is given by Eq. (7.6). The bubble

Figure 7.8: Posterior distributions over the BPL+CBC model parameters. The posterior on Ω_{ref} allows to obtain an upper limit at 95% CL of 6.1×10^{-9}. Also, an upper limit at 95% CL is obtained for $\Omega_* = 5.6 \times 10^{-7}$. The wide posteriors on n_2 and f_* show no preference for any particular value.

Broken power law model			
	$f_* = 1\,\mathrm{Hz}$	$f_* = 25\,\mathrm{Hz}$	$f_* = 200\,\mathrm{Hz}$
$n_2 = -1$	3.3×10^{-7}	3.5×10^{-8}	2.8×10^{-7}
$n_2 = -2$	8.2×10^{-6}	6.0×10^{-8}	3.7×10^{-7}
$n_2 = -4$	5.2×10^{-5}	1.8×10^{-7}	3.7×10^{-7}

Table 7.2: Upper limits for the energy density amplitude, $\Omega_*^{95\%}$, in the broken power law model for fixed values of the peak frequency, f_*, and negative power law index, n_2.

wall velocity is set to $v_w \rightarrow 1$ and so is the efficiency κ_ϕ. The narrow prior on Ω_{ref} stems from previous estimates of the CBC background [100]. The prior on α is not higher than 10 because Eqs. (7.4) and (7.6) may not be applicable, and large α does not translate into an increase in the GW amplitude. The prior on β/H_{pt} could not contain values lower than 10^{-1} because it would imply the transitions would never complete. The inverse duration β/H_{pt} is related to the mean bubble separation by $R_{pt}H_{pt} = (8\pi)^{1/3} v_w H_{pt}/\beta$ [167], so for very small values of β/H_{pt}, the large separation between bubbles would not allow the transition to complete. The temperatures chosen are large enough so as to have a signal comparable to our current sensitivity. These values are well motivated by particle Physics (see section 7.1). Consequently, the model fitted to the data is $\Omega_{GW}(f, \underline{\theta}_{GW})$, where $\underline{\theta}_{GW} = (\Omega_{ref}, \alpha, T_{pt}, \beta/H_{pt})$. A summary of the priors used are in Table 7.3.

Phenomenological model		
Parameter	Prior type	Prior range
Ω_{ref}	LogUniform	$(10^{-10}, 10^{-7})$
α	LogUniform	$(10^{-3}, 10)$
β/H_{pt}	LogUniform	$(10^{-1}, 10^3)$
T_{pt}	LogUniform	$(10^5, 10^{10} \text{ GeV})$
v_w	–	1
κ_ϕ	–	1
κ_{sw}	–	$f(\alpha, v_w) \in [0.1 - 0.9]$

Table 7.3: Priors used for the parameters of the phenomenological+CBC model in the Bayesian search. The narrow prior on Ω_{ref} stems from previous estimates of the CBC background [100]. The prior on α is not higher than 10 because Eqs. (7.4) and (7.6) may not be applicable, and large α does not translate into an increase in the GW amplitude. The prior on β/H_{pt} could not contain values lower than 10^{-1} because it would imply the transitions would never complete. The temperatures chosen are large enough so as to have a signal comparable to our current sensitivity.

From this search, the Bayes factor obtained is $\log \mathcal{B}_{\text{noise}}^{\text{CBC+BC}} = -0.74$, showing again no evidence for a signal described by this model. The posterior distributions obtained are in Figure 7.9. The posterior on Ω_{ref} allows to obtain an UL at 95% CL of 5.91×10^{-9}, in agreement with the O3 isotropic result [21]. The inverse duration β/H_{pt} shows preference for larger values, which is expected. The posteriors on α and T_{pt} show no preference for any particular region. However, exclusions at 95% CL are obtained in parameter space. Values of $\alpha > 1$, $T_{pt} > 10^8 \text{GeV}$ and $\beta/H_{pt} < 1$ are excluded at 95% CL [100].

The search was repeated using delta priors on β/H_{pt} and T_{pt} in order to get upper limits at 95% CL on Ω_{coll}. The results are in Table 7.4. The ULs vary between 4.0×10^{-9} to 1.0×10^{-8}, with more stringent upper limits at large β/H_{pt} or large T_{pt}. For very large β/H_{pt} and T_{pt} there is not enough sensitivity to place constrains to the model parameters. In all of these runs, the UL at 95% CL on Ω_{ref} is between 5.30×10^{-9} and 6.05×10^{-9}, which are consistent with the result from the O3 isotropic analysis [21].

Phenomenological model (bubble collisions)				
$\Omega_{coll}^{95\%}$ (25 Hz)				
$\beta/H_{pt} \setminus T_{pt}$	10^7 GeV	10^8 GeV	10^9 GeV	10^{10} GeV
0.1	9.2×10^{-9}	8.8×10^{-9}	1.0×10^{-8}	7.2×10^{-9}
1	1.0×10^{-8}	8.4×10^{-9}	5.0×10^{-9}	–
10	4.0×10^{-9}	6.3×10^{-9}	–	–

Table 7.4: The 95% CL upper limits on $\Omega_{coll}^{95\%}$(25 Hz) for fixed values of β/H_{pt} and T_{pt}, and $v_w = \kappa_\phi = 1$. The dashed lines denote no sensitivity for exclusion.

In the case in which only SWs source the GWB, the spectrum is given by Eq. (7.4). The priors are the same used for the BC case, Table 7.3. The only difference is that the efficiency is dependent on the strength of the transition and the bubble wall velocity, given by Eq. (F.1). From this search, the Bayes factor is $\log \mathcal{B}_{\text{noise}}^{\text{CBC+SW}} = -0.66$, showing no evidence for a signal. The posterior distribution on Ω_{ref} allows to obtain an UL at 95% CL of 5.86×10^{-9}. The posteriors on α, T_{pt} and β/H_{pt} show no
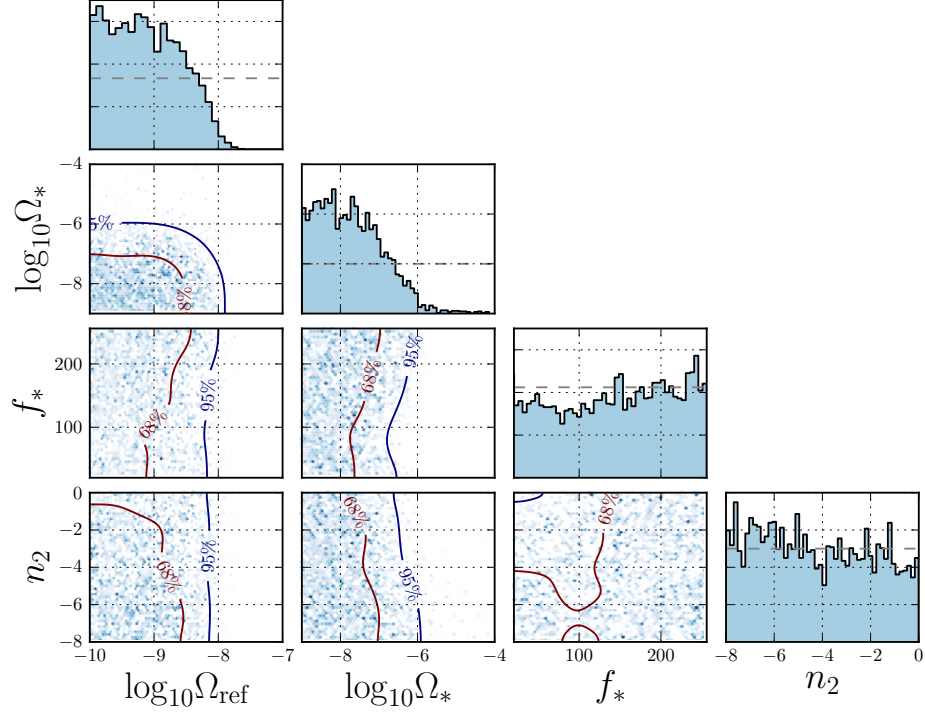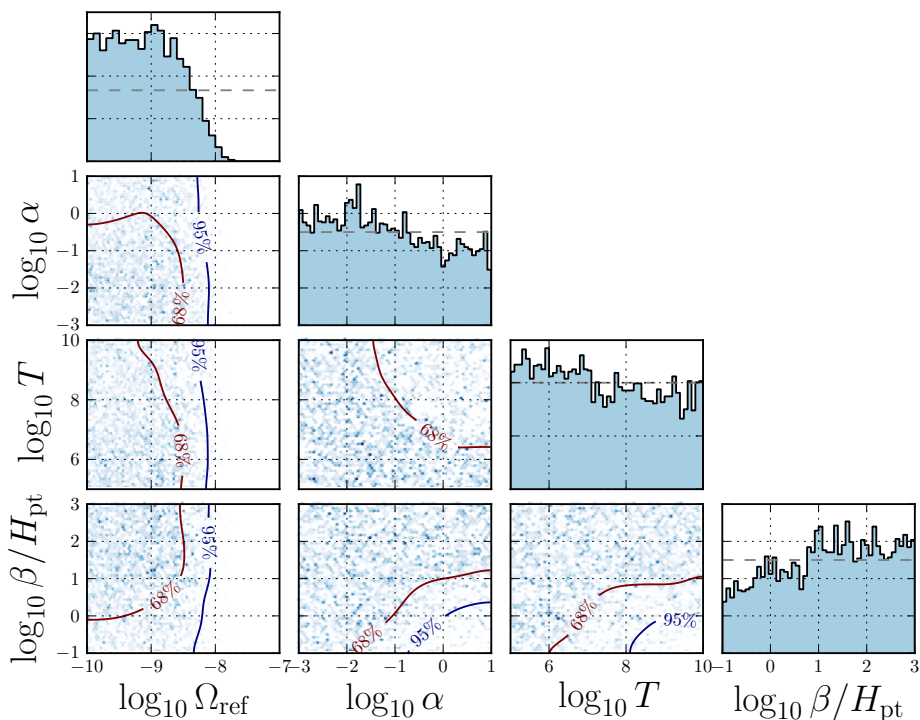
Figure 7.9: Posterior distributions for the phenomenological(BC)+CBC model parameters. The posterior on Ω_{ref} allows to obtain an UL at 95% CL of 5.91×10^{-9}. β/H_{pt} shows preference for larger values. The posteriors on α and T_{pt} show no preference for any particular region. However, exclusions at 95% CL are obtained in parameter space. Values of $\alpha > 1$, $T_{pt} > 10^8 \text{GeV}$ and $\beta/H_{pt} < 1$ are excluded at 95% CL.

preference for any particular region. As noted above, the amplitude of the spectra from BC is larger than those from SW for the same set of parameters. For this reason, the constraints on the SW model are less stringent.

The search was repeated though setting delta priors over β/H_{pt} and T_{pt}. The results are in Table 7.5. The dashed lines denote no sensitivity for exclusion.

Phenomenological model (sound waves)		
$\Omega_{BC}^{95\%}$ (25 Hz)		
$\beta/H_{pt} \setminus T_{pt}$	10^7 GeV	10^8 GeV	10^9 GeV
0.1	–	–	–
1	6.09×10^{-10}	3.26×10^{-9}	1.41×10^{-10}
10	–	–	–

Table 7.5: The 95% CL upper limits on $\Omega_{SW}^{95\%}$(25 Hz) for fixed values of β/H_{pt} and T_{pt}, and $v_w == 1$. The dashed lines denote no sensitivity for exclusion.

Finally, the search was repeated for lower v_w. The results are in Table 7.6. The Bayes factors indicate that there is no evidence for a signal described by the phenomenological model in the data. The predicted energy density Ω_{sw} is lower than with $v_w = 1$. There is no difference in the UL on Ω_{cbc} as v_w is varied.

In summary, using the data from the three observing runs from LIGO-Virgo we have been able to place ULs at 95% CL on the normalized energy density from unresolved CBCs and a FOPT. The data can exclude part of the parameter space at large temperatures. In a scenario where bubble collisions dominate, with $v_w = 1$ and $\kappa_\phi = 1$, part of the parameter space with $T_{pt} > 10^8 \text{GeV}$, $\alpha > 1$ and $\beta/H_{pt} < 1$ is excluded at 95% CL. In the case of dominant sound waves, the exclusions are limited for
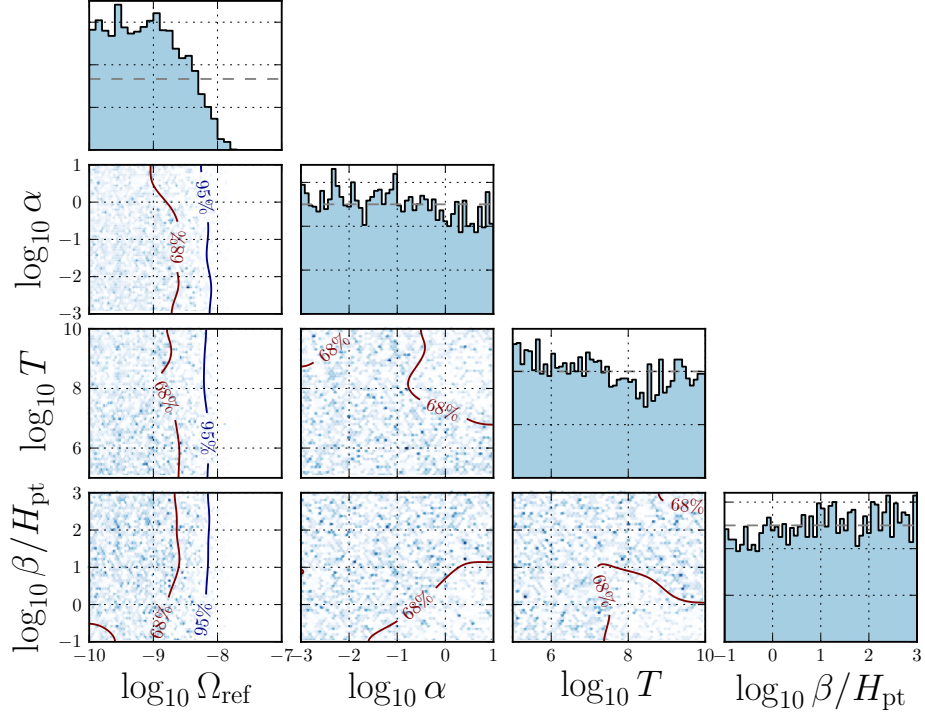
Figure 7.10: Posterior distributions on the phenomenological(SW)+CBC model parameters. Image retrieved from Ref. The posterior distribution on Ω_{ref} allows to obtain an UL at 95% CL of 5.86×10^{-9}. The posteriors on α, T_{pt} and β/H_{pt} show no preference for any particular region.

Phenomenological model (sound waves)		
v_w	$\log \mathcal{B}_{\mathrm{noise}}^{\mathrm{CBC+SW}}$	UL at 95% CL on Ω_{sw}
0.7	-0.607	5.93×10^{-9}
0.8	-0.597	5.77×10^{-9}
0.9	-0.668	5.84×10^{-9}

Table 7.6: Upper limits on the energy density in GWs from SWs, $\Omega_{sw}^{95\%}$, for fixed values of the bubble wall velocity.

$\beta/H_{pt} < 0.1$ and $T_{pt} > 10^8$GeV. These results show the importance of using LIGO-Virgo GW data to place constraints on new phenomena related to strong FOPTs in the early Universe.

7.4   Primordial Black Holes

Primordial Black Holes (PBHs) could have formed in the early Universe from gravitational collapse of large inhomogeneities in the early Universe [170]. As listed in Ref. [149], there are many scenarios how such inhomogeneities could have formed. Prototypical examples include quantum fluctuations generated during cosmological inflation and cosmological first order phase transitions. PBHs could have a mass $M \sim c^3 t/G \sim 10^{15} t/(10^{-23} s)g$, so the mass range is very wide considering t since Planck time until now. E.g.: PBHs formed at the Planck time ($t = 10^{-43}$s) would have a mass of 10^{-5}g, while those formed at $t = 1s$ could have a mass as high as $10^5 M_\odot$. Also, the PBH mass is proportional to the horizon mass at the time the PBH forms.

Many are the possible scenarios under which these inhomogeneities may have collapsed. As provided by Ref [149], there is a list of these scenarios, collapse from inhomogeneities during the radiation-dominated era, critical collapse, collapse from single-field inflation, collapse from multi-field inflation [171], from inhomogeneities during matter-dominated era [172], collapse of cosmic string loops [173], collapse from bubble collisions, collapse of scalar field and domain walls [174]. We will focus on the collapse of large inhomegeneities generated during inflation. In this case, overdense regions in space would stop expanding and re-collapse [175] during radiation dominated era [6]. To explain the collapse, we first introduce the density contrast induced by these fluctuations at some scale, denoted by δ. If the density contrast exceeds the critical value δ_c, the region will collapse gravitationally and form a PBH after the fluctuation re-enters horizon. An estimate of the value of δ_c was first obtained by Carr in Ref. [176], where he studied the Jeans mass of the fluctuation. This study led to $\delta_c = 1/3$. More recent numerical studies have shown that the value of δ_c is a bit higher. In our search we assume $\delta_c \in [0.4, 2/3]$ [177].

The concept of a region entering the horizon mnetioned above is explained in what follows. During inflation, the length of large curvature perturbations increased exponentially. Some of these length scales became even larger than the Hubble horizon [7] (see black curves in Figure 7.11). After inflation, the large curvature perturbations on a comoving scale [8] k re-entered the horizon when $k = aH$, where a is the scale factor (the "size" of the Universe), that is when the physical length scale of the perturbation became smaller than the Hubble horizon.

7.4.1   Parameters describing PBHs

In what follows, the Lambda Cold Dark Matter (ΛCDM) model applies with an age of the Universe of $t_o = 13.8$Gyr. From The Friedmann equation, the density ρ and temperature T are given by

$$H^2 = \frac{8\pi\,G}{3}\,\rho = \frac{4\pi^3\,G}{45}\,g_*\,T^4\,.\tag{7.9}$$

As mentioned above, PBHs produced by critical collapse formed when large curvature perturbations of scale k re-entered the horizon (see Figures 7.11 and 7.12). For that reason, it can be assumed that the mass of the PBH is equivalent to M_k. Consequently, M follows the scaling law [178]

$$M = \kappa M_k \left(\delta_m - \delta_c\right)^\gamma\,,\tag{7.10}$$

---

[6]The radiation-dominated era is the stage after reheating, where many of the light elements get produced [150]

[7]Hubble horizon is a conceptual horizon defining the boundary between particles that are moving slower than the speed of light relative to an observer at one given time and a causally un-connected region of space time. From causality, a particle outside the light cone of a particle P cannot "connect" in any way to the particle P, unless its speed is faster than the speed of light, which is not possible. Hence, anything outside the Hubble volume is irrelevant for particle P as it can never reach it.

[8]A small comoving distance between two nearby objects in the Universe is the distance between them which remains constant with time if the two objects are moving with the Hubble flow. In other words, it is the distance between them that would be measured with rulers at the time they are being observed (the proper distance) divided by the ratio of the scale factor of the Universe then to now, i.e.: the proper distance multiplied by $(1 + z)$, where z is the redshift.
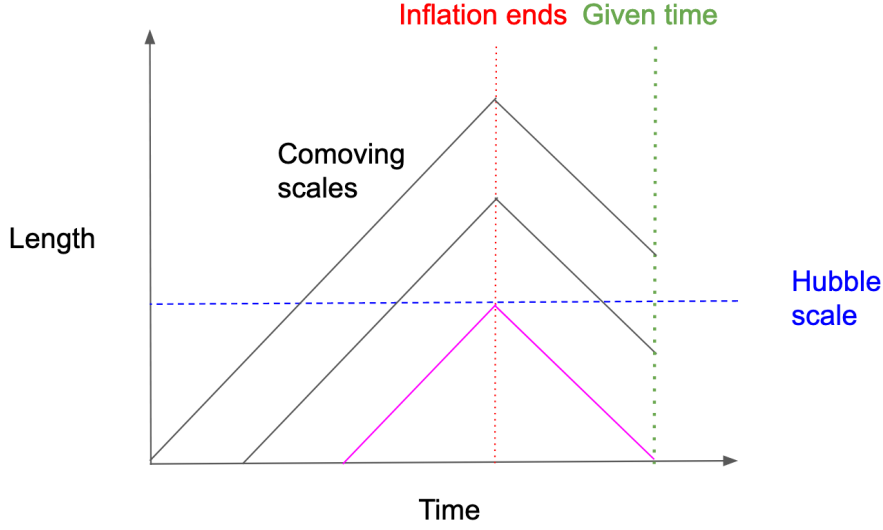
Figure 7.11: Evolution of comoving length scales (associated with the Fourier wavelengths of the scalar field fluctuations) during and after inflation. The end of inflation is represented by the vertical dotted red line. Before inflation, the length of the scales increases exponentially. After inflation, they start decreasing. The largest scales by the end of inflation are those that "started" first. In this schematics, the pink scale is the only one that did not grow to super-horizon sizes during inflation, while the black ones did. I.e.: the length scales such as that of the pink comoving scale did not grow over Hubble scales. This can also be expressed as the pink scales did not "exit" the horizon. Super-horizon is manifested as curvature perturbations. As super-horizon modes re-enter the horizon, they source acoustic oscillations in the post-inflationary plasma. Those scales that enter the earliest oscillate for longer and so they damp the most by the time the CMB is generated at recombination. So, the longest-wavelength modes are most evident in the temperature spectrum of the CMB

where M_k is given by

$$M_k \approx 1.4 \times 10^{13} \left(\frac{k}{\mathrm{Mpc}^{-1}} \right)^{-2} \left(\frac{g_{*,s}^4 g_*^{-3}}{106.75} \right)^{-1/6}. \tag{7.11}$$

In Eq. (7.10), δ_m is the density contrast, related to the curvature perturbations δ_ζ by $\delta_m = \delta_\zeta - 3/8\delta_\zeta^2$. The value of κ is dependent on the procedure used to smooth the primordial perturbations [179]. The value $\gamma = 0.36$ is the universal critical exponent during radiation domination [180]. In most PBH studies, in order to ease the calculation, all PBHs are assumed to have the same mass M or at least mass in a range $[M - \Delta M, M + \Delta M]$ for $\Delta M < M$.

The fraction of the Universe's mass in PBHs at their formation time t_i is denoted by $\beta(M)$. It is given by [149]

$$\beta(M) \equiv \frac{\rho_{\mathrm{PBH}}(t_i)}{\rho(t_i)} = \frac{4M}{3T_i} \frac{n_{\mathrm{PBH}}(t)}{s(t)} \approx 7.99 \times 10^{-29} \gamma^{-1/2} \left(\frac{g_{*i}}{106.75} \right)^{1/4} \left(\frac{M}{M_\odot} \right)^{3/2} \left(\frac{n_{\mathrm{PBH}}(t_0)}{1 \, \mathrm{Gpc}^{-3}} \right), \tag{7.12}$$

which relates it with the number density of PBHs $n_{\mathrm{PBH}}(t)$. In Eq. (7.12), the subscript i indicates the values are at the epoch of PBH formation. The current density parameter for PBHs is given by [149]

$$\Omega_{\mathrm{PBH}} \equiv \frac{\rho_{\mathrm{PBH}}}{\rho_{\mathrm{crit}}} = \frac{M \, n_{\mathrm{PBH}}(t_0)}{\rho_{\mathrm{crit}}} = \beta \, \Omega_{\mathrm{CMB}} \, (1 + z) \sim 10^6 \, \beta \left(\frac{t}{\mathrm{s}} \right)^{-1/2} \sim 10^9 \, \beta \left(\frac{M}{M_\odot} \right)^{-1/2}, \tag{7.13}$$

which allows to rewritte Eq. (7.12) as

$$\beta(M) \approx 7.06 \times 10^{-18} \gamma^{-1/2} \left(\frac{h}{0.67} \right)^2 \left(\frac{g_{*i}}{106.75} \right)^{1/4} \Omega_{\mathrm{PBH}}(M) \left(\frac{M}{10^{15} \, \mathrm{g}} \right)^{1/2}. \tag{7.14}$$
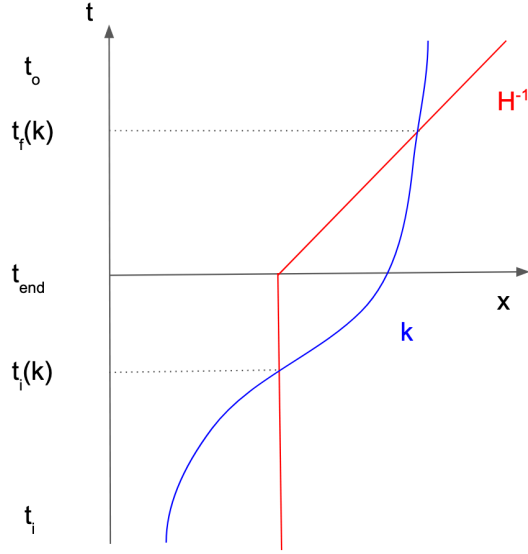
Figure 7.12: Scale k re-entering the Hubble horizon (red solid line). The vertical axis represents time and the horizontal space. Inflation takes place from t_i to t_{end}. During inflation, large curvature perturbations (blue solid line) enlarge exponentially until the point where they exit the Horizon at $t_i(k)$. After inflation, the Horizon increases while the rate of growth of the large curvature perturbations diminishes. This leads to the scale k reentering the Horizon.

It is convenient to define f_{PBH}, given by [181]

$$f_{PBH} \equiv \frac{\Omega_{PBH}}{\Omega_{CDM}} \approx 3.8\,\Omega_{PBH} \approx 2.4\,\beta_{eq}, \tag{7.15}$$

where β_{eq} is the PBH mass fraction at matter-radiation equality. The parameter f_{PBH} is the ratio of the current PBH mass density to the CDM density, which has the value 0.26 [182]. Constraining Ω_{PBH} places constraints on f_{PBH}. Depending on the mass of the PBH, it may have evaporated by today. Black holes radiate thermally with a temperature given by

$$T_{\mathrm{BH}} = \frac{\hbar\,c^3}{8\pi\,G\,M\,k_{\mathrm{B}}} \sim 10^{-7}\left(\frac{M}{M_\odot}\right)^{-1}\mathrm{K}\,, \tag{7.16}$$

so they evaporate completely in a timescale $\tau(M) \sim \frac{G^2\,M^3}{\hbar\,c^4} \sim 10^{64}\left(\frac{M}{M_\odot}\right)^3$ yr. This implies that only PBHs with a mass smaller than 10^{15}g could have evaporated by now. For a BH of mass $M \equiv M_{10}\cdot 10^{10}$g the temperature is $T_{BH} \simeq 1.06\cdot M_{10}^{-1}$TeV, so the BH does not have neither charge nor angular momentum. The mass loss rate of an evaporating BH can be expressed as

$$\frac{\mathrm{d}M_{10}}{\mathrm{d}t} = -5.34\times 10^{-5}\,f(M)\,M_{10}^{-2}\,\mathrm{s}^{-1}\,, \tag{7.17}$$

where $f(M)$ is a measure of the number of emitted particle species, normalised to unity for a BH with mass much larger than 10^{17}g (see extensive review in Ref. [149]). If the contribution from all particles of the SM are added up to 1TeV, $f(M) = 15.35$ and the lifetime of a PBH is given by $\tau \approx 407\left(\frac{f(M)}{15.35}\right)^{-1}M_{10}^3$ s.

7.5 Implication for the formation of PBHs from the three observing runs

The PBH formation is accompanied by a GWB generated at second order in the cosmological perturbation theory due to scalar perturbations [183]. The spectrum of the generated GWB is given in terms of the curvature power spectrum. In our search, we do not choose any particular model of

inflation. We parametrize the peak in the curvature power spectrum by its position k_*, its width Δ and the integrated power A. It must be noted that instead of indicating the position of the peak in terms of frequencies, the wavenumber is used. The relation between the wavenumber and frequency is $k = 2\pi f/c$, and using the definition of megaparsec: $1\text{Mpc} \simeq 3.26 \times 10^6$ light-years, the final relation we use is $f/Hz = 1.6 \cdot 10^{-15} k/\text{Mpc}^{-1}$. We choose a log-normal shape

$$\mathcal{P}_\zeta(k) = \frac{A}{\sqrt{2\pi}\Delta} \exp\left[-\frac{\ln^2(k/k_*)}{2\Delta^2}\right] \tag{7.18}$$

for the peak in the curvature power spectrum. A similar study was done in Ref. [184] for data from the two first observing runs. The curvature power spectrum is represented in Figure 7.13 for different sets of $\{f_*, A, \Delta\}$. In the $\Delta \to 0$ limit the spectrum reduces to a Dirac delta function $\lim_{\Delta\to 0}\mathcal{P}_\zeta(k) = A\delta(ln(k/k_*))$. For $\Delta << 1$ the amplitude of the induced GWB as well as the PBH abundance become independent of Δ. For $\Delta \gtrsim 1$ these quantities are determined by the peak amplitude $\mathcal{P}_\zeta(k_*) = \frac{A}{\sqrt{2\pi}\Delta}$.
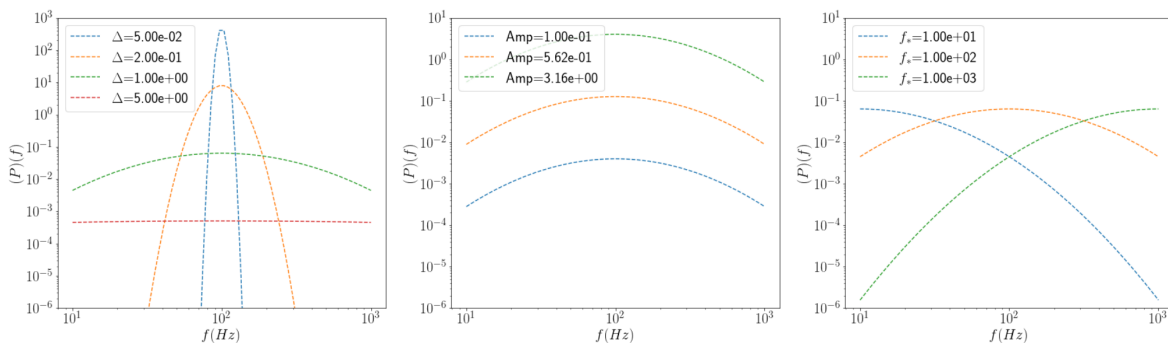

Figure 7.13: Curvature power spectrum for different sets of $\{f_*, A, \Delta\}$. **Left** $A = 1$ and $f_* = 100$Hz. Smaller Δ lead to narrower peaks. **Centre** $\Delta = 1$ and $f_* = 100$Hz. **Right** $\Delta = 1$ and $A = 1$. Different f_* only shift the spectrum.

From CMB observations, the amplitude of the curvature power spectrum is of the order of $\mathcal{O}(10^{-9})$, which implies a very weak GWB that cannot be probed by any foreseeable detector. Nevertheless, for PBHs to form, the curvature power spectrum amplitude needs to be of the order of $\mathcal{O}(0.01)$ at small scales, which leads to a GWB that can be probed by the LIGO-Virgo network. Peaks in the curvature power spectrum with an amplitude of $\mathcal{O}(0.01)$ can be generated by features in the inflaton potential, such as an inflection point in single field inflation [185] or the change of the potential from convex to concave in thermal inflation [186].

We ran a Bayesian search over the O3 isotropic data using as spectrum of the scalar induced GWB [187, 188]

$$\Omega_{GW}(f) = 0.387 \cdot \Omega_R \left(\frac{g_{*,s}^4 g_*^{-3}}{106.75}\right)^{-1/3} \frac{1}{6} \int_{-1}^{1} dx \int_{1}^{\infty} dy \mathcal{P}\left(\frac{y-x}{2}\right) \mathcal{P}\left(\frac{x+y}{2}\right) F(x,y), \tag{7.19}$$

where $\Omega_R = 5.38 \times 10^{-5}$ is the radiation abundance [182] and $g_{*,s}$ and g_* are the relativistic degrees of freedom. The LIGO-Virgo network has the highest sensitivity in the frequency range between 10-500Hz, which corresponds to wavenumbers between $\sim 10^{16} - 10^{17}\text{Mpc}^{-1}$. These scales re-entered the horizon when temperatures were above 10^8GeV, which corresponds to $g_{*,s} = g_* \simeq 100$. The spectrum peaks at around the same wavenumber as the curvature power spectrum. The GWB spectrum is represented in Figure 7.14 for different combinations of Δ, f_*, A, and is added to the non-negligible contribution from CBCs (Ω_{ref} is chosen to be 6×10^{-9}). For fixed values of A, f_*, the larger the width of the peak in the curvature power spectrum, the smaller in amplitude the GWB spectrum. For fixed Δ, f_*, as the integrated power of the peak in the curvature power spectrum increases, the amplitude of the GWB spectrum increases as well. For fixed Δ and A, f_* indicates the frequency at which the GWB peaks. The GWB spectrum is given in terms of the function
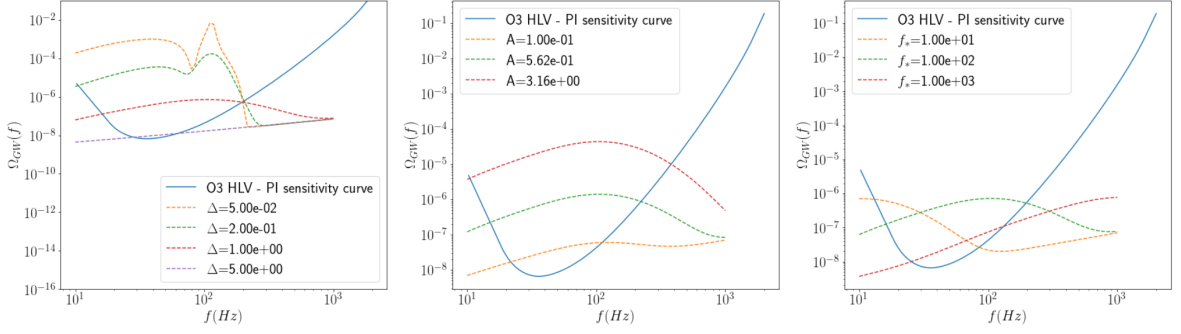
Figure 7.14: Spectrum of the GWB for different values of Δ, f_*, A added to the contribution from CBCs is compared with the PI sensitivity curve (solid blue line). **Left** $A = 1$ and $f_* = 100$Hz. The larger the width of the peak in the curvature power spectrum, the smaller in amplitude the GWB spectrum is. **Centre** $\Delta = 1$ and $f_* = 100$Hz. As the integrated power of the peak in the curvature power spectrum increases, the amplitude of the GWB spectrum increases as well. **Right** $\Delta = 1$ and $A = 1$. The peak frequency in the curvature power spectrum only shifts the spectrum in frequency.

$$F(x,y) = \frac{288(x^2 + y^2 - 6)^2(x^2 - 1)^2(y^2 - 1)^2}{(x-y)^8(x+y)^8}$$
$$\times \left[\left(x^2 - y^2 + \frac{x^2 + y^2 - 6}{2} ln \left| \frac{y^2 - 3}{x^2 - 3} \right| \right)^2 + \frac{\pi^2}{4}(x^2 + y^2 - 6)^2 \theta(y - \sqrt{3}) \right], \qquad (7.20)$$

represented in Figure 7.15. Alongside with $F(x,y)$, the integrand of Eq.(7.19) is dependent on the square of the curvature power spectrum, so for $\Delta << 1$ the GWB spectrum has a peak amplitude of $\Omega_{GW} = \mathcal{O}(10^{-5})A^2$.
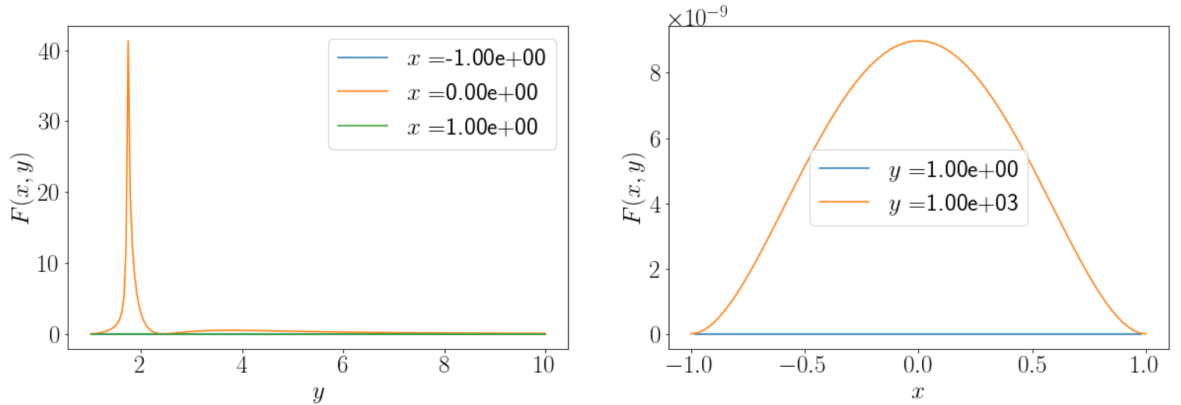
Figure 7.15: $F(x,y)$ evaluated for different values of x and y. **Left** F(x,y) for fixed values of $x = \{-1, 0, 1\}$. Extreme values -1 and 1 lead to a flat function, while for x=0 a peak arises close to y=2. **Right** F(x,y) for fixed values of $y = \{1, 1000\}$. y=1 leads to a flat function. For larger y, F(x,y) resembles a Gaussian centered in 0 and its amplitude increases as y increases.

The parameters of our search are $\underline{\theta} = (\Omega_{ref}, A, k_*, \Delta)$, with priors summarised in Table 7.7. The priors on the integrated power of the peak A and the peak wavenumber k_* are chosen so that the resulting spectrum can be probed by the current LIGO-Virgo network. The width Δ is chosen to cover narrow and wide peaks. Finally, the prior on Ω_{ref} stems from previous estimates of the CBC background [100].

Running the search led to a Bayes factor $\log \mathcal{B}_{\text{noise}}^{\text{CBC+PBH}} = -0.8$ which shows again no evidence for a signal. The posterior distributions for the parameters of the spectrum are in Figure 7.16. The posterior on Ω_{ref} allows to obtain a UL at 95% CL of 6.0×10^{-9}, which is consistent with the UL obtained in the O3 isotropic search [21]. Data excludes part of the parameter space in k_*/Mpc^{-1} and A. The region where the LIGO-Virgo interferometers have the highest sensitivity, $k_* \in [10^{16}, 10^{17}]\text{Mpc}^{-1}$, is

Parameter	Prior
Ω_{ref}	LogUniform(10^{-10}, 10^{-7})
A	LogUniform(10^{-3}, $10^{0.5}$)
k_*/Mpc^{-1}	LogUniform(10^{13}, 10^{21})
Δ	LogUniform(0.05, 5)

Table 7.7: Prior distributions used for the amplitude of the CBC background at 25 Hz, Ω_{ref}, the integrated power A of the peak in the curvature power spectrum, its position k_* and its width Δ.

where exclusions at 95% CL are obtained. The posterior on Δ shows no preference for any range of values.
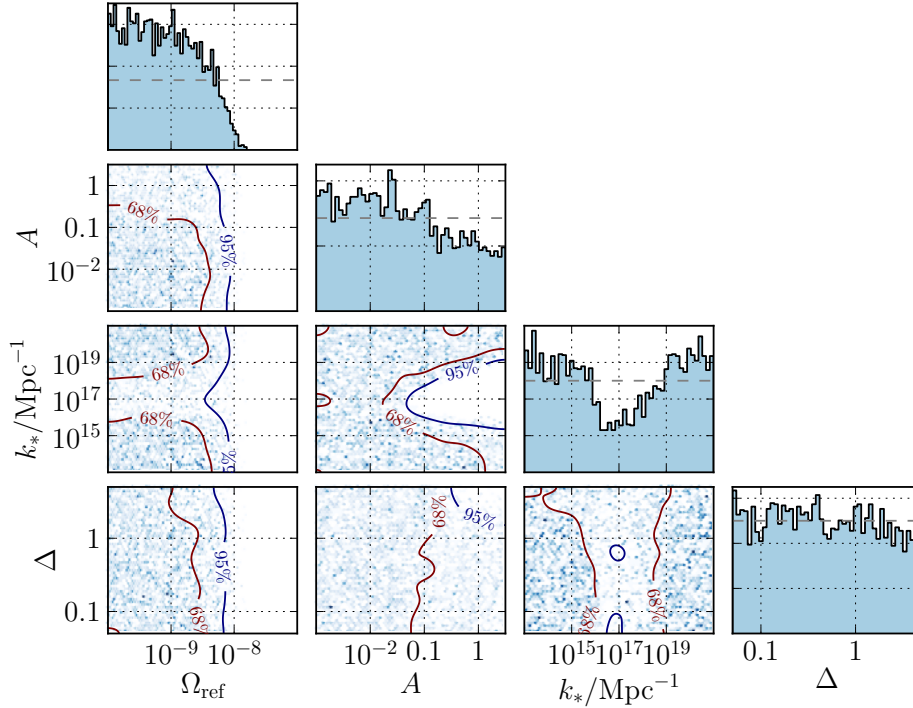
Figure 7.16: Posterior distributions on the parameters of the curvature power spectrum describing the peak of the curvature perturbations. The region were the LIGO-Virgo interferometer have the highest sensitivity, $k_* \in [10^{16}, 10^{17}]\text{Mpc}^{-1}$, is where exclusions at 95% CL are obtained in the plane $k_*/\text{Mpc}^{-1} - A$. The posterior on Δ shows no preference for any range of values.

We then re-ran the Bayesian search through setting delta priors on Δ and k_* to set upper limits on A. The results are in Table 7.8. The most stringent ULs are obtained for $k_* = 10^{17}\text{Mpc}^{-1}$, which corresponds to ~ 100 Hz, where the interferometers have their highest sensitivity. For large widths, $\Delta >> 1$, the UL on A is independent on the scale (see purple dashed spectra in Figure 7.17). The most stringent UL is obtained for a narrow peak $\Delta = 0.05$ and $k_* = 10^{17}\text{Mpc}^{-1}$. In all these runs, the ULs at 95% CL on Ω_{ref} are between 5.5×10^{-9} to 6.6×10^{-9}, which are in agreement with the O3 isotropic results.

The next step in our analysis consisted on comparing the direct bounds set on A by LIGO-Virgo with the indirect bounds from BBN and CMB and the constraints from PBH formation. The indirect bounds from the BBN come from the fact that an extra component of radiation such as the GWB speeds up the expansion of the Universe, which can be checked by light element abundances produced in the epoch of the BBN [188, 11]. This extra radiation can be parametrized by the effective number of neutrino species, N_ν, which is related to the energy density spectrum $\Omega_{gw} h^2 \sim 5.6 \cdot 10^{-6}(N_\nu - 3)$ [188]. For a fixed value of baryon number, N_ν can be constrained from the observational abundances of

	$k_* = 10^{15}\,\text{Mpc}^{-1}$	$k_* = 10^{17}\,\text{Mpc}^{-1}$	$k_* = 10^{19}\,\text{Mpc}^{-1}$
$\Delta = 0.05$	2.1	0.02	1.4
$\Delta = 0.2$	2.2	0.03	1.6
$\Delta = 1$	1.6	0.05	1.8
$\Delta = 5$	0.2	0.2	0.3

Table 7.8: Upper limits on the integrated power A of the peak in the curvature power spectrum at 95% CL for fixed values of the peak position k_* and width Δ.
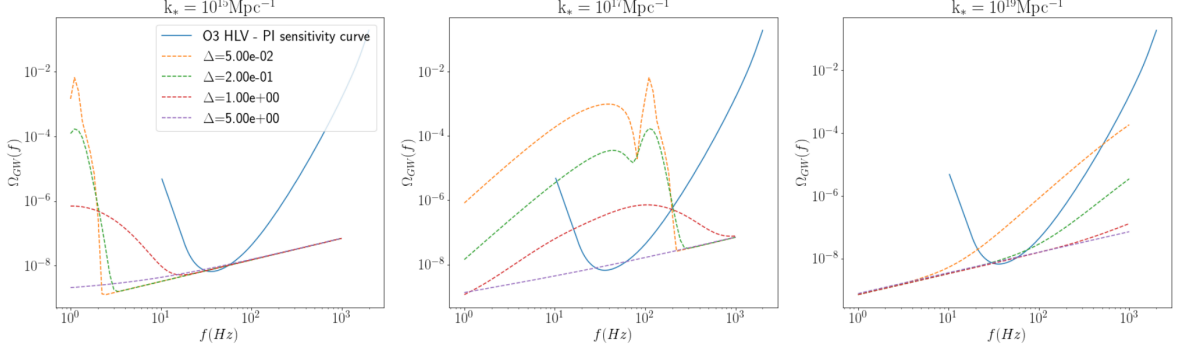

Figure 7.17: Spectrum of the GWB from the formation of PBHs ($A = 1$) added to the contribution from CBCs. The spectrum is obtained for different values of the width of the curvature power spectrum. The same spectra are plotted for increasing peak frequencies from left to right.

^4He and D, and thus $\Omega_{GW}h^2$ as well. In Ref. [188] an indirect bound on the abundance of GWs of $\Omega_{GW}h^2 < 1.8 \times 10^{-6}$ is obtained. Similarly, a GWB at the time of decoupling of the CMB would alter the observed CMB and the matter power spectra [11], leading to a bound on the abundance of GWs of $\Omega_{GW}h^2 < 1.7 \times 10^{-6}$ [189].

To compute the bounds on A obtained from constraints in the PBH formation, we calculated the PBH abundance from the peak in the curvature power spectrum following the procedure in Ref. [190]. It was computed for two benchmark cases. For that purpose, Eq.(7.10) is used. As mentioned above, $\delta_c \in [0.4, 2/3]$, so the two values chosen were 0.45 and 0.65, which were paired with $\kappa = 11.0$ and $\kappa = 3.0$, respectively. The difference in the PBH abundance estimation between the two benchmark cases reflects the uncertainties in the calculation of the PBH formation. In Figure 7.18, the BBN/CMB bounds (shaded blue area) are compared with the LIGO-Virgo bounds for a very narrow peak $\Delta \to 0$ of the curvature power spectrum (shaded red area) and the bounds from PBH formation (green solid lines). The uppermost axis shows the masses associated with a certain scale.

The bounds from LIGO-Virgo are more constraining than the indirect bounds from BBN and CMB in the region $10^{16} - 10^{19} \text{Mpc}^{-1}$. However, the constraints from the PBH formation are the most stringent in the whole range of scales. Nevertheless, with the LIGO-design sensitivity (dashed red line) and that of ET (dashed orange line), the bounds will be more constraining than those from PBH formation. The same procedure was then repeated but assuming a log-normal peak with $\Delta = 1$ as the curvature power spectrum, Eq. (7.18). The results are in Figure 7.19 leading to the same conclusions [191].

In summary, the Bayesian analysis does not show evidence for a signal but indicates that the data has the sensitivity to exclude part of the parameter space of the model. We have obtained constraints depending on the width of the peak, its location, and the integrated power of the peak. These constraints are stronger than the ones arising from BBN and CMB observations in the range $\mathcal{O}(10^{15}) < k_*/\text{Mpc}^{-1} < \mathcal{O}(10^{18})$. These constraints, reaching $A \simeq 0.02$ for a narrow peak at $k_* \simeq 10^{17}\text{Mpc}^{-1}$, are still strong enough to compete with the constraints arising from the abundance of PBHs that such peak in the curvature power spectrum corresponds to. However, we find that current ground-based experiments at their design performance, and the future Einstein Telescope will reach the required sensitivity, providing a very powerful probe of the standard formation mechanism of very light PBHs.
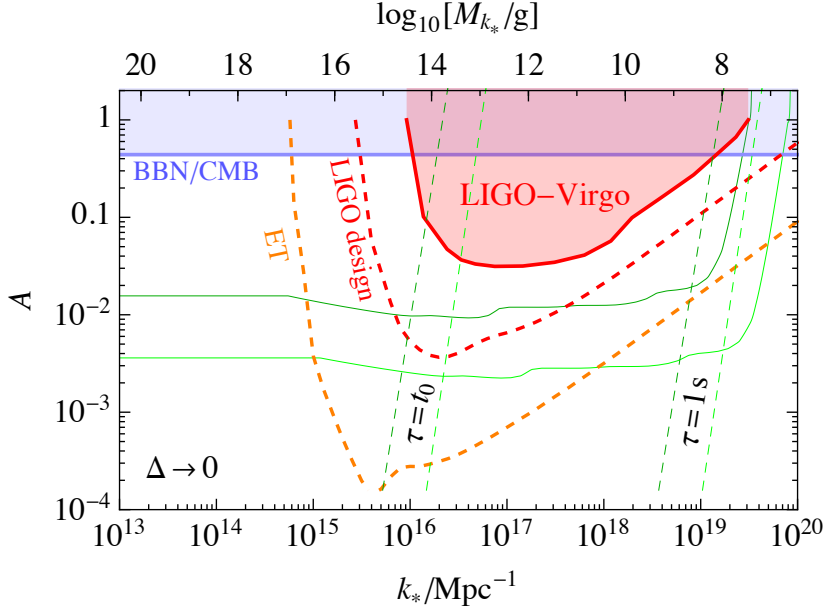
Figure 7.18: Comparison of bounds set on A from the LIGO-Virgo network, BBN, CMB, and PBH formation. The bounds from LIGO-Virgo (shaded red region) are obtained with a Dirac delta function peak in the curvature power spectrum, i.e.: $\Delta \to 0$. The bounds from the BBN and CMB (shaded blue region) are indirect bounds on the abundance of GWs. The bounds from PBH formation are obtained by calculating the PBH abundance from the peak in the curvature power spectrum, Eq. (7.18). It was calculated for two benchmark cases: $\{\kappa = 3.0, \delta_c = 0.65\}$, upper solid green line and $\{\kappa = 11.0, \delta_c = 0.45\}$, lower solid green line. The dashed red line represents the bound that would be obtained with the LIGO-Design sensitivity and in orange with ET.
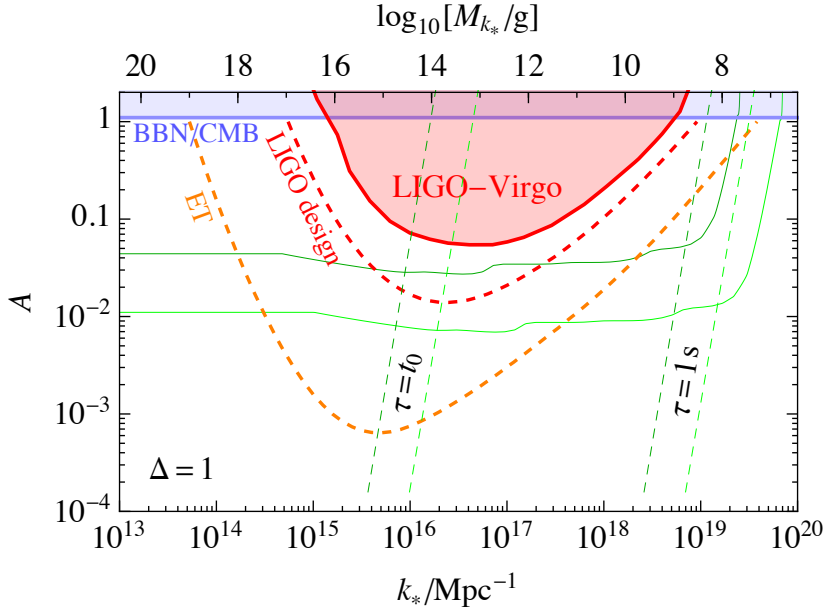
Figure 7.19: Comparison of bounds set on A from the LIGO-Virgo network, BBN, CMB, and PBH formation. The bounds from LIGO-Virgo (shaded red region) are obtained for $\Delta = 1$ in the spectrum given by Eq.(7.18). The bounds from the BBN and CMB (shaded blue region) are indirect bounds on the abundance of GWs. The bounds from PBH formation are obtained by calculating the PBH abundance from the peak in the curvature power spectrum, Eq. (7.18). It was calculated for two benchmark cases: $\{\kappa = 3.0, \delta_c = 0.65\}$, upper solid green line and $\{\kappa = 11.0, \delta_c = 0.45\}$, lower solid green line. The dashed red line represents the bound that would be obtained with the LIGO-Design sensitivity and in orange with ET.

Chapter 8

Conclusions

In this PhD document, several studies on Gravitational Waves using LIGO/Virgo data have been presented, in which I was involved and that led to a number of publications in journals.

I made contributions to the development of novel instrumented baffles for Virgo via the development of necessary simulations and laboratory work related to the calibration of photo sensors. The instrumented baffle was installed in the Virgo Input Mode Cleaner end mirror in April 2021 and it is part of the regular Virgo operations since then. In this thesis, the results from the new baffle have been presented. The data have been used to measure the scattered light inside the cavity, which presents features dominated by scattering processes from the mirrors facing the instrumented baffle in the triangular cavity. The data were compared to simulations, which provides a fair description of the data. This shows the potential of using data measured by instrumented baffles alongside with a simulation tool to define quality criteria for mirror surfaces, detect defects in the mirrors, and in general improve the understanding of the scattered light inside ground-based gravitational wave experiments like Virgo.

In the physics analysis side, the thesis focused on the search for an isotropic stochastic gravitational wave background (GWB) using data from Advanced LIGO and Virgo O1-O3 observing runs. No signal of a GWB has been found yet and 95% confidence level upper limits on the energy density spectrum amplitude were set as a function of the frequency, significantly improving previous bounds. In addition, by combining the information of the stochastic search with that of the compact binary coalescence (CBC) in LIGO-Virgo, new information of the merging rate of black holes at large redshift has been obtained. The results on the isotropic GWB have been reinterpreted in terms of several models for new phenomena in the early universe. In any case, in the Bayesian analysis a simultaneous fit is performed in the data to constrain the parameter of the model and the energy density in gravitational waves from a possible unresolved CBC contribution (foreground) of astrophysical origin. The document first explores the presence of strong first order phase transitions leading to gravitational waves and upper limits are imposed on the parameters of the phase transition at large temperatures, inaccessible to colliders. This demonstrates the potential of the LIGO-Virgo data to place constrains on strong first-order phase transitions in the early universe. The data are also used to place constrains on models describing the inflationary formation of primordial black holes accompanied by scalar fluctuations, leading to gravitational waves. Again the LIGO-Virgo data are able to constrain part of the phase space of the model. We have obtained constraints depending on the width of the peak in the spectrum describing the GWB from primordial black holes, its location, and the integrated power of the peak. The resulting constraints are stronger than those arising from big bang nucleosynthesis or cosmic microwave background observations. In addition, we find that the constraints from LIGO and Virgo, at their design sensitivity, and from the Einstein Telescope can compete with those related to the abundance of the formed primordial black holes.

The signals from a gravitational wave background are the holly grail in the study of the early universe using gravitational waves and will remain at the center of the physics program for the future experiments. This will come together with further developments in the understanding of the noise in the experiments.

Conventions

The conventions used in this thesis are summarized in what follows.

- Greek indices refer to spacetime coordinates.

- Latin indices refer to space coodinates.

- The Fourier transform is defined as

$$s(t) = \frac{1}{\sqrt{2\pi}} \int_{-\infty}^{\infty} \tilde{s}(f) e^{2\pi \mathrm{ift}} \mathrm{dt}.$$

- The parameter c is used to denote the speed of light and it has a value of $\mathrm{c} = 2.998 \times 10^{10}$cm/sec. It is set to 1 in most derivations.

- The parameter G is used to denote Newton's gravitational constant and it takes the value $\mathrm{G} = 6.673 \times 10^{-8}\mathrm{cm}^3/\mathrm{gm} \cdot \sec^2$.

- The parameter $\rho_{\mathrm{c,o}}$ denotes the critical energy density required today to close the Universe, and it takes the value $\rho_{\mathrm{c,o}} = 3\mathrm{c}^2\mathrm{H}_{\mathrm{o}}^2/(8\pi\mathrm{G}) \simeq 1.6 \times 10^{-8}\mathrm{h}_{100}^2\mathrm{ergs}/\mathrm{cm}^3$.

- The parameter H_{o} denotes the Hubble expansion rate today, and takes the value

$$\mathrm{H}_{\mathrm{o}} = \mathrm{h}_{100} \cdot 100 \frac{\mathrm{Km}}{\sec \cdot \mathrm{Mpc}} = 3.2 \times 10^{-18}\mathrm{h}_{100}\frac{1}{\sec} = 1.1 \times 10^{-28}\mathrm{c} \cdot \mathrm{h}_{100}\frac{1}{\mathrm{cm}}.$$

- The parameter h_{100} is a dimensionless parameter used to account for the different values of H_o found in the literature. It takes values between $\frac{1}{2}$ and 1 [88].

- Variables in bold or underlined represent vectors.

- Unless stated otherwise, speeds equal to 1 or $1/\sqrt{3}$ correspond to the speed of light or sound, respectively.

- The parameter m_{Pl} is used to denote the Planck mass and takes the value 1.22×10^{19} GeV.

- Signs in the Minkowski metric: $\eta_{\mu\nu} = \mathrm{diag}(-1, 1, 1, 1)$

- In General relativity, indices are raised and lowered with the flat metric $\eta_{\mu\nu}$.

- The symbol $\Box \equiv \eta_{\mu\nu}\partial^\mu\partial^\nu = \partial_\mu\partial^\nu$ represents the flat space d'Alembertian.

- The parameter $\hbar$ is Planck's constant, which takes the value $1.05 \cdot 10^{-34}\mathrm{J} \cdot \mathrm{s}$ [9].

Appendices

Appendix A

Polarization basis

As seen in chapter 1, the Fourier coefficients $h_{ab}(f, \hat{\Omega})$ are expanded in terms of the + and x polarization tensors

$$h_{ab}(f, \hat{\Omega}) = h_+(f, \hat{\Omega})e^+_{ab}(\hat{\Omega}) + h_x(f, \hat{\Omega})e^x_{ab}(\hat{\Omega}), \tag{A.1}$$

where $e^A_{ab}(\hat{\Omega})$ are the polarization tensors for the plus and cross polarizations, denoted by $A = +, x$. They are given by

$$e^+_{ab}(\hat{\Omega}) = \hat{m}_a\hat{m}_b - \hat{n}_a\hat{n}_b, \tag{A.2}$$

$$e^x_{ab}(\hat{\Omega}) = \hat{m}_a\hat{n}_b + \hat{n}_a\hat{m}_b, \tag{A.3}$$

where $\hat{\Omega}$, $\hat{m}$ and $\hat{n}$ are the unit vectors (see Figure A.1), defined as

$$\hat{\Omega} = \cos\phi\sin\theta\hat{x} + \sin\phi\sin\theta\hat{y} + \cos\theta\hat{z}, \tag{A.4}$$

$$\hat{m} = \sin\phi\hat{x} - \cos\phi\hat{y}, \tag{A.5}$$

$$\hat{n} = \cos\phi\cos\theta\hat{x} + \sin\phi\cos\theta\hat{y} - \sin\theta\hat{z}. \tag{A.6}$$
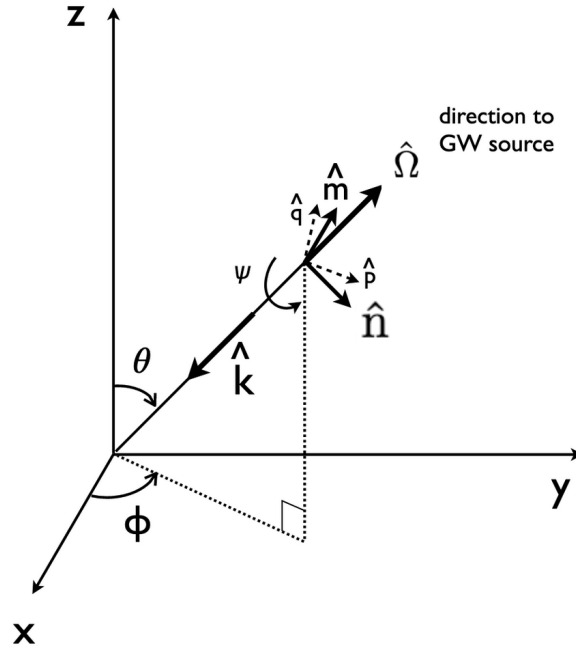
Figure A.1: Figure retrieved from Ref. [80]. Convention for the unit vectors $\{\hat{\Omega}, \hat{m}, \hat{n}\}$ in terms of which the polarization tensors $e^A_{ab}(\hat{\Omega})$ are expressed. The unit vector $\hat{\Omega}$ points towards the GW source. The other two unit vectors lie in the place perpendicular to $\hat{\Omega}$. The unit vectors $\hat{q}$ and $\hat{p}$ would be used in the case of a rotation in the $\{\hat{m}, \hat{n}\}$ plane of Ψ.

The polarization tensors satisfy $e^A_{ab}(\hat{n})e^{A',ab}(\hat{n}) = 2\delta^{A,A'}$. For waves propagating in the z direction, $\hat{m}$ and $\hat{n}$ can be identified as $\hat{x}$ and $\hat{y}$, respectively, so the polarization tensors are expressed in matrix form as

$$e^+_{ab} = \begin{pmatrix} 1 & 0 \\ 0 & -1 \end{pmatrix}_{ab} \quad , \quad e^x_{ab} = \begin{pmatrix} 0 & 1 \\ 1 & 0 \end{pmatrix}_{ab}. \tag{A.7}$$

Appendix B

Derivation of the cavity power in a Fabry-Perot cavity

The field stored in an FP cavity of length L is denoted by E_{cav}. The input test mass (ITM) has a reflection factor denoted by r_{ITM} and a transmittance factor denoted by t_{ITM}. Similarly, the end test mass (ETM) has reflection and transmittance factors denoted by r_{ETM} and t_{ETM}, respectively. The incoming field is denoted by E_{in}. A schematic representation of the FP and the fields involved in the calculation of E_{cav} is in Figure B.1.
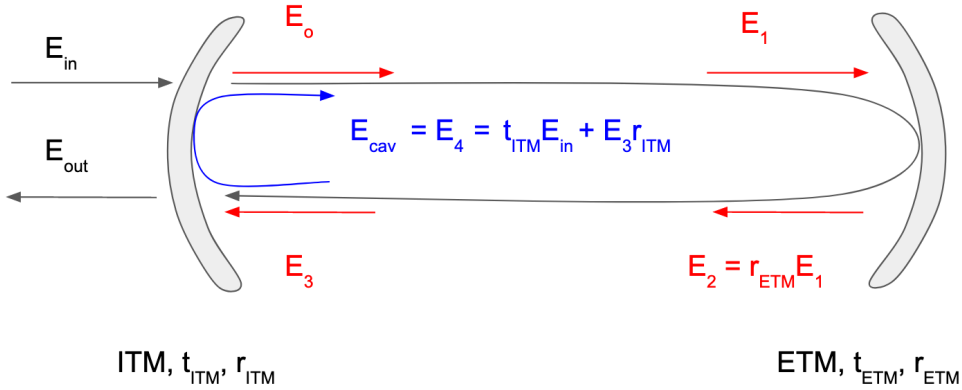
Figure B.1: Schematic representation of the field stored within a FP cavity with input mirror denoted by ITM and end mirror by ETM. Their transmissivities and reflectivities are represented by $t_{mirrorname}$ and $r_{mirrorname}$, respectively.

Following the schematic representation of fields in Figure B.1, E_1, E_2 and E_3 are given by

$$
\begin{aligned}
E_1 &= E_{cav}e^{-ikL}, \\
E_2 &= E_1 r_{ETM}, \\
E_3 &= E_2 e^{-ikL}, \\
E_4 &= t_{ITM}E_{in} + E_3 r_{ITM} = t_{ITM}E_{in} + E_{cav}r_{ETM}r_{ITM}e^{-2ikL},
\end{aligned}
\tag{B.1}
$$

where k is the wavenumber, given by $k = 2\pi/\lambda$, with λ the laser wavelength. Under stationary conditions, the field denoted by E_4 in Figure B.1 represent the field stored in the cavity. The reason is that under resonance, the field reflected by ITM has the same phase as the incoming field, so the fields add up constructively, $E_{cav} = E_4 = t_{ITM}E_{in} + E_3 r_{ITM}$. Consequently, the field stored in the cavity is given by

$$
E_{cav} = \frac{t_{ITM}E_{in}}{1 - r_{ITM}r_{ETM}e^{-2ikL}} .
\tag{B.2}
$$

The field reflected by the cavity is given by

$$E_{out} = r_{ITM}E_{in} + t_{ITM}E_3 = r_{ITM}E_{in} - t_{ITM}e^{-2ikL}E_{cav} \tag{B.3}$$

B.0.1 Stationary conditions

Under stationary conditions, the length of the cavity is a multiple of the wavelength of the laser $n\lambda$, where n is an integer, plus a very small deviation δ. The exponential in Eq. (B.2) can thus be approximated by

$$e^{-2ikL} = e^{-2i\pi L/\lambda} = e^{-2i\pi(n\lambda+\delta)/\lambda} = e^{-2i\pi n}e^{-2i\pi\delta/\lambda} \sim 1, \tag{B.4}$$

where the small deviation has been taken to be $\delta \sim 0$ and the resonant condition is considered, i.e.: n is even. The power transmittance is defined as the square of the transmittance factor $T = t^2$. Also, from energy conservation $r^2 + t^2 = 1$. Eq. (B.2) can be further simplified by using a series of simplifications derived below. The denominator in Eq. (B.2) can be simplified as

$$\frac{1}{1 - r_{ITM}r_{ETM}} = \frac{1 + r_{ITM}r_{ETM}}{1 - (r_{ITM}r_{ETM})^2} = \frac{1 + r_{ITM}r_{ETM}}{1 - (1 - T_{ITM})(1 - T_{ETM})}$$
$$\simeq \frac{1 + r_{ITM}r_{ETM}}{T_{ITM} + T_{ETM} + \mathcal{O}(T_{ITM}T_{ETM})}, \tag{B.5}$$

where in the last equality terms of order above $\mathcal{O}(T_{ITM}T_{ETM})$ have been discarded. This approximation is reasonable since in real IFOs, the ITM and ETM have transmittances $T_{ITM} = 0.014, T_{ETM} = 5 \cdot 10^{-6} \Rightarrow T_{ITM}T_{ETM} << 1$. The numerator in Eq. (B.5) can be further simplified as

$$1 + r_{ITM}r_{ETM} = 1 + \sqrt{(1 - T_{ITM})(1 - T_{ETM})} \simeq 1 + \sqrt{1 - T_{ITM} - T_{ETM}} \simeq 2 - \frac{T_{ITM} + T_{ETM}}{2}, \tag{B.6}$$

where the last equality is obtained by Taylor expanding $\sqrt{1 - T_{ITM} - T_{ETM}}$. Finally, with the simplifications from Eqs. (B.5) and (B.6) the cavity field is

$$E_{cav} = \frac{t_{ITM}E_{in}}{1 - r_{ITM}r_{ETM}} = t_{ITM}E_{in}\frac{4 - (T_{ITM} + T_{ETM})}{2(T_{ITM} + T_{ETM})}. \tag{B.7}$$

Considering the real values used as transmittances, $T_{ITM} = 0.014, T_{ETM} = 5 \cdot 10^{-6}$, the fraction in Eq. (B.7) can be simplified to $(4 - T_{ITM})/(2T_{ITM}) \simeq 2/T_{ITM}$. The cavity field squared is the cavity power, which is given by

$$E_{cav} \simeq t_{ITM}E_{in}\frac{2}{T_{ITM}} \Rightarrow P_{cav} = |E_{cav}|^2 \simeq T_{ITM}P_{in}\frac{4}{T_{ITM}^2} = \frac{4}{T_{ITM}}P_{in}, \tag{B.8}$$

where $P_{in} = |E_{in}|^2$. The power reflected by the cavity E_{out} is given by the reflected input field added to the transmitted cavity field

$$E_{out} = E_{in}r_{ITM} + E_{cav}t_{ITM} \simeq E_{in}\left(r_{ITM} + 2\right). \tag{B.9}$$

The reflected power is then given by $P_{out} \equiv |E_{out}|^2 \simeq P_{in}\left(r_{ITM} + 2\right)^2$.

B.0.2 Off resonance

Off resonance means that $\delta \simeq \lambda/4$, in which case Eq. (B.2) becomes

$$E_{cav} = \frac{t_{ITM}E_{in}}{1 + r_{ITM}r_{ETM}}. \tag{B.10}$$

Following the same procedure as in Eq. (B.5), the denominator in Eq. (B.10) can be simplified

$$\frac{1}{1 + r_{\text{ITM}}r_{\text{ETM}}} = \frac{1 - r_{\text{ITM}}r_{\text{ETM}}}{1 - (r_{\text{ITM}}r_{\text{ETM}})^2} = \frac{1 - r_{\text{ITM}}r_{\text{ETM}}}{1 - (1 - T_{\text{ITM}})(1 - T_{\text{ETM}})}$$
$$\simeq \frac{1 - r_{\text{ITM}}r_{\text{ETM}}}{T_{\text{ITM}} + T_{\text{ETM}} + \mathcal{O}(T_{\text{ITM}}T_{\text{ETM}})}. \tag{B.11}$$

The numerator $1 - r_{\text{ITM}}r_{\text{ETM}}$ can also be simplified following the same procedure as in Eq. (B.6). Discarding terms of order above $\mathcal{O}(T_{\text{ITM}}T_{\text{ETM}})$, Eq. (B.11) can thus be rewritten as

$$\frac{1}{1 + r_{\text{ITM}}r_{\text{ETM}}} \simeq \frac{\frac{T_{\text{ITM}} + T_{\text{ETM}}}{2}}{T_{\text{ITM}} + T_{\text{ETM}}} = \frac{1}{2}. \tag{B.12}$$

The cavity power in off resonance is thus given by

$$E_{\text{cav}} \simeq t_{\text{ITM}}E_{\text{in}}\frac{1}{2} \Rightarrow P_{\text{cav}} = |E_{\text{cav}}|^2 \simeq T_{\text{ITM}}P_{\text{in}}\frac{1}{4}. \tag{B.13}$$

The power reflected by the cavity E_{out} is given by the reflected input field added to the transmitted cavity field

$$E_{\text{out}} = E_{\text{in}}r_{\text{ITM}} + E_{\text{cav}}t_{\text{ITM}} \simeq E_{\text{in}}\left(r_{\text{ITM}} + \frac{t_{\text{ITM}}^2}{2}\right). \tag{B.14}$$

The reflected power is then given by $P_{\text{out}} \equiv |E_{\text{out}}|^2 \simeq P_{\text{in}}^2\left(r_{\text{ITM}}^2 + r_{\text{ITM}}T_{\text{ITM}} + \mathcal{O}(T_{\text{ITM}}^4)\right)^2.$

Appendix C

Pound Drever Hall method

Resonance is achieved in GW detectors by tuning the frequency of the laser to be in resonance with the FP cavity, for which the Pound Drever Hall (PDH) [192] servo scheme is used. To correct the frequency of the source an error signal is required. It is obtained by phase modulating the source at frequency Ω_{mod} as mentioned in section 2.2.1. The amplitude of the field in Eq. (2.38) is partially directed to a photodiode that will read a current given by

$$B(t)\bar{B}(t) = E_o\bar{E}_o\Big[R\bar{R} - i\frac{\Gamma}{2}(R\bar{R}_- - R\bar{R}_+)e^{-i\Omega_{mod}t} - i\frac{\Gamma}{2}(R\bar{R}_+ - R\bar{R}_-)e^{i\Omega_{mod}t}\Big]. \tag{C.1}$$

The next step consists on mixing the current from Eq. (C.1) with the demodulation current

$$D(t) = e^{i\Phi}e^{2i\pi\Omega_{mod}t} + e^{-i\Phi}e^{-2i\pi\Omega_{mod}t}, \tag{C.2}$$

where Φ is a variable that de-phases the field. For $\Phi = 0$ the demodulation is said to be in *phase*, while for $\Phi = \pi/2$ it is said to be in *quadrature*. The demodulated signal is thus given by $B(t)\bar{B}(t) \times D(t)$. A low pass filter is used to retain the demodulated current (DC) terms in the result, so the final current is the *demodulated filtered current* (DFC), given by

$$DFC = i\frac{\Gamma}{2}E_o\bar{E}_o\Big[e^{i\Phi}(R\bar{R}_+ - R\bar{R}_-) + e^{-i\Phi}(R\bar{R}_- - R\bar{R}_+)\Big]. \tag{C.3}$$

The reflectance of the cavity for the carrier field is given by

$$R = -\frac{1 - \sigma + 2if}{1 - 2if}, \tag{C.4}$$

where f is the source offset with respect to resonance. For the sidebands, the modulation frequency is assumed to be antiresonant, i.e.: shifted by half a FSR from the resonant frequency. At antiresonance, the reflectance of the cavity and R_+, R_- are close to 1, so

$$DFC = i\frac{\epsilon}{2}E_o\bar{E}_o\Big[Xe^{i\Phi} + \bar{X}e^{-i\Phi}\Big], \tag{C.5}$$
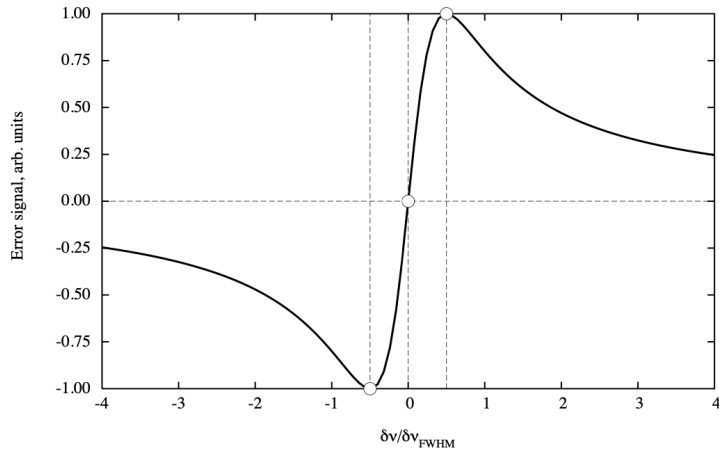
Figure C.1: Figure retrieved from Ref. [46]. Pound Drever Hall servo scheme error curve.

where $X \equiv \bar{R} - R = \frac{4i(2-\sigma)f}{1+4f^2}$. The demodulation must be in quadrature. The error curve is plotted in Figure C.1. The frequency interval between the two extremes is the FWHM of the resonance. There exists a range of frequencies on which the error signal is proportional to the frequency excursion, and this is the starting point of the PDH technique for serving cavities.

Appendix D

Hermite-Gauss and Laguerre-Gauss modes

The fundamental solution for the paraxial diffraction equation is given by Eq. (3.16). This solution can be separated in a function dependent on z and y. Eq. (D.1) is a solution where u(z), P[u(z)x] and Q[u(z)y] are real functions, and A(z) and q(z) complex functions.

$$\Psi(x, y, z) = e^{A(z)} e^{ikr^2/(2q(z))} P[u(z)x] Q[u(z)y] \tag{D.1}$$

The PDE can be rewritten as Eq. (D.2)[46], where $X \equiv u(z)x$ and $Y \equiv u(z)y$. $q(z)$ is required to be the same as in the fundamental solution $\partial q/\partial z - 1 = 0$ and Eqs. (D.3) and (D.4) must be satisfied. Δ' and Δ'' are real arbitrary constants.

$$
\begin{aligned}
& 2ik\left(\frac{\partial A}{\partial z} + \frac{1}{q}\right) P(X)Q(Y) + \frac{k^2 r^2}{q^2}\left(\frac{\partial q}{\partial z} - 1\right) P(X)Q(Y) \\
& + 2ik\left(\frac{\partial u}{\partial z} + \frac{u}{q}\right)\left(x\frac{\partial P}{\partial X}Q(Y) + y\frac{\partial Q}{\partial Y}P(X)\right) \\
& + u^2\left(\frac{\partial^2 P}{\partial X^2}Q(Y) + \frac{\partial^2 Q}{\partial Y^2}P(X)\right) = 0
\end{aligned}
\tag{D.2}
$$

$$u^2\frac{\partial^2 P}{\partial X^2} + 2ikx\left(\frac{\partial u}{\partial z} + \frac{u}{q}\right)\frac{\partial P}{\partial X} + \Delta'P = 0 \tag{D.3}$$

$$u^2\frac{\partial^2 Q}{\partial Y^2} + 2iky\left(\frac{\partial u}{\partial z} + \frac{u}{q}\right)\frac{\partial Q}{\partial Y} + \Delta''Q = 0 \tag{D.4}$$

From Eq. (D.4), since u, P and Q are real $\partial u/\partial z + u/q$ has to be pure complex, so the real part of $\partial u/\partial z + u/q$ is null. This non-reality allows to obtain u(z), Eq. (D.5), where μ is chosen so that $u(0) = \sqrt{2}/w_o \Rightarrow u(z) = \sqrt{2}/w(z)$.

$$\mathcal{R}\left\{\frac{\partial u}{\partial z} + \frac{u}{z - ib}\right\} = 0 \Rightarrow \frac{1}{u}\frac{\partial u}{\partial z} = -\frac{z}{z^2 + b^2} \to u(z) = \frac{\mu}{\sqrt{b^2 + z^2}} \tag{D.5}$$

Eq. (D.3) can then be re-written as

$$\frac{2}{w^2}\frac{\partial^2 P}{\partial X^2} - \frac{4}{w^4}X\frac{\partial P}{\partial X} + \Delta'P = 0\,. \tag{D.6}$$

The solution of Eq. (D.6) exists if $\Lambda'w^2/2 = 2n$, where n is an integer. Eq. (D.6) thus defines the Hermite polynomial of order n $P(X) \equiv H_n(X)$ [46]. Similarly, Eq. (D.4) defines the Hermite polynomial of order m $Q(Y) \equiv H_m(Y)$ [46]. This definitions allow to rewrite the PDE in Eq. (D.2) as

$$2ik\left(\frac{\partial A}{\partial z} + \frac{1}{q}\right) - (m + n)\frac{4}{w^2} = 0 \Rightarrow A(z) = \ln\left(\frac{1}{z - ib}\right) - i(m + n)\mathrm{atan}\left(\frac{z}{b}\right). \tag{D.7}$$

The PDE in Eq. (D.7) can be solved leading to the solution of the exponential in Eq. (D.1),

$$A(z) = \ln\left(\frac{1}{z - ib}\right) - i(m + n)\arctan(z/b). \tag{D.8}$$

The PDE then has Hermite-Gauss solutions, given by Eq. (D.9), where $c_{m,n}$ is a constant.

$$HG_{(m,n)}(x, y; z) = c_{m,n}e^{ikz}H_m\left(\sqrt{2}\frac{x}{w(z)}\right)H_n\left(\sqrt{2}\frac{y}{w(z)}\right)e^{-i(m+n+1)atan(z/b)}e^{-r^2/w^2(z)}e^{ikr^2/(2R(z))} \tag{D.9}$$

The properties of the Hermite polynomials, given by Eq. (D.10) are

$$H_n(x) = e^{x^2}\left(-\frac{d}{dx}\right)^n e^{-x^2}; H_n(x) = \sum_{s=0}^{n/2}(-1)^s\frac{n!}{(n-2s)!s!}(2x)^{n-2s} \tag{D.10}$$

- They obey the differential equation $H_n''(x) - 2xH_n'(x) + 2nH_n(x) = 0$.

- Their derivatives are given by $H_n'(x) = 2nH_{n-1}(x)$.

- They obey the recurrent relation: $H_{n+1}(x) = 2xH_n(x) - 2nH_{n-1}(x)$.

- They obey the orthogonality relation: $\int_{-\infty}^{\infty}H_m(x)H_n(x)e^{-x^2}dx = \sqrt{\pi}2^m m!\delta_{m,n}$, which allows to compute the normalization constant for the HG modes: $c_{m,n} = \left[\frac{2}{\pi w^2}\frac{1}{2^{m+n}m!n!}\right]^{1/2}$.

- They obey a closure relation $\frac{1}{\sqrt{\pi}}\sum_p\frac{1}{2^p p!}H_p(x)H_p(x')e^{-(x^2+x'^2)/2} = \delta(x - x')$.

- Using the recursion formula it can be shown that there exist a translation formula $H_n(x + \Delta/2) = \sum_{k=0}^{n}C_n^k H_{n-k}(x)\Delta^k$.

- There is a scaling formula that HG modes satisfy: $H_n(\beta x) = \sum_{k=0}^{n/2}\frac{n!}{k!(n-2k)!}\beta^{n-2k}(\beta^2-1)^k H_{n-2k}(x)$.

- There is a reduction formula: $H_m(x)H_n(x) = \sum_{s=0}^{\min(m,n)}\frac{m!n!2^s}{(m-s)!(n-s)!s!}H_{m+n-2s}(x)$.

- A general expression of the Fourier transform for any mode:

$$\tilde{\Psi}_{m,n}(Z, p, q) = \frac{\pi w^2}{Z}\left(\frac{i}{Z}\right)^{m+n}(2Z-Z^2)^{(m+n)/2}H_m\left(\frac{pw}{\sqrt{2(2Z - Z^2)}}\right)H_n\left(\frac{qw}{\sqrt{2(2Z - Z^2)}}\right)e^{-\frac{w^2(p^2+q^2)}{4Z}}$$

.

- There is a useful Fourier transform involving the Hermite polynomials: $\frac{1}{\sqrt{\pi}}\int e^{-x^2}H_n(x)e^{ipx}dx = (ip)^n e^{-p^2/4}$. With this transformation the plane wave expansion can be expressed in terms of Hermite polynomials: $e^{ipx} = e^{-p^2/4}\sum_{n\geq 0}\frac{(ip)^n}{2^n!}H_n(x)$.

A graphical representation of the Hermite-Gauss modes (n,m) for n,m $\in [0, 2]$ is in Figure D.1. They were generated with SIS (section 3.2).

When polar coordinates (r, ϕ) are used instead of Cartesian (x,y), another set of solutions called the Laguerre-Gauss modes can be found, Eq. (D.11). The Laguerre-Gauss modes are given in terms of the Laguerre-Gauss polynomials, Eq. (D.12).

$$LG_{m,n}(r, \phi; z) = c_{m,n}e^{ikz}\left(\sqrt{2}\frac{r}{w(z)}\right)^n L_m^{(n)}\left(\frac{2r^2}{w^2(z)}\right)e^{-i(2m+n+1)atan(z/b)}e^{-r^2/w^2(z)}e^{ikr^2/(2R(z))}\cos(n\phi) \tag{D.11}$$

$$L_m^{(n)}(x) = \frac{e^x}{m!x^n}\left(\frac{d}{dx}\right)^m(x^{n+m}e^{-x}) \tag{D.12}$$

The LG polynomials satisfy

(a) HG(0,0)   (b) HG(0,1)   (c) HG(0,2)

(d) HG(1,0)   (e) HG(1,1)   (f) HG(1,2)

(g) HG(2,0)   (h) HG(2,1)   (i) HG(2,2)
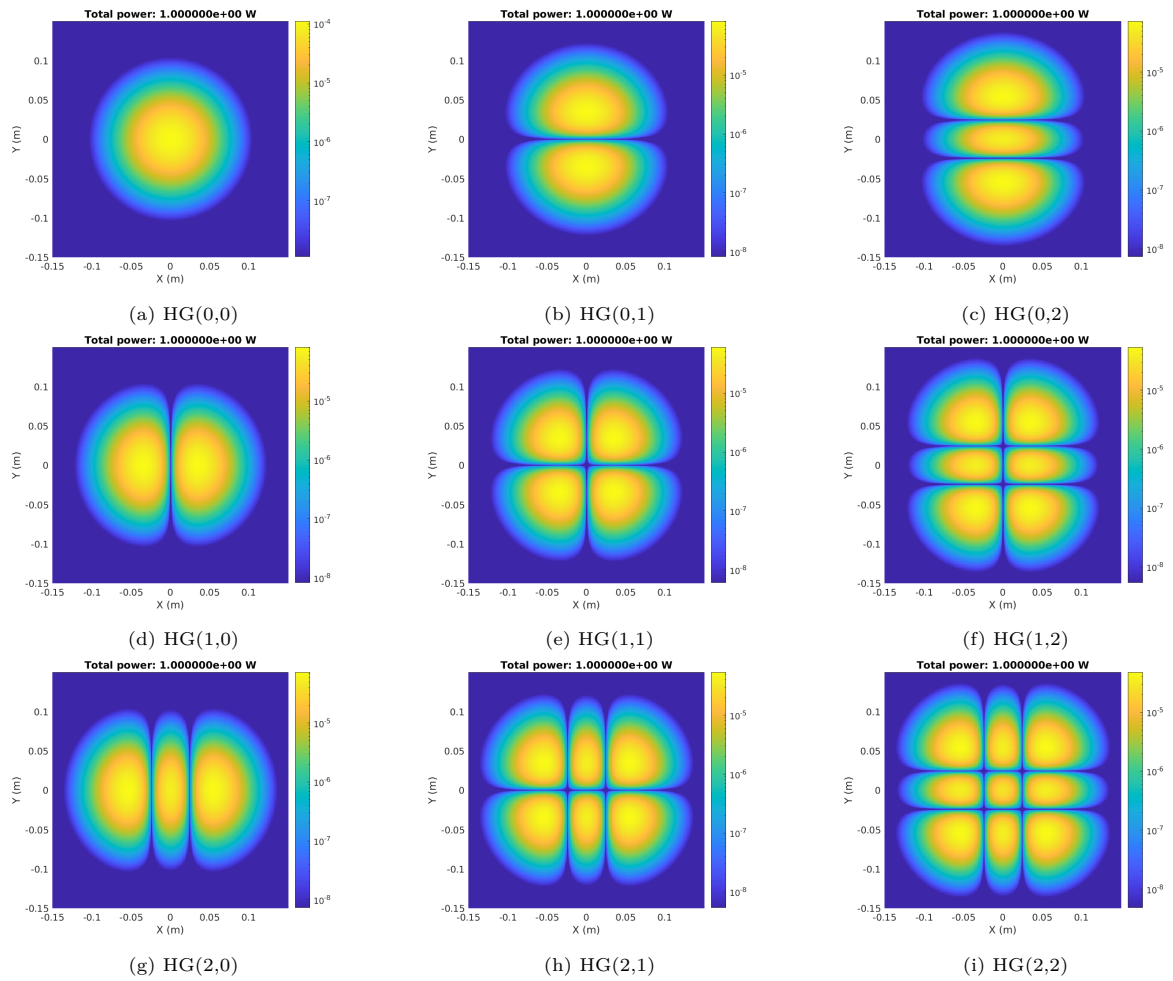
Figure D.1: Graphical representation of the Hermite-Gauss modes (n,m) for n,m $\in [0, 2]$. The shape of the mode HG(n,m) is equal to that of HG(m,n) though rotated 90º. For larger values of n, m the mode will have more blobs. Figure generated with SIS.
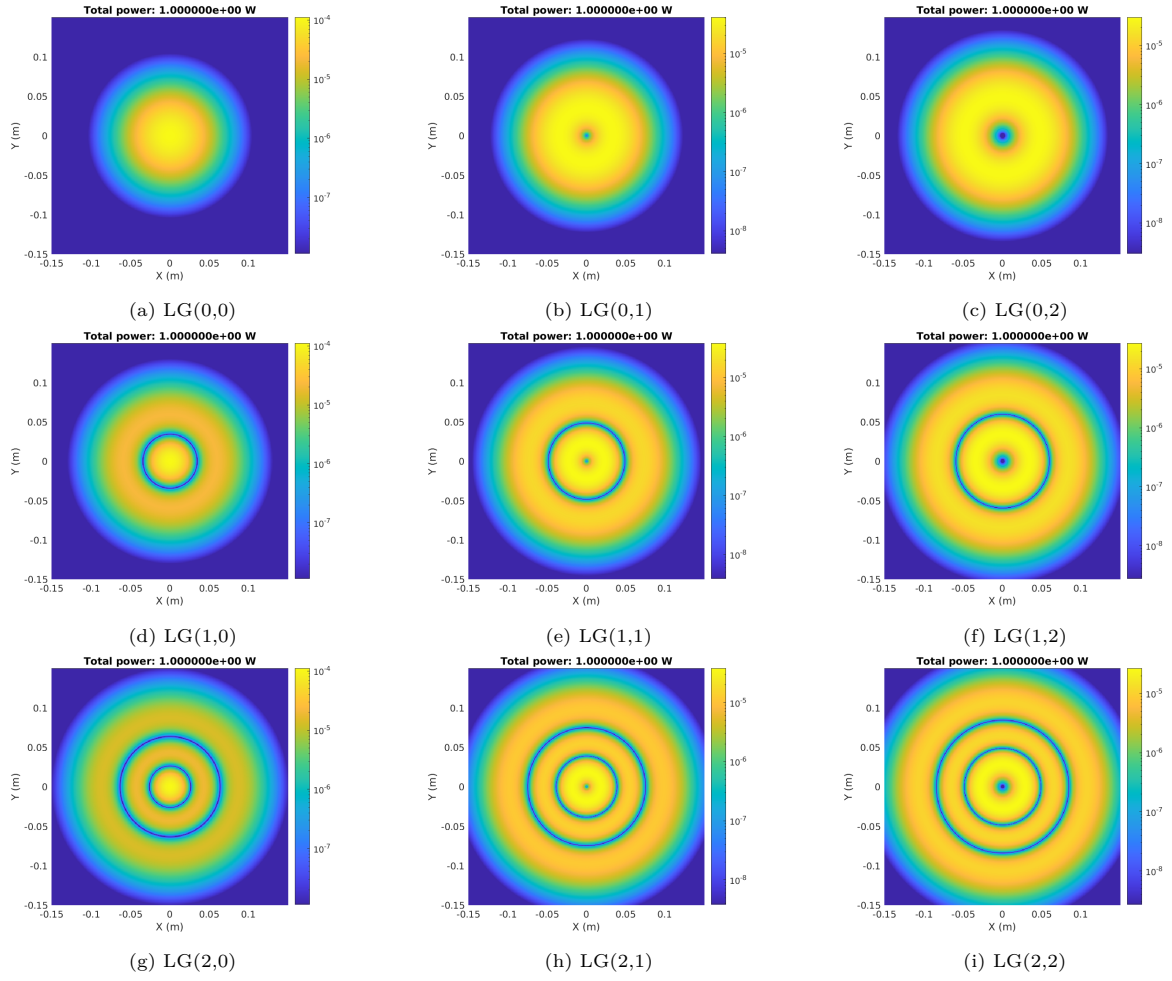
Figure D.2: Graphical representation of the Laguerre-Gauss modes (l,m) for l,m $\in [0,2]$. For larger values of l, m the mode will have more concentric rings. The mode LG(l,m) has rings of highest power where the mode LG(m,l) has rings of lowest power. Figure generated with SIS.

- The recursion relation $(m+1)L_{m+1}^{(n)}(x) = (2m+n+1-x)L_m^{(n)}(x) - (m+n)L_{m-1}^{(n)}(x)$

- The normalization relation [58] $\int_0^\infty L_m^{(n)2}(x)x^n e^{-x}dx = \frac{(m+n)!}{m!}$, which allows to compute the normalization constants $c_{mn} = \frac{2}{w}\sqrt{\frac{m!}{\pi(1+\delta_{n0})(m+n)!}}$.

A graphical representation of the Laguerre-Gauss modes (l,m) for l,m $\in [0,2]$ is in Figure D.2. They were generated with SIS (section 3.2).

134

Appendix E

Paraxial ray analysis

The previous sections have described the propagation of light beam in vacuum. In what follows the propagation of paraxial rays through optical systems is explained. The propagation of paraxial rays through various optical structures can be described by ray transfer matrices. A paraxial ray in a given cross section of an optical system is characterized by its distance from the optic's main axis x and by the angle or slope with respect to the axis x'. Figure E.1 represents the propagation of a paraxial ray through an optical element with input and output planes represented by the dashed lines.
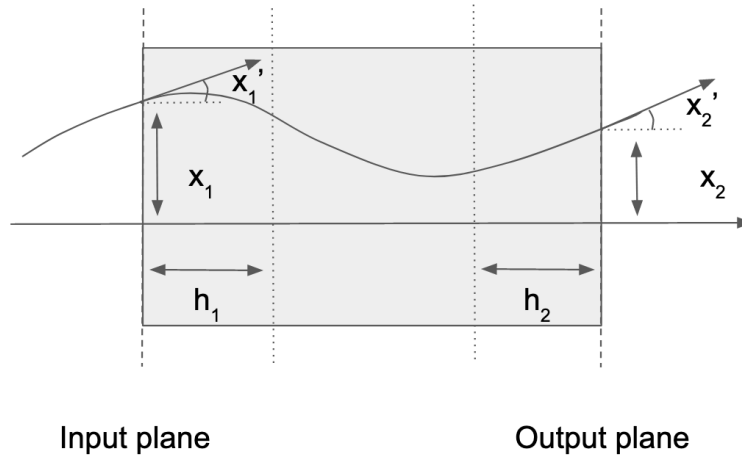
Figure E.1: Propagation of a paraxial ray through an optical element with input and output planes represented by the dashed lines. The principal planes are represented by dotted lines. The paraxial ray is characterized by the distance to the optic's main axis x and by the angle or slope with respect to the axis x'.

The ray transfer matrix for the optical element represented in Figure E.1 is given by

$$
\begin{vmatrix} x_2 \\ x'_2 \end{vmatrix} = \begin{vmatrix} A & B \\ C & D \end{vmatrix} \begin{vmatrix} x_1 \\ x'_1 \end{vmatrix} ,
\tag{E.1}
$$

where the central matrix is referred to as ABCD matrix. The elements A, B, C and D are related to the focal length of the system f and the location of the principal planes [58] as

$$
f = -\frac{1}{C} \quad , \quad h_1 = \frac{D-1}{C} \quad , \quad h_2 = \frac{A-1}{C} .
\tag{E.2}
$$

Each optical element has a different ABCD matrix. For instance, the ray transfer matrix for propagation through a distance d in vacuum is given by the matrix in Fig. E.2 [57, 58].
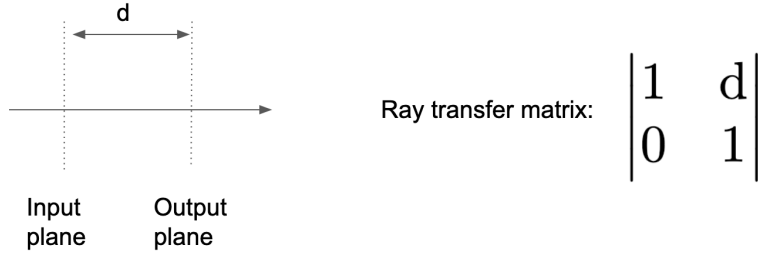
Figure E.2: Ray transfer matrix for propagation through a distance d in vacuum. The arrow represents the propagation direction.

The ray transfer matrix of rays passing through a thin lens of focal length f is given by the matrix in Fig. E.3 [57, 58].
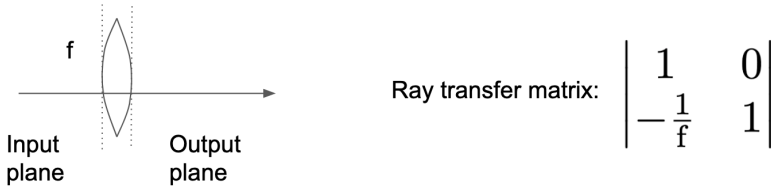
Figure E.3: Ray transfer matrix of rays passing through a thin lens of focal length f. The arrow represents the propagation direction.

The ray transfer matrix of rays passing through a medium of length d with a reflective index that varies quadratically with the distance r from the optical axis, $n = n_o - \frac{1}{2}n_2 r^2$, is given by the matrix in Fig. E.4 [57, 58]. Laser crystals and gas lenses are represented by this matrix.
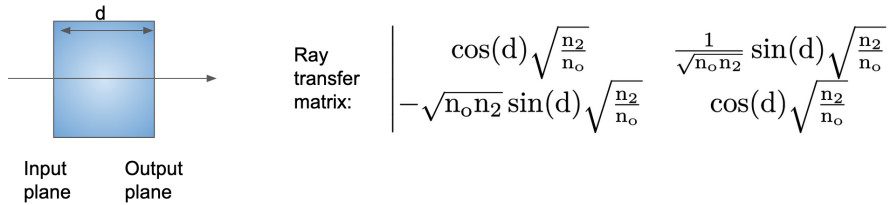
Figure E.4: Ray transfer matrix of rays passing through a medium of length d with a reflective index that varies quadratically with the distance r from the optical axis, $n = n_o - \frac{1}{2}n_2 r^2$. The arrow represents the propagation direction.

The ray transfer matrix of rays passing through a dielectric material of index n and length d is given by the matrix in Fig. E.5 [57, 58].

Figure E.5: Ray transfer matrix of rays passing through a dielectric material of index n and length d. The arrow represents the propagation direction.

Light rays that resonate within a FP cavity experience a periodic focusing action. The effect on the rays is the same as the one due to the passage through a periodic sequence of lenses [57]. Figure E.6

136

represents the periodic sequence of n lenses represented by their ABDC matrices. Once the rays pass by all the lenses, the distance of the beam from the main propagation axis will be x_n and it will have a slope x'_n.
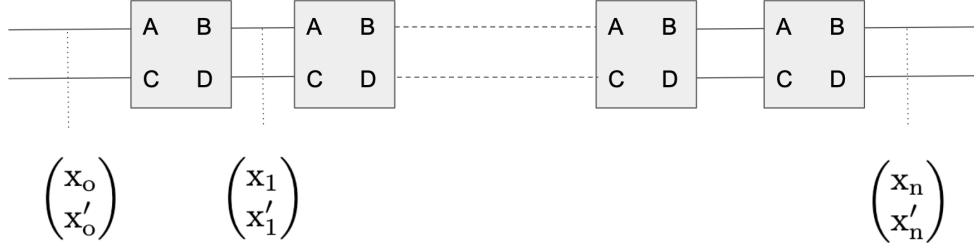
Figure E.6: Periodic sequence of n lenses represented by their ABDC matrices. The effect on the rays passing through is the same as on rays resonating with a FP cavity. One the rays pass by all the lenses, the distance of the beam from the main propagation axis will be x_n and it will have a slope x'_n.

The overall transfer matrix after n consecutive optical elements with the same ABDC matrix is

$$
\begin{bmatrix} A & B \\ C & D \end{bmatrix} = \frac{1}{\sin \Theta} \begin{bmatrix} A \sin(n\Theta) - \sin(n-1)\Theta & B \sin(n\Theta) \\ C \sin(n\Theta) & D \sin(n\Theta) - \sin(n-1)\Theta \end{bmatrix} , \tag{E.3}
$$

where $\cos(\Theta) \equiv \frac{1}{2}(A + D)$. These periodic sequences of lenses are stable when the trace $A + D$ obeys $-1 < \Theta < 1$.

Appendix F

Efficiency of sound waves

The efficiency associated with sound waves κ_{sw} quantifies the fraction of the latent heat which goes into the bulk motion, i.e.: the fraction of vacuum energy converted into the kinetic energy of the bulk flow. This efficiency is dependent on the strength of the transition α and the bubble wall velocity v_w, i.e.: on whether there is a deflagration, hybrid or detonation scenario, as shown in Figure F.1.
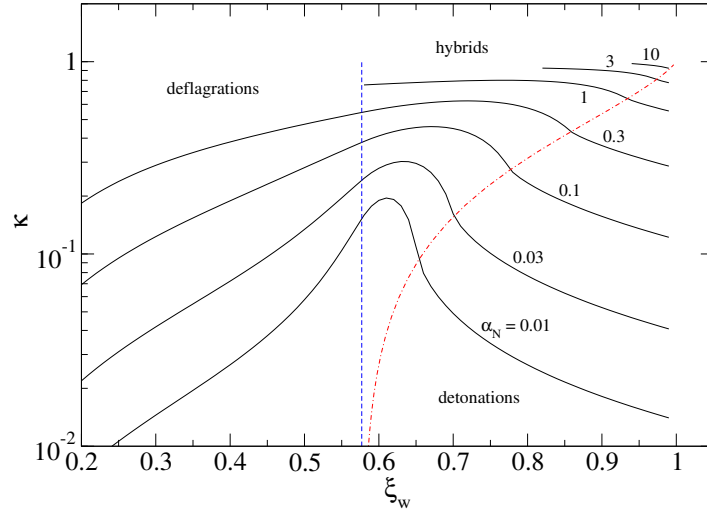
Figure F.1: Efficiency of the sound waves as a function of the strength of the transition and the bubble wall velocity. Image retrieved from Ref. [163].

In Ref. [163], a fit to the numerical results in Figure F.1 is done, and the efficiency can thus be approximated by Eqs. F.1. The fit has a precision better that 15% for the region $10^{-3} < \alpha < 10$.

$$\kappa_{\mathrm{sw}}(\alpha,\mathrm{v_w}) = \begin{cases} 0, & \text{if } \mathrm{v_w} < 1 - (3\alpha)^{-10/13} \\ \dfrac{c_s^{11/5}\kappa_1\kappa_2}{(c_s^{11/5} - v_w^{11/5})\kappa_2 + v_w c_s^{6/5}\kappa_1}, & \text{if } \mathrm{v_w} \le \mathrm{c_s} \\ \kappa_2 + dk(-c_s + v_w) + [-\kappa_2 + \kappa_{JD} - dk(-c_s + v_J)]\times \\ (-c_s + v_J)^{-3}(-c_s + v_w)^3, & \text{if } \mathrm{c_s} < \mathrm{v_w} < \mathrm{v_J} \\ \kappa_{JD}\kappa_{vw1}(-1 + v_J)^3 v_J^{2.5} v_w^{-2.5}\times \\ \dfrac{1}{\kappa_{JD}v_J^{2.5}[(-1 + v_J)^3 - (-1 + v_w)^3] + \kappa_{vw1}(-1 + v_w)^3}, & \text{if } \mathrm{v_w} \ge \mathrm{v_J} \end{cases}$$

$$(\text{F.1})$$

The quantities used in Eq. (F.1) are defined in Eqs. (F.2).

138

$$c_s = 1/\sqrt{3}$$

$$v_J = \frac{\sqrt{2/3\alpha + \alpha^2} + c_s}{1 + \alpha}$$

$$dk = -0.9 \log \frac{\sqrt{\alpha}}{1 + \sqrt{\alpha}}$$

$$\kappa_1 = 6.9 \cdot \alpha \cdot v_w^{1.2} \frac{1}{1.36 + \alpha - 0.037\sqrt{\alpha}}$$

$$\kappa_2 = \alpha^{0.4} \frac{1}{0.017 + (0.997 + \alpha)^{0.4}}$$

$$\kappa_{JD} = \alpha^{0.5} \frac{1}{0.135 + (0.98 + \alpha)^{0.5}}$$

$$\kappa_{vw1} = \alpha \frac{1}{0.73 + \alpha + 0.083\sqrt{\alpha}} \tag{F.2}$$

Acronyms

GW Gravitational Wave.

ADSP Angular density of scattered power

ADCs Analog-to-digital converter

BBH Binary Black Hole

BBN Big Bang nucleosynthesis

BC Bubble collisions

BPL Broken power law

BNS Binary neutron star

BRDF Bidirectional reflectance distribution function

BSDF Bidirectional scatter distribution function

BSM Beyond Standard model

CMB Cosmic Microwave Background

CL Credible/confidence level

CI Credible/confidence interval

CSD Cross-spectral density

DFT Discrete Fourier transform

DC Demodulated current

EW Electro-weak

ET Einstein Telescope

FFT Fast Fourier transform

FV False vacuum

FOPT First Order Phase Transitions

FT Fourier transform

FSR Free spectral range

GR General Relativity

GWB Gravitational wave background

H1 LIGO-Hanford interferometer

IFO Interferometer

ITF Interferometer

IMC Input mode cleaner

L1 LIGO-Livingstone interferometer

NN Newtonian Noise

ORF Overlap reduction function

PCB Printed Circuit Board

PDE Paraxial Diffraction Equation

PI curve Power-law integrated sensitivity curve

PDF Posterior density function

PDH Pound Drever Hall

PT Phase transitions

QCD Quantum chromodynamics

QFT Quantum Field Theory

SM Standard Model

SNR Signal to noise ratio

SR Special relativity

SW Sound waves

SIS Stationary Interferometer Simulation

TEM Transverse Electromagnetic Modes

TIS Total integrated scattering

TV True vacuum

TCS Thermal Compensation System

UL Upper limit

V1 Virgo interferometer

Bibliography

[1] Einstein, Albert, "über gravitationswellen," *Sitzungsber. Preuss. Akad. Wiss. Berlin (Math. Phys.)*, pp. 154–167, 1918.

[2] ——, "The formal foundation of the general theory of relativity," *Sitzungsber. Preuss. Akad. Wiss. Berlin (Math. Phys.)*, pp. 1030–1085, 1914.

[3] ——, "The field equations of gravitation," *Sitzungsber. Preuss. Akad. Wiss. Berlin (Math. Phys.)*, pp. 844–847, 1915.

[4] ——, "Approximative integration of the field equations of gravitation," *Sitzungsber. Preuss. Akad. Wiss. Berlin (Math. Phys.)*, pp. 688–696, 1916.

[5] R. M. Wald, *General Relativity*. Chicago, USA: Chicago Univ. Pr., 1984.

[6] I. W. Harry, "Can we hear black holes collide?" Ph.D. dissertation, Cardiff U., Cardiff U., 2011.

[7] S. Weinberg, *Gravitation and Cosmology: Principles and Applications of the General Theory of Relativity*. New York: John Wiley and Sons, 1972.

[8] D. H. Perkins, *Introduction to high energy physics*, 1982.

[9] M. Maggiore, *Gravitational Waves. Vol. 1: Theory and Experiments*, ser. Oxford Master Series in Physics. Oxford University Press, 2007.

[10] D. Keitel, "Improving robustness of continuous-gravitational-wave searches against signal-like instrumental artefacts and a concept for an octahedral gravitational-wave detector in space," Ph.D. dissertation, Leibniz U., Hannover, 7 2014.

[11] S. Kandhasamy, "Searches for stochastic gravitational waves and long gravitational wave transients in LIGO S5 data," Ph.D. dissertation, Minnesota U., 2013.

[12] C. D. Ott, A. Burrows, L. Dessart, and E. Livne, "A new mechanism for gravitational-wave emission in core-collapse supernovae," *Phys. Rev. Lett.*, vol. 96, p. 201102, May 2006. [Online]. Available: https://link.aps.org/doi/10.1103/PhysRevLett.96.201102

[13] L. Blanchet, T. Damour, G. Esposito-Farèse, and B. R. Iyer, "Gravitational radiation from inspiralling compact binaries completed at the third post-newtonian order," *Phys. Rev. Lett.*, vol. 93, p. 091101, Aug 2004. [Online]. Available: https://link.aps.org/doi/10.1103/PhysRevLett.93.091101

[14] J. G. Baker, J. Centrella, D.-I. Choi, M. Koppitz, and J. van Meter, "Binary black hole merger dynamics and waveforms," *Phys. Rev. D*, vol. 73, p. 104002, May 2006. [Online]. Available: https://link.aps.org/doi/10.1103/PhysRevD.73.104002

[15] B. P. Abbott, R. Abbott, F. Acernese, R. Adhikari, P. Ajith, B. Allen, G. Allen, M. Alshourbagy, R. S. Amin, S. B. Anderson, and j. . T. a. . W. et al., title = SEARCH FOR GRAVITATIONAL-WAVE BURSTS ASSOCIATED WITH GAMMA-RAY BURSTS USING DATA FROM LIGO SCIENCE RUN 5 AND VIRGO SCIENCE RUN 1,, vol. 715, no. 2, pp. 1438–1452, may 2010. [Online]. Available: https://doi.org/10.1088/0004-637x/715/2/1438

[16] B. P. Abbott, R. Abbott, R. Adhikari, P. Ajith, B. Allen, G. Allen, R. S. Amin, S. B. Anderson, W. G. Anderson, M. A. Arain, and et al., "Search for gravitational-wave bursts in the first year of the fifth ligo science run," *Phys. Rev. D*, vol. 80, p. 102001, Nov 2009. [Online]. Available: https://link.aps.org/doi/10.1103/PhysRevD.80.102001

[17] R. Abbott, T. D. Abbott, F. Acernese, K. Ackley, C. Adams, N. Adhikari, R. X. Adhikari, V. B. Adya, C. Affeldt, D. Agarwal, and et al., "All-sky search for short gravitational-wave bursts in the third advanced ligo and advanced virgo run," *Phys. Rev. D*, vol. 104, p. 122004, Dec 2021. [Online]. Available: https://link.aps.org/doi/10.1103/PhysRevD.104.122004

[18] B. P. Abbott, R. Abbott, T. D. Abbott, S. Abraham, F. Acernese, K. Ackley, C. Adams, V. B. Adya, C. Affeldt, M. Agathos, and et al., "Optically targeted search for gravitational waves emitted by core-collapse supernovae during the first and second observing runs of advanced ligo and advanced virgo," *Phys. Rev. D*, vol. 101, p. 084002, Apr 2020. [Online]. Available: https://link.aps.org/doi/10.1103/PhysRevD.101.084002

[19] J. Kissel, "Calibrating and improving the sensitivity of the LIGO detectors"," Ph.D. dissertation, Louisiana State U., 2010.

[20] A. Nitz, I. Harry, D. Brown, C. M. Biwer, J. Willis, T. D. Canton, C. Capano, T. Dent, L. Pekowsky, A. R. Williamson, and et al., "gwastro/pycbc: v2.0.2 release of pycbc," Mar. 2022. [Online]. Available: https://doi.org/10.5281/zenodo.6324278

[21] e. a. Abbott, R., "Upper limits on the isotropic gravitational-wave background from advanced ligo and advanced virgo's third observing run," *Phys. Rev. D*, vol. 104, p. 022004, Jul 2021. [Online]. Available: https://link.aps.org/doi/10.1103/PhysRevD.104.022004

[22] P. A. Rosado, "Gravitational wave background from binary systems," *Phys. Rev. D*, vol. 84, p. 084004, Oct 2011. [Online]. Available: https://link.aps.org/doi/10.1103/PhysRevD.84.084004

[23] T. Regimbau and V. Mandic, "Astrophysical Sources of Stochastic Gravitational-Wave Background," *Class. Quant. Grav.*, vol. 25, p. 184018, 2008.

[24] C. Wu, V. Mandic, and T. Regimbau, "Accessibility of the gravitational-wave background due to binary coalescences to second and third generation gravitational-wave detectors," *Phys. Rev. D*, vol. 85, p. 104024, May 2012. [Online]. Available: https://link.aps.org/doi/10.1103/PhysRevD.85.104024

[25] A. Buonanno, G. Sigl, G. G. Raffelt, H.-T. Janka, and E. Müller, "Stochastic gravitational-wave background from cosmological supernovae," *Phys. Rev. D*, vol. 72, p. 084001, Oct 2005. [Online]. Available: https://link.aps.org/doi/10.1103/PhysRevD.72.084001

[26] P. Sandick, K. A. Olive, F. Daigne, and E. Vangioni, "Gravitational waves from the first stars," *Phys. Rev. D*, vol. 73, p. 104024, May 2006. [Online]. Available: https://link.aps.org/doi/10.1103/PhysRevD.73.104024

[27] V. B. Ferrari, S. Matarrese, and R. Schneider, "Gravitational wave background from a cosmological population of core-collapse supernovae," *Monthly Notices of the Royal Astronomical Society*, vol. 303, pp. 247–257, 1999.

[28] E. Howell, D. Coward, R. Burman, D. Blair, and J. Gilmore, "The gravitational wave background from neutron star birth throughout the cosmos," *Monthly Notices of the Royal Astronomical Society*, vol. 351, no. 4, pp. 1237–1246, 07 2004. [Online]. Available: https://doi.org/10.1111/j.1365-2966.2004.07863.x

[29] T. W. B. Kibble, "Topology of cosmic domains and strings," *Journal of Physics A: Mathematical and General*, vol. 9, no. 8, pp. 1387–1398, aug 1976. [Online]. Available: https://doi.org/10.1088/0305-4470/9/8/029

[30] S. Sarangi and S.-H. Tye, "Cosmic string production towards the end of brane inflation," *Physics Letters B*, vol. 536, no. 3, pp. 185–192, 2002. [Online]. Available: https://www.sciencedirect.com/science/article/pii/S0370269302018245

[31] R. e. a. Abbott, "Constraints on cosmic strings using data from the third advanced ligo–virgo observing run," *Phys. Rev. Lett.*, vol. 126, p. 241102, Jun 2021. [Online]. Available: https://link.aps.org/doi/10.1103/PhysRevLett.126.241102

[32] R. Jeannerot, J. Rocher, and M. Sakellariadou, "How generic is cosmic string formation in supersymmetric grand unified theories," *Phys. Rev. D*, vol. 68, p. 103514, Nov 2003. [Online]. Available: https://link.aps.org/doi/10.1103/PhysRevD.68.103514

[33] T. Vachaspati and A. Vilenkin, "Gravitational radiation from cosmic strings," *Phys. Rev. D*, vol. 31, pp. 3052–3058, Jun 1985. [Online]. Available: https://link.aps.org/doi/10.1103/PhysRevD.31.3052

[34] M. Sakellariadou, "Erratum: Gravitational waves emitted from infinite strings," *Phys. Rev. D*, vol. 43, pp. 4150–4150, Jun 1991. [Online]. Available: https://link.aps.org/doi/10.1103/PhysRevD.43.4150.2

[35] S. Olmez, V. Mandic, and X. Siemens, "Gravitational-Wave Stochastic Background from Kinks and Cusps on Cosmic Strings," *Phys. Rev. D*, vol. 81, p. 104028, 2010.

[36] X. Siemens, V. Mandic, and J. Creighton, "Gravitational-wave stochastic background from cosmic strings," *Phys. Rev. Lett.*, vol. 98, p. 111101, Mar 2007. [Online]. Available: https://link.aps.org/doi/10.1103/PhysRevLett.98.111101

[37] T. Damour and A. Vilenkin, "Gravitational wave bursts from cosmic strings," *Phys. Rev. Lett.*, vol. 85, pp. 3761–3764, Oct 2000. [Online]. Available: https://link.aps.org/doi/10.1103/PhysRevLett.85.3761

[38] A. Arvanitaki, S. Dimopoulos, S. Dubovsky, N. Kaloper, and J. March-Russell, "String axiverse," *Phys. Rev. D*, vol. 81, p. 123530, Jun 2010. [Online]. Available: https://link.aps.org/doi/10.1103/PhysRevD.81.123530

[39] D. J. Marsh, "Axion cosmology," *Physics Reports*, vol. 643, pp. 1–79, 2016, axion cosmology. [Online]. Available: https://www.sciencedirect.com/science/article/pii/S0370157316301557

[40] R. Brito, S. Ghosh, E. Barausse, E. Berti, V. Cardoso, I. Dvorkin, A. Klein, and P. Pani, "Stochastic and resolvable gravitational waves from ultralight bosons," *Phys. Rev. Lett.*, vol. 119, p. 131101, Sep 2017. [Online]. Available: https://link.aps.org/doi/10.1103/PhysRevLett.119.131101

[41] L. Tsukada, T. Callister, A. Matas, and P. Meyers, "First search for a stochastic gravitational-wave background from ultralight bosons," *Phys. Rev. D*, vol. 99, no. 10, p. 103015, 2019.

[42] W. E. East and F. Pretorius, "Superradiant instability and backreaction of massive vector fields around kerr black holes," *Phys. Rev. Lett.*, vol. 119, p. 041101, Jul 2017. [Online]. Available: https://link.aps.org/doi/10.1103/PhysRevLett.119.041101

[43] R. Brito, S. Ghosh, E. Barausse, E. Berti, V. Cardoso, I. Dvorkin, A. Klein, and P. Pani, "Gravitational wave searches for ultralight bosons with ligo and lisa," *Physical Review D*, vol. 96, 06 2017.

[44] X.-L. Fan and Y. Chen, "Stochastic gravitational-wave background from spin loss of black holes," *Phys. Rev. D*, vol. 98, p. 044020, Aug 2018. [Online]. Available: https://link.aps.org/doi/10.1103/PhysRevD.98.044020

[45] M. S. Turner, "Detectability of inflation-produced gravitational waves," *Phys. Rev. D*, vol. 55, pp. R435–R439, Jan 1997. [Online]. Available: https://link.aps.org/doi/10.1103/PhysRevD.55.R435

[46] J.-Y. Vinet, "Gravitational wave interferometry - optics and related topics (the virgo physics book vol. ii)) manual," *VIR-0987A-05*, June 2005. [Online]. Available: https://tds.virgo-gw.eu/?call_file=VIR-0987A-05.pdf

[47] B. J. Meers, "Recycling in laser-interferometric gravitational-wave detectors," *Phys. Rev. D*, vol. 38, pp. 2317–2326, Oct 1988. [Online]. Available: https://link.aps.org/doi/10.1103/PhysRevD.38.2317

[48] A. Cirone, I. Fiori, F. Paoletti, M. M. Perez, A. R. Rodríguez, B. L. Swinkels, A. M. Vazquez, G. Gemme, and A. Chincarini, "Investigation of magnetic noise in advanced virgo," *Classical and Quantum Gravity*, vol. 36, no. 22, p. 225004, oct 2019. [Online]. Available: https://doi.org/10.1088/1361-6382/ab4974

[49] G. Vajente, "Analysis of sensitivity and noise sources for the Virgo gravitational wave interferometer," Ph.D. dissertation, Scuola Normale Superiore di Pisa.

[50] M. Mehmet and H. Vahlbruch, "The squeezed light source for the advanced virgo detector in the observation run o3," *Galaxies*, vol. 8, no. 4, 2020. [Online]. Available: https://www.mdpi.com/2075-4434/8/4/79

[51] F. Acernese, M. Agathos, K. Agatsuma, D. Aisa, N. Allemandou, A. Allocca, J. Amarni, P. Astone, G. Balestri, G. Ballardin, and et al., "Advanced virgo: a second-generation interferometric gravitational wave detector," *Classical and Quantum Gravity*, vol. 32, no. 2, p. 024001, dec 2014. [Online]. Available: https://doi.org/10.1088/0264-9381/32/2/024001

[52] G. Ballardin, L. Bracci, S. Braccini, C. Bradaschia, C. Casciano, G. Calamai, R. Cavalieri, R. Cecchi, G. Cella, E. ambrosio, V. Dattilo, A. Virgilio, L. Fabbroni, F. Fidecaro, F. Frasconi, A. Gaddi, A. Gennai, G. Gennaro, A. Giazotto, and Z. Zhang, "Measurement of the virgo superattenuator performance for seismic noise suppression," *Review of Scientific Instruments - REV SCI INSTR*, vol. 72, 09 2001.

[53] T. Accadia, F. Acernese, M. Alshourbagy, P. Amico, F. Antonucci, S. Aoudia, N. Arnaud, C. Arnault, K. G. Arun, P. Astone, and et al., "Virgo: a laser interferometer to detect gravitational waves," *Journal of Instrumentation*, vol. 7, no. 03, pp. P03 012–P03 012, mar 2012. [Online]. Available: https://doi.org/10.1088/1748-0221/7/03/p03012

[54] A. Singha, S. Hild, and J. Harms, "Newtonian-noise reassessment for the virgo gravitational-wave observatory including local recess structures," *Classical and Quantum Gravity*, vol. 37, no. 10, p. 105007, apr 2020. [Online]. Available: https://doi.org/10.1088/1361-6382/ab81cb

[55] J. Aasi, J. Abadie, B. P. Abbott, R. Abbott, T. D. Abbott, M. Abernathy, T. Accadia, F. Acernese, C. Adams, T. Adams, and et al., "The characterization of virgo data and its impact on gravitational-wave searches," *Classical and Quantum Gravity*, vol. 29, no. 15, p. 155002, jun 2012. [Online]. Available: https://doi.org/10.1088/0264-9381/29/15/155002

[56] A. Matas, I. Dvorkin, A. Romero-Rodríguez, and T. Regimbau, "Application of gating to stochastic searches in o3," *LIGO Document P2000546-v2*, Jan 2021. [Online]. Available: https://dcc.ligo.org/DocDB/0172/P2000546/002/gating-mdc.pdf

[57] H. Kogelnik and T. Li, "Laser beams and resonators," *Appl. Opt.*, vol. 5, no. 10, pp. 1550–1567, Oct 1966. [Online]. Available: http://opg.optica.org/ao/abstract.cfm?URI=ao-5-10-1550

[58] A. E. Siegman, *Lasers.* Oxford, England: Cambridge University Press, 1987.

[59] D. Rockmore, "The fft: An algorithm the whole family can use," *Computing in Science Engineering*, vol. 2, pp. 60 – 64, 02 2000.

[60] H. Yamamoto, "Sis (stationary interferometer simulation) manual," *LIGO Document T070039-v8*, July 2013. [Online]. Available: https://dcc.ligo.org/cgi-bin/private/DocDB/ShowDocument?.submit=Identifier&docid=T070039&version=8

[61] T. Edo, A. Romero-Rodríguez, and H. Yamamoto, "Sis 20 documents," *LIGO Document T2000311-v2*, Nov 2021. [Online]. Available: https://dcc.ligo.org/LIGO-T2000311

[62] R. A. Day, G. Vajente, and M. P. du Mezeray, "Accelerated convergence method for fast fourier transform simulation of coupled cavities," *J. Opt. Soc. Am. A*, vol. 31, no. 3, pp. 652–660, Mar 2014. [Online]. Available: http://opg.optica.org/josaa/abstract.cfm?URI=josaa-31-3-652

[63] H. Yamamoto, "Sis20 primer," *LIGO Document G2000796-v2*, May 2020. [Online]. Available: https://dcc.ligo.org/cgi-bin/private/DocDB/ShowDocument?.submit=Identifier& docid=G2000796&version=

[64] P. Hello and J.-Y. Vinet, "Analytical models of thermal aberrations in massive mirrors heated by high power laser beams," *Journal de Physique*, vol. 51, no. 12, pp. 1267–1282, 1990. [Online]. Available: https://hal.archives-ouvertes.fr/jpa-00212444

[65] W. Jia, H. Yamamoto, K. Kuns, A. Effler, M. Evans, P. Fritschel, and et al., "Point absorber limits to future gravitational-wave detectors," *Phys. Rev. Lett.*, vol. 127, p. 241102, Dec 2021. [Online]. Available: https://link.aps.org/doi/10.1103/PhysRevLett.127.241102

[66] M. Abramowitz and I. A. Stegun, Eds., *Handbook of Mathematical Functions with Formulas, Graphs and Mathematical Tables.* New York: Dover Publications, Inc., 1965.

[67] F. Oberhettinger, *Tables of Bessel transforms / Fritz Oberhettinger.* Springer-Verlag Berlin, 1972.

[68] K. Thorne, "Light scattering and proposed baffle configuration for the ligo," *LIGO Document T890017-x0*, Jan 2021. [Online]. Available: https://dcc.ligo.org/DocDB/0028/T890017/000/ T890017-00.pdf

[69] J.-Y. Vinet, V. Brisson, and S. Braccini, "Scattered light noise in gravitational wave interferometric detectors: Coherent effects," *Phys. Rev. D*, vol. 54, pp. 1276–1286, Jul 1996. [Online]. Available: https://link.aps.org/doi/10.1103/PhysRevD.54.1276

[70] J. C. Stover, *Optical Scattering: Measurement and Analysis*, second edition ed. Bellingham, Wash., USA : SPIE Optical Engineering Press, 1995. [Online]. Available: https://www.spiedigitallibrary.org/ebooks/PM/ Optical-Scattering-Measurement-and-Analysis-Second-Edition/eISBN-9780819478443/10. 1117/3.203079

[71] F. E. Nicodemus, J. C. Richmond, J. J. Hsia, I. W. Ginsberg, and T. Limperis, *Geometrical Considerations and Nomenclature for Reflectance.* USA: Jones and Bartlett Publishers, Inc., 1992, p. 94–145.

[72] W. Jia, A. Effler, and V. Frolov, "Scattered light in the ligo livingston arm cavities," *LIGO Document T1800224-v1*, Mar 2019. [Online]. Available: https://dcc.ligo.org/cgi-bin/private/ DocDB/ShowDocument?.submit=Identifier&docid=T1800224&version=

[73] and J Aasi, B. P. Abbott, R. Abbott, T. Abbott, M. R. Abernathy, K. Ackley, C. Adams, T. Adams, P. Addesso, R. X. Adhikari, V. Adya, C. Affeldt, and N. A. and, "Advanced LIGO," *Classical and Quantum Gravity*, vol. 32, no. 7, p. 074001, mar 2015. [Online]. Available: https://doi.org/10.1088/0264-9381/32/7/074001

[74] F. Acernese, M. Agathos, L. Aiello, A. Allocca, A. Amato, S. Ansoldi, S. Antier, M. Arène, N. Arnaud, and e. a. Ascenzi, "Increasing the astrophysical reach of the advanced virgo detector via the application of squeezed vacuum states of light," *Phys. Rev. Lett.*, vol. 123, p. 231108, Dec 2019. [Online]. Available: https://link.aps.org/doi/10.1103/PhysRevLett.123.231108

[75] A. Romero-Rodríguez, A. Allocca, A. Chiummo, M. Martínez, L. M. Mir, and H. Yamamoto, "Determination of the light exposure on the photodiodes of a new instrumented baffle for the virgo input mode cleaner end-mirror," *Classical and Quantum Gravity*, vol. 38, no. 4, p. 045002, dec 2020. [Online]. Available: https://doi.org/10.1088/1361-6382/abce6b

[76] O. Ballester, O. Blanch, L. Cardiel, M. Cavalli-Sforza, A. Chiummo, C. García, J. M. Illa, C. Karathanasis, M. Kolstein, M. Martínez, A. Menéndez-Vázquez, L. M. Mir, J. Mundet, A. Romero-Rodríguez, D. Serrano, and H. Yamamoto, "Measurement of the stray light in the advanced virgo input mode cleaner cavity using an instrumented baffle," *Classical and Quantum Gravity*, vol. 39, no. 11, p. 115011, may 2022. [Online]. Available: https://doi.org/10.1088/1361-6382/ac6a9d

[77] F. Acernese, P. Amico, N. Arnaud, D. Babusci, R. Barille, F. Barone, L. Barsotti, M. Barsuglia, F. Beauville, M.-A. Bizouard, F. Bondu, L. Bosi, C. Bradaschia, L. Bracci, S. Braccini, A. Brillet, V. Brisson, L. Brocco, and M. Yvert, "Results of the virgo central interferometer commissioning," *Classical and Quantum Gravity*, vol. 21, p. S395, 02 2004.

[78] H. Yamamoto, M. Barton, B. Bhawal, M. Evans, and S. Yoshida, "Simulation tools for future interferometers," *Journal of Physics: Conference Series*, vol. 32, pp. 398–403, mar 2006. [Online]. Available: https://doi.org/10.1088/1742-6596/32/1/061

[79] P. Saulson, *Advanced Interferometric Gravitational-wave Detectors*, D. Reitze and H. Grote, Eds. WSP, 2019.

[80] J. Romano and N. Cornish, "Detection methods for stochastic gravitational-wave backgrounds: A unified treatment," *Living Reviews in Relativity*, vol. 20, 04 2017.

[81] C. Andrieu, N. Freitas, A. Doucet, and M. Jordan, "An introduction to mcmc for machine learning," *Machine Learning*, vol. 50, pp. 5–43, 01 2003.

[82] J. Skilling, "Nested sampling," *AIP Conference Proceedings*, vol. 735, no. 1, pp. 395–405, 2004. [Online]. Available: https://aip.scitation.org/doi/abs/10.1063/1.1835238

[83] V. Mandic, E. Thrane, S. Giampanis, and T. Regimbau, "Parameter estimation in searches for the stochastic gravitational-wave background," *Phys. Rev. Lett.*, vol. 109, p. 171102, Oct 2012. [Online]. Available: https://link.aps.org/doi/10.1103/PhysRevLett.109.171102

[84] G. J. Feldman and R. D. Cousins, "Unified approach to the classical statistical analysis of small signals," *Phys. Rev. D*, vol. 57, pp. 3873–3889, Apr 1998. [Online]. Available: https://link.aps.org/doi/10.1103/PhysRevD.57.3873

[85] H. Jeffreys, *Theory of Probability*, 3rd ed. Oxford, England: Oxford, 1961.

[86] R. Smith and E. Thrane, "Optimal search for an astrophysical gravitational-wave background," *Phys. Rev. X*, vol. 8, p. 021019, Apr 2018. [Online]. Available: https://link.aps.org/doi/10.1103/PhysRevX.8.021019

[87] W. Penny, J. Mattout, and N. Trujillo-Barreto, "Chapter 35 - bayesian model selection and averaging," in *Statistical Parametric Mapping*, K. FRISTON, J. ASHBURNER, S. KIEBEL, T. NICHOLS, and W. PENNY, Eds. London: Academic Press, 2007, pp. 454–467. [Online]. Available: https://www.sciencedirect.com/science/article/pii/B9780123725608500358

[88] B. Allen and J. D. Romano, "Detecting a stochastic background of gravitational radiation: Signal processing strategies and sensitivities," *Phys. Rev. D*, vol. 59, p. 102001, Mar 1999. [Online]. Available: https://link.aps.org/doi/10.1103/PhysRevD.59.102001

[89] N. J. Cornish and J. D. Romano, "When is a gravitational-wave signal stochastic?" *Physical Review D*, vol. 92, p. 042001, 2015.

[90] A. C. Jenkins, "Cosmology and fundamental physics in the era of gravitational-wave astronomy," *arXiv:2202.05105 [gr-qc]*, 2022.

[91] B. Allen, "The Stochastic gravity wave background: Sources and detection," in *Les Houches School of Physics: Astrophysical Sources of Gravitational Radiation*, 4 1996, pp. 373–417.

[92] L. ISSERLIS, "ON A FORMULA FOR THE PRODUCT-MOMENT COEFFICIENT OF ANY ORDER OF A NORMAL FREQUENCY DISTRIBUTION IN ANY NUMBER OF VARIABLES," *Biometrika*, vol. 12, no. 1-2, pp. 134–139, 11 1918. [Online]. Available: https://doi.org/10.1093/biomet/12.1-2.134

[93] V. Kalogera, B. Sathyaprakash, M. Bailes, M.-A. Bizouard, A. Buonanno, A. Burrows, M. Colpi, M. Evans, S. Fairhurst, S. Hild, M. Kasliwal, L. Lehner, I. Mandel, V. Mandic, S. Nissanke, M. Papa, S. Reddy, S. Rosswog, C. Van Den Broeck, and J. van den Brand, "The next generation global gravitational wave observatory: The science book," 11 2021.

[94] B. P. Abbott, R. Abbott, T. D. Abbott, M. R. Abernathy, F. Acernese, K. Ackley, C. Adams, T. Adams, P. Addesso, and R. e. a. Adhikari, "Upper limits on the stochastic gravitational-wave background from advanced ligo's first observing run," *Phys. Rev. Lett.*, vol. 118, p. 121101, Mar 2017. [Online]. Available: https://link.aps.org/doi/10.1103/PhysRevLett.118.121101

[95] P. D. Lasky, C. M. F. Mingarelli, T. L. Smith, J. T. Giblin, E. Thrane, D. J. Reardon, R. Caldwell, M. Bailes, N. D. R. Bhat, S. Burke-Spolaor, S. Dai, J. Dempsey, G. Hobbs, M. Kerr, Y. Levin, R. N. Manchester, S. Osłowski, V. Ravi, P. A. Rosado, R. M. Shannon, R. Spiewak, W. van Straten, L. Toomey, J. Wang, L. Wen, X. You, and X. Zhu, "Gravitational-wave cosmology across 29 decades in frequency," *Phys. Rev. X*, vol. 6, p. 011035, Mar 2016. [Online]. Available: https://link.aps.org/doi/10.1103/PhysRevX.6.011035

[96] E. Thrane and J. D. Romano, "Sensitivity curves for searches for gravitational-wave backgrounds," *Phys. Rev. D*, vol. 88, p. 124032, Dec 2013. [Online]. Available: https://link.aps.org/doi/10.1103/PhysRevD.88.124032

[97] B. P. Abbott, R. Abbott, T. D. Abbott, M. R. Abernathy, F. Acernese, K. Ackley, C. Adams, T. Adams, P. Addesso, and R. e. a. Adhikari, "Gw150914: Implications for the stochastic gravitational-wave background from binary black holes," *Phys. Rev. Lett.*, vol. 116, p. 131102, Mar 2016. [Online]. Available: https://link.aps.org/doi/10.1103/PhysRevLett.116.131102

[98] B. P. Abbott, R. Abbott, T. D. Abbott, M. R. Abernathy, K. Ackley, C. Adams, P. Addesso, R. X. Adhikari, and at al, "Exploring the sensitivity of next generation gravitational wave detectors," *Classical and Quantum Gravity*, vol. 34, no. 4, p. 044001, jan 2017. [Online]. Available: https://doi.org/10.1088/1361-6382/aa51f4

[99] M. Fitz Axen, S. Banagiri, A. Matas, C. Caprini, and V. Mandic, "Multiwavelength observations of cosmological phase transitions using lisa and cosmic explorer," *Phys. Rev. D*, vol. 98, p. 103508, Nov 2018. [Online]. Available: https://link.aps.org/doi/10.1103/PhysRevD.98.103508

[100] B. P. e. a. Abbott, "Gw170817: Implications for the stochastic gravitational-wave background from compact binary coalescences," *Phys. Rev. Lett.*, vol. 120, p. 091101, Feb 2018. [Online]. Available: https://link.aps.org/doi/10.1103/PhysRevLett.120.091101

[101] T. Callister, L. Sammut, S. Qiu, I. Mandel, and E. Thrane, "Limits of astrophysics with gravitational-wave backgrounds," *Phys. Rev. X*, vol. 6, p. 031018, Aug 2016. [Online]. Available: https://link.aps.org/doi/10.1103/PhysRevX.6.031018

[102] K. Martinovic, P. Meyers, M. Sakellariadou, and N. Christensen, "Simultaneous estimation of astrophysical and cosmological stochastic gravitational-wave backgrounds with terrestrial detectors," *Physical Review D*, vol. 103, 02 2021.

[103] S. Marassi, R. Schneider, and V. Ferrari, "Gravitational wave backgrounds and the cosmic transition from Population III to Population II stars," *Monthly Notices of the Royal Astronomical Society*, vol. 398, no. 1, pp. 293–302, 08 2009. [Online]. Available: https://doi.org/10.1111/j.1365-2966.2009.15120.x

[104] J. e. a. Aasi, "Searching for stochastic gravitational waves using data from the two colocated ligo hanford detectors," *Phys. Rev. D*, vol. 91, p. 022003, Jan 2015. [Online]. Available: https://link.aps.org/doi/10.1103/PhysRevD.91.022003

[105] A. Matas, "Conventions for stochastic searches," *LIGO Document T2100181-v1*, Apr 2021. [Online]. Available: https://dcc.ligo.org/DocDB/0175/T2100181/001/representations_of_data.pdf

[106] A. Matas and J. Romano, "Frequentist versus bayesian analyses: Cross-correlation as an approximate sufficient statistic for ligo-virgo stochastic background searches," *Physical Review D*, vol. 103, 03 2021.

[107] T. Callister, A. Biscoveanu, N. Christensen, M. Isi, A. Matas, O. Minazzoli, T. Regimbau, M. Sakellariadou, J. Tasson, and E. Thrane, "Polarization-based tests of gravity with the stochastic gravitational-wave background," *Physical Review X*, vol. 7, 12 2017.

[108] S. Vitale, C.-J. Haster, L. Sun, B. Farr, E. Goetz, J. Kissel, and C. Cahillane, "Physical approach to the marginalization of ligo calibration uncertainties," *Phys. Rev. D*, vol. 103, p. 063016, Mar 2021. [Online]. Available: https://link.aps.org/doi/10.1103/PhysRevD.103.063016

[109] L. Sun, E. Goetz, J. S. Kissel, J. Betzwieser, S. Karki, A. Viets, M. Wade, D. Bhattacharjee, V. Bossilkov, P. B. Covas, L. E. H. Datrier, R. Gray, S. Kandhasamy, Y. K. Lecoeuche, G. Mendell, T. Mistry, E. Payne, R. L. Savage, A. J. Weinstein, S. Aston, A. Buikema, C. Cahillane, J. C. Driggers, S. E. Dwyer, R. Kumar, and A. Urban, "Characterization of systematic error in advanced LIGO calibration," *Classical and Quantum Gravity*, vol. 37, no. 22, p. 225008, oct 2020. [Online]. Available: https://doi.org/10.1088/1361-6382/abb14e

[110] J. Whelan, E. Robinson, J. Romano, and E. Thrane, "Treatment of calibration uncertainty in multi-baseline cross-correlation searches for gravitational waves," *Journal of Physics: Conference Series*, vol. 484, 05 2012.

[111] C. J. Moore, R. H. Cole, and C. P. L. Berry, "Gravitational-wave sensitivity curves," *Classical and Quantum Gravity*, vol. 32, no. 1, p. 015014, dec 2014. [Online]. Available: https://doi.org/10.1088/0264-9381/32/1/015014

[112] E. Thrane and J. Romano, "Sensitivity curves for searches for gravitational-wave backgrounds," *Physical Review D*, vol. 88, 10 2013.

[113] B. Abbott, R. Abbott, R. Adhikari, A. Ageev, B. Allen, R. Amin, S. Anderson, W. Anderson, M. Araya, H. Armandula, F. Asiri, P. Aufmuth, C. Aulbert, S. Babak, R. Balasubramanian, S. Ballmer, B. Barish, D. Barker, C. Barker-Patton, and J. Zweizig, "Analysis of first ligo science data for stochastic gravitational waves," *Physical Review D*, vol. 69, p. 122004, 06 2004.

[114] B. O'Reilly, M. Branchesi, S. Haino, G. Gemme, M. Coughlin, and L. Singer, "Noise curves used for simulations in the update of the observing scenarios paper," *LIGO Document T2000012-v1*, Jan 2020. [Online]. Available: https://dcc.ligo.org/LIGO-T2000012-v1

[115] J. Zweizig and K. Riles, "Information on self-gating of $h(t)$ used in o3 continuous-wave and stochastic searches," *LIGO Document T2000384-v4*, Jan 2021. [Online]. Available: https://dcc.ligo.org/DocDB/0168/T2000384/004/SelfGatingDetails.pdf

[116] R. Abbott, T. D. Abbott, S. Abraham, F. Acernese, K. Ackley, A. Adams, C. Adams, R. X. Adhikari, V. B. Adya, Affeldt, and et al., "Gwtc-2: Compact binary coalescences observed by ligo and virgo during the first half of the third observing run," *Phys. Rev. X*, vol. 11, p. 021053, Jun 2021. [Online]. Available: https://link.aps.org/doi/10.1103/PhysRevX.11.021053

[117] K. Janssens, K. Martinovic, N. Christensen, P. M. Meyers, and M. Sakellariadou, "Impact of schumann resonances on the einstein telescope and projections for the magnetic coupling function," *Phys. Rev. D*, vol. 104, p. 122006, Dec 2021. [Online]. Available: https://link.aps.org/doi/10.1103/PhysRevD.104.122006

[118] E. Thrane, N. Christensen, and R. M. S. Schofield, "Correlated magnetic noise in global networks of gravitational-wave detectors: Observations and implications," *Phys. Rev. D*, vol. 87, p. 123009, Jun 2013. [Online]. Available: https://link.aps.org/doi/10.1103/PhysRevD.87.123009

[119] E. Thrane, N. Christensen, R. M. S. Schofield, and A. Effler, "Correlated noise in networks of gravitational-wave detectors: Subtraction and mitigation," *Phys. Rev. D*, vol. 90, p. 023013, Jul 2014. [Online]. Available: https://link.aps.org/doi/10.1103/PhysRevD.90.023013

[120] T. A. Callister, M. W. Coughlin, and J. B. Kanner, "Gravitational-wave geodesy: A new tool for validating detection of the stochastic gravitational-wave background," *The Astrophysical Journal*, vol. 869, no. 2, p. L28, dec 2018. [Online]. Available: https://doi.org/10.3847/2041-8213/aaf3a5

[121] K. Janssens, T. A. Callister, N. Christensen, M. W. Coughlin, I. Michaloliakos, J. Suresh, and N. van Remortel, "Gravitational-wave geodesy: Defining false alarm probabilities with respect to correlated noise," *Phys. Rev. D*, vol. 105, p. 082001, Apr 2022. [Online]. Available: https://link.aps.org/doi/10.1103/PhysRevD.105.082001

[122] B. P. Abbott, R. Abbott, T. D. Abbott, S. Abraham, F. Acernese, K. Ackley, C. Adams, V. B. Adya, C. Affeldt, and M. e. a. Agathos, "Search for the isotropic stochastic background using data from advanced ligo's second observing run," *Phys. Rev. D*, vol. 100, p. 061101, Sep 2019. [Online]. Available: https://link.aps.org/doi/10.1103/PhysRevD.100.061101

[123] B. P. Abbott, R. Abbott, T. D. Abbott, M. R. Abernathy, F. Acernese, K. Ackley, C. Adams, T. Adams, P. Addesso, and R. X. A. et al, "Effects of data quality vetoes on a search for compact binary coalescences in advanced LIGO's first observing run," *Classical and Quantum Gravity*, vol. 35, no. 6, p. 065010, feb 2018. [Online]. Available: https://doi.org/10.1088/1361-6382/aaaafa

[124] D. Meacher, M. Coughlin, S. Morris, T. Regimbau, N. Christensen, S. Kandhasamy, V. Mandic, J. D. Romano, and E. Thrane, "Mock data and science challenge for detecting an astrophysical stochastic gravitational-wave background with advanced ligo and advanced virgo," *Phys. Rev. D*, vol. 92, p. 063002, Sep 2015. [Online]. Available: https://link.aps.org/doi/10.1103/PhysRevD.92.063002

[125] J. Buchner, A. Georgakakis, K. Nandra, L.-T. Hsu, C. Rangel, M. Brightman, A. Merloni, M. Salvato, J. Donley, and D. Kocevski, "X-ray spectral modelling of the agn obscuring region in the cdfs: Bayesian model selection and catalogue," *Astronomy Astrophysics*, vol. 564, 01 2014.

[126] F. Feroz and M. P. Hobson, "Multimodal nested sampling: an efficient and robust alternative to Markov Chain Monte Carlo methods for astronomical data analyses," *Monthly Notices of the Royal Astronomical Society*, vol. 384, no. 2, pp. 449–463, 01 2008. [Online]. Available: https://doi.org/10.1111/j.1365-2966.2007.12353.x

[127] T. Callister, M. Fishbach, D. E. Holz, and W. M. Farr, "Shouts and murmurs: Combining individual gravitational-wave sources with the stochastic background to measure the history of binary black hole mergers," *The Astrophysical Journal*, vol. 896, no. 2, p. L32, jun 2020. [Online]. Available: https://doi.org/10.3847/2041-8213/ab9743

[128] M. Satoh, S. Kanno, and J. Soda, "Circular polarization of primordial gravitational waves in string-inspired inflationary cosmology," *Phys. Rev. D*, vol. 77, p. 023526, Jan 2008. [Online]. Available: https://link.aps.org/doi/10.1103/PhysRevD.77.023526

[129] N. Barnaby and M. Peloso, "Large non-gaussianity in axion inflation," *Phys. Rev. Lett.*, vol. 106, p. 181301, May 2011. [Online]. Available: https://link.aps.org/doi/10.1103/PhysRevLett.106.181301

[130] M. Kamionkowski, A. Kosowsky, and M. S. Turner, "Gravitational radiation from first-order phase transitions," *Phys. Rev. D*, vol. 49, pp. 2837–2851, Mar 1994. [Online]. Available: https://link.aps.org/doi/10.1103/PhysRevD.49.2837

[131] N. Seto and A. Taruya, "Measuring a parity-violation signature in the early universe via ground-based laser interferometers," *Phys. Rev. Lett.*, vol. 99, p. 121101, Sep 2007. [Online]. Available: https://link.aps.org/doi/10.1103/PhysRevLett.99.121101

[132] K. Martinovic, C. Badger, M. Sakellariadou, and V. Mandic, "Searching for parity violation with the ligo-virgo-kagra network," *Physical Review D*, vol. 104, 10 2021.

[133] S. G. Crowder, R. Namba, V. Mandic, S. Mukohyama, and M. Peloso, "Measurement of Parity Violation in the Early Universe using Gravitational-wave Detectors," *Phys. Lett. B*, vol. 726, pp. 66–71, 2013.

[134] S. E. Gossan, P. Sutton, A. Stuver, M. Zanolin, K. Gill, and C. D. Ott, "Observing gravitational waves from core-collapse supernovae in the advanced detector era," *Phys. Rev. D*, vol. 93, p. 042002, Feb 2016. [Online]. Available: https://link.aps.org/doi/10.1103/PhysRevD.93.042002

[135] T. Damour and G. Esposito-Farese, "Tensor-multi-scalar theories of gravitation," *Classical and Quantum Gravity*, vol. 9, no. 9, pp. 2093–2176, sep 1992. [Online]. Available: https://doi.org/10.1088/0264-9381/9/9/015

[136] T. Damour and A. Vilenkin, "Cosmic strings and the string dilaton," *Phys. Rev. Lett.*, vol. 78, pp. 2288–2291, Mar 1997. [Online]. Available: https://link.aps.org/doi/10.1103/PhysRevLett.78.2288

[137] M. Maggiore, "Gravitational wave experiments and early universe cosmology," *Physics Reports*, vol. 331, no. 6, pp. 283–367, 2000. [Online]. Available: https://www.sciencedirect.com/science/article/pii/S0370157399001027

[138] D. Croon, T. Gonzalo, L. Graf, N. Košnik, and G. White, "Gut physics in the era of the lhc," 03 2019.

[139] S. J. Huber, T. Konstandin, G. Nardini, and I. Rues, "Detectable gravitational waves from very strong phase transitions in the general NMSSM," *Journal of Cosmology and Astroparticle Physics*, vol. 2016, no. 03, pp. 036–036, mar 2016. [Online]. Available: https://doi.org/10.1088/1475-7516/2016/03/036

[140] P. Huang, A. J. Long, and L.-T. Wang, "Probing the electroweak phase transition with higgs factories and gravitational waves," *Phys. Rev. D*, vol. 94, p. 075008, Oct 2016. [Online]. Available: https://link.aps.org/doi/10.1103/PhysRevD.94.075008

[141] A. Hebecker, J. Jaeckel, F. Rompineve, and L. Witkowski, "Gravitational waves from axion monodromy," *Journal of Cosmology and Astroparticle Physics*, vol. 2016, 06 2016.

[142] R. Jinno and M. Takimoto, "Probing a classically conformal $b-l$ model with gravitational waves," *Phys. Rev. D*, vol. 95, p. 015020, Jan 2017. [Online]. Available: https://link.aps.org/doi/10.1103/PhysRevD.95.015020

[143] V. Brdar, L. Graf, A. J. Helmboldt, and X.-J. Xu, "Gravitational waves as a probe of left-right symmetry breaking," *Journal of Cosmology and Astroparticle Physics*, vol. 2019, no. 12, pp. 027–027, dec 2019. [Online]. Available: https://doi.org/10.1088/1475-7516/2019/12/027

[144] A. Romero, K. Martinovic, T. A. Callister, H.-K. Guo, M. Martínez, M. Sakellariadou, F.-W. Yang, and Y. Zhao, "Implications for first-order cosmological phase transitions from the third ligo-virgo observing run," *Phys. Rev. Lett.*, vol. 126, p. 151301, Apr 2021. [Online]. Available: https://link.aps.org/doi/10.1103/PhysRevLett.126.151301

[145] B. Harling, A. Pomarol, O. Pujolas, and F. Rompineve, "Peccei-quinn phase transition at ligo," *Journal of High Energy Physics*, vol. 2020, 04 2020.

[146] R. D. Peccei and H. R. Quinn, "Constraints imposed by CP conservation in the presence of pseudoparticles," *Phys. Rev. D*, vol. 16, pp. 1791–1797, Sep 1977. [Online]. Available: https://link.aps.org/doi/10.1103/PhysRevD.16.1791

[147] A. Barrau, "Primordial black holes as a source of extremely high energy cosmic rays," *Astroparticle Physics*, vol. 12, no. 4, pp. 269–275, 2000. [Online]. Available: https://www.sciencedirect.com/science/article/pii/S0927650599001036

[148] D. B. Cline, D. A. Sanders, and W. Hong, "Further evidence for some gamma-ray bursts consistent with primordial black hole evaporation," *The Astrophysical Journal*, vol. 486, no. 1, pp. 169–178, sep 1997. [Online]. Available: https://doi.org/10.1086/304480

[149] B. Carr, K. Kohri, Y. Sendouda, and J. Yokoyama, "Constraints on primordial black holes," *Reports on Progress in Physics*, vol. 84, no. 11, p. 116902, nov 2021. [Online]. Available: https://doi.org/10.1088/1361-6633/ac1e31

[150] A. Mazumdar and G. White, "Review of cosmic phase transitions: their significance and experimental signatures," *Reports on Progress in Physics*, vol. 82, no. 7, p. 076901, jun 2019. [Online]. Available: https://doi.org/10.1088/1361-6633/ab1f55

[151] S. Coleman, "Erratum: Fate of the false vacuum: semiclassical theory," *Phys. Rev. D*, vol. 16, pp. 1248–1248, Aug 1977. [Online]. Available: https://link.aps.org/doi/10.1103/PhysRevD.16.1248

[152] C. G. Callan and S. Coleman, "Fate of the false vacuum. ii. first quantum corrections," *Phys. Rev. D*, vol. 16, pp. 1762–1768, Sep 1977. [Online]. Available: https://link.aps.org/doi/10.1103/PhysRevD.16.1762

[153] A. Linde, "Fate of the false vacuum at finite temperature: Theory and applications," *Physics Letters B*, vol. 100, no. 1, pp. 37–40, 1981. [Online]. Available: https://www.sciencedirect.com/science/article/pii/0370269381902811

[154] M. Hindmarsh, S. J. Huber, K. Rummukainen, and D. J. Weir, "Shape of the acoustic gravitational wave power spectrum from a first order phase transition," *Phys. Rev. D*, vol. 96, p. 103520, Nov 2017. [Online]. Available: https://link.aps.org/doi/10.1103/PhysRevD.96.103520

[155] E. Witten, "Cosmic separation of phases," *Phys. Rev. D*, vol. 30, pp. 272–285, Jul 1984. [Online]. Available: https://link.aps.org/doi/10.1103/PhysRevD.30.272

[156] M. Hindmarsh, M. Lüben, J. Lumma, and M. Pauly, "Phase transitions in the early universe," *SciPost Physics Lecture Notes*, 02 2021.

[157] J. Ellis, M. Lewicki, and J. M. No, "Gravitational waves from first-order cosmological phase transitions: lifetime of the sound wave source," *Journal of Cosmology and Astroparticle Physics*, vol. 2020, no. 07, pp. 050–050, jul 2020. [Online]. Available: https://doi.org/10.1088/1475-7516/2020/07/050

[158] E. Harrison, "Masks of the universe," *Masks of the Universe, by Edward Harrison, Cambridge, UK: Cambridge University Press, 2011*, vol. 54, 11 2011.

[159] D. Weir, "Gravitational waves from a first order electroweak phase transition: a review," *Philosophical Transactions of The Royal Society A Mathematical Physical and Engineering Sciences*, vol. 376, 05 2017.

[160] P. S. B. Dev and A. Mazumdar, "Probing the scale of new physics by advanced ligo/virgo," *Phys. Rev. D*, vol. 93, p. 104001, May 2016. [Online]. Available: https://link.aps.org/doi/10.1103/PhysRevD.93.104001

[161] C. Caprini *et al.*, "Science with the space-based interferometer eLISA. II: Gravitational waves from cosmological phase transitions," *JCAP*, vol. 04, p. 001, 2016.

[162] M. Hindmarsh, M. Lüben, J. Lumma, and M. Pauly, "Phase transitions in the early universe," *SciPost Phys. Lect. Notes*, p. 24, 2021. [Online]. Available: https://scipost.org/10.21468/SciPostPhysLectNotes.24

[163] J. R. Espinosa, T. Konstandin, J. M. No, and G. Servant, "Energy Budget of Cosmological First-order Phase Transitions," *JCAP*, vol. 06, p. 028, 2010.

[164] H.-K. Guo, K. Sinha, D. Vagie, and G. White, "Phase transitions in an expanding universe: Stochastic gravitational waves in standard and non-standard histories," *Journal of Cosmology and Astroparticle Physics*, vol. 2021, pp. 001–001, 01 2021.

[165] R.-G. Cai and S.-J. Wang, "Effective picture of bubble expansion," *Journal of Cosmology and Astroparticle Physics*, vol. 2021, no. 03, p. 096, mar 2021. [Online]. Available: https://doi.org/10.1088/1475-7516/2021/03/096

[166] R. Jinno, H. Seong, M. Takimoto, and C. M. Um, "Gravitational waves from first-order phase transitions: ultra-supercooled transitions and the fate of relativistic shocks," *Journal of Cosmology and Astroparticle Physics*, vol. 2019, no. 10, pp. 033–033, oct 2019. [Online]. Available: https://doi.org/10.1088/1475-7516/2019/10/033

[167] D. Weir, "Gravitational waves from a first order electroweak phase transition: a review," *Philosophical Transactions of The Royal Society A Mathematical Physical and Engineering Sciences*, vol. 376, 05 2017.

[168] A. Kosowsky and M. S. Turner, "Gravitational radiation from colliding vacuum bubbles: Envelope approximation to many-bubble collisions," *Phys. Rev. D*, vol. 47, pp. 4372–4391, May 1993. [Online]. Available: https://link.aps.org/doi/10.1103/PhysRevD.47.4372

[169] C. Caprini, R. Durrer, T. Konstandin, and G. Servant, "General properties of the gravitational wave spectrum from phase transitions," *Phys. Rev. D*, vol. 79, p. 083519, Apr 2009. [Online]. Available: https://link.aps.org/doi/10.1103/PhysRevD.79.083519

[170] S. Hawking, "Gravitationally collapsed objects of very low mass," *Mon. Not. Roy. Astron. Soc.*, vol. 152, p. 75, 1971.

[171] L. Randall, M. Soljačić, and A. H. Guth, "Supernatural inflation: inflation from supersymmetry with no (very) small parameters," *Nuclear Physics B*, vol. 472, no. 1, pp. 377–405, 1996. [Online]. Available: https://www.sciencedirect.com/science/article/pii/0550321396001745

[172] M. Y. Khlopov, B. A. Malomed, and Y. B. Zeldovich, "Gravitational instability of scalar fields and formation of primordial black holes," *Monthly Notices of the Royal Astronomical Society*, vol. 215, no. 4, pp. 575–589, 08 1985. [Online]. Available: https://doi.org/10.1093/mnras/215.4.575

[173] A. C. Jenkins and M. Sakellariadou, "Primordial black holes from cusp collapse on cosmic strings," *arXiv: Cosmology and Nongalactic Astrophysics*, 2020.

[174] S. G. Rubin, M. Y. Khlopov, and A. S. Sakharov, "Primordial black holes from nonequilibrium second order phase transition," *Grav. Cosmol.*, vol. 6, pp. 51–58, 2000.

[175] B. J. Carr and S. W. Hawking, "Black Holes in the Early Universe," *Monthly Notices of the Royal Astronomical Society*, vol. 168, no. 2, pp. 399–415, 08 1974. [Online]. Available: https://doi.org/10.1093/mnras/168.2.399

[176] B. J. Carr, "The Primordial black hole mass spectrum," *Astrophys. J.*, vol. 201, pp. 1–19, 1975.

[177] I. Musco, "Threshold for primordial black holes: Dependence on the shape of the cosmological perturbations," *Phys. Rev. D*, vol. 100, p. 123524, Dec 2019. [Online]. Available: https://link.aps.org/doi/10.1103/PhysRevD.100.123524

[178] V. Vaskonen and H. Veermäe, "Did nanograv see a signal from primordial black hole formation?" *Phys. Rev. Lett.*, vol. 126, p. 051303, Feb 2021. [Online]. Available: https://link.aps.org/doi/10.1103/PhysRevLett.126.051303

[179] S. Young, "The primordial black hole formation criterion re-examined: Parametrisation, timing and the choice of window function," *International Journal of Modern Physics D*, vol. 29, 10 2019.

[180] M. W. Choptuik, "Universality and scaling in gravitational collapse of a massless scalar field," *Phys. Rev. Lett.*, vol. 70, pp. 9–12, Jan 1993. [Online]. Available: https://link.aps.org/doi/10.1103/PhysRevLett.70.9

[181] B. Carr and F. Kuhnel, "Primordial Black Holes as Dark Matter: Recent Developments," *Ann. Rev. Nucl. Part. Sci.*, vol. 70, pp. 355–394, 2020.

[182] N. Aghanim, Y. Akrami, M. Ashdown, J. Aumont, C. Baccigalupi, M. Ballardini, A. Banday, R. Barreiro, N. Bartolo, S. Basak, R. Battye, K. Benabed, J.-P. Bernard, M. Bersanelli, P. Bielewicz, J. Bock, J. Bond, J. Borrill, F. Bouchet, and A. Zonca, "Planck 2018 results: Vi. cosmological parameters," *Astronomy Astrophysics*, vol. 641, 09 2020.

[183] S. Matarrese, O. Pantano, and D. Saez, "General relativistic dynamics of irrotational dust: Cosmological implications," *Phys. Rev. Lett.*, vol. 72, pp. 320–323, Jan 1994. [Online]. Available: https://link.aps.org/doi/10.1103/PhysRevLett.72.320

[184] S. Kapadia, K. Pandey, T. Suyama, S. Kandhasamy, and P. Ajith, "Search for the stochastic gravitational-wave background induced by primordial curvature perturbations in ligo's second observing run," 09 2020.

[185] J. S. Bullock and J. R. Primack, "Non-gaussian fluctuations and primordial black holes from inflation," *Phys. Rev. D*, vol. 55, pp. 7423–7439, Jun 1997. [Online]. Available: https://link.aps.org/doi/10.1103/PhysRevD.55.7423

[186] M. Lewicki, O. Pujolas, and V. Vaskonen, "Escape from supercooling with or without bubbles: gravitational wave signatures," 06 2021.

[187] K. Inomata and T. Terada, "Gauge independence of induced gravitational waves," *Physical Review D*, vol. 101, 01 2020.

[188] K. Kohri and T. Terada, "Semianalytic calculation of gravitational wave spectrum nonlinearly induced from primordial curvature perturbations," *Phys. Rev. D*, vol. 97, p. 123532, Jun 2018. [Online]. Available: https://link.aps.org/doi/10.1103/PhysRevD.97.123532

[189] L. Pagano, L. Salvati, and A. Melchiorri, "New constraints on primordial gravitational waves from planck 2015," *Physics Letters B*, vol. 760, pp. 823–825, 2016. [Online]. Available: https://www.sciencedirect.com/science/article/pii/S0370269316304191

[190] S. Young, I. Musco, and C. T. Byrnes, "Primordial black hole formation and abundance: contribution from the non-linear relation between the density and curvature perturbation," *JCAP*, vol. 11, p. 012, 2019.

[191] A. Romero-Rodríguez, M. Martínez, O. Pujolàs, M. Sakellariadou, and V. Vaskonen, "Search for a scalar induced stochastic gravitational wave background in the third ligo-virgo observing run," *Phys. Rev. Lett.*, vol. 128, p. 051301, Feb 2022. [Online]. Available: https://link.aps.org/doi/10.1103/PhysRevLett.128.051301

[192] R. Drever, J. Hall, F. Kowalski, J. Hough, G. Ford, A. Munley, and H. Ward, "Laser phase and frequency stabilization using an optical resonator," *Appl. Phys. B*, vol. 31, pp. 97–105, 06 1983.